UNIVERSITY OF OXFORD
DEPARTMENT OF MATERIALS

JONATHAN QUINSON
KEBLE COLLEGE

Tailored Carbon-based Nanomaterials for Biological Energy Electrocatalysis

A dissertation submitted in partial fullfilment of the requirement
for the degree of **Doctor of Philosophy in Materials Science**

Trinity Term 2015

I confirm that the work presented in this dissertation is my own. Where information has been derived from other sources, I confirm that this has been indicated in the dissertation.

Abstract

Hydrogenases are energy relevant bio-electrocatalysts. Their study and applications require immobilisation on carbon scaffolds and benefit from carbon materials design. The present thesis first compares eleven carbon materials for the adsorption of hydrogenase-1 from *E. coli*. All of them accommodate the enzyme in an electroactive configuration. A high surface area and/or abundance of 'edge' carbon planes are identified as important features to improve studies and applications of hydrogenases. The nanomaterials screened facilitate the coupling of infrared spectroscopy and electrochemistry for study of adsorbed species. This is demonstrated for the first time with a flavin mononucleotide molecule and the hydrogenase and opens the way to unprecedented investigation of (bio)electrocatalysts.

In situ growth of multi-wall carbon nanotubes (MWCNTs) inside quartz columns by aerosol assisted chemical vapour deposition (AACVD) is investigated. Control over the column filling and the thickness of the MWCNT forest profile along the column is achieved. The flow rate of carrier gas is identified as a key parameter for this control. The final structures obtained are columns with their inner walls covered with a porous, interconnected and conductive carbon network. Through H_2-driven biocatalysis, the conversion of acetophenone to 1-phenylethanol is achieved in a flow reactor configuration. The MWCNT columns are shown to be successful and simple, yet versatile, platforms for flow (bio/electro)catalysis.

Finally, large quantities of hetero-MWCNTs are obtained by an original combination of AACVD and chemical vapour deposition. The MWCNTs are extensively characterised and display continuous junctions between nitrogen-doped and un-doped sections along a single MWCNT. The controlled change of chemical properties but also graphitic structure obtained is exploited for the first time to perform spontaneous and selective (1) oxidation reactions and (2) immobilisation of platinum particles on different parts of a single MWCNT. This new approach could be relevant for localised immobilisation of enzymes along a nanomaterial.

This thesis achieves three different degree of carbon nanomaterials design to develop scaffolds suitable for bio-electrocatalyst immobilisation in targeted applications.

Acknowledgements

To start with, I would like to thank my two supervisors: Prof Kylie A. Vincent, for accepting me in the first place within her group despite the absence of funding, and subsequently for arranging a collaborative project with Prof Nicole Grobert to make it possible for me to join The University of Oxford. I would like to thank Prof Nicole Grobert for giving me a chance to learn about nanomaterials and to be part of her group.

A bit more than 3 years working in two different groups + different groups in different departments = a lot of people to thank. I hope to forget no one and would like to thank those who helped me on a daily basis, those who helped me more sporadically and those who did not helped, because nevertheless they are all part of my PhD experience. I do not wish to thank specifically anyone here, I believe that each person mentioned in the next lines knows I will always appreciate what they mean to me.

With no logical order, I would like to thank: Dr Philip A. Ash (*UK*), Dr Frank Dillon (*Ireland*), Dr Antal A. Koós (*Hungary*), Dr Seyyed Shayan Meysami (*Iran*) , Dr Zabeada Aslam *(UK*), Dr Geoffrey Otieno (*Kenya*), Dr Rebecca J. Nicholls (*UK*), Dr Laura Miranda (*Spain*), Dr Emilio Lopez (*Spain*), Dr Lavina Snoek (*Netherlands*), Dr Jingyu Sun (*China*), Dr Andrew Searle *(UK*), Dr Adrian Murdock (*Australia*), Dr Madhuri Dutta (*India*), Fatma Dinc (*Turkey*), Dr Juan G. Lozano (*Spain*), Teodor-Matei Cirstea (*Germany-Romania*), Nataliia Stepina (*Ukraine*), Arunvinay Prabakaran (*India*), Dr Jude Britton (*UK*), Vitaly Babenko (*Ukraine*), Karwei Soo (*BBC*), Christina Hookhan (*UK*), Anakha Ajayan (*US*), Sabina Caneva (*UK*), Chloe Guilbaud (*France*), Serena Bochereau (*France-US-Belgium*), Michelle Lim (*Malaysia*), Thomas F. Bottein (*France*), Benoit Grosjean (*France*), Christian van Engers (*Netherlands*), Tailor Uekert (*USA*), Remi Tanimoto (*Japan*), Duncan Johnstone (*UK*), Phillip Tucciarone (*US*), Ceren Zor (*Turkey*), Dr Zulkifli Idris *(Malaysia*), Dr Juan Liu (*China*), Charlotte McKenna (*UK*), George Lane (*UK*), Chris Lippard (*UK*), Jun Li (*China*), Dr Adam

Healy (*UK*), Dr Simantini Nayak (*India*), Dr Matteo Duca (*Italy*), Pathinan Paengnakorn (*Thailand*), Ben Bluestone (*UK*), Charlie Stevens (*UK*), Jenny Bradley (*UK*), Tom Lyle (*UK*), Lucie Dearlove (*UK*), Thomas Bloomfield (*UK*), Robert Spence (*UK*), Michael Ash (*UK*), Justin Weeks (*UK*), HysunSeo Park (*South Corea*), Dr Holly Reeve (*UK*), Dr Daniel Grabarczyk (*UK-Poland*), Tom Lonsdale (*UK*), Sergio Kogikowski Junior (*Brazil*), Benjamin Aucott (*UK*), Min-Wen Chung (*Taiwan*), Kouji Urata (*UK-Japan*), Eleanor Hall (*UK*), Chloe Tomlinson (*UK*), Ingvild Gudim (*Norway*), Ricardo Hidalgo (*Costa Rica*), Gary Chang (*Taiwan*), Theodore Silkstone Carter (*UK*), Lok Yi Lee (*China*), Ian McPherson (*UK*), Nathan Coutard (*France*), Richa Pandey (*India*), Laura O'Neil (*UK*), Vincent Tobin (*UK*).

Member of staff and technicians: Dr Robert Jacobs, Dr Colin Johnston, Mrs Gabriella Chapman, Dr Neil P. Young, Dr Alison Crossley, Mr Greg Cook, Ms Fay Chicken, Dr Gareth Hughes, Mr Chris Salter, Ms Marion Beckett, Mr Richard Tuner.

I also thank Keble College staff and funding schemes (Keble Association Fund, Faith Ivens-Franklin Travel Fund) as well as the EPSRC for the EPSRC-DTA award (EP/J500495/1) and the INSPIRE grant (EP/J015202/1) funding my time in Oxford. Big thank to the Keble College MCR and the Oxford University Rock 'n' Roll Dancesport Club for ongoing entertainment and support.

A last but important 'thank you' goes to all my family: without them I would not have gone through the thing I have gone through and this report would probably not be the same.

If I were optimistic I would be sad
Jonathan Quinson

To: "you, me, them, everybody, everybody"
The Blues Brothers

Table of contents

Number of words: *ca.* 62 400

Academic output

- **Published journal articles:**

[1] **Comparison of carbon materials as electrodes for enzyme electrocatalysis: hydrogenase as a case study**
Jonathan Quinson*; Ricardo Hidalgo; Philip A. Ash; Frank Dillon; Nicole Grobert; Kylie A. Vincent*
Faraday Discussions, **172**, 2014; Pages: 473-496, DOI:10.1039/C4FD00058G

[2] **Carbon electrode interfaces for synthesis, sensing and electrocatalysis: general discussion**
Yury Gogotsi; Richard McCreery; Stephen M. Lyth; Robert Dryfe; John Foord; Matěj Velický; Julie Macpherson; Matteo Duca; Katherine Holt; Manuel Alvarez-Guerra; Heisi Kurig ; Surbhi Sharma; Patrick R. Unwin; George Zheng Chen; Milo Shaffer; Taiwo Alaje; Robert Hamers; Mark Newton; Philip A. Ash; Keith Stevenson; Siegfried Waldvogel; Jingping Hu; Aleix Güell; ***Jonathan Quinson***
Faraday Discussions, **172**, 2014; Pages: 497-520, DOI: 10.1039/C4FD90038C

[3] **Immobilization of Magnetic Nanoparticles onto Conductive Surfaces Modified by Diazonium Chemistry**
Nadia Ktari; ***Jonathan Quinson****; Bruno Teste; Jean-Michel Siaugue; Frederic Kanoufi; Catherine Combellas*
LANGMUIR; Volume: 28; Issue: 34; Pages: 12671-12680; DOI: 10.1021/la302403z; 28 August 2012

- **Manuscripts in preparation or expected based on results obtained during the DPhil:**

[4] **Spectroscopic study of immobilized FMN under direct electrochemical control**
Jonathan Quinson*; Ricardo Hidalgo; Philip A. Ash; Kylie A. Vincent (co-authors and title TBC)*
IN PREPARATION

[5] **AACVD synthesis of MWCNT columns**
Jonathan Quinson*; Thomas F. Bottein; Frank Dillon; Nicole Grobert*
*IN PREPARATION (****Carbon****)*

[6] **Carbon nanotube columns for flow catalysis mediated by an enzyme cascade**
Jonathan Quinson*; Holly A. Reeve; Thomas F. Bottein; Kylie Vincent; Nicole Grobert*
*IN PREPARATION (****Advanced Functional Materials****)*

[7] **Unusual MWCNT structures obtained by AACVD**
Jonathan Quinson*; Nicole Grobert*
*IN PREPARATION (****Carbon****)*

[8] **Towards Janus Nano-Structures by designed MWCNT Forests: controlled immobilization of particles**
Jonathan Quinson*; Frank Dillon; Kylie A. Vincent; Nicole Grobert*
*IN PREPARATION (****Advanced Materials****)*

[9] **AACVD synthesis of MWCNT forests with intratubular junctions**
Jonathan Quinson*; Frank Dillon; Rebecca J. Nicholls; Antal A. Koós; Nicole Grobert*
*IN PREPARATION (****Carbon****)*

[10] **Multiple parameters study of MWCNTs grown by AACVD**
Seyyed Shayan Meysami; ***Jonathan Quinson****; Nicole Grobert (co-authors and title TBC)*
*IN PREPARATION (****Materials Today****)*

[11] **Synthesis of different multi-wall carbon nanotubes by aerosol-assisted chemical vapour deposition for fabrication of buckypaper**
Seyyed Shayan Meysami; Benoit Grosjean; ***Jonathan Quinson****; Nicole Grobert (co-authors and title TBC)*
IN PREPARATION

[12] **Synthesis, characterisation and electrocatalytic properties of FeCo nanoalloys**
Chris Lippard; Frank Dillon; ***Jonathan Quinson****; Nicole Grobert (co-authors and title TBC)*
IN PREPARATION

[13] **WS2 3D Nanoflowers with 2D Nanosheets as Electrocatalysts for Hydrogen Evolution Reaction (HER)**
Arunvinay Prabakaran; Frank Dillon; ***Jonathan Quinson****; Jodie Melbourne; Lewys Jones; Matteo Duca; Rebecca J. Nicholls; Jude Britton ; Antal A Koós; Kylie A. Vincent; Peter D. Nellist; Nicole Grobert*
IN PREPARATION

[14] **Magnetic MWCNT buckypaper for novel actuators**
Karwei So, ***Jonathan Quinson****, Frank Dillon; Nicole Grobert (co-authors and title TBC)*
EXPECTED

[15] **Electronic properties of MWCNTs with intra-tubular junctions**
Juan G. Lozano; ***Jonathan Quinson****; Nicole Grobert (co-authors and title TBC)*
EXPECTED

[16] **Carbon nanotube columns for electrocatalytic water remediation**
Ceren Zor; ***Jonathan Quinson****; Holly A. Reeve; Matteo Ducca, Kylie A. Vincent (co-authors and title TBC)*
EXPECTED

- **Talks:**

[1] **Solicited speaker** by the organisers for the 2nd Annual World Congress of Smart Materials-2016 (WCSM-2016), March *4-6,* 2016, Singapore
Solicited speaker by the organisers for the 4th Annual World Congress of Advanced Materials-2015 (WCAM-2015),May 27-29, 2015, Chongqing, China

[2] **Comparison of carbon materials as electrodes for enzyme electrocatalysis: hydrogenase as a case study**
Jonathan Quinson*; Ricardo Hidalgo; Philip A. Ash; Frank Dillon; Nicole Grobert; Kylie A. Vincent*
Faraday Discussions 172: carbon in electrochemistry, 28-30 July 2014-Sheffield, UK

[3] **Synthesis and Characterization of hetero-CNTs**
Jonathan Quinson*; Frank Dillon; Rebecca J. Nicholls; Antal A. Koós; Kylie A. Vincent; Nicole Grobert*
HeteroNanocarb2013 Conference, Castelldefels, Barcelona, Spain 22-26 September 2013
Co-winner of the **prize for the Best Young Researcher talk**.

[4] **Carbon: from soot and diamond to nanotechnology**
Jonathan Quinson
Talk given at Keble College in the context of the post-graduate students discussion evenings.
Informal talk aimed at reaching an audience of scientists and non-scientists. 14th May 2014

[5] **WS_2 3D Nanoflowers with 2D Nanosheets as Electrocatalysts for Hydrogen Evolution Reaction (HER)**
Arunvinay Prabakaran; Frank Dillon; ***Jonathan Quinson****; Jodie Melbourne; Lewys Jones*
Matteo Duca; Rebecca J. Nicholls; Jude Britton ; Antal A Koós; Kylie A. Vincent; Peter D. Nellist; Nicole Grobert
2015 MRS spring meeting, San Francisco, California, USA, 6-10 April 2015

- **Conference and symposium posters:**

[1] **Carbon-based materials for biological energy electrocatalysis**
Jonathan Quinson*; Ricardo Hidalgo; Philip A. Ash; Kylie A. Vincent; Nicole Grobert*
3rd Year DPhil students poster presentation, Department of Materials, The University of Oxford, United-Kingdom

[2] **Carbon-based materials for biological energy electrocatalysis**
Jonathan Quinson*; Kylie Vincent; Nicole Grobert*
NanoteC12 Conference, University of Sussex, Brighton, United-Kingdom, 29 August 2012- 1st September 2012

[3] **Electrocatalytic CO_2 reduction using modified electrodes**
Shlomi Elias; ***Jonathan Quinson****; George J. P. Britovsek; Anthony R. J. Kucernak*
242nd National Meeting of the American-Chemical-Society (ACS), Denver, CO; 28 August-01 September 2011

- **Acknowledged in:**

Breaking the Surface Selection Rule: *In situ* Observation of Formate Adsorbed on Nanoparticles during Formic Acid Electro-oxidation. *Ian McPherson, Philip A. Ash, Robert M.J. Jacobs, Kylie A. Vincent.* **Publication** *IN PREPARATION*

Holly A. Reeve, New approaches for cofactor recycling; application to chemical synthesis and electrochemical devices, **DPhil thesis**, The University of Oxford, 2014.

Adam J. Healy, Development of an Infrared spectroelectrochemical approach for studying hydrogenase active site chemistry, **DPhil thesis**, The University of Oxford, 2013.

Karwei So, Magnetic carbon nanostructures towards selective response macrostructures, 2nd year DPhil **talk**, 3rd March 2015, Oxford, UK.

Benoit Grosjean, Synthesis of different multi-wall carbon nanotubes by aerosol-assisted chemical vapour deposition for fabrication of buckypaper, **Master Project Report**, 2014.

Thomas F. Bottein, Carbon Nanotube columns for continuous catalysis and energy applications, **Master Project Report**, 2013.

Thomas Bloomfield, Developments towards IR spectroelectrochemistry for hydrogenase enzymes on composite carbon particles, **Part II thesis**, The University of Oxford, 2012.

Presentations from Kylie A. Vincent's group members:
Kylie A. Vincent, Ian McPherson, Gary Chang, Ricardo Hidalgo, Holly A. Reeve

Oxford University – KETEP, KIER (Korea Institute of Energy Research), KERI, 4th Annual **Workshop** project meeting, 2nd March 2015, St Hugh College Oxford, UK, attended by Prof Nicole Grobert who gave a talk using some of the data obtained during the DPhil.

EPSRC INSPIRE Award 2011 – research highlights: Robust Biocatalysis for Energy Solutions and Chemical Synthesis. **Poster** presented by Prof Vincent and Prof Grobert to highlight the research initiated after receiving the award. EPSCR meeting, 2014.

List of abbreviations and symbols

AACVD	Aerosol-Assisted Chemical Vapour Deposition
ADF	Annular Dark Field
ADH	Alcohol Dehydrogenase
AFM	Atomic Force Microscopy
APG	Abraded Pyrolytic Graphite
ATR	Attenuated Total Reflectance
BET	Brunauer-Emmett-Teller
BJH	Barrett-Joyner-Halenda
BP	Black Pearls 2000 (carbon powder)
BPS	4,4'-sulfonyldiphenol
C/N	MWCNT/(N-MWCNT) junction between an un-doped and a nitrogen-doped section within a single MWCNT
CE	Counter Electrode
CNC	Carbon Nanotube Column
CNP	Carbon Nano Powder
CNT	Carbon Nanotube
CVD	Chemical Vapour Deposition (technique)
Cys	Cysteine
DET	Direct Electron Transfer
EDS	Energy Dispersive X-ray Spectroscopy (sometimes referred to as EDX in the literature)
EELS	Energy Electron Loss Spectroscopy
FMN	Flavin Mononucleotide
GNF	Graphite Nano Fibers
HCCP	Phosphonitrilic chloride trimer (also called hexachlorocyclotriphosphazene)
HNP	Hydrothermal Nano Particles
HPLC	High Performance Liquid Chromatography
HRTEM	High Resolution Transmission Electron Microscope/Microscopy
Hyd-1	Hydrogenase-1 from *Escherichia coli* (*E. coli*)
ID	Inner Diameter
IR	Infrared
KPB	Potassium Phosphate Buffer
MB	Methylene Blue
MET	Mediated Electron Transfer
MG	Micron-sized graphite (flakes)
ML	Mogul L (carbon powder)
MV	Methylviologen
MWCNT	Multi-Wall Carbon Nanotube
N/C	N-MWCNT/MWCNT junction between nitrogen-doped and an un-doped section within a single MWCNT
NADH	Nicotinamide Adenine Dinucleotide
N-MWCNT	Nitrogen containing (or enriched in nitrogen, or doped with nitrogen) MWCNT also referred as CN_x in the literature
PG	Pyrolytic Graphite
PGE	Pyrolytic Graphite Edge (to qualify a PG electrode with the edge plane exposed)
PZS	Poly(cyclotriphosphazene-4,4’-sulfonildiphenol)

RDE	Rotating Disc Electrode
RE	Reference Electrode
rpm	Rotations Per Minute
sccm	Standard Cubic Centimetres per Minute
SCE	Standard Calomel Electrode (reference electrode)
SDS	Sodium Dodecyl Sulphate
SEM	Scanning Electron Microscope/Microscopy
SHE	Standard Hydrogen Electrode (reference electrode)
Si@C	Silicon core-Carbon shell (nanoparticles)
SWCNT	Single Wall Carbon Nanotube
m-SWCNT	metallic-SWCNT
s-SWCNT	semi-conducting SWCNT
TEA	Triethylamine
TEM	Transmission Electron Microscope/Microscopy
TGA	Thermogravimetric analysis
THF	Tetrahydrofuran
UV-vis	Ultraviolet-visible (spectroscopy)
XPS	X-ray photoelectron spectroscopy
VX	Vulcan XC72R
WE	Working Electrode

List of tables

List of figures

Chapter 1: Introduction

"What we find changes who we become."
Peter Morville

1.1. Outline

In the last 40 years, the world energy demand has increased by more than 50 % [1] due to a growing population and industrialisation of third world countries like China [1]. To match this demand not only reliable energy production but also responsible consumption and management are major challenges for mankind [2]. Indeed, about 80 % of our energy is currently obtained for from oil, coal and natural gas [1]. Their extraction by processes like mining and their conversion to energy by combustion produce undesirable green-house gases like carbon dioxide or methane which contribute to global-warming [2]. A consequence is dramatic climate changes with direct impact on the eco-system, for instance through ice melting in the north pole [3]. Also these rapid changes are putting at risk human lives, for example by favouring new diseases with no guarantee for human beings to have time to adapt [3]. In addition, fossil fuel stocks are depleting and geo-localised [2] for instance in the Middle-East. This raises political, military and economic concerns directly impacting citizens' daily life and cost-of living due to instability in the supply-demand balance. This has been illustrated over the last decades by the rising price of oil each time the political situation is unstable in the Middle-East, as for the 1979 energy crisis along with the Iranian Revolution [4]. To cover the remaining 20 % of energy provision, non-fossil sources are exploited. Nuclear accounts for 5 % [1] but raises safety concerns, for instance with the recent example of Fukushima central accident [5]. Another *ca.* 5 % comes from wind, solar, tidal or hydropower [1] but with technologies still at early stages of development and/or with limited geographical implementations, so not possible to develop worldwide [2].

A safe, sustainable and global way to produce energy would be greatly beneficial. At the same time, more efficient routes to consume the energy produced will help to ensure a stable balance in the energy supply/demand. An option to jointly achieve these two objectives is to get inspiration from Nature and bio-processes. One way to get inspiration from Nature is to use renewable feedstocks to produce bio-derived fuels. Biofuels, like bio-ethanol, already account for 10 % of the world energy production and can be produced by fermentation of plants matter by living organisms. Another way to get inspiration from Nature is to exploit biocatalysis to produce energy. For instance, enzymes and micro-organisms are efficient in producing electrons [6] by oxidation of sustainable feedstocks like glucose [7] or dihydrogen [8] and this has been a source of inspiration to develop fuel cells to produce electricity. Furthermore, biocatalysis is a growing area for production of chemicals. Biocatalysts can perform chemical transformation with low energy requirement, under mild conditions of pressure and temperature [9, 10]. This leads to relatively low energy demand and minimises energy waste, thus costs. Biocatalysts are also selective, which is important to ultimately reduce costs and to increase safety for consumers [11]. In drug industries for instance, selectivity limits the production of undesirable by-products which are possibly hazardous. Since selectivity limits the number of purification steps required before commercialisation of a safe drug, it also reduces the overall cost. Bio-processes then offer great opportunities to produce biofuels, electricity, and other fine chemicals like drugs. This is why between 2005-2007 bioprocesses already represented sales over US$ 187 billion in areas as diverse as bio-fuels industries, bio-pharmaceuticals, bio-chemicals or bio-food [10].

Due to the multiple benefits of biocatalysis, top industries like pharmaceutical companies, expressed over the recent years their will to increase the number of biocatalytic processes in their toolbox [10]. However, to develop more broadly the use of biocatalysts at

industrial scale, more research and development is required. This is for instance to propose cost-efficient options to improve properties like the life-time of devices, biocatalyst recovery and/or stability under different conditions of pH or temperature. These challenges can be addressed by selecting the right biocatalyst for the right purpose but also by the simple immobilisation of biocatalysts on supports [7, 12]. As a result, an important amount of academic research has been devoted in recent years to the design of supports for biocatalyst immobilisation like silica, polymer and carbon materials [12-14]. Carbon materials in particular are emerging candidates with multiple benefits combining compatibility with a range of biocatalysts, ease in chemical modification, stability over time and over a range of media with different pH and temperature [12, 15]. Moreover, since carbon materials are conductive, they are useful to immobilise bio-redox-catalysts. This class of biocatalysts facilitate redox half reactions thanks to electron transfers between the catalyst and a conductive electrode, or between different catalysts in electronic contact. For instance, research on enzyme fuel cells [12, 16] has been exploiting the property of bio-redox-catalysts immobilised on carbon to produce energy. In an enzyme fuel cell, an enzyme produces electrons by oxidation of a fuel which leads to the production of electricity, like the enzyme hydrogenase oxidising H_2 to produce electrons. Various other proof of concept studies in recent years have demonstrated that carbon materials are suitable supports for applications in a range of fields like bio-nanotechnology, biology, medicine, bio-electronics, bio-sensing or bio-energy [12, 15-18]. To best address different end-goals for each application, like high output current in enzyme-fuel-cells or high production yield in biocatalysis for synthesis, different properties from diverse carbon materials can be specifically exploited. These are for instance the size, the morphology or the specific surface area. Development of tailored carbon materials for targeted goals is then a key for future technologies.

The aim of this thesis is to open new opportunities in the immobilisation of enzymes by tailoring carbon materials across different length scales for specific goals. The relevance of different degrees of design to solve challenges in biocatalyst immobilisation is illustrated by the case study of a hydrogenase enzyme. Hydrogenases are bio-redox-catalysts able to split H_2 to H^+ and electrons or perform the reverse electrocatalytic reaction. Their activity can be studied and exploited in energy devices like fuel cells [19] or for the production of chemicals [20]. This is achieved once the enzymes are immobilised on conductive materials as detailed in **Chapter 1**. This introduction chapter stresses how different degrees of carbon material design are required to develop new methods of studies and emerging applications of immobilised enzymes. The materials and methods selected for this purpose are presented in **Chapter 2**.

First degree of design: powdered materials as electrode

A first degree of design consists of controlling the properties of individual materials, like size or surface area. Various carbon powders made of materials expressing different combinations of properties are used as electrodes and compared in **Chapter 3** for the adsorption of hydrogenase 1 from *Escherichia coli* (Hyd-1). The possible benefits from one material powder compared to another are explored to understand which properties are required to make a material an effective platform for hydrogenase immobilisation. It is shown that the atomic organisation in the carbon structure has an impact on the enzyme loading on the material. It is also shown that controlling the specific surface area of materials can improve the current obtained from enzyme electrocatalytic activity, which is relevant for instance for future optimisation of enzyme fuel cells.

Studies of enzymes also benefit from tailored materials. To contribute to the development of a technique coupling infrared spectroscopy and electrochemistry, carbon nanomaterials were investigated to study electroactive species directly adsorbed on carbon materials. The technique is expected to bring unique opportunities in the study of biocatalysts by

controlling the electrochemical activity of immobilised enzymes while recording spectroscopic signals to give information on catalytic mechanisms. In **Chapter 3**, by tailoring the materials used towards sub-micrometre size, a milestone in the development of the technique is achieved. Acquisition of spectroscopic data from species under direct electrochemical control after adsorption onto carbon material is presented, which opens the way to new studies for a range of electrocatalysts.

Second degree of design: carbon scaffolds

Carbon materials in the form of a powder are however not ideal for all applications and methods of studies of enzymes. For instance powdered materials are difficult to implement as catalyst supports in flow chemistry, where chemicals are produced by continuously passing a flow of reactants through a reactor. Since flow chemistry is expected to be increasingly implemented in industrial processes for chemical synthesis [10], a second degree of control is proposed to address the challenging use of carbon powder in flow systems. In **Chapter 4**, the design of carbon scaffolds consisting of vertically-aligned multi-wall carbon nanotube (MWCNT) forests directly grown on quartz substrates to create 'MWCNT columns' is detailed. The proposed design lead to extremely simple and yet versatile carbon scaffolds, demonstrated for the first time as suitable flow reactors for successful chemical transformations catalysed by enzymes.

Third degree of design: tailored materials for localised immobilisation in carbon scaffolds

Achieving the immobilisation of enzymes in a carbon scaffold is a first step. Getting spatial control on enzyme immobilisation within the scaffold is a difficult subsequent step that could lead to specialised applications and devices at the nanoscale. A novel approach to simple immobilisation of objects with spatial control along a nanomaterial is presented in **Chapter 5**. The approach relies on inducing and controlling a change in composition along a MWCNT. This leads to MWCNTs with intratubular junctions showing segments with distinct structures and properties along a single MWCNT. To prove for the first time that

these materials can be used for localised immobilisation of particles or molecules, a key achievement in this thesis is to propose a method to produce large quantities of MWCNTs and MWCNT scaffolds with intratubular junctions. The synthesis approach presented leads to large quantities of material and this allows a more detailed characterisation of these MWCNTs than in previous reports. For the first time, it is established that the spatial control achieved over the properties of the MWCNT ensemble allows spatial control over (1) the reactivity of the material and (2) the immobilisation of nano-objects on this material. This opens new opportunities to control the immobilisation of catalysts in a carbon scaffold.

Finally in **Chapter 6**, the findings of this work are summarised and future research is highlighted.

1.2. Literature review

1.2.1. Biological electrocatalyst immobilisation on carbon materials: the example of hydrogenase

1.2.1.1. Benefits of biocatalyst immobilisation on carbon materials

Over the last decades, using enzymes as catalysts to perform chemical transformations has increasingly been considered and implemented in the production of chemicals, drugs, fuels or electricity [6, 10]. The growing interest in enzymes comes from several factors. First, bio-catalysis can be performed from a renewable feedstock like biomass. Second, enzymes are bio-degradable. Third, enzymes can be highly selective to perform a specific reaction. Fourth, enzymes can operate under mild conditions of temperature and pressure. Biocatalysis is then considered as a less-hazardous and more sustainable route compared for instance to most organic and inorganic synthesis methods for chemical transformations [21]. A crucial step to make the most of the biocatalysts is their immobilisation on supports. Immobilisation is a common approach to facilitate biocatalyst study [13, 22] and in recent years it quickly became a critical step for an increasing number of applications from bio-medicine to bio-energy or production of chemicals [13, 22]. This is first because immobilisation can optimise the activity and stability of biocatalysts by preventing their denaturation *via* favourable biocatalyst/support interactions. This confers for instance long term resistance to temperature or solvents to enzymes [13, 22]. The second interest in immobilisation of biocatalysts is to facilitate their recovery and recycling [13, 22]. An important feature of catalysts is that they kinetically favour a chemical reaction and are not consumed during the process. Therefore they can be simply recovered after reaction if they are immobilised on a support. Immobilisation avoids filtration processes or multiple treatments to isolate a catalyst from a reaction mixture. Immobilisation is then an attractive cost-effective option for large scale use of biocatalysts in industries [13, 22]. The importance of biocatalyst immobilisation

is reflected by a wide literature on the strategies to make the most of biocatalyst activity [21, 23]. Part of the research in the field of biocatalyst immobilisation focuses on the routes to perform the immobilisation. This includes covalent attachment [24], electrostatic interaction [25, 26], hydrophobic/hydrophilic interactions [27] with a support. However specific immobilisation strategies often require a case by case support/enzyme study due to the complex nature and surface properties of enzymes. A second important area of research focuses on the control over the properties of the support in use. A variety of materials compatible with biocatalysts have been developed to improve enzyme stability and recyclability like silica-based materials [13, 14], polymers [13, 14] and to a lesser extent carbon materials [13, 14].

Carbon materials play an increasing role as support for enzyme immobilisation, because they combine a set of useful properties that are not found in other materials [15]. First, the increasing interest in nanotechnology has largely contributed to the design of carbon materials at a nanoscale [28], leading to materials with relatively small size and large surface areas. These properties are directly relevant to immobilise more enzyme molecules in small volume to enhance the performance of devices [22]. For instance it can lead to higher electrocatalytic current in the field of enzyme fuel cells [8, 12, 29]. A nanomaterial also has a scale matching the typical size of enzymes of several nanometres. Controlling the properties of the material at this scale is directly relevant to favour interaction with the enzyme to optimise their immobilisation [30, 31]. Second, carbon materials offer a surface suitable for immobilisation of enzymes by robust adsorption which is the preferred immobilisation method for enzymes due to its efficiency and simplicity [14]. Carbon materials can also be chemically modified to develop more complex covalent attachment of the enzymes if needed [24, 32, 33]. At the same time carbon materials are relatively inert and stable under biological conditions [15]. It could be argued that silica-based supports present

the same benefits and are already widely developed as support for enzyme immobilisation [13, 14]. Indeed, control over the pore size of a silica matrix to match the size of an enzyme for improved immobilisation is possible. Also silica surfaces can be chemically modified for further covalent immobilisation [13]. However a major drawback of silica is its low electron conductivity [15]. In contrast, carbon materials have a better conductivity and so are preferred supports in bio-electronics or bio-sensors where electron exchange with the enzyme is key [15]. For instance, carbon is a common electrode material for study and applications of bio-electrocatalysts, as detailed in the next section.

1.2.1.2. Benefits of bio-electrocatalyst immobilisation on carbon materials: the example of hydrogenase

Bio-electrocatalysts are enzymes requiring an electron exchange to achieve catalytic activity. Due to the need for electron transfer and the redox properties of bio-electrocatalysts, electrochemistry has been a preferred tool to study their activity in a technique known as protein film electrochemistry [34, 35] illustrated in **Figure 1.1**.

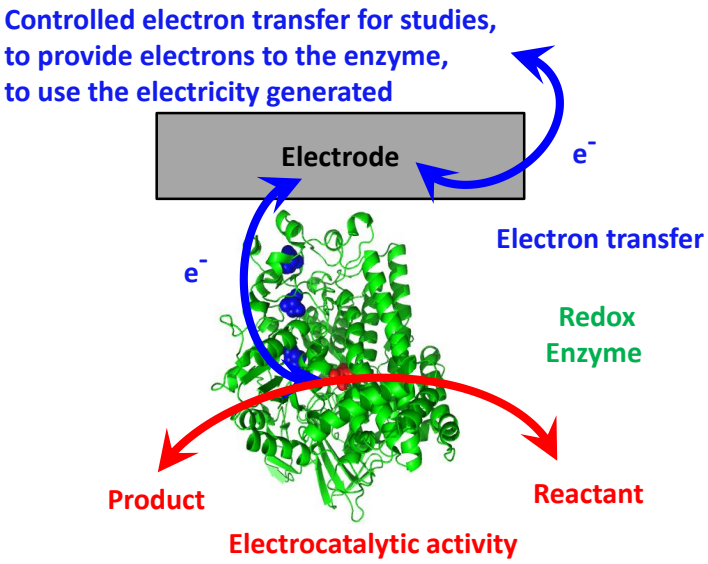

Figure 1.1. Schematic representation of protein film electrochemistry for bio-electrocatalyst studies showing the importance of electron transfer at an electrode. Catalytic centre and catalytic activity are in red, electron transfers and electron pathway in the enzyme are in blue and the enzyme in green.

Protein film electrochemistry requires the immobilisation of redox proteins (green) on a conductive material (grey) playing the role of electrode to achieve electron transfer (blue) to/from the catalytic centre buried into the enzyme (red) from/to the conductive material. In particular, the successful immobilisation of bio-electrocatalysts on carbon electrodes by simple adsorption has been largely exploited for this technique [34, 35]. Controlling the electron transfer between the electrode and the enzyme helps to understand the activity of the enzymes (as it will be more deeply discussed in **Section 1.2.1.3**). It is also possible to produce electrons in the case of an oxidation and so to produce electricity. Finally it is possible to perform a chemical transformation. As a consequence, this electrochemical investigation of bio-electrocatalysts has led to important breakthroughs in the development of bio-sensors [36], bio-energy [37] but also production of chemicals [20]. For all applications, the development of suitable carbon electrodes and carbon supports is key but several limitations remain, especially to achieve higher enzyme loading and stability. A strong expectation in the bio-electrochemistry community is that design of carbon materials to be used could improve the performances of enzyme electrodes [15, 29]. The reasons why further material design is needed and how the materials could be tailored is illustrated in this thesis through the example of hydrogenase, a bio-electrocatalyst presented in the next paragraph and relevant for a variety of energy-related applications.

Hydrogenases are complex biological units of *ca.* 90,000 g mol^{-1}, about 5 nm in size and made essentially of amino acids. They are bio-electrocatalysts able to kinetically favour H_2 splitting into H^+ and electrons or the reverse reaction:

$$H_{2\,(g)} \leftrightarrow 2H^+_{\,(aq)} + 2e^- \qquad \textbf{(A)}$$

To date platinum is the preferred material to perform reaction (**A**) but is an expensive metal catalyst and a non-renewable resource [38]. Hydrogenases are then envisioned as a possible substitute to platinum. A first interest in hydrogenases for instance is that their field of

applications cover energy production by forming H_2 [37]. A second interest is in electricity production by splitting H_2 into protons and electrons which is directly relevant for enzyme H_2 fuel cells [27]. Since H_2 fuels cells are expected to be found as power supply in an increasing number of devices like portable electronic or vehicles [39], this makes immobilised hydrogenases possible biocatalysts for future energy devices. However, due to the limited availability of hydrogenases to date, enzyme fuel cells may not be the best commercial alternative to platinum. An important third area of research in hydrogenases is then to understand the fundamental mechanisms that make the enzymes so efficient in producing or splitting hydrogen. Understanding better this activity could lead to genetic variants [40] outperforming existing enzymes. It could also inspire the design of bio-mimicking complexes [41-44] reproducing enzyme activity but possibly simpler to obtain at industrial scale in the future. A major motivation in artificially reproducing hydrogenase activity is that hydrogenases use metal atoms like nickel and iron (for so called [NiFe] hydrogenases) or two iron atoms ([FeFe] hydrogenases) at their catalytic site (further detailed in **Section 1.2.3**). These metal atoms are key for the activity of the enzyme and cheaper than platinum so could lead to cheap and efficient bio-inspired-catalysts [45]. For instance nickel based bio-mimicking inorganic complexes outperforming the activity of hydrogenases have been reported but their stability can be limited [41]. A fourth interest in hydrogenases is to support the production of chemicals by using the electrons produced when splitting H_2 to perform further chemical transformations [20]. This makes hydrogenases extremely versatile biocatalysts as illustrated in **Figure 1.2**, counterpart of **Figure 1.1** for the specific case of hydrogenases. For a better understanding of the catalytic activity and production of H_2, electricity or chemicals by hydrogenases, a common requirement is the immobilisation of the hydrogenase on carbon materials.

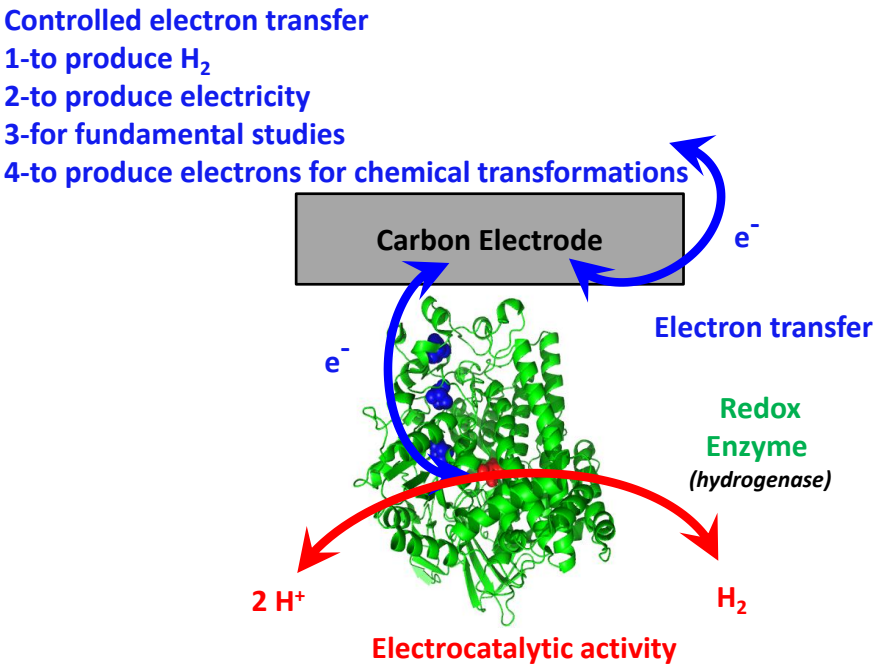

Figure 1.2. Schematic representation of protein film electrochemistry for hydrogenase studies and possible applications. Catalytic centre and catalytic activity are in red, electrons transfers and electron pathway in the enzyme are in blue and the hydrogenase in green.

1.2.1.3. Challenges in bio-electrocatalyst immobilisation

To exploit hydrogenase activity, a common approach is the enzyme immobilisation on conductive material and in particular carbon. However, the immobilisation of redox proteins can lead to different configurations. Only few orientations of the enzyme relative to the carbon surface lead to a configuration where a fast and efficient direct electron transfer (DET) can be achieved to/from the electrode from/to the enzyme [46]. This is because the electron pathway from the inside/outside of the protein is possible thanks to a chain of redox centres: for example iron sulphur [FeS] clusters (blue) within the hydrogenase (green), **Figure 1.3a**. Electrons are relayed from one cluster to another by change in their redox state. The closest cluster to the outside surface of the protein, referred to as distal cluster, must be as close to the electrode as possible to ensure electron transfer between the electrode and the protein. DET is desired to ultimately improve the efficiency of a device but is not simple to

achieve. In practice, the redox enzyme is likely to be immobilised in a distribution of orientations relative to the carbon surface [47] and so not always in a DET configuration. The distal cluster could even be too far from the electrode for a direct electron transfer to occur, **Figure 1.3b.** To electrochemically access enzymes immobilised in a configuration that does not favour DET, a mediator can be used [48]. A mediator is a molecular shuttle that can diffuse in the solution and due to its redox properties can relay the electrons between the electrode and the distal cluster. Electrons are then provided to the enzyme regardless of the orientation of the enzyme to the electrode. This gives a mediated electron transfer (MET) configuration for which common mediators are methylviologen (MV) and methylene blue (MB). A first drawback with these mediators is their toxicity [15, 27]. Second, the electron transfer relies on diffusion of the mediator to the enzyme. This can lead to slower kinetics in the electrocatalysis, thus reducing the efficiency of electron transfer. DET is more desirable and must be favoured because it avoids the use of intermediate molecules, simplify the study of enzymes and limits cost for implementation in enzyme-based devices [15].

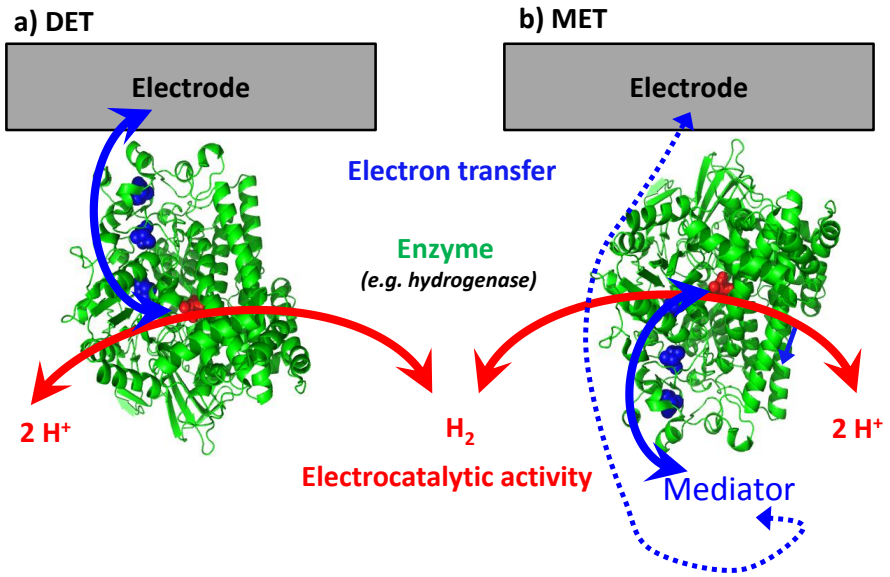

Figure 1.3. Schematic representation of (a) DET and (b) MET. Depending on enzyme orientation with respect to the electrode material DET (a) is possible. If DET is not achieved, improved electrochemical signal can be obtained using a mediator for MET (b). Catalytic centre is in red and [FeS] clusters in blue within the protein in green.

A possible way to favour the DET configuration is to carefully consider the properties of the carbon material used to develop the electrode, like graphitisation as explained in the next section. Since the support used is key for hydrogenase study and applications a range of carbon materials has been considered to develop and optimise hydrogenase electrodes. These carbon materials are reviewed in this thesis to identify what an ideal material for hydrogenase immobilisation is and what the limitations to the development of optimised hydrogenase supports are to date.

1.2.2. Carbon materials for hydrogenase immobilisation to date

Due to their electroactivity, hydrogenases have been extensively studied by electrochemical techniques after immobilisation on carbon electrodes (**Figure 1.2**). The requirement to develop a suitable electrode is to achieve a high loading of immobilised electro-active enzyme to reach a high electrocatalytic current, and thus a high signal to measure and study. Immobilisation can also help to achieve better stability of the enzyme over the time of the experiment. High enzyme loading and stability are the exact same requirements for the applications of hydrogenase in fuel cells [27] or production of H_2 [37] and chemicals [20], with stability required over weeks or months of operation. To date, the carbon materials reported as supports are not optimised for one of the specific possible applications of hydrogenases. As a consequence the materials investigated for hydrogenase immobilisation so far have often been directly relevant to develop fuel cells or H_2 production devices. The literature review proposed in this section is then articulated around the characteristics and properties of the carbon materials used as support, rather than the final applications considered. The literature review covers the carbon materials reported until summer 2015 for hydrogenase immobilisation. The variety of carbon materials considered for this

mmobilisation is highlighted and the difficulty to conclude on the benefits of one material compared to another is also addressed.

1.2.2.1. Amorphous carbon materials

The first carbon material considered to immobilise hydrogenases is an amorphous carbon reported in 1984 by Berezin and co-workers [49]. Amorphous carbon materials mainly consist of a mixture of sp^2 (carbon-carbon double bond) and sp^3 (tetravalent carbon) carbon atoms without crystalline structure but where short-range order (few nanometres) can be observed [50]. Amorphous carbons are common electrode materials because they combine a suitable conductivity with a relative chemical and electrochemical inertness in a variety of solvents. The carbon material used was not characterised in the paper by Berezin and co-workers but is probably a carbon powder [49]. In 2002, the same group investigated hydrogenase immobilisation on a 'carbon filament' [51, 52] and a 'carbon cloth' material [53]. No structural characterisation of the materials was performed. The description provided in the reports [51-53] suggests that these carbon materials are essentially made of fibre-looking structures. This type of material is commonly used in electrochemistry and a general morphology is illustrated in **Figure 1.4** with scanning electron microscope (SEM) images of a 'carbon paper'. Carbon paper is a material made of carbon structures showing a diameter usually around 5-20 µm and with a general aspect and morphology close to other filament-like carbon structures. There are no extended graphitic domains in the materials consisting of a mixture of sp^2 and sp^3 carbon atoms [50]. The choices and criteria for the selection of one material rather than another are not detailed despite the fact that experiments were conducted by the same researchers [49, 51-53]. This observation suggests that the material selection was driven by the only fact that amorphous carbons are common electrode materials in electrochemistry and commercially available. Using commercially available supports is indeed an argument to simplify possible long term commercial applications of devices like

enzyme fuel cells [52]. Although characterisation of the materials was not detailed, these studies established key features of hydrogenase activity and application. First, simply leaving a solution of hydrogenase in contact with a carbon surface ensures robust and simple adsorption [49]. Second is the possibility to develop enzyme H_2 fuel cells [51] where the enzyme has a relatively good activity in comparison to platinum. The conclusions from those studies, in agreement with others [54], state that platinum can be a better catalyst than hydrogenase at high H_2 pressure (1 atm) but is comparable at lower pressure (0.1 atm). Hydrogenases suffer far less irreversible poisoning by CO and H_2S, small molecules found in H_2 feedstocks which irreversibly poison platinum. This means that enzyme fuel cells could operate with lower grade gases, so cheaper gases compared to platinum fuel cells. Third, over long time the stability of the hydrogenase-based device was relatively high: more than 50 % stability maintained after six months of storage [52]. This observation justifies the need for hydrogenase immobilisation to improve the lifetime of hydrogenase devices like fuel cells. Unfortunately, for all these materials, acid treatment was performed to overcome the hydrophobicity of the carbon network [51-53] or a polymer binder [49] was needed to facilitate the hydrogenase adsorption and stabilise the electrode. This adds some steps and complexity to the development of the electrode.

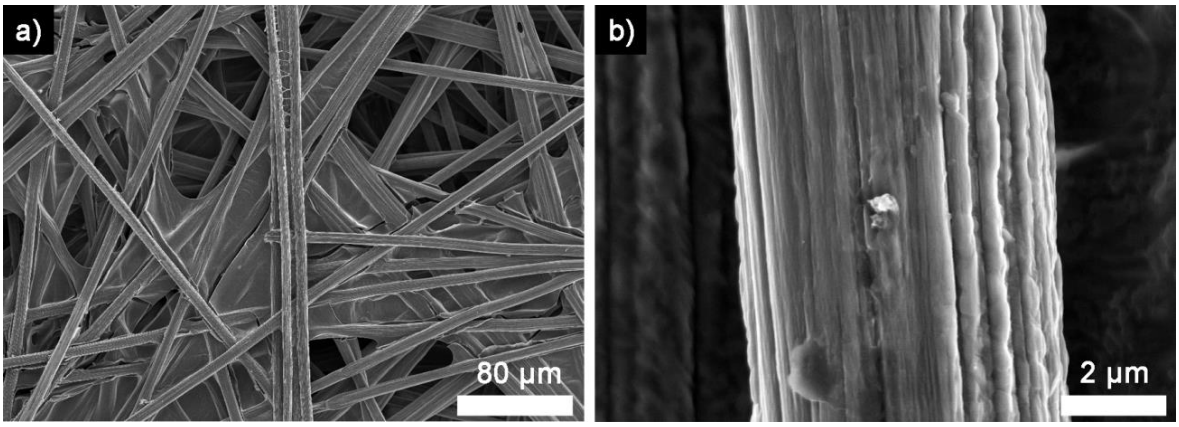

Figure 1.4. Scanning electron micrographs (SEM) of carbon paper (TGP-H-030 from Toray) at different magnification. The general morphology is similar to other structures made of filament-like materials as carbon cloth or filament.

Based on these observations, Szot *et al*. [55] investigated a method to improve hydrogenase loading and stability on an electrode. The study proposed a layer-by-layer network formation using charged amorphous carbon particles without binder. The goal was to electrostatically entrap and stabilise a charged hydrogenase into a conductive particle film [55]. This approach facilitates the electrode preparation because it avoids the use of a binder. However it appears relatively complex in the light of recent reports: an emerging trend is the direct immobilisation of the enzyme on as-received commercial amorphous carbon powders [19, 56]. For instance, in 2013 an amorphous carbon powder has been used to maximise the surface of carbon available for enzyme adsorption. This lead to a 'high surface area electrode' [56] for efficient hydrogenase fuel cells. For the first time a power density above 1 mW cm^{-3} for this type of enzyme-based device was achieved. In this study by Xu and Armstrong, enzyme immobilisation was performed by simply adsorbing the enzyme directly on the as-received commercial material. Similarly, in 2014, Ogo and co-workers performed the direct adsorption of an hydrogenase on an as-received commercial amorphous carbon powder. The authors report a promising high activity for enzyme fuel cells, achieving 637 times more activity for H_2 oxidation (estimated for 1 mg of catalyst) for hydrogenase compared to platinum under equivalent conditions [19]. These recent results are extremely promising for hydrogenase fuel cells to compete with other fuel cells devices and reflect the high activity of the hydrogenase selected and recently isolated [19]. The carbon powders were in both cases chosen without detailed explanation. A possible reason is that no pre-treatment is needed prior to combination with the enzyme, which facilitates the electrode preparation. The materials are commercially available which facilitates their used and makes them relevant for future commercialisation of enzyme-based devices [52]. The selection was also probably made because powders should offer a surface area higher than the previously mentioned carbon filament or cloth. Indeed, carbon powders are used in fuels cells for their

high specific surface area (*ca.* 1000 m^2 g^{-1}) [57] to achieve higher catalytic current. SEM images shown in **Figure 1.5** for an amorphous carbon powder confirm than the material has a smaller typical size than the previous filament-like materials (**Figure 1.4**), suggesting it can be assembled into overall higher surface area electrode. However no full quantification of the electrode total surface area was provided in the reports [19, 56]. No estimation of how well the enzyme uses the surface of the electrode obtained from those powders can be established for further optimisation. It is then difficult to compare and quantify the benefit of using carbon paper, filament or cloth to carbon powders.

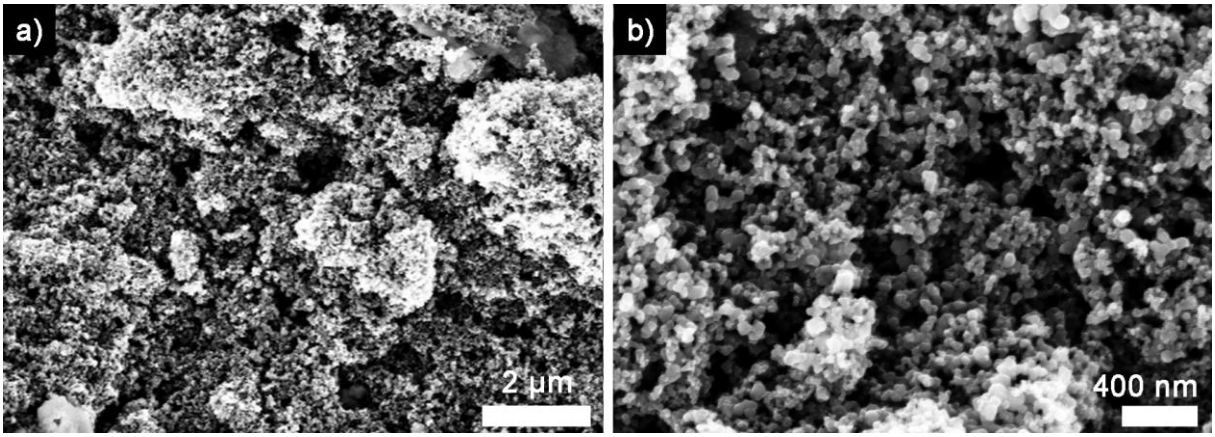

Figure 1.5. SEM micrographs of an amorphous carbon powder (BP 2000, Cabot corporation) at different magnification.

These examples illustrate the possibility to simply immobilise hydrogenases on as-received commercially available materials. From a practical point of view, these materials provide enzyme loadings that are sufficient to achieve electrocatalytic current suitable for enzyme study or application. However little is known on the enzyme-amorphous carbon interaction. For instance, effect of the carbon morphology and size on the activity of the hydrogenase is not investigated. How well the surface area available is used by the enzymes is not fully addressed and direct electron transfer (DET) is not necessarily achieved since a mediator is often required. Deeper knowledge on these properties could lead to further development and better selection of a suitable carbon material for hydrogenase electrodes.

1.2.2.2. Graphitic materials: pyrolytic graphite

Instead of using electrodes made of amorphous carbon, a generally preferred approach to date to optimise enzyme loading and stability on the electrode is to use a graphitic carbon material. DET can be favoured by electrostatic interaction or covalent modification of the carbon surface [58]. However chemical modifications of carbon materials add steps to the electrode preparation. Multiple steps possibly limit reproducibility of results [53] and are more complex to implement in view of commercialisation. A preferred and simpler approach to favour DET without chemical modification consists of promoting edge planes with graphitic carbon materials [30]. Graphitic carbons are indeed made of both basal and edge carbon planes as illustrated in **Figure 1.6**. Graphitic carbons are mainly made of domains constituted of sp2 carbon atoms forming carbon-carbon double bonds, with a minority of domains made of atoms in sp^3 hybridisation (tetravalent carbon). Presence of edge planes can be explained by considering a building block for sp^2 domains: a graphene sheet schematised in **Figure 1.6a**. Graphene is an ideal 2D carbon structure made only of sp^2 carbon [59]. Several graphene sheets can interact with each other by π-π interaction to lead to stacked layers forming three dimensional domains of sp^2 hybridisation in the carbon material, **Figure 1.6b**. The more graphitic the material, the higher the sp^2 hybridisation, the larger the sp^2 domains and the fewer the atoms in sp^3 hybridisation [59]. The sp^2 domains have a typical scale of few nanometres for the less graphitic materials like amorphous carbon, up to millimetres for highly graphitic materials like highly ordered pyrolytic graphite. The imperfection in the stacking of several graphene-like planes in graphitic carbons leads to a step-like structure, explaining the presence of both basal and edge planes, **Figure 1.6b**. It has been reported that enzyme immobilisation happens preferentially at these ‘edge’ carbon planes and a DET configuration is favoured [30, 31]. This is likely due to the presence of dangling bonds, functional groups and defects, providing more reactive sites

favouring enzyme interaction with the material. Therefore, graphitic carbon materials are considered to be simple materials to control hydrogenase loading by controlling the abundance of edge-planes.

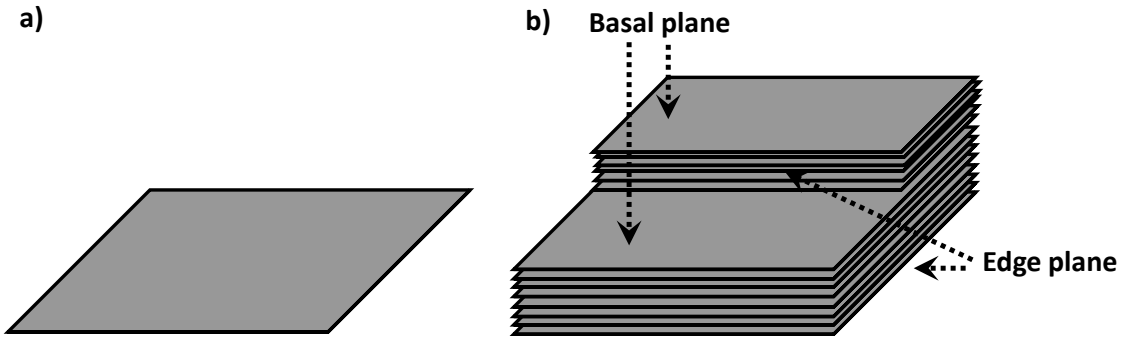

Figure 1.6. (a) Schematic representation of an atom thick graphitic sp^2 carbon plane: graphene. (b) Superposition of graphene-like carbon planes leads to graphitic carbon domains within a graphitic carbon material, thus showing both basal and edge planes.

Among carbon materials, pyrolytic graphite (PG) has a pronounced graphitic structure [60] and has been a preferred material for hydrogenase protein film electrochemistry [35, 61] because it is commercially available and gives satisfying results. DET (**Figure 1.3a**) is easily achieved and so there is no need for a mediator or chemical modification [62]. PG has ordered graphitic domains, is very soft, and a freshly cleaved surface for enzyme adsorption is readily prepared by mild abrasion [60]. PG can be used as a block material to form planar electrodes made of a macroscopically flat block of PG [35] with the edge plane exposed, **Figure 1.7a**. It has also been used in the form of powder made of PG particles with size usually of about 5-10 µm [62, 63], **Figure 1.7b**. Particles have been used to assemble a three dimensional 'high surface area electrode' [27, 63] allowing a higher loading of hydrogenase [63] compared to the planar electrodes. However the total surface area developed in the electrode is rarely fully quantified. Thus estimating enzyme loading achieved is a complex task but is usually considered to be in the pmol cm^{-2} range [35] on planar pyrolytic graphite electrode. This is actually enough to study the enzyme by electrochemical techniques.

Protein film electrochemistry studies on PG electrodes gave deep insight into hydrogenase electrocatalytic properties. For instance by comparing features of hydrogenases from different organisms [64] or with different genetic modifications [40] under various conditions of temperature, pH, presence of inhibitors, etc. [35] Redox enzymes often show rates of catalysis with turnover frequency higher than 1 000 s^{-1} when immobilised on PG supports, leading to electrocatalytic current high enough for applications in fuel cells [65] or chemical synthesis [20].

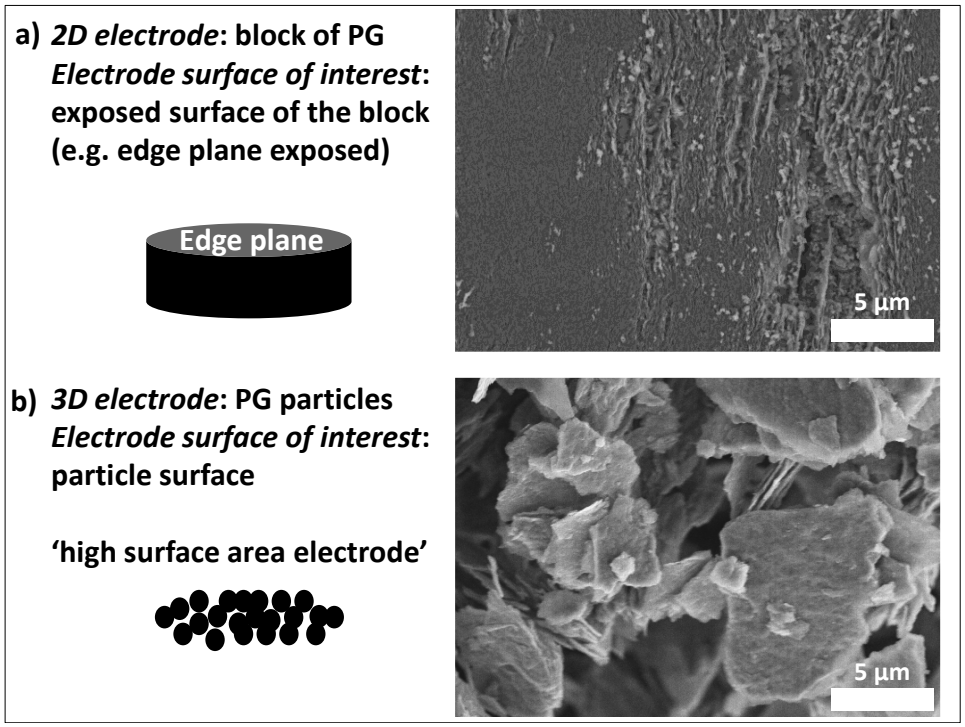

Figure 1.7. Schematic representation and top view SEM images of (a) a PG block with the edge plane exposed and (b) PG particles obtained by abrasion of a PG block.

PG is so convenient that it is probably the most broadly used electrode material for hydrogenase immobilisation [35]. However PG has some drawbacks. Adsorption is aided by the fresh abrasion with glass paper and/or alumina just prior to protein immobilisation [35, 60] likely due to changes in the chemical composition of the surface on contact with air or water. The preference for fresh preparation of the planar electrode or the particles is suitable for a daily lab-scale production but limits batch processing of larger quantities. Also the still

large proportion of basal surface on the particles [62] probably means that the total surface area of PG particles prepared by abrasion is not well utilised for enzyme loading. There is also little control over the size of PG particles (typically a few micrometres [62, 63]) obtained by the abrasion technique, **Figure 1.7b**. This prevents further design to possibly develop more edge plane surface and improve the enzyme loading.

1.2.2.3. Carbon nanotubes for hydrogenase immobilisation

Another important and popular material in the development of supports and bio-electrodes are carbon nanotubes (CNTs) [66]. Research on CNTs has considerably been boosted in the last decades [67] by the Nature paper published in 1991 by Ijima [68]. CNTs quickly benefited from an important interest in various fields of research because they combine outstanding thermal [66], electrical [66] and optical [66] properties. Also their nanometre scale and high specific surface area [69], outstanding mechanical stability [69] as well as the possibility to chemically modify their surface [69], make them a popular materials to support various catalysts [70-72] including enzymes [16, 24, 73, 74]. CNTs are suitable for a range of applications [66] including chemical synthesis [75, 76], medicine [18], bioelectronics [18] or bio-sensors [17]. Their unusual combination of properties comes from their structure which can be understood starting with a graphene sheet. If a graphene sheet is an ideal atomic layer of sp^2 honey comb carbon, single-wall CNTs (SWCNTs) and multi-wall CNTs (MWCNTs) are conceptually obtained by rolling one (for SWCNT) or several (for MWCNT) graphene sheets as displayed in **Figure 1.8**. CNTs are then hollow tubular carbon materials made of sp2 carbon atoms, with an external diameter typically less than 100 nm and a length typically from a few hundreds of nanometres to several centimetres [77].

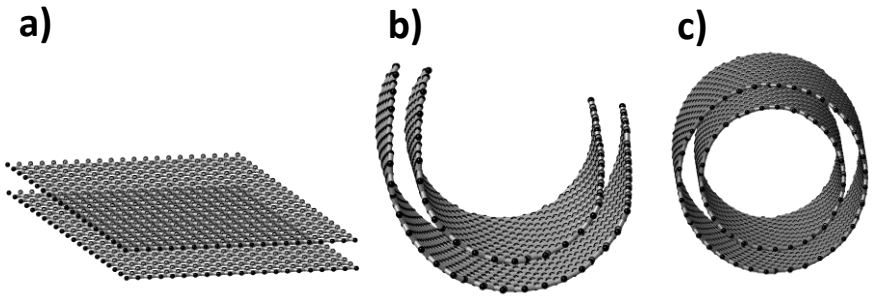

Figure 1.8. Schematic representation of (a) a superposition of two graphene sheets, (b) the same being conceptually rolled up to give (c) MWCNTs, in this case double-wall CNTs. Models were obtained *with the help of Dr Rebecca Nicholls, Department of Materials, University of Oxford*.

Since an additional property of CNTs is their electrical conductivity [66], they have been extensively studied as electrode materials for hydrogenases. This is illustrated in **Table 1.1** which summarises the most important literature on alternative carbon materials to PG reported for hydrogenase immobilisation. This table first illustrates that roughly 75 % of publications that do not use PG use CNTs. The remaining 25 % use the amorphous carbons previously mentioned in **Section 1.2.2.1**. A general trend regarding the origin of the CNTs can be established from **Table 1.1**. CNTs are mainly obtained from commercial suppliers because it is a convenient and simple way to obtain SWCNTs or MWCNTs and could facilitate the possible commercialisation of enzyme electrodes [52]. Nevertheless, using commercial materials can also be a drawback because there is little control over the properties of the material obtained. More control could be achieved with homemade materials but CNTs obtained from homemade synthesis were used in only four publications for hydrogenase immobilisation. This is about three times less that the number of reports using commercial CNTs. As it will be detailed later, this can be explained by the need for specific equipment to synthesise CNTs. Secondly, **Table 1.1** illustrates that in most cases a mediator is needed. DET is then not always achieved on CNTs which can be detrimental to the efficiency of a device based on the resulting enzyme electrode. Finally and more

Table 1.1. Alternative materials to PG reported for hydrogenase immobilisation

Hydrogenase	Material	Material origin	Modification	Mediator	Date	Ref
Thiocapsa roseopersicina [NiFe]	pounded carbon black on gold	-	fluoroplastic binder in acetone	MV or no mediator	1984	[49]
Thiocapsa roseopersicina [NiFe]	carbon filament	commercial	acid treatment	MV or no mediator	2002	[51]
Thiocapsa roseopersicina [NiFe]	carbon cloth	commercial	acid and base treatment	MV or no mediator	2002	[53]
Thiocapsa roseopersicina [NiFe]	carbon filament	commercial	acid treatment	MV/redox polymer for immobilisation or no mediator	2002	[52]
Thiocapsa roseopersicina [NiFe]	SWCNTs, MWCNTs	commercial	acid treatment	no mediator	2006	[78]
Thiocapsa roseopersicina [NiFe]	MWCNTs	commercial	modified with S-(2-aminoethylthio)-2-thiopyridine hydrochloride	MV or no mediator	2010	[79]
Thiocapsa roseopersicina [NiFe]	SWCNT forest	synthesised	no	no mediator	2011	[37]
Desulfovibrio gigas [NiFe]	PG	commercial	covalent bonding through diazonium functionalisation	MV or no mediator	2005	[58]
Desulfovibrio gigas [NiFe]	MWCNT forest	synthesised	covalent bonding through diazonium functionalisation	no mediator	2007	[24]
Clostridium acetobutylicum [FeFe]	SWCNTs	commercial	surfactant	no mediator	2007	[80]
Clostridium acetobutylicum [FeFe]	SWCNTs	commercial	surfactant	MV	2008	[81]
Clostridium acetobutylicum [FeFe]	m/s-SWCNTs on carbon cloth	synthesised	surfactant further removed by acid treatment	MV or no mediator	2011	[73]
Allochromatium vinosum [NiFe]	SWCNTs	synthesised	modified with a polymyxin binder	-	2008	[82]
Desulfovibrio fructosovorans [NiFe]	SWCNTs, MWCNTs, amine-modified SWCNTs, acid- modified SWCNTs	commercial	acid treatment or not	MV or no mediator	2008	[25]
Desulfovibrio fructosovorans [NiFe]	SWCNTs MWCNTs	commercial	no	polymeric MV	2011	[83]
Aquifex aeolicus [NiFe]	SWCNTs	commercial	acid treatment or not	MB or no mediator	2009 2012	[26] [74]
Aquifex aeolicus [NiFe]	charged particles	commercial	charge surface modification	MV or no mediator	2013	[55]
Aquifex aeolicus [NiFe]	SWCNTs, amine-modified MWCNTs, acid-modified MWCNTs	commercial	acid treatment or not	MV, MB	2013	[84]
Aquifex aeolicus [NiFe]	carbon nanofibres	synthesised	thermal treatment	no mediator	2014 2014	[85] [86]
Escherichia coli Hydrogenase 1 [NiFe]	MWCNTs	commercial	functionalisation with 1-pyrene butyric acid	no mediator	2012	[33]
Escherichia coli Hydrogenase 1 [NiFe]	amorphous carbon powder	commercial	no	no mediator	2013	[56]
Citrobacter sp. S-77 [NiFe]	amorphous carbon powder	commercial	no	no mediator	2014	[19]

importantly, **Table 1.1** highlights that in most cases several treatments are performed on the as-received CNTs prior to combination with the hydrogenase. This is for instance acid treatment [87], diazonium chemistry functionalisation [24], or modification by π-π interaction [33] for instance with pyrene butyric acid. These surface treatments facilitate covalent attachment of the enzymes and/or attempt to overcome CNT hydrophobicity [88] and associated difficult dispersion in aqueous solution [89]. This intrinsic hydrophobicity of CNTs is actually a major drawback of the material itself and achieving better CNT dispersion is a challenging area of research on its own [89].

To develop simpler electrodes there is a need to completely alleviate the challenging dispersion of CNTs in aqueous solvents, the use of surfactants or the need for a polymer-binder. A possible option is to consider CNT materials that are not in the form of a powder. This is possible with vertically-aligned CNTs represented in **Figure 1.9**, also known as CNT forests [90]. The first interest in this CNT geometry is that all the CNTs are aligned to each other with their axis perpendicular to a substrate, **Figure 1.9b**. This confers a degree of orientation, of connexion with the substrate and a macroscopic mechanical stability that is not as simply achieved after dispersion, **Figure 1.9a**. CNT properties like conductivity, high surface area, stability over a range of chemical and thermal environments are also maintained in the forest geometry. The second and main advantage is that no dispersion step is required prior to enzymes adsorption. For all these reasons, in 2007, De Lacey and co-workers directly grew a MWCNT forest onto a gold wire to develop a high surface area electrode [24]. This was done to optimise enzyme loading and at the same time improve the electronic contact between the carbon surface made of MWCNTs and the conducive electrode support made of gold [24]. The electrode obtained had an electrochemically active surface area 50 times higher after MWCNT growth than for the bare gold electrode. The approach involved chemical modification by diazonium chemistry of the as-synthesised

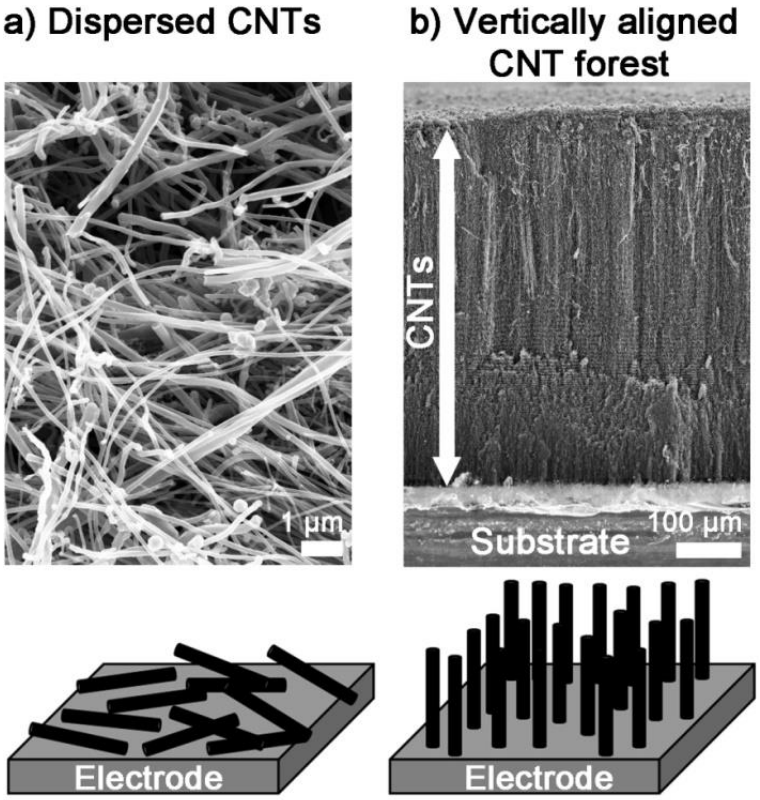

Figure 1.9. Top: SEM micrographs of (a) dispersed CNTs deposited on a substrate and (b) vertically-aligned CNT forest directly grown or immobilised on a substrate. Bottom: schematic representation of the same. If the substrate (grey) is conductive an electrode is obtained.

forests to achieve further covalent linkage of the enzymes. Stability over a month under continuous operational conditions was achieved, showing the robustness of the electrode developed. The approach certainly overcomes the dispersion of MWCNTs but still require chemical modification of the as-synthesised materials. In 2011, Kihara *et al*. were the first to report a forest of SWCNTs as an efficient material for direct adsorption of a hydrogenase in a DET configuration [37]. In this study no chemical modification of the SWCNTs was needed prior to hydrogenase adsorption. This illustrates the opportunity opened by vertically-aligned CNT materials to create mediatorless high surface area carbon electrode and exploit hydrogenase aptitude to produce or split H_2 by simple adsorption of the

bio-electrocatalyst. To the best of my knowledge, these two examples are the only examples to date of CNT forests for hydrogenase immobilisation.

The limited consideration for CNT forests for hydrogenase immobilisation despite the advantages of this geometry can be linked to the need for homemade synthesis. In both cases [24, 37] the forests were obtained by a chemical vapour deposition (CVD) [91] technique schematised in **Figure 1.10**. In CVD synthesis of CNTs, a hydrocarbon source is broken down into smaller carbon fragments at high temperature around 700-800 °C in inert atmosphere. In the presence of a catalyst, usually in the form of metal particles pre-deposited on a substrate or formed *in situ* during the synthesis, these fragments recombined to build up the tubes that can grow into the forest geometry on the substrate. The first benefit of this approach is to cover surfaces with aligned CNTs and develop a high surface area electrode. The second interest comes from the homemade synthesis. This potentially gives more control than commercial materials over the CNT properties like length, diameter, graphitisation but also general chemistry [92, 93]. Controlling these properties, for instance by controlling the nature of hydrocarbon source used, the duration of synthesis or the temperature of experiments [92, 93], could possibly lead to improved hydrogenase immobilisation. However, no optimisation of these characteristics or the nature of the substrate used is detailed in the two examples mentioned [24, 37]. This is probably because the focus was to prove the benefit of the forest geometry itself rather than optimising the material/enzyme interaction.

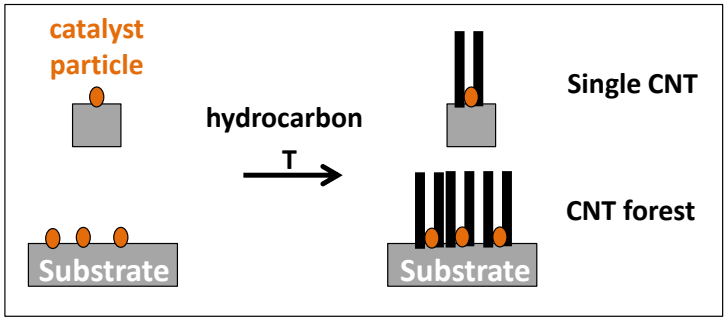

Figure 1.10. Schematic representation of CVD growth of single CNT (top) and CNT forest (bottom).

1.2.2.4. The complex case of carbon nanotubes

CNTs, whether commercial or homemade, dispersed or as forests, SWCNT or MWCNT, can successfully be used to immobilise hydrogenases. The hydrogenase activity is maintained after immobilisation and practical applications for instance in fuel cells [33, 84] have been demonstrated. However the discrepancy between theoretical expectations and experimental observations is somehow puzzling. By looking closer at their intrinsic features, CNTs do not appear as an optimal material for hydrogenase adsorption. First is their challenging hydrophobicity. Second, due to their morphology, most of their accessible surface comes from the tubes outer walls constituted of basal-like plane, with only the open tips made of edge plane-like carbon (**Figure 1.6b** and **Figure 1.8c**). Therefore CNTs should be a relatively poor surface for hydrogenase adsorption in the first place. The use of a mediator is often required with CNTs (**Table 1.1**), even after chemical treatment, which means that a DET configuration is not necessarily favoured in the CNT/hydrogenase interaction. This could also be explained by the abundance of basal planes in a CNT. It has already been mentioned (**Section 1.2.2.2**) that basal planes are suggested to be less favourable for enzyme immobilisation compared to edge-planes [30, 31]. A faster electronic transfer is also believed to occur at edge planes *vs* basal planes and this difference has been intensively discussed by Compton and co-workers [94], especially using PG materials. However recent local electron transfer measurements performed by scanning electrochemical microscopy on graphene and

CNTs by Unwin and co-workers [95, 96] challenge this model. Due to the discrepancy in results and conclusions about faster electron transfer at basal or edge plane, it is difficult to establish how the material structure truly affects the enzyme activity. Improvement in various local characterisation techniques could resolve this important and highly debated question [97] and results would certainly be relevant for a better understanding of enzyme/CNT interaction.

CNTs then show properties that do not make them ideal candidates for hydrogenase adsorption in a DET configuration. Nevertheless it cannot be denied that CNTs bring some benefit to the development of hydrogenase electrodes. For instance, current enhancements up to 10 times [25, 26] are reported for hydrogenases immobilised on CNTs compared to a reference experiment without CNTs. The way in which CNT electrodes lead to higher apparent activity and loading of hydrogenases was investigated by Lojou *et al.* who used acid functionalisation to develop COOH groups [25] on SWCNTs with different lengths as schematised in **Figure 1.11**. In that study, these COOH groups favour on purpose hydrogenase (spheres) orientation into a MET configuration: the distal cluster (dark point, equivalent to the entry/exit point of electrons into the enzyme, **Section 1.2.1.3**) is distant from the carbon materials. However with a shorter length of the same acid functionalised CNT (SWCN-cut), a DET configuration is also achieved. This is because with smaller CNTs the distal cluster of the hydrogenase is more likely to be in direct contact with a carbon surface. This is possible even though the SWCNT on which enzyme is directly immobilised does not favour DET in the first place. This geometrical demonstration to favour DET and so higher enzyme activity is actually valid for any nanomaterials. Due to their nanometre scale, nanomaterials can statically favour a DET configuration by ‘trapping’ hydrogenases into a carbon network.

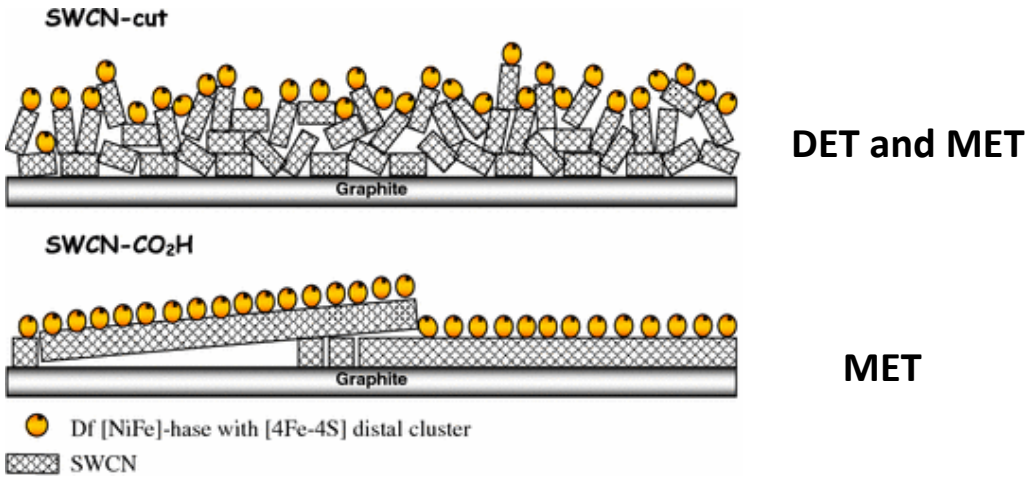

Figure 1.11. Schematic representation of the relevance of carbon material design for hydrogenase adsorption to favour DET. CNT are in grey, enzyme in yellow and distal cluster (see text) in black. From Reference [25]. Reprinted and adapted with kind permission from Springer Science and Business Media, Licence 3463741079885.

This observation explains how CNTs are suitable to develop enzyme electrode despite their drawbacks but question the benefit to develop electrodes made of CNTs. If the most important characteristic to achieve high enzyme electro-active loading in a DET configuration is a nano-size, alternative carbon nanomaterials are readily available. These are for instance amorphous carbon powders already demonstrated in enzyme fuels cells with high electrocatalytic current [19], without the drawback of challenging dispersion faced with CNTs. The lack of clear evidence to the benefit of CNT to develop hydrogenase electrodes is due first to the fact that CNT electrodes are not compared with electrodes made of other materials within a same study to date. Second, practical limitations make it challenging to compare the literature of CNTs with other carbon materials for hydrogenase immobilisation. CNTs are selected mainly for their nanoscale and a high surface area to develop electrodes with improved enzyme/material interaction due to the expected size match between the material and the enzyme. However, for CNTs as well as for previously mentioned materials, the surface area developed by the materials is rarely quantified in studies where it is combined with hydrogenases. The specific surface area developed by CNTs can range from

10 to more than 1000 m^2 g^{-1} in the literature [98]. As a comparison PG particles have a specific surface area of about 40 m^2 g^{-1} [62]. In the absence of systematic quantification of specific surface areas it is difficult to conclude on the benefit to use CNTs to develop 'high surface area' enzyme electrodes compared to other materials.

1.2.2.5. Recent trends and gaps in carbon materials literature for hydrogenase immobilisation

Two different approaches are believed to favour a DET to make the most of hydrogenase activity: using graphitic materials with abundance of edge planes (**Section 1.2.2.2**) or nanomaterials (**Section 1.2.2.3**). A natural next step would be to combine the two previous approaches within the same material. This combination has been reported only recently: in 2014, Lojou *et al*. [85, 86] reported hydrogenase adsorption onto carbon nanofibres. The nanomaterial was selected because it shows predominance of carbon edge planes as represented in **Figure 1.12**. The fact that the walls of the fibres are made of edge-planes should favour enzyme loading and stability (see **Section 1.2.2.2.**). This is to the best of my knowledge the first and only example where a material with abundance of edge planes other than PG particles was selected and reported for hydrogenase immobilisation. In this study again, no direct comparison with another material is performed. The real benefit to use this material compared to PG particles, amorphous carbon or CNTs is then difficult to establish.

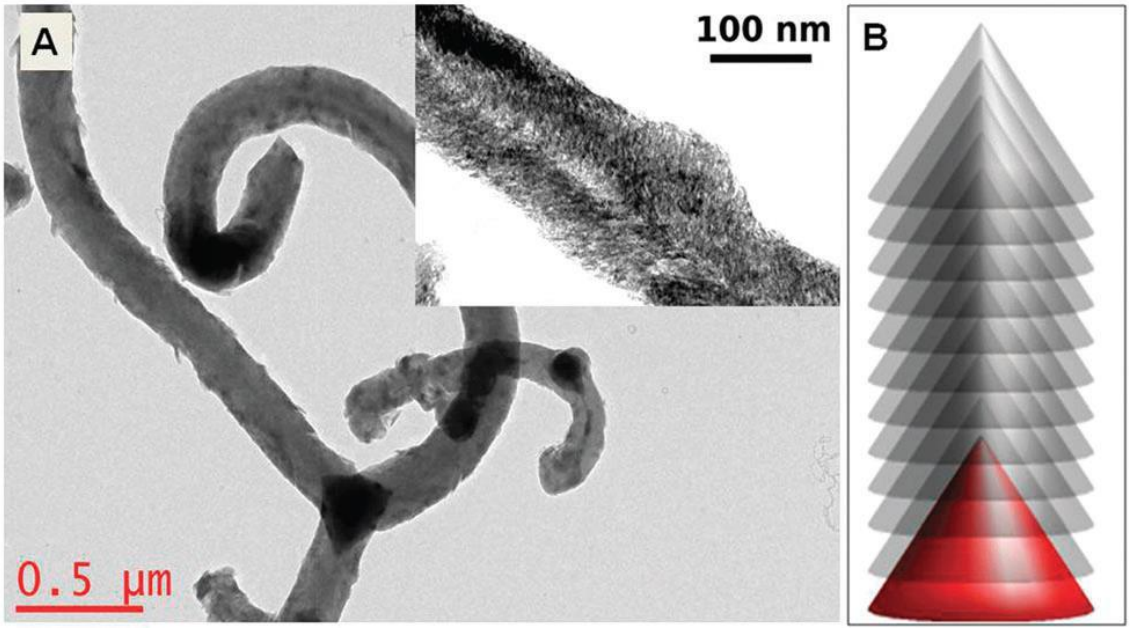

Figure 1.12. (a) Transmission electron microscope (TEM) image of a carbon nanofiber and (b) associated schematic representation of the carbon planes in the fibre (red). Reproduced from Ref [85] with permission of the PCCP Owner Societies, License 3564190717485.

An additional important limitation to compare several results from different publications can also be illustrated with the previous example [85]. The enzyme used was isolated from the thermophilic organism *Aquifex aeolicus* and experiments performed at 60 °C [85]. In another publication with PG particles the enzyme is isolated from *Escherichia coli* and experiments performed at 25 °C [63]. Using different hydrogenases under different conditions is a result from the interest of different research groups in different enzymes. Indeed hydrogenases can be isolated from different organisms [99] and several types of hydrogenases can be found per organism. Different atoms can make the active site and so some hydrogenases are most active for H_2 production and others are most active for H_2 splitting. Some hydrogenases have an activity sensitive to poisoning agents like O_2, CO, H_2S, CN^- [100]. Some originating from hyperthermophilic organisms can operate at temperatures as high as 85 °C [55] where most enzymes usually operate most efficiently at *ca.* 30 °C. Also

different enzymes can show a different combination of properties and this means that different hydrogenases have different activity. A simple comparison of the publications presented in this review and summarised in **Table 1.1** shows that the literature covers not only a range of different materials with different chemical or thermal treatments, but also a range of different hydrogenases. Identifying the real benefit of one material or one electrode design to another for hydrogenase immobilisation is then difficult due to the lack of unified studies of the same enzyme on different carbon materials. A last limitation in comparing various carbon materials is that there is no simple way to evaluate the electrocatalytic performances achieved by the enzyme on different electrodes. If all electrodes were planar electrodes illustrated in **Figure 1.13**, a simple intensive parameter to report is the current achieved per geometrical surface area of electrode at a given potential. However, the use of micro/nano material leads to high surface area electrodes where a powder of nanomaterials is for instance deposited onto a supporting planar electrode, **Figure 1.13**. The total surface area (S) of the electrode so obtained is higher than the planar electrode surface (S_G) which favours the immobilisation of more enzyme molecules, leads to higher electrocatalytic current and has been recently suggested to stabilise the hydrogenase because of the 3D particle network formed [101]. Due to their nanometre or micrometre size, all the reviewed materials summarised in **Table 1.1** are suitable to develop 'high surface area electrodes' for improved studies and applications of hydrogenase in biological fuel cells [51, 102] or H_2 production devices [73]. However the actual total surface area (S) developed is rarely quantified [25, 56, 63, 84], the electrocatalytic current achieved is rarely reported per mass of material used or per surface of material available. The data reported rarely make it possible to evaluate this information. Historically S_G is preferred because it is a relevant parameter for planar-2D electrodes. Also the fields of batteries or fuel cells ultimately report current values per actual 'size' of a device [101]. For instance it can be the power density

achieved considering a geometrical volume, in this sense geometrical surfaces are more meaningful. A major drawback of using S_G as a reference surface is that how efficiently the total surface (S) of the electrode is used is rarely addressed. This makes the comparison of different electrodes from different reports even more challenging.

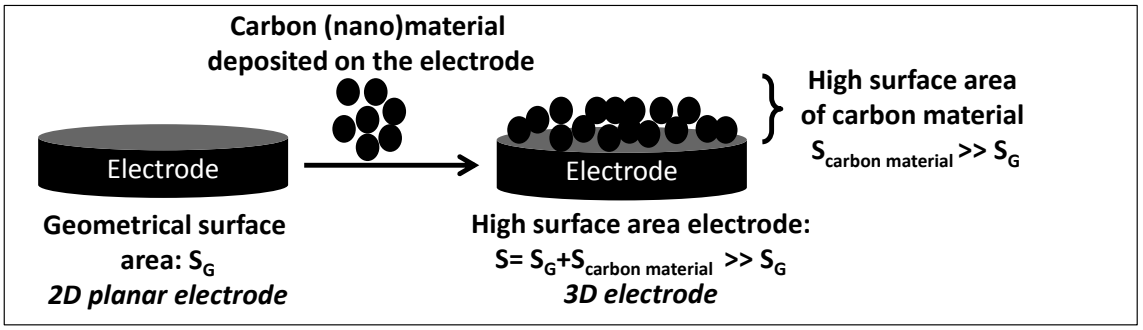

Figure 1.13. Schematic representation of the formation of high surface area 3D electrodes.

1.2.2.6. Conclusions and possible development of new carbon materials

PG, whether used as a block electrode or particles, is a widely used carbon material for hydrogenase immobilisation but fresh abrasion limits its relevance to a daily lab scale production and use. CNTs are commercially available and have been heavily considered as an alternative material due to their high surface area and nanoscale. However dispersed CNTs are more challenging to use in aqueous solutions than other carbon material powders. Powdered materials are also readily available for hydrogenase immobilisation without the need for further modification and have been proved to be suitable for devices like enzyme fuel cells. To develop better performing high surface area electrodes the trend is then towards powders of materials with a nano-size. Only recent research focuses on developing an abundance of edge planes onto a carbon nanomaterial to improve hydrogenase loading. A major limitation is that all these different materials and options to develop hydrogenase electrodes are investigated with different enzymes under different conditions. Any conclusion on the benefits of developing one electrode compared to another is then challenging. A unified study of the same bio-electrocatalyst on various carbon materials

would be beneficial to identify and tailor more efficient carbon electrodes and this is addressed in **Chapter 3**.

Another trend is that alternative materials to PG are so far mainly considered for fuel cells or H_2 production due to the well-established relevance of hydrogenases in these fields [8, 12, 29]. However, the interest in hydrogenases is not limited to these areas of research. In the next section of this literature review it is explained how selecting and tailoring suitable carbon materials could help in developing new methods of studies and new applications of hydrogenases. In **Section 1.2.3** it is detailed how design of carbon nanomaterials used as dispersed powders could help the development of a technique to study hydrogenases. The technique is based on coupling the conventional protein film electrochemsitry technique to IR spectroscopic measurements for a better fundamental knowledge on catalytic intermediates and electrocatalytic mechanism. However powdered carbon materials are not ideal for all hydrogenase applications. **Section 1.2.4** details why continuous catalysis is a promising area of development for hydrogenases and how novel carbon scaffolds based on CNT forests could help to exploit hydrogenase activity in flow systems. Finally, **Section 1.2.5** suggests how inducing a change in composition along a CNT could lead to a new concept to spatially control immobilisation of objects and potentially hydrogenase molecule within a forest made of these CNTs. This approach could be relevant for new devices where facile and controlled functionalisation at the nanoscale is key.

1.2.3. Coupling IR spectroscopy and electrochemistry by carbon material design

Due to their electrocatalytic activity, hydrogenases have been extensively studied by protein film electrochemistry [34, 35] (**Section 1.2.2**). However, electrochemical measurements give mainly information on the electrocatalysis kinetics and thermodynamics but little structural information. A rather detailed understanding of hydrogenase activity has been established

along the years but some mechanistic features are still in the shadow [101]. To improve hydrogenase understanding, new investigation techniques are required and their development could greatly benefit from carbon material design.

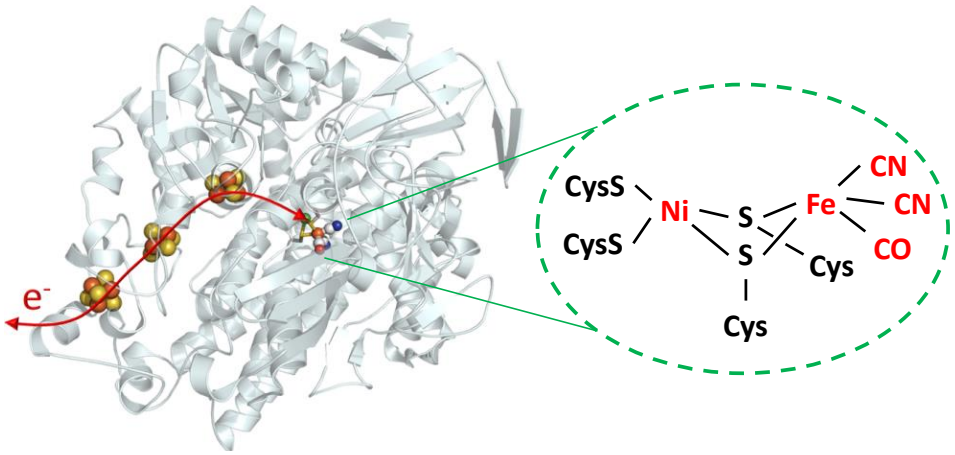

Figure 1.14. LEFT: representation of the crystal structure of a hydrogenase molecule showing how the enzyme is equipped for electron exchange from the outside of the enzyme to the buried catalytic active site: the protein framework is shown in 'ribbon' format in grey, [FeS] clusters are shown in elemental colours. The electron pathway from/to the outside of the protein to/from the active side in the middle of the ribbon structure is in red. ***With the assistance of Ricardo Hidalgo, Department of Chemistry, University of Oxford.*** **RIGHT: enlargement of the active site of an [NiFe] hydrogenase showing ligands CO and CN^- as well as the cysteine (Cys) amino acid.**

1.2.3.1. Need for a new technique to study hydrogenases

Few techniques make it possible to control and change the redox states of a bio-electrocatalyst and simultaneously acquire a characteristic signal from it. In order to gain more insight into hydrogenase features and properties, it is desirable to couple electrochemistry and vibrational spectroscopy. In particular IR spectroscopy is interesting because CN^- and CO are rather unusual biological ligands present at the active site, where the catalytic reaction happens This is represented in **Figure 1.14** for a [NiFe] hydrogenase. These ligands are characterised by IR active vibrational modes: CN^- gives 2 bands around

2000-2100 cm^{-1} and CO one band around 1810-1930 cm^{-1}. The bands from the ligands do not overlap with the intense amide bands around 1650 cm^{-1} for the amide I and 1545 cm^{-1} for the amide II band of the enzyme [103, 104]. The integral CN^- and CO bands are then ideal probes to investigate changes at the active site during catalysis or in the various potential-dependent states of the enzyme. The need for coupling protein film electrochemistry and IR spectroscopy has been covered in a review by Ash and Vincent [105] and spectroscopy of immobilised enzymes under electrochemical control is a technique still being developed [103, 105]. When fully optimised, it is expected that this technique would lead to real-time analysis under fast and direct electrochemical control of the influence of parameters such as pH, gas composition, presence of poisoning agents etc. on spectroscopic signals and so on enzyme catalytic activity. This could lead to deep insight into mechanistic features of hydrogenases. **Figure 1.15** illustrates the idea behind combining the benefit of electrochemical control achieved in protein film electrochemistry with IR spectroscopy.

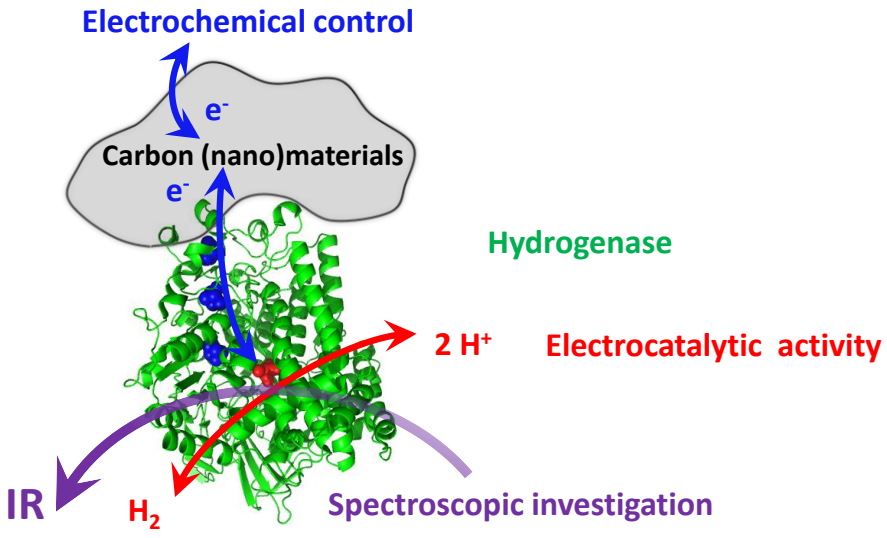

Figure 1.15. Schematic representation of coupled IR spectroscopy and electrochemistry using carbon materials. The enzyme is in green, the [FeS] clusters in blue and the active site in red.

1.2.3.2. Challenges in coupling IR spectroscopy and electrochemistry

To understand why design of carbon materials could help the coupling of IR spectroscopy and electrochemistry some background on the technique is useful. IR spectroscopy can be performed in various modes: transmission, reflection-absorption, attenuated total reflectance (ATR) [105]. The ATR mode is attractive for a practical reason: ATR spectroscopic data can be obtained by depositing a powder of material on an internal reflection element, **Figure 1.16**. This element will be a silicon prism in this thesis because it does not have specific features in the IR wavenumber region of interest for hydrogenase study. It is then possible to build on top of the deposited powder an electrochemical cell by connecting the carbon film to a conductive carbon electrode. Once the enzymes are immobilised on the carbon particles it is possible to control the enzyme electrochemical activity and at the same time record IR data [103, 104].

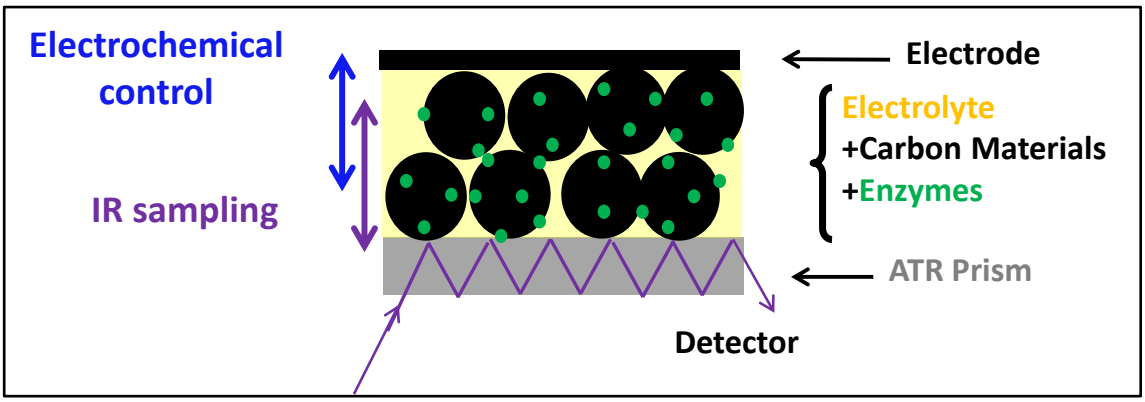

Figure 1.16. Schematic representation of a set up coupling IR spectroscopy and electrochemistry in a ATR mode for investigation of bio-electrocatalysts.

To optimise the signal-to-noise ratio, a popular way to conduct ATR measurements from immobilised species consists of depositing a gold or silver under (or over) layer on the prism before (or after) the immobilisation of the organic film of immobilised molecules to investigate [106]. This is to achieve 'surface enhanced infrared absorption' [107]. The main issue in this approach is the use of gold or silver. These metals have their own redox properties and can react with the aqueous solvent and electrolyte needed to perform the

electrochemical control. This limits the voltage range [58] or 'electrochemical window' that can be investigated compared to the relatively more inert carbon-only electrode. Developing carbon based electrodes compatible with IR spectroscopy in an ATR-mode could lead to a technique allowing deep investigation of enzymes in a wider electrochemical window. Last but important, carbon is a suitable material to immobilise hydrogenase (**Section 1.2.2**).

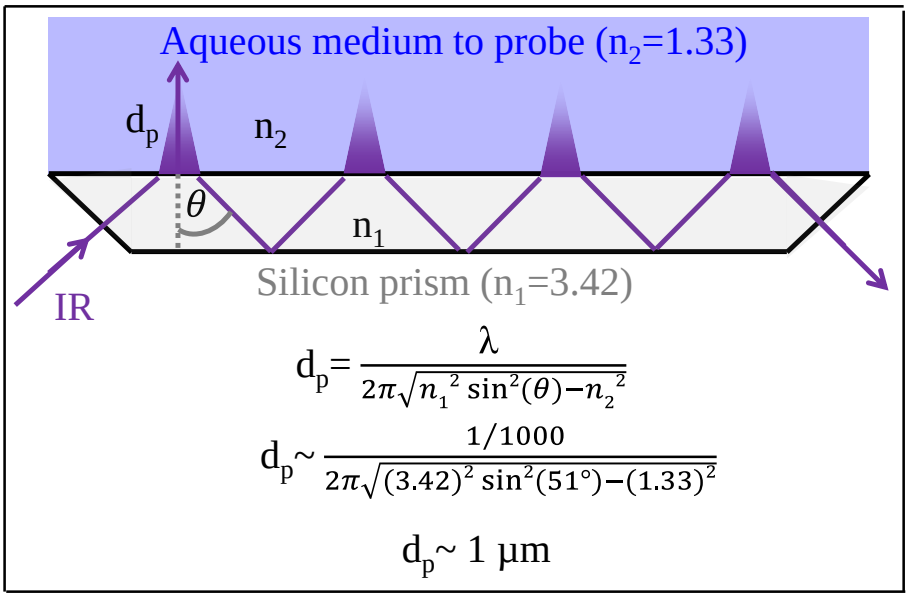

Figure 1.17. Schematic representation of the ATR prism and evanescent waves penetration in the medium to be investigated.

However, protein film electrochemistry measurements are often possible with relatively low loading of electroactive enzyme (below 1 pmol cm^{-2}) [35] in particular because the catalytic current measured is amplified by enzyme catalytic turnover. In contrast, spectroscopic signals are not amplified by catalytic activity. There is then a mismatch in the sensitivity, and so in the minimal loadings of enzyme required, when coupling these two techniques. In addition, IR spectroelectrochemical signals based on ATR mode involve evanescent waves [105] as illustrated in **Figure 1.17**. It is possible to roughly estimate the penetration depth (d_p) of the waves in the sample to probe [108], deposited on top of the prism. Considering a refractive index of n_1=3.42 for the silicon prism and n_2=1.33 for a medium to probe mainly composed of water, an angle of 51° between the IR beam and the

silicon flat surface (as it will experimentally be used in this thesis), this gives a penetration depth d_p in the order of 1 µm for a wavenumber of 1000 cm^{-1}. The molecules to be probed or investigated after immobilisation on carbon materials must then be at least within 1 µm from the prism. Therefore the typical size of the carbon materials to be used as electrode must preferentially be less than 1 µm.

In recent years, important improvements have been made to perform IR spectroscopy of hydrogenases under electrochemical control by Prof Vincent's group in Oxford. However, the first material used was PG particles [103]. Due to low control on size and shape with the preferred abrasion methods, the particles with size around 5-20 µm [63] could not be used without a polymer binder (Nafion). Further attempt with a carbon powder with a nanoscale also required the use of a binder [104]. Rather than directly immobilised, the hydrogenases are likely to be trapped together with the particles into a polymer matrix. This means that the enzyme may need to diffuse to the electrode to exchange electrons so a fast electron transfer is not guaranteed. This fast electron transfer is however required to simplify the enzyme electrode preparation, to discard any influence of the polymer/mediator needed for electron transfer and to give better control over the electrochemical response. To achieve DET and fast electron transfer for coupling spectroscopy and electrochemistry, alternative electrode materials would be greatly beneficial.

1.2.3.3. Towards improved coupling of IR spectroscopy and electrochemistry by carbon material design

A simple conclusion based on geometrical considerations is that carbon nanomaterials with a size less than about 1 µm should facilitate the coupling between ATR-IR spectroscopy and electrochemistry. Developing the technique towards such micro/nanomaterials has been suggested [105] but not implemented and is investigated in **Chapter 3**. Several options illustrated in **Figure 1.18** are possible to improve IR signal from the adsorbed species in the

ATR configuration. First, improving the electro-active loading of enzymes using tailored carbon based material (for example different size or surface area) so that most of the material surface is covered with enzyme and most of the immobilised enzyme sample sit as close to the prism as possible, **Figure 1.18b**. Second, developing structures like carbon nanotubes forests directly connected to the prism to get a carbon-functionalised prism and overcome the challenging dispersion of CNTs, **Figure 1.18c**. Third, improving penetration depth of IR signal in the volume probed by lowering the amount of carbon for instance by using hollow/porous structures or using core-shell materials with IR transparent cores like a silicon core and a carbon shell, **Figure 1.18d**.

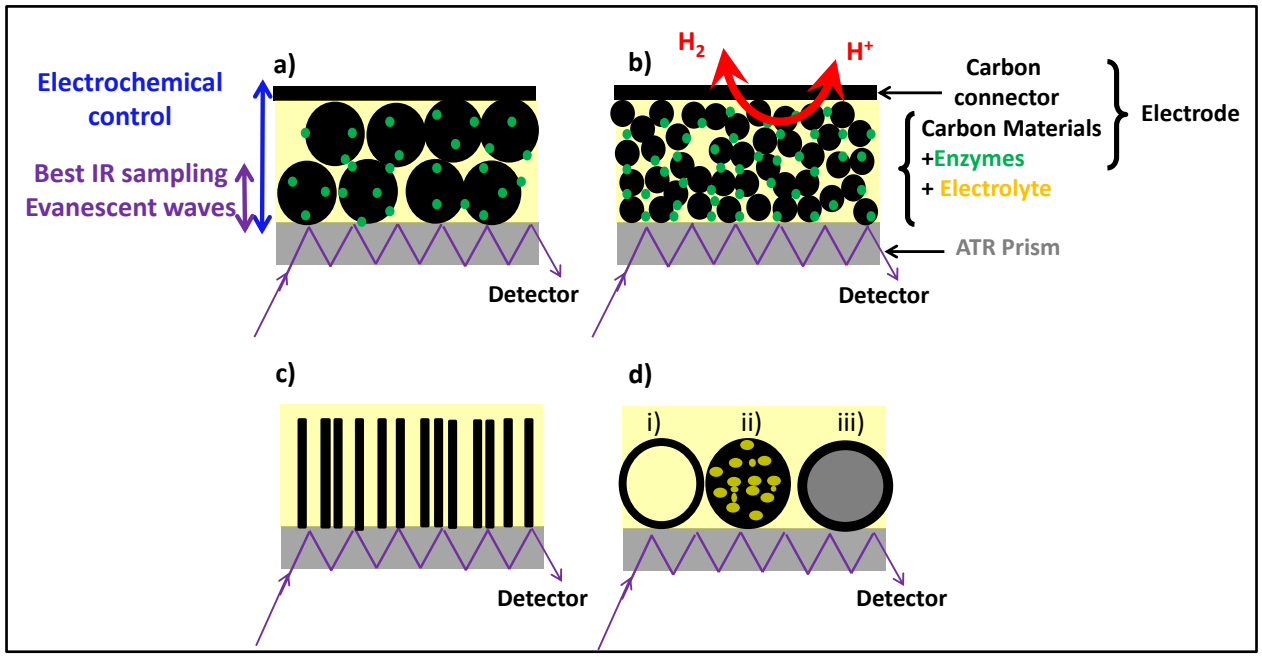

Figure 1.18. Schematic representation of an ATR spectroelectrochemical cell. (a) Electrochemical control decreases with distance from electrode while IR signal penetration depth decreases with distance to silicon optical prism. (b) Possible improvement to hydrogenase loading using smaller size particles. (c) Possibility to grow materials (*e.g.* CNTs) to functionalise prism and bring immobilised enzymes even closer to the prism. (d) Other materials that could be used to improve signal by maximising IR penetration depth: (i) hollow material, (ii) porous materials; (iii) silicon core – carbon shell particles.

1.2.4. Novel carbon scaffolds for flow-bio-redox catalysis

In addition to improve stability, facilitate studies or applications (**Section 1.2.1** to **1.2.3**), supporting catalysts present a major advantage for chemical production in flow catalysis [13, 22]. **Section 1.2.4** first gives an introduction to flow catalysis, to show how immobilisation of catalysts facilitates their use in flow reactors to continuously produce chemicals without the drawbacks of batch synthesis. Second, an enzyme based method recently developed to produce chemicals is presented. This method exploits the redox properties of hydrogenases to split H_2 to electrons and transfer these electrons through a carbon support. Combining the promising redox-enzyme-based chemical synthesis to flow catalysis could be relevant for various industries for the production of fine chemicals. Achieving this combination could benefit from the development of a flow-bio-catalytic device. An introduction to the field of flow catalysis and flow biocatalysis is first proposed. A severe limitation to couple flow catalysis and bio-redox systems is then identified: it is the lack of simple carbon supports to perform the coupling. This section finally identifies carbon scaffolds that could contribute to the development of flow-bio-redox catalysis.

1.2.4.1. Flow and bio catalysis: a promising combination for industrial production of chemicals

In 2011, top pharmaceuticals companies identified flow chemistry as the most important key area of research for sustainable development of chemical production [10]. In flow chemistry, a reactant is converted into a product in a continuously flowing stream of liquid or gas, **Figure 1.19a**. Flow chemistry then consists of performing a chemical transformation in a continuous or semi-continuous mode in a flow reactor. Flow chemistry offers a wide range of benefits in comparison to batch processing [109]: continuous operation, *in line* purification and characterisation, possible automation, facility to scale up production of chemicals, ease of product separation, possibility to miniaturise the flow system to increase

safety, minimise waste and by-products, minimise energy consumption [110-114]. These benefits reduce costs to synthesise chemicals which explain the increasing interest in flow chemistry for chemical production [10]. In particular, when a catalyst is used as illustrated in **Figure 1.19b,** flow catalysis is often performed in heterogeneous processes as the catalysts [110, 115, 116] or biocatalysts [117-119] are immobilised on inert solid supports. Flow catalysis further reduces costs of chemical production by improving the stability of the catalysts under operating conditions and catalyst recovery after reactions have been performed.

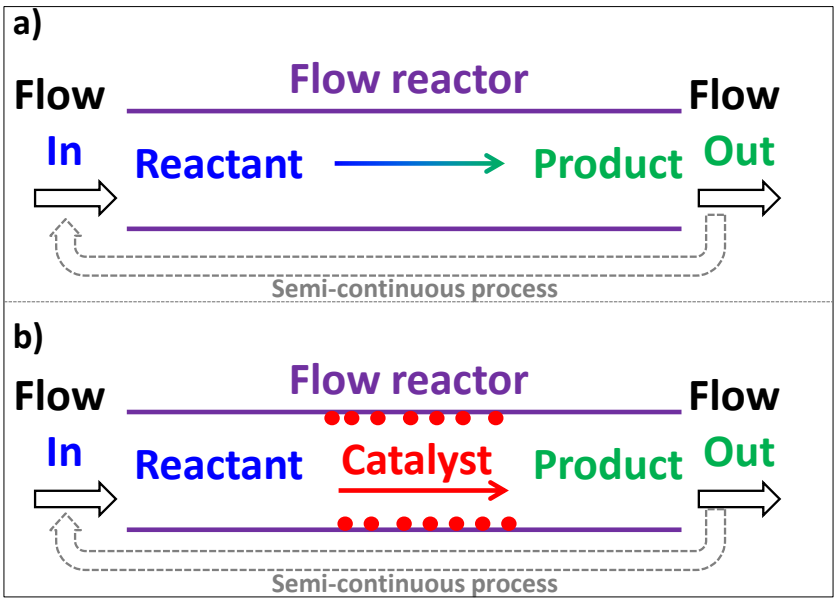

Figure 1.19. Schematic representation of a reactor for (a) flow chemistry and (b) flow heterogeneous catalysis.

The second area of research identified by pharmaceutical companies as key for future chemicals production is an increasing need for bio-processes [10]. For instance, enzymes are increasingly used as catalysts in the synthesis of fine chemicals because they can operate under mild conditions of temperature and pressure. This leads to safer and less energy demanding processes compared to other catalysts [10]. Also the near perfect regio- and enantio-selectivity of many enzymes make them a powerful tool in the selective synthesis of

chiral intermediates that are usually difficult to obtain by other routes. This high selectivity minimises waste and by-products, reducing production costs, time and energy. For instance using biocatalysts limits the number of purification steps required in drug production [10]. In particular, about 30 % of the main industrial biotransformations for production of fine chemicals are based on bio-redox processes [120]. A key limitation to use most enzymes with redox properties for chemical synthesis is the need for molecules called cofactors [118, 121]. Cofactors are required in stoichiometric quantities and without cofactors, like nicotinamide adenine dinucleotide (NADH), the enzyme cannot perform catalysis and reaction does not proceed. During catalysis the cofactor is consumed as illustrated in **Figure 1.20** for NADH oxidised to NAD^+. Recycling of cofactors (reforming NADH from NAD^+) is essential because the cofactor is often more expensive than the desired product [118, 121]. A preferred way to recover the cofactors in most industrial applications is to use a sacrificial reactant to regenerate the cofactor. This generates waste and so compromises the advantage of using biocatalysts in chemical synthesis.

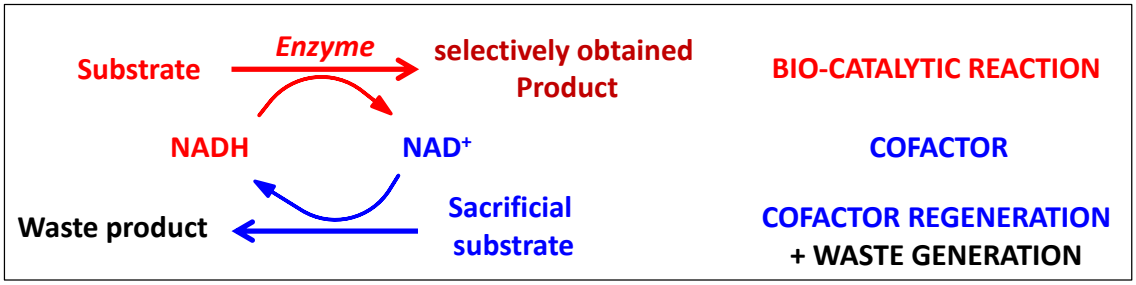

Figure 1.20. Schematic representation of redox biocatalysis illustrating the need for cofactor re-generation with the example of NAD^+/NADH. Most cofactor regeneration processes generate undesirable waste products.

Taking advantage of both heterogeneous flow catalysis and biocatalysis is a natural option to address at the same time the most important challenges faced by industries in fine chemicals production. However this is not a simple task, with pharmaceuticals companies stating that 'much more development is required to extend continuous to

biologics/bio-pharmaceutical processing' [10]. This is first expressing the need for a simple route to implement biocatalysts in flow systems. Second, it indirectly addresses the need to recycle the cofactor more efficiently for flow-bio-redox catalysis. Both challenges can be jointly addressed by the careful design of carbon scaffolds compatible with flow systems.

1.2.4.2. Hydrogenase-mediated chemical synthesis

An emerging area of research in the field of hydrogenase takes advantage of the ability of the immobilised redox enzyme to oxidise H_2 into protons and electrons to drive electron dependent reactions [62]. For instance several challenges in cofactor regeneration have been recently addressed by Prof Vincent's group at the University of Oxford using a cascade of enzymes [20], illustrated in **Figure 1.21**.

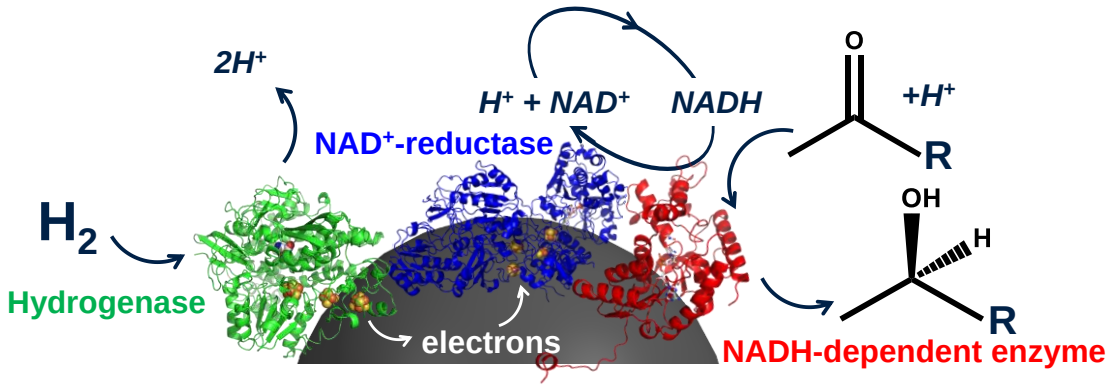

Figure 1.21. Schematic representation of enzyme-catalysed H_2-driven ketone reduction. The electrons from H_2 are passed from the hydrogenase (green) to the NAD^+-reductase (blue) through a conductive carbon material (black) to supply NADH to an NADH-dependent enzyme (red). *Adapted from Holly Reeve's DPhil thesis, Department of Chemistry, University of Oxford* [122].

The overall reaction is a chemical transformation using an enzyme-based cofactor recycling system [20]. A first property exploited is the ability to immobilise enzymes on conductive carbon materials. The immobilisation can be as simple as direct adsorption [20]. The second property exploited is the ability of hydrogenase, green in **Figure 1.21**, to split H_2 used as fuel into two electrons and two protons. A third property exploited is the

conductivity of carbon: the two electrons are transferred to a second enzyme (blue) through a carbon material (black) where the hydrogenase and this second enzyme are co-immobilised. The carbon material in some way mimics a complex electron transfer chain that could be found from one biological unit to another in an organism and acts as an electron transfer 'wire' between the two enzymes. In **Figure 1.21**, the second enzyme is a NAD^+-reductase able to convert NAD^+ to NADH. Under a thermodynamic driving force simply established by maintaining a 1 bar partial pressure of H_2, the co-adsorbed NAD^+-reductase uses the electron provided by the hydrogenase for the selective reduction of NAD^+ to NADH. Hence NADH can be generated and supplied *in situ*. A third enzyme (red) in the presence of the right reactant can further perform a specific reactant-to-product conversion using the formed NADH. The third enzyme can also be immobilised onto the carbon material, but can also be in solution. In the example presented, the third enzyme is an immobilised alcohol dehydrogenase (ADH) performing conversion of a ketone to an alcohol in the presence of NADH. During the catalytic reaction performed by the ADH, NADH is consumed while NAD^+ is formed. The formed NAD^+ can then be re-converted to NADH by the NAD^+-reductase just as described previously and summarised in **Figure 1.22**. This offers an elegant continuous *in situ* recycling system for NADH. The overall reaction is 100 % atom efficient and no waste is produced since only H_2 and catalytic NAD^+ cofactor quantities are required in addition to the reactant. One proton and two electrons from the splitting of H_2 are used for the reduction of NAD^+ to NADH, the second proton is used for the conversion of the ketone to alcohol. Since all the enzymes can be immobilised, the product is not contaminated with either enzyme or by-products and advantageously no mediator is needed for the electron transfer. The opportunity to select the third enzymes from a library of biocatalysts leads to an extremely modular system, relevant for a range of chemical transformations.

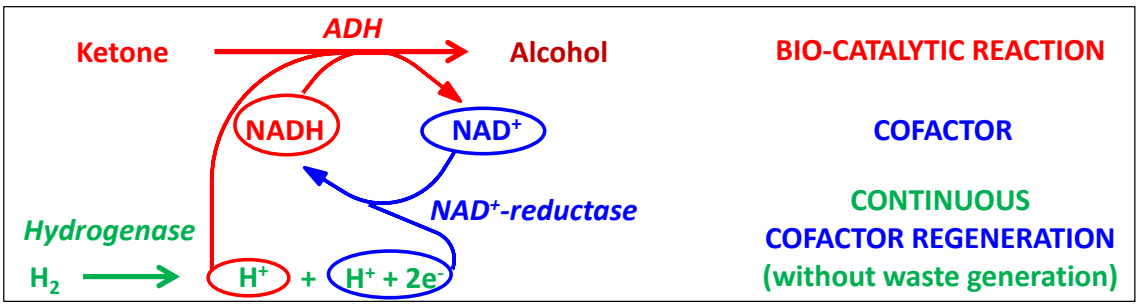

Figure 1.22. Schematic representation of enzyme-catalysed H_2-driven cofactor recycling for ketone bio-reduction.

A key parameter in this approach is to co-immobilise the enzymes on a suitable carbon material. The first material considered to develop in 2011 this system in a batch mode were PG particles because it is a suitable material for the immobilisation of hydrogenase and the NAD^+-reductase [20] (**Section 1.2.2.2**). These enzyme-modified particles already offer significant advantages over existing cofactor regeneration methods by using H_2 to drive recycling the NAD^+/NADH. However, PG particles can be of limited usefulness due to limited lab scale production and the need to produce the material on a daily basis by an abrasion technique (**Section 1.2.2**). The chemical industry expresses an increasing interest in carrying (bio)catalytic steps in flow reactors [10]. Developing bio-redox catalysis towards flow systems is then an approach with a direct relevance for industrial production and could be achieved with suitable carbon scaffolds.

1.2.4.3. Need for simple carbon scaffolds for flow-bio-redox catalysis

Advancing bio-processes and more specifically bio-electro and bio-redox processes towards flow catalysis is possible through the identification of suitable scaffolds to immobilise the catalysts. Materials usually considered as supports for flow catalysis are zeolites [123], silicas [115, 124], polymers [115, 116, 125] or carbon materials [115]. Carbon materials in particular combine a set of interesting properties. They possibly show a high surface area, a nanoscale, they are suitable to immobilise hydrogenase (**Section 1.2.2**) and most importantly they show higher conductivity than the other supports. Carbon materials are then the most

promising materials to upgrade the hydrogenase system presented in **Figure 1.21** to a flow configuration. A natural approach to develop a suitable carbon scaffold for flow catalysis is to integrate one of the wide range of carbon materials [70] reported over the last decades for the immobilisation of particles [70, 71, 115, 126], molecules [42, 70] or enzymes [8, 24, 30, 127]. Unfortunately, most of these materials are available as powders, like pyrolytic graphite or amorphous carbons (**Section 1.2.2**). To be used in flow systems, these powders often need to be packed into reactors like columns [76, 114, 128]. This requires several bar pressure [129, 130], sonication [131] and usually need for a filler [132] to ensure stability of the carbon network in the reactor. For instance, powder of CNTs require pressure as high as 50 MPa to be packed in a column [130]. Alternatively these powders can be used in fluidised-bed/slurry reactors. In that configuration a gas/liquid is passed through a solid catalyst powder in a reactor, until the content of the reactor including the solid catalyst swirl [133]. This provides efficient mixing but usually requires high velocity, high pressure and large tanks which make the process highly energy demanding and possibly hazardous. Powdered carbon materials are then relatively difficult to implement in flow (bio)catalysis. A different approach to design flow reactors could be beneficial and CNT forests (**Section 1.2.2.3**) are promising candidates.

1.2.4.4. CNTs in flow systems and flow catalysis

Due to their high surface area, good mechanical stability, ability to adsorb molecules and their nanosize (**Section 1.2.2.3**), CNTs are good candidate for flow devices. In the past, CNTs have been implemented in chromatography [130] or membranes and filters [132, 134]. However they have been more rarely suggested or demonstrated in flow catalysis [69, 76, 128, 135, 136]. This can be explained by several factors. First, this results from the need for intensive packing processes if the CNTs are used as dispersed materials [130]. Second, it can be explained by the challenging dispersion of CNTs [89] especially in aqueous solutions [88]

due to their strong hydrophobicity. These challenges can be overcome by considering alternative CNT geometries like CNT forests [90]. In this configuration the alignment obtained and detailed in **Section 1.2.2.3** confers a degree of organisation to as-synthesized CNTs that cannot be achieved with powders of CNTs. Vertically-aligned CNT forests can be further chemically modified [24, 137], decorated with catalyst particles [135, 138] or accommodate biomolecules [24, 37]. As a consequence, vertically-aligned CNTs have been proved to be suitable for various flow reactors [136] and devices [90, 139] for filtration [140], chromatography [141, 142] or water desalination [143]. However, CNT forests have been more rarely suggested for flow catalysis [69, 135, 136]. The experimental demonstration of vertically-aligned CNTs in flow catalysis is actually limited to date to two examples to the best of my knowledge.

In 2007, Ishigami *et al.* studied the hydrosilylation of 1-octene to octylsilane by platinum catalysts particles deposited onto MWCNT forests [69]. The process to obtain the flow reactor is illustrated in **Figure 1.23a**. It is rather complex and involves deposition of aluminium on a silicon substrate prior to MWCNT growth from ferrocene and xylene precursors by CVD in an open channel of width 2.5 mm. Platinum particles were then deposited on the MWCNTs by techniques requiring steps at temperature higher than 250 °C. The flow system is built up around the formed CNT forest by sealing the open channel. Hydrosylilation was performed at 50 °C at a flow rate of 1 µL min^{-1} with nearly 100 % yield and longer catalyst lifetime (up to 40 hours) with MWCNTs compared to a case without. This is attributed to better individualisation and stability of the supported particles, less subject to sintering in the MWCNT forest. However the aluminum layer and the nanotubes peeled off the channel surface under acid treatment preventing further chemical modification of the carbon surface. The second example was published in 2008 by Popp and Schneider [135] who studied the hydrogenation of *p*-choloronitrobenzene to *p*-chloroaniline at 27 bar

with a flow rate of 0.6 mL min^{-1}. They achieved a yield of 2.6 % with palladium particles deposited *in-situ* by chemical reduction of a palladium salt onto the MWCNTs grown from propylene by CVD. The full sequence to obtain the reactor is illustrated in **Figure 1.23b**. It is a multiple step approach requiring an alumina template and etching step in hydrofluoric acid, a chemical unfortunately extremely harmful. The final flow device is also built around the MWCNT forest after synthesis. It is important to note that for both examples the main selection criteria for the CNTs was to offer a high surface area and the conductivity of the materials was not exploited. In both cases multiple steps before or after the growth of the CNTs were needed prior to obtain the flow reactor. In both cases catalyst deposition or experimental conditions require a high pressure and/or temperature. In both cases the catalysts are metal particles and not enzymes.

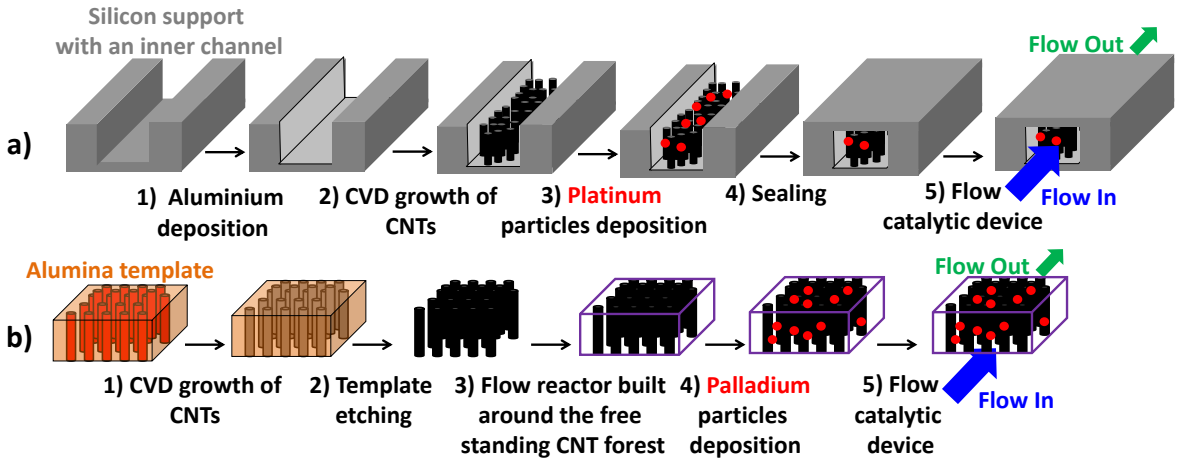

Figure 1.23. Schematic representation of the flow catalytic devices developed in (a) Ref [69] and (b) Ref [135].

Avoiding templates, chemical pre-treatment of the substrates, etching step or need to build a device after CNT synthesis would greatly simplify the implementation of CNTs in flow systems. A simpler approach identified in this thesis is to directly grow CNTs in a hollow cylinder to fill it with vertically-aligned CNTs, **Figure 1.24**. By analogy with chromatographic systems and flow reactors, these hollow cylinders are referred to as

'columns' in this thesis. The column geometry is readily compatible with a flow, **Figure 1.24a**, as reported for stationary phase development in chromatography [141, 142]. This approach is conceptually close to the development of 'inner wall-functionalised' flow reactors [69, 113, 114] where the reactor inner channel's walls are functionalised with a support for catalysts, **Figure 1.24b**. Direct growth of CNTs into a column also avoids the immobilisation step of the CNTs in the inner channel or any need for supportive binder or frit [144]. Vertically-aligned CNTs have indeed been observed to be in good mechanical contact with the surface they are grown on [136]. Another advantage is that direct growth of CNTs could be performed at temperature lower than 1000 °C [70, 144] whereas it would require temperature higher than 2000 °C to achieve the same direct filling with other carbon like graphitised carbon [144]. However, in all reports found where this type of approach is detailed to date the hydrocarbon flow required to grow the CNTs by CVD is forced to pass through the column during synthesis. Only one column can be obtained at a time [140, 141, 145, 146]. A direct consequence of this method of production is the limited availability of CNT columns, which probably account for the limited investigation of these columns in flow catalysis. Limited production is also likely to be the reason why their application in flow biocatalysis and bio-redox-catalysis more specifically has not been suggested or reported to the best of my knowledge.

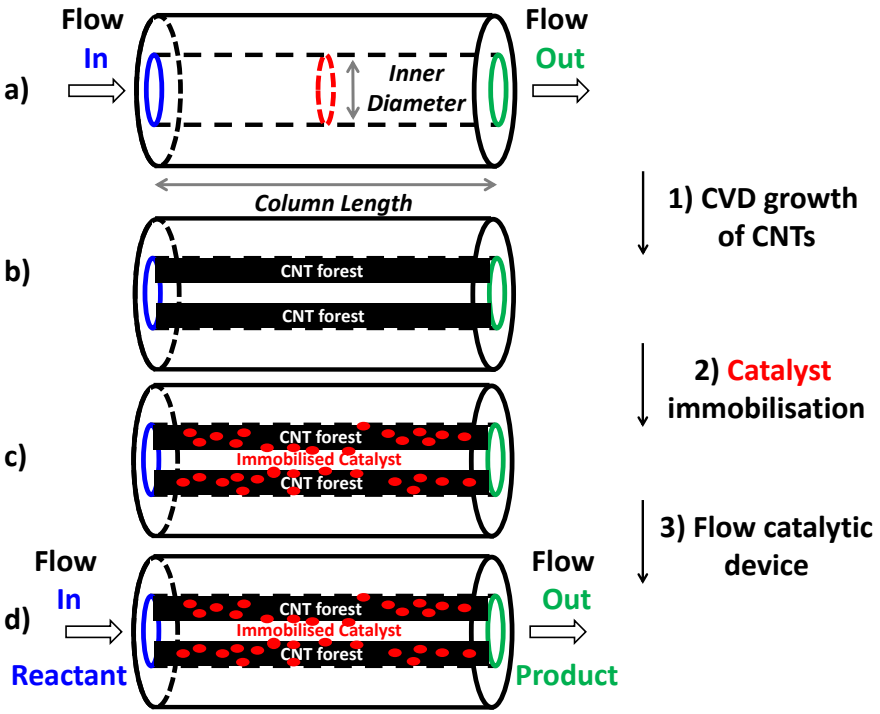

Figure 1.24. (a) Schematic representation of a column with a geometry readily compatible with flow catalysis. (b) Flow reactor than could be obtained by covering the inner diameter surface of the column with CNT forests (black) to support (c) catalysts (red) to develop (d) a flow catalytic device.

1.2.4.5. The challenging option of CNTs for flow-bio-redox catalysis

Homemade CNT forests are suitable for hydrogenase immobilisation [24, 37] and can be grown onto various surfaces. They are interesting candidates to develop scaffolds compatible with flow systems for novel hydrogenase applications. The opportunity to perform enzyme-mediated catalysis with CNTs based flow devices is however limited to date by the following: (1) the implementation of CNTs in flow devices is usually complex and requires multiple steps; (2) in case CNTs are grown *in situ* in a column, the hydrocarbon source used to grow the CNTs is forced to pass through the column. Therefore only one scaffold can be obtained at a time.

To transpose to a flow configuration a vast number of reported reactions supported by CNTs, it would be beneficial to have a simpler route to obtain CNT scaffolds readily compatible with flow catalysis. This is addressed in **Chapter 4**. Tubular substrates like

columns illustrated in **Figure 1.24** are identified as interesting possible scaffolds. It is expected that by optimisation of the production of these columns their field of application could be considerably broaden. In particular it would be relevant to transpose the hydrogenase-mediated chemical transformation system described in **Figure 1.21** to flow systems. First, transposing this enzyme cascade would be relevant due to the promising range of chemical transformations that could be performed. Second, using enzyme in aqueous solution is a perfect example to show that CNT forests are compatible with flow biocatalysis in aqueous solutions, despite the strong hydrophobicity of CNTs. Third, it is a way to prove that other properties than the high surface area of CNTs can be exploited in flow systems. For instance taking advantage of the conductivity of a CNT network to support bio-redox-synthesis in a flow reactor has not been considered to date to the best of my knowledge.

1.2.5. Controlled properties along CNTs for localised immobilisation of hydrogenases

Carbon powders may be suitable to develop electrodes (**Section 1.2.2**, **Section 1.2.3**) but are less suitable for flow systems which require the design of an ensemble of materials. For instance an ensemble can be columns filled with vertically-aligned CNTs to obtain a scaffold compatible with a flow (**Section 1.2.4**). To date, enzyme or other object immobilisation is performed with little spatial control within the ensemble. A further degree of design would be to locally achieve a spatially controlled immobilisation on a material, and ultimately within an ensemble of this material. Starting with the previously detailed example of co-immobilised enzymes for cofactor regeneration, a conceptual new material design to achieve localised immobilisation is proposed in this section. The design exploits more properties of the CNTs than those considered in **Section 1.2.4.** The additional properties

considered are: (1) the natural geometry of the nanotube and (2) a possible control over different surface properties along the tube.

1.2.5.1. New concept for hydrogenase localised immobilisation

The enzyme cascade based on hydrogenases [20] described in the previous section can be performed on carbon particles as illustrated in **Figure 1.25a**. If the carbon particles are interesting materials, it will be challenging to achieve immobilisation of one type of enzyme on one side rather than the other, as illustrated in **Figure 1.25b**. Such a partitioning of the enzymes could however lead to a natural gradient of electrons between the two sections in the case of an oxido-reduction process. This could hypothetically bring novel properties by creating directional current flow. A major limitation to test this hypothesis is that performing a complete or even partial localised immobilisation of enzymes on one part of a nanomaterial rather than the other is challenging. More broadly, performing a nano/micro spatial control for a nano-object immobilisation on a uniform nano/micro-object is a difficult task. If bulk immobilisation processes are well established to functionalise nanomaterials [24, 71], much less work has been carried to achieve a spatial control at the nanoscale over this functionalisation. The challenge is that particle-like materials have a zero dimension (0D) without spontaneous asymmetry. This means that from a geometrical point of view, there are no preferred parts on the particles to favour an asymmetric functionalisation. A one dimension material (1D) could facilitate a controlled immobilisation as illustrated in **Figure 1.25c** because this material has two natural extremities. This 1D structure is reminiscent of a CNT and it can be postulated that developing CNTs with different morphology or composition could favour different properties along the tubes. This could be further exploited for immobilisation of different species like enzymes along a nanomaterial or along an ensemble of this material like a CNT forest.

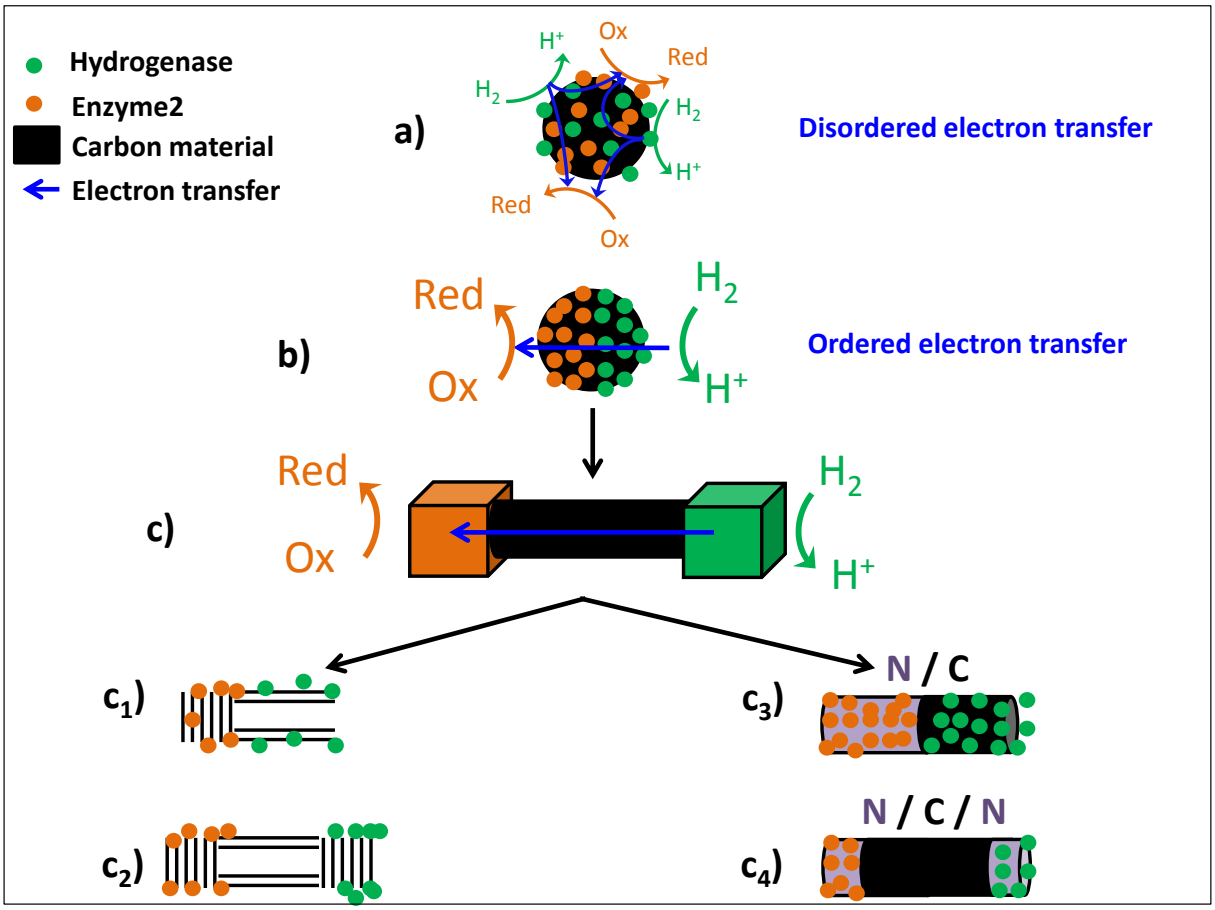

Figure 1.25. Schematic representation of: (a) an enzyme redox cascade on carbon particles; (b) an hypothetical situation where localised immobilisation of enzymes could be performed on the particles; (c) a simpler 1D carbon material that could also be compatible with the configuration hypothesised in (b). 1D carbon materials that could favour the structure hypothesised in (c) by a simple carbon material design are proposed in (c_1) and (c_2): 1D materials with a carbon lattice orientation change; (c_3) and (c_4): 1D materials with a chemical composition change.

Obtaining CNTs with different properties along the nanotube for localised enzyme immobilisation is conceptually possible by two approaches. First by changing the carbon planes from basal-like to edge-like. This should induce different interactions of the enzyme with the carbon surface: preferential interaction of the enzyme with the edge-like plane as detailed in **Section 1.2.2**. Second, by inducing a compositional change within the material. Changing the orientation of the carbon planes within a material as represented in option (c_1)

and its extension (c_2) should be possible. It could be attempted but the opportunity seems limited to a specific catalyst [147] that leads to tubes made of basal or edge-like walls depending on the temperature of reaction. Control over the carbon plane orientation has been achieved during independent experiments at two distinct temperatures. The possibility to experimentally induce a change in the orientation of the carbon planes along a nanotube by changing the temperature *during* the same experiment has never been considered or reported to the best of my knowledge. Since this last option has experimental limitations, an exclusive focus is given to an alternative option.

A simpler option to develop the asymmetric material (c) could be to use the CNT (c_3) in **Figure 1.25c.** This is a CNT with a change in composition where half of the carbon lattice is doped or enriched with an element like nitrogen and the other half is not. Nitrogen doping of CNTs has been established as a simple way to favour redox enzyme loading since the presence of nitrogen in the carbon lattice alters the properties of the CNTs. For instance, after acidic treatment, a higher enzyme loading was demonstrated on nitrogen-doped CNTs (N-CNTs) compared to the un-doped counterparts [148]. This was established by study of two independent doped and un-doped batches. The better loading is probably due to more defects in the N-CNT structure leading to more anchor points for the enzymes to be immobilised. Different behaviour can then be expected on the non-doped (C) section and the nitrogen-doped (N) section if they can be combined within a single material. Option (c_4) is similar to option (c_3) but now the two N sections are separated with a C section. One could expect preferential immobilisation of enzyme on the chemically modified N sections. Previous reports address the synthesis of CNT with a change in composition and are reviewed in **Section 1.2.5.4**. Prior to this, a broader introduction to asymmetric functionalisation of CNTs is given. This introduction highlights why the material design (c_3), together with the general approach proposed in this thesis to design asymmetric materials,

have great potential applications when achieving a simple spatial control at the nanoscale over reactivity or functionalisation is key.

1.2.5.2. Asymmetric functionalisation of CNTs: a review

Beyond the scope of the application proposed in this report for hydrogenase immobilisation, the material (c_3) illustrated in **Figure 1.25** addresses a broader field of research and broader challenges. It is equivalent to the design of a Janus material which in their simplest and broadest description are objects with asymmetric properties or composition onto the same object [149]. A block co-polymer or a particle with only one half covered with a metal can be considered Janus objects [150]. Janus structures have specific properties brought by their asymmetric nature, such as magnetic properties [149], and can show different reactivity on their different sections [149, 151]. One simple example to illustrate both the benefit and challenges of tubular Janus structures is the creation of nano-swimmers [151]. Nano-swimmers are not relevant for the objectives of this thesis but are a convenient example and case study. Nano/micro-swimmers can be obtained by deposition of platinum particles only at one end of a 1D material as illustrated in **Figure 1.26**. In the presence of H_2O_2, a reaction is catalysed by the platinum creating H_2O and O_2. The localised formation of O_2 bubbles only at the extremity covered with platinum leads to the propulsion of the material in a given direction which illustrates localised reactivity. Another point to stress with this specific example is the asymmetric functionalisation achieved with an asymmetric process: an electric field is applied to the material. The material is polarised and the reduction of a platinum salt to platinum particles occurs only at one extremity of the tube. In most cases where asymmetric nano/micro-structures are reported, the final asymmetry is in fact induced by the technique used for modification or decoration of the carbon material and not by the properties of the material itself [149].

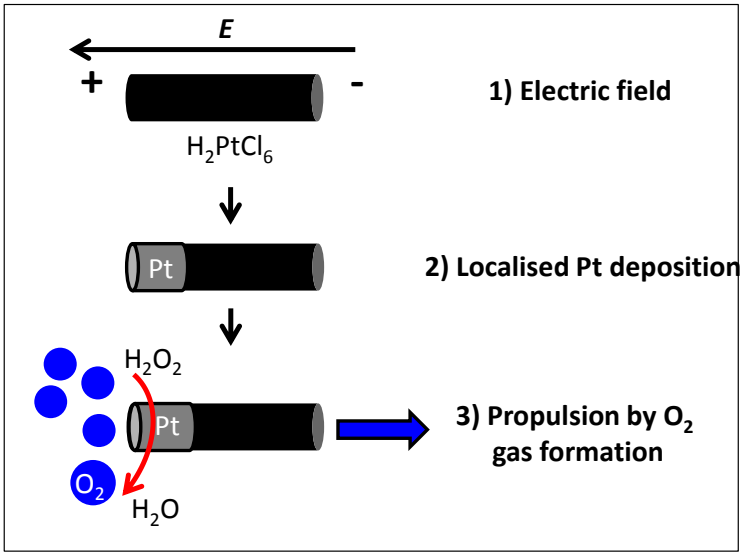

Figure 1.26. Example of Janus carbon micro-tube and possible application for nano-swimmers as developed in Ref [151].

Obtaining Janus materials is then often limited to specific asymmetric techniques to date, which can be a bottleneck to obtain them in large quantities and/or by simple and more widely established bulk techniques. Materials with a natural asymmetry like 1D materials may favour further simpler asymmetric functionalisation. However, despite their favourable geometry, tubular 1D materials have been far less considered than particles to develop Janus materials [149]. For instance, the few examples where Janus-like structures were obtained with CNTs are summarised in **Figure 1.27**. Asymmetric chemical functionalisation of CNTs has been performed taking advantage of the different reactivity of CNTs tips (edge plane, more reactive) over sidewalls (basal plane, less reactive) [152]. Free-standing vertically-aligned CNT forests [90] can be used to facilitate an asymmetric decoration. With this geometry it is possible to 'macroscopically' perform different chemical functionalisation at different extremities of the tubes [153, 154] or immobilise particles preferentially at the tips [155]. This can be done for example by pouring the right extremity in the right solutions of reactant and flipping the forest to functionalise the other end with another reactant.

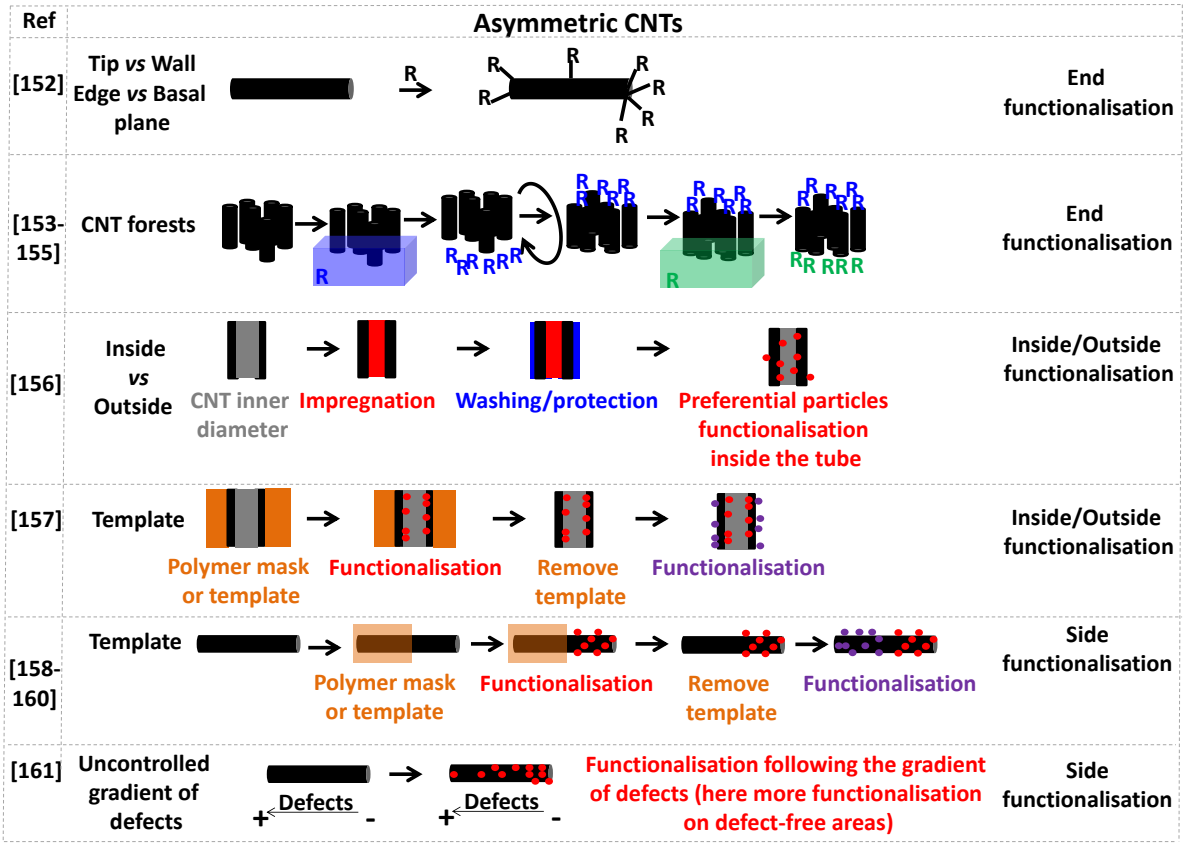

Figure 1.27. Possible general approaches to obtain asymmetric CNTs as detailed in the text.

Playing with the difference in hydrophobicity/hydrophylicity of the inside and outside of the tube also enables the localised immobilisation of particles inside or outside the CNT [156]. For asymmetric decoration of nanoparticles inside or outside the CNTs [157] polymer masks or templates are often required in a multi-step approach which adds complexity to the process. In view to immobilise enzymes, side functionalisation of the CNT would be more beneficial to exploit the carbon nanotube exposed surface. The same template approach can be used to functionalise asymmetrically the CNT walls [158-160]. However most treatments required to remove the template or masks would not be compatible with enzyme stability because it requires organic solvents or high or low pH. It is then not a suitable route localised immobilisation of enzymes which are too sensitive to harsh experimental conditions. Another option is to use ultra-long vertically-aligned CNTs (between 1 and 10 mm long)

where a gradient in defects along the CNTs occurs naturally. It can be used to induce different particle loadings along the tube [161] and ultimately possibly different enzyme loadings. However there is little control over the gradient of defects formed and hence little control over the localised loading of particles.

Asymmetric structures based on CNTs are then limited in number to date. Their formation focuses on post-synthesis asymmetric decoration or functionalisation *via* specific processes [158], specific CNT geometry [153] or specific CNT length [161]. A simpler approach would be to induce in a controlled way different composition in CNTs *via* their synthesis. Due to the expected different properties possibly achieved along the CNTs, different particle loading or reactivity should be 'spontaneously' achieved on the different parts of the material even when using a bulk modification method and regardless of the method selected. Such material would lead to a simpler route to obtain carbon Janus-like micro-structures as is illustrated in **Figure 1.25** with enzymes. To the best of my knowledge controlling different properties along CNTs to control immobilisation of objects has never been suggested. This concept needs to be proved and this starts by identifying suitable CNTs showing a structural change along the tube.

1.2.5.3. Opportunities to tailor CNTs for asymmetric functionalisation: CNTs with junctions

Modifying CNT properties *via* careful synthesis is the subject of considerable interest because it is a direct way to tune individual nanomaterials and so directly control bulk material properties. For instance, it is well established that elements such as boron, silicon or nitrogen can be incorporated in the CNT structure [92, 93, 162]. Hetero-atomic substitution gives control over individual nanotube electrical, surface, mechanical, morphological properties to match specific criteria in multiple applications of CNTs like electronics, energy or catalysis [66]. In particular, modifying carbon nanotubes with nitrogen [92] is known to

introduce defects in the graphitic carbon network [162]. So called N-CNTs are easier to chemically functionalise than their un-doped counterpart [163]. Nitrogen doping also helps to improve the efficiency of devices. For instance, better efficiency of platinum fuels-cells is observed when using N-CNTs rather than un-doped CNTs [164]. This is due to a more uniform coverage of the outer surface of the tubes with platinum particles, possibly due to more defects and favourable nucleation points on the N-CNT surface.

A step further to tune CNT properties is the option to develop intratubular junctions within a single CNT. This gives nanotubes with distinct segments displaying different properties along the same tube. The nature of reported junctions is as diverse as SWCNT to MWCNT junction (SWCNT/MWCNT) [165]; different diameter junctions [166, 167]; coaxial MWCNTs [168] with N-MWCNTs wrapped by un-doped MWCNTs (C@N); isotopic C^{12}/C^{13} junctions within MWCNTs [169, 170] and SWCNTs [171]; boron carbonitride to un-doped MWCNTs (BCN/C) junctions [172-174]; boron doped to un-doped MWCNTs [174] (B/C); nitrogen-doped to un-doped MWCNTs [175] and SWCNTs [176] (N/C) or even a controlled nitrogen gradient [177] along a MWCNT. It is worth noting that materials showing sections with or without nitrogen doping as presented in **Figure 1.25** have already been reported. Transmission electron microscope (TEM) images of these structures are shown in **Figure 1.28** together with the typical TEM image of un-doped MWCNT, **Figure 1.28a,** and N-MWCNT, **Figure 1.28b**. A MWCNT has thick walls (area with darker contrast in the TEM image) and well defined inner diameter (area with brighter contrast in-between the areas with darker contrast) whereas the N-MWCNT has a more corrugated structure. These typical morphologies can be combined along a single nanotube, **Figure 1.28c**, and this is a first assessment of the successful formation of a junction. Beyond the morphology and structure, other properties may differ along the nanotube. However, despite the variety of junctions demonstrated, these materials have not been considered for

localised immobilisation of species. A review of CNTs with junctions is then proposed in this thesis to understand better the knowledge and limitations on these structures to date.

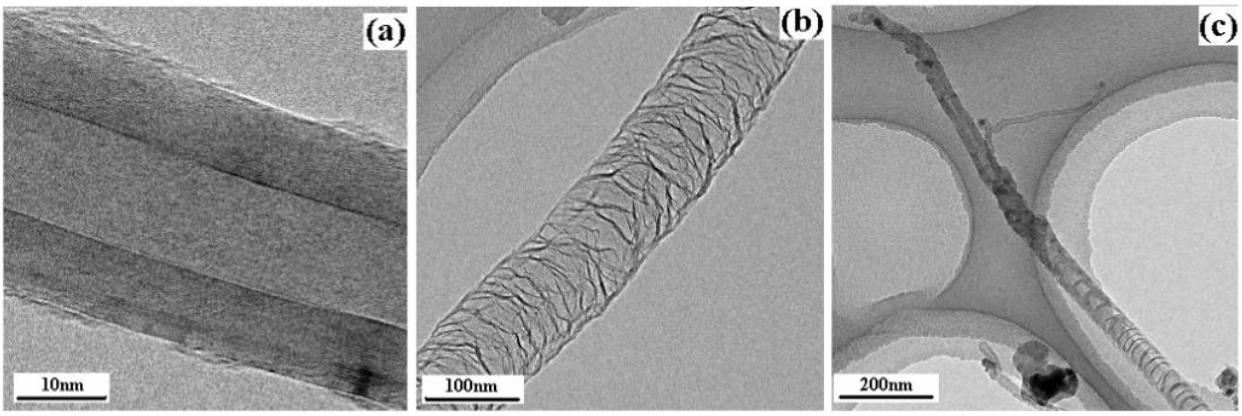

Figure 1.28. TEM images of individual (a) MWCNT, (b) N-MWCNT and (c) a MWCNT/N-MWCNT intratubular junction (C/N). Reproduced by permission of IOP Publishing from Ref [178].

1.2.5.4. Synthesis, characterisation and applications of CNTs with junctions to date

Key publications on CNTs with junctions are summarised in **Table 1.2** and the techniques reported for their characterisation in **Table 1.3**. A specific focus is given to materials with a junction between nitrogen-doped (N) and un-doped (C) CNTs. This is because they correspond to the structure identified in **Figure 1.25** to achieve a localised immobilisation of hydrogenase on a carbon nanomaterial. The nature of the hydrocarbon precursor used to grow the CNTs by CVD for instance, controls the properties of the CNTs [92, 179]. Therefore inducing different properties along the CNTs is achieved by changing the composition of the precursors *during* a single experiment, *as* the CNTs are formed. To form a CNT/N-CNT (C/N) junction there is a need to switch from a hydrocarbon precursor that does not contain nitrogen, like CH_4, to a hydrocarbon precursor that contains nitrogen, like a mixture of CH_4 and N_2 [180]. Trying to connect CNTs obtained in two independent and successive steps does not lead to the desired junctions [180], or leads to non-continuous junctions between the two segments [167]. The phase of hydrocarbon precursors used before

Table 1.2. Overview of the literature on CNTs with various junctions. A * indicates that the influence of order of precursor was investigated. N/R means that no yield was reported. 'Claim' means that a specific claim on the ability to produce large quantities is made. A 'X' in the alignment column means that the CNT are vertically-aligned and obtained without template unless otherwise specified. A particular focus is given to N/C junctions in the second half of the table.

Junction	Structure	Precursor phase	Yield	Length of CNTs	Alignment	Application	Date	Ref
m/m; m/s	SWCNT	-	N/R	-	-	electronic	1999	[181]
$^{12}C/^{13}C$ *	MWCNT	Gases (C_2H_4)	N/R	~ 190 µm	X	-	2001 2003	[169] [170]
$^{13}C/^{12}C$	SWCNT	Gases (CH_4)	N/R	< 70 µm	-	-	2008	[171]
Various junctions	SWCNT and MWCNT	Gases (C_2H_4, CH_4)	N/R	-	-	-	2006	[165]
Diameter change	MWCNT	Gases (C_2H_2)	Claim N/R	-	X (template)	-	2001	[166]
BCN/C	MWCNT	Gases (CH_4, N_2, B_2H_6)	N/R	~10 µm	X	electronic	2002 2007	[172] [173]
B/C	MWCNT	Gases (CH_4, B_2H_6)	N/R	~10 µm	X	-	2008	[174]
2 steps junctions	MWCNT	-	N/R	-	X	electronic	2004	[167]
N@C	MWCNT	Liquids (benzylamine, toluene)	N/R	-	-	-	2007	[168]
C/N *	MWCNT	Gases (CH_4/N_2)	N/R	-	X	-	2001	[180]
C/N	MWCNT	Solid and Gas (iron phtalocyanine, ammonia)	Claim N/R	~10 µm	-	electronic	2004	[182]
C/N	MWCNT	Solids (ferrocene / melamine)	Claim N/R	few µms	-	electronic	2005	[178]
C/N	MWCNT	Solids (ferrocene / melamine)	Claim N/R	~15 µm	X	electronic	2006 2007	[183] [184]
C/N *	MWCNT	Solid and Gas (iron phtalocyanine, ammonia)	N/R	~10 µm	X	electronic	2006	[185]
C/N *	MWCNT	Liquid (xylene, pyridine)	N/R	~ 800 µm	X	-	2010	[177]
C/N *	MWCNT	Liquids (hexane, ethylenediamine)	N/R	-	-	-	2011	[175]
C/N	SWCNT	Liquid and Gas (C_2H_2, pyridine, acetonitrile)	N/R	~130 µm	X	-	2011	[176]
C/N	MWCNT	Liquid (hexamethylenetetramine, pyridine, benzene)	Claim N/R	~ 20 µm	X	electronic	2013	[186]

and after the switch can be two solids [178], two gases [180], two liquids [175], a liquid [176] or solid [185] with injection of a gas like ammonia to induce doping. As summarised in **Table 1.2,** a variety of hydrocarbon precursors then lead to the desired structures. This is

encouraging to develop and investigate CNTs with junctions because their synthesis does not seem to be limited to strict experimental conditions. In most cases vertically-aligned forests are obtained [176]. This suggests the possibility to get control over the properties of not only individual CNT but also a forest made of these CNTs.

However the syntheses developed to date are not satisfying in terms of quality and yields of materials. A number or reports explicitly stressed and acknowledged that creating junctions is still challenging [165, 168, 178, 180, 181, 185, 186], especially because the integrity of the CNT structures must be maintained which means that the junctions developed between the two sections must be sharp and continuous. There is also an acknowledged need to be able to produce larger amounts of these materials [174, 175, 177, 178, 183, 186]. As a fact, publications highlighted with a 'claim' note in **Table 1.2**, explicitly make a claim on the ability to produce large quantity of materials. Unfortunately even when this claim is made, it is never supported by quantitative results. This probably stresses remaining limitations in the production of these materials. To improve the production, a better understanding of the mechanism at stake is certainly required. This mechanism is not fully investigated in most publications. One way to get better control on the production could then be achieved by studying the influence of order of precursor used on the resulting CNTs. In most cases the influence of order of injection of the two precursors to control the sequence of growth of the different section is not studied or not detailed. With solid precursors this is because the order of injection is fixed by the sublimation temperature of the precursors used [178]. For liquid and gaseous precursors it is experimentally possible to control the order. Cases where a specific study of the influence of the order of injection of precursors is reported are marked by '*' in **Table 1.2**. In most cases the opportunity to invert the order of precursor injection to get more control over the structure formed is not investigated. In the few cases where this investigation is performed, it is shown that carbon

nanotubes with junctions are still produced. However this is reported as a side observation [175] and not fully exploited to establish a growth mechanism as it will be in this thesis. The limited optimisation of the growth can be explained by the fact that application of the material to date did not require large amount of CNTs. Indeed, an exclusive focus on electronics [182] and photo-electronics [187] properties and applications has been given to CNTs with intratubular junctions, **Table 1.2**. The related studies only require few individual nanotubes [167, 173, 178, 181, 182, 184-186, 188] to assess p-n junction behaviour to develop diodes for instance.

Table 1.3. Overview of the different techniques used to characterise CNTs with junctions. A * indicates that the influence of order of precursor was investigated. A 'X' means that the technique was used to characterise the junction. A particular focus is given to N/C junctions in the second half of the table.

Junction	SEM	TEM/HRTEM	AFM	EDX	XPS	EELS	Raman	TGA	Date	Ref
m/m; m/s	-	-	X	-	-	-	-	-	1999	[181]
$^{12}C/^{13}C$ *	X	X	-	X	-	-	X-along the tube	-	2001 2003	[169] [170]
$^{13}C/^{12}C$	X	X	X	-	-	-	X-along the tube	-	2008	[171]
Various junctions	-	X	-	-	-	-	X-not along the tube	-	2006	[165]
Diameter change	X	-	-	-	-	-	-	-	2001	[166]
BCN/C	X	X	-	-	-	X	-	-	2002 2007	[172] [173]
B/C	X	X	-	X	X	-	-	-	2008	[174]
2 steps junctions	X	X	-	-	-	-	-	-	2004	[167]
N@C	X	X	-	X	-	X	-	X	2007	[168]
C/N *	X	X	-	-	-	-	-	-	2001	[180]
C/N	-	X	-	X	-	X	-	-	2004	[182]
C/N	-	X	-	-	-	-	-	-	2005	[178]
C/N	X	X	-	-	-	-	-	-	2006 2007	[183] [184]
C/N *	X	X	-	-	-	X	-	-	2006	[185]
C/N *	X	X	-	X	X	-	X-not along the tube	-	2010	[177]
C/N *	-	X	-	X	-	-	-	-	2011	[175]
C/N	X	X	-	-	-	X	X-along the tube	-	2011	[176]
C/N	X	X	-	X	X	-	X-along the tube	-	2013	[186]

The limited production also accounts for the relatively limited characterisation of CNTs with junctions to date. Characterisation is mainly performed with technique requiring little amount of materials (few milligrams). Techniques previously used are summarised in **Table 1.3** and they are all relatively common in the field of materials science like scanning electron microscopy (SEM), transmission electron microscopy (TEM) and high resolution TEM (HRTEM), atomic force microscopy (AFM), energy dispersive X-ray spectroscopy (EDX), X-ray photoelectron spectroscopy (XPS), electron energy loss spectroscopy (EELS). These techniques have been selected because they give information with spatial resolution from few angstroms to few micrometres on the morphology and composition of nanomaterial. Most of them require access to specific equipment. This can explain why CNTs with junctions have to date been confined to the field of material science. In contrast, Raman spectroscopy is a widely used characterisation technique for carbon materials [189] and can be found in most modern research centres and universities. The technique is detailed in **Chapter 2** and is promising as a simple way to characterise CNTs with junctions because it gives information on the graphitic structure of the carbon materials. Raman spectroscopy can be combined with confocal microscopy [186] to obtain localised information on the graphitic structure of the CNT *along* the tube. This is suitable to characterise the expected change in composition. For example, since nitrogen doping alters the graphitic structure of CNTs [92], Raman spectroscopy can be a good indication to establish if a section along a CNT with junction has been affected by nitrogen doping. Surprisingly, despite being simple and widely reported to characterise carbon materials, this technique has rarely been reported to characterise CNTs with junctions. A closer look to **Table 1.2** and **Table 1.3** reveal common features on materials where Raman spectroscopy along the tube could be performed. First: the nanotubes were in a forest configuration; second: the length achieved was longer than 20 µm. This makes sense considering that Raman confocal microscopy has

usually a spatial resolution of about 1-2 µm. The junctions themselves with a size inferior to 100 nm (**Figure 1.28**) cannot be directly identified by Raman confocal microscopy. To accurately characterise CNTs on both segments on each side of the junction with Raman spectroscopy, it is easier to control the orientation of the tubes [176], so the possible location of the junction as illustrated in **Figure 1.29**. Therefore it is easier to work with forests rather than dispersed CNTs. However, even in this forest configuration, the limited length (**Table 1.2**) achieved for the CNTs with junctions limits their characterisation by Raman spectroscopy. This is because the length of each section, L_1 and L_2 in **Figure 1.29**, must be longer than the spatial resolution of the Raman spectroscopy measurement (D) to acquire Raman data on one specific section only. Similarly, the limited length and yield achieved to date account for the fact that investigation of the materials by other techniques like thermogravimetric analysis (TGA, detailed in **Chapter 2**) has rarely been considered. TGA could give information on the oxidation resistance of CNTs with junctions, therefore on the reactivity of the CNTs with oxygen. Only one example could be found for TGA analysis of a carbon material with a change in composition. This analysis was however not performed on materials with a junction along the tube but on a core@shell C@N material [168]. It must be concluded that due to practical limitations on length and yield of material achieved to date, very little is known or established on the different graphitic structure and reactivity possibly developed along CNTs with intra-tubular junctions.

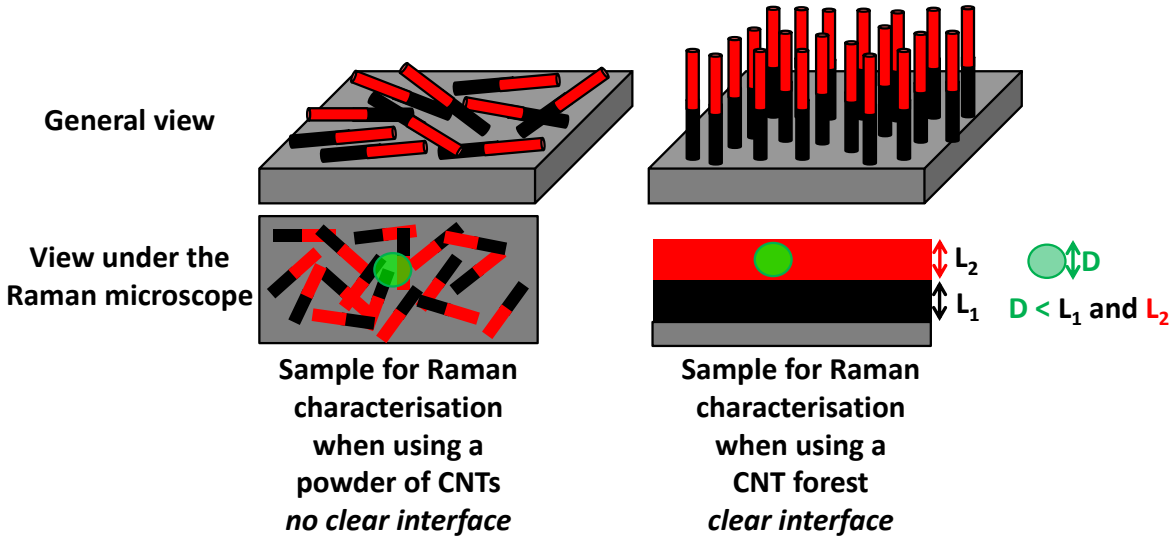

Figure 1.29. Schematic representation to illustrate the preference for a forest geometry for Raman characterisation of CNT with intratubular junctions. Each colour red or black corresponds to different segments with different properties within a single CNT with junction. The green spot corresponds to the Raman laser spot and schematises the spatial resolution of the measurement.

1.2.5.5. Overcoming limitations in production and characterisation of CNTs with intratubular junctions

In summary, developing CNTs with junctions and different properties has already been explored in the scientific literature. Unfortunately these materials have a limited production to date. This is probably why all studies related to the applications of these structures have a specific focus on their electronic properties. This also accounts for the confinement of the material to areas of research where specific techniques like electron microscopy are commonly used. Key achievements to broaden the scope of applications and study of these materials and to support the conceptual idea presented in **Figure 1.25** are the following. First, achieve the production of large quantities and long (> 20 µm) vertically-aligned CNTs with junctions. This can be done by studying the influence of order of precursors to be able to understand better the growth of these structures. Second, establish that the independent structural properties of the sections on both sections of the junctions are maintained. In

particular to open new opportunities for using these materials outside the field of material science and nano-electronics, it would be beneficial to identify a simple method that is available in most laboratories to characterise the junctions. In this sense Raman spectroscopy has probably been overlooked. Third, prove that control over the structural properties developed during the synthesis of CNTs with junctions helps in achieving a spatial control over reactivity along the material. This could be done by showing for the first time a localised functionalisation along the nanotube using bulk modification methods, without the need for a process inducing an asymmetric modification. All these inter-dependent challenges are jointly addressed in **Chapter 5**.

1.2.5.6. AACVD production of MWCNTs with intratubular junctions

A major challenge to broaden the scope of application of CNTs with junctions is to develop a new production method. SWCNT can be metallic or semi-conducting but their synthesis often leads to a mixture of both species [77] and they are strongly hydrophobic. In contrast MWCNTs are slightly less hydrophobic than SWCNTs and so slightly more suitable for hydrogenase and enzyme adsorption [83]. MWCNTs are always metallic and their production is generally simpler to control so cheaper than for SWCNTs [77, 190]. In this thesis an exclusive focus has then been given to MWCNTs. Among methods to obtain MWCNTs are laser-ablation techniques, arc-discharge and CVD [190]. CVD (**Figure 1.10**) is probably the most popular production technique because it is simpler than the other methods, can be performed at atmospheric pressure and relatively lower temperature and yet achieve higher yields [190]. CVD also offers a wide range of parameters to control the growth and properties of the MWCNTs. For instance graphitisation, and so defects in the carbon lattice, can easily be tailored by using different precursors [191]. In particular with the aerosol-assisted chemical vapour deposition (AACVD) technique fully detailed in **Chapter 2**, it is possible to produce vertically-aligned forests of MWCNTs on various

substrates from potentially any liquid hydrocarbon precursors [179]. Since the properties of the MWCNTs like graphitic structure, oxidation resistance, general morphology and structure depend strongly on the precursor used [179], this confers to AACVD a range of parameters to tune the MWCNT structures as required. The second advantage of the AACVD synthesis is the opportunity to obtain 'doped' MWCNTs by using precursors containing nitrogen, silicon or boron atoms, which modifies further the morphology and properties of the MWCNTs [92, 93]. Finally the technique consists of co-injection of the liquid precursor and catalyst and so could be compatible with continuous synthesis of MWCNTs. The last advantage is then the opportunity to possibly scale up the production of MWCNTs [192]. Among the CVD techniques AACVD can be considered as versatile. However its versatility may not have been pushed to its limit and it may offer opportunities not fully investigated. In particular the opportunity to develop MWCNTs with a compositional change along the MWCNTs by AACVD has not been reported. The multiple opportunities offered by AACVD to develop MWCNT with junctions are then investigated in **Chapter 5**.

1.3. Conclusions

Improving enzyme studies and applications requires the development of new carbon electrodes and scaffolds with different degrees of design. A first degree of design comes with the use of powdered materials. To optimise hydrogenase electrodes, the opportunity to investigate powdered materials with specific features, like high surface area or abundance of edge planes, has been reported only recently. Due to the lack of a unified study comparing these carbon materials for the immobilisation of the same bio-electrocatalyst under equivalent experimental conditions, it is difficult to conclude on the real benefit of one material compared to another. In this thesis, to clarify the influence of a given carbon material on hydrogenase immobilisation, a range of carbon material powders were identified, selected and obtained from commercial suppliers or synthesised as presented in **Chapter 2**. The materials are expected to show desirable properties for hydrogenase study and applications, like high surface area or a nanoscale. These materials are characterised in **Chapter 3** and compared in a unified study of the electrocatalytic activity of a same hydrogenase adsorbed on the different materials. The coupling of IR spectroscopy and electrochemistry has also been limited by the lack of suitable carbon material powder to be used as electrode. The same nanomaterials are then further considered in **Chapter 3** to improve the coupling of the two techniques for studies of species directly immobilised on carbon electrodes.

A second degree of design is the use of an ensemble of carbon material. Hydrogenases are well established as suitable catalysts in enzyme fuel cells after immobilisation on carbon electrodes made of powdered materials. Hydrogenases have also been recently demonstrated in an enzyme cascade system to perform chemical synthesis. Upgrading the system to a flow configuration could be relevant for industrial up-scaling. Unfortunately powders of materials mainly considered to date for hydrogenase immobilisation are not simple to implement in

flow systems. CNT forests are more promising materials to develop high surface area conductive network for hydrogenase immobilisation but their use in flow devices suffers severe limitations. In particular there is a lack of simple CNT scaffolds compatible with a flow reactor configuration. In **Chapter 4**, the development of CNT ensemble in the form of CNT forests directly grown into quartz columns is investigated to obtain devices readily compatible with flow-bio-redox catalysis and chemical synthesis.

When adsorbed on a carbon material, hydrogenase or other objects are usually randomly immobilised along the materials. Achieving a spatial control over the immobilisation of nano-object onto nanomaterials could give an extra degree of control, to possibly improve the efficiency of devices. For instance, this could lead to be a better electron transfer between co-adsorbed enzymes on a conductive material in the case of chemical synthesis assisted by hydrogenases. To achieve localised functionalisation, an extra degree of design is required for which CNTs are promising candidates because their properties can be easily tailored. Inducing different composition on different segments of a single CNT could favour spontaneous immobilisation of objects on these different segments due to different properties. A main drawback to date to test this hypothesis is the limited production of CNTs with intratubular junctions between segments of different composition. Besides, the scope of applications of CNTs with junctions has been limited to the creation of components for electronic. To address these limitations, **Chapter 5** presents first an AACVD based method to produce large quantities of CNTs with junctions. Second this chapter attempts to fill a conceptual gap in the literature by addressing the spontaneous, controlled and localised reactivity and immobilisation of objects along a CNT. For a solid proof of concept, an asymmetric functionalisation should be induced for the first time by the material design, without the need to locally modify the nanomaterial after synthesis.

Chapter 2: Materials and methods

"Highly organized research is guaranteed to produce nothing new."
Frank Herbert

Part of this Materials and methods section was published in Ref [193] and reproduced by permission of the Royal Society of Chemistry.

The research presented in this thesis aims at improving and developing new methods of study and applications of bio-electrocatalysts (**Chapter 1**). This is performed through the careful selection and design of different carbon materials. **Chapter 2** provides general information on the carbon materials used, the way they were obtained, specific sample preparation and the techniques selected for their characterisation. However, **Chapter 2** does not provide full materials characterisation or full interpretation of data used as examples which are addressed in more details in the following results chapters.

In order to develop high surface area electrodes for hydrogenase immobilisation (**Section 1.2.2**), eleven carbon materials were selected. These materials are commercially available or synthesised in-house and introduced in **Section 2.1** and **Section 2.2** respectively. The materials are expected to show properties leading to a high loading of hydrogenases, like different general morphology, a sub-micron-size, a high degree of graphitisation or a high surface area. These properties were evaluated respectively by scanning electron microscopy (SEM), transmission electron microscopy (TEM), Raman spectroscopy and nitrogen porosimetry, all introduced in **Section 2.3**. Additional techniques useful for this thesis are also covered in **Section 2.3**, like electron energy loss spectroscopy (EELS) required to assess a change in composition within MWCNTs with junctions (presented in **Section 1.2.5** and investigated in **Chapter 5**). Thermogravimetric analysis (TGA) was found to be a simple and useful technique to investigate for the first time the reactivity of MWCNTs with junctions. To also prove for the first time that local functionalisation of MWCNT forests with a change in composition is possible, elemental analysis by dispersive

X-ray spectroscopy (EDS) was required to complete the panel of characterisation techniques used in this thesis.

More specifically, the electroactivity of hydrogenases was investigated on different carbon materials in **Chapter 3**. Electrochemistry was then an important tool for this work. The electrochemical set up used, sample preparation and the electrochemical measurements performed are detailed in **Section 2.4**. The carbon materials, due to their expected nano-scale, were also selected to favour the coupling of IR spectroscopy and electrochemistry (**Section 1.2.3**). An introduction to the experimental set up, data analysis and data presentation required for this particular technique is given in **Section 2.5**. In **Chapter 4**, applications of hydrogenase for production of chemicals in flow systems are investigated. The methods used to follow the chemical transformations are presented in **Section 2.6.** Finally, in **Chapter 5**, localised functionalisation of MWCNT forests with a change in composition is performed with platinum particles as a test system. This is performed to illustrate for the first time that different loading with particles can be spontaneously achieved and controlled along a CNT forest with intratubular junction. The platinum deposition methods used are then detailed in **Section 2.7**.

2.1. Commercial materials

One option to improve hydrogenase loading on carbon electrodes is to use high surface area materials (**Section 1.2.2**). For this reason, carbon black powders commercially available and already broadly used in the field of fuel cells were selected: Mogul L (ML), Vulcan XC72R (VX) and Black Pearls 2000 (BP) were obtained from Cabot Corporation and used as received. For the same reason a carbon nanopowder (less than 50 nm particle size according to the supplier) referred to as CNP, was obtained from Sigma-Aldrich and used as received.

Developing abundance of edge-planes in a carbon material is another option to increase hydrogenase loading (**Section 1.2.2**). In order to include a material displaying an

important amount of edge-like planes in the panel of materials screened, graphite platelet nanofibers (GNF) were purchased from Sigma-Aldrich and used as received.

Pyrolytic graphite (PG) has been a preferred material for hydrogenase investigation due the simplicity to adsorb bio-electrocatalysts on its surface (**Section 1.2.2.2**). In the literature, PG particles are used to obtain high surface area electrodes. They are usually freshly prepared by abrasion prior to enzyme adsorption, produced in the required quantity and not stored [63]. Fresh abrasion is supposed to favour enzyme interaction with the material. A similar material was selected in this study. However, the flakes obtained in this work were not obtained by abrasion *just prior* to enzyme adsorption but several grams of a powder made of pyrolytic graphite particles was produced. The powder was stored over time in a glass container and used as needed. The material used in this work will be referred to as abraded pyrolytic graphite (APG) to mark the difference with the usual denomination 'PG particles' for freshly prepared particles. This production of APG was preferred in this work to make the comparison with other as-received or as-produced materials studied more meaningful. Indeed, none of the other ten materials selected required a post-treatment just prior to enzyme immobilisation. APG flakes were obtained by abrasion of a block of PG (obtained from Momentive Performance Materials) with glass paper (Norton Abrasives, P400 grade).

2.2. Carbon materials synthesis

2.2.1. Micron-sized graphite flakes: MG

In order to favour a higher loading of hydrogenase and to achieve a sub-micron size to facilitate the coupling of IR spectroscopy and electrochemistry (**Section 1.2.3**), a smaller equivalent of APG was considered to develop a higher surface area material. Micron-sized graphite flakes were prepared by modifying a method used to prepare graphene through

exfoliation [194]. In a typical experiment 10 g of millimetre-sized graphite flakes (Aldrich, +100 mesh) were placed in 500 mL of isopropanol (≥ 99.5 %, Sigma-Aldrich) and left for 200 hours in an ultrasonic bath (Fisherbrand, FB11301, 600 W, 45kHz). This breaks down the millimetre graphite flakes to smaller size flakes. The mixture was then left for at least 12 hours to sediment, and a grey suspension containing smaller graphite flakes (*ca.* < 1 µm as assessed by SEM and TEM in **Chapter 3**) was pipetted off from the remaining bulk graphite flakes (*ca.* > 1 µm) at the bottom of the flask. The grey suspended material was then sedimented by centrifugation at 3100 × *g* (Hettich, Rotina 420R). After centrifugation the supernatant was decanted and the precipitated material was collected. The solvent was left to evaporate overnight at 80 °C leading to 0.5-1 g of a grey powder comprising micron size graphite flakes (MG).

2.2.2. Hydrothermal synthesis of carbon nanoparticles: HNP

To develop carbon particles with a high surface area and a sub-micrometre size to facilitate the coupling of IR spectroscopy and electrochemistry (**Section 1.2.3.3**), a hydrothermal synthesis method was used due to the simplicity of the technique. Several reports investigated this versatile hydrothermal technique to obtain carbon nanoparticles [195, 196]. However results obtained in one report are difficult to compare with another. This is because the size of the digestion vessels needed, **Figure 2.1**, volume of solutions and concentrations of reactants may vary between different reports [197, 198]. It was then necessary to perform an in-house screening of several experimental parameters to achieve control over HNP size and yield (results are reported in **Table A1** and **Figure A1 in Appendices**). Parameters such as time, glucose concentration and temperature were investigated to optimise the carbon particle size to be as small as possible and the overall yield more than 100 mg per experiment. A yield of 100 mg was indeed found a sufficient mass to perform enough

experiments with the same batch of particles to assess the reproducibility of electrochemical measurements.

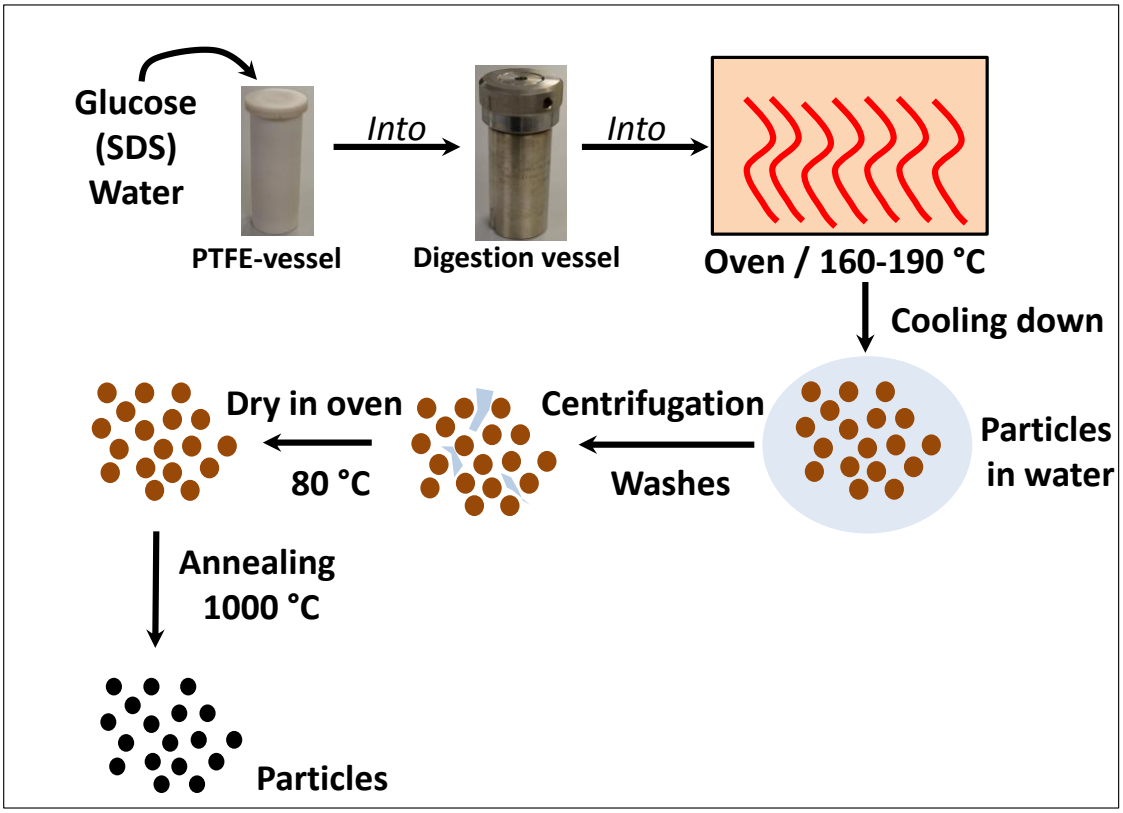

Figure 2.1. Schematic representation of hydrothermal particle synthesis.

It was established in this thesis, in agreement with the literature [198], that time and temperature are important parameters to control since a variation of one hour or 10 °C has a strong impact on the particle size and yield (**Figure A1**). The mechanism for the formation of HNP is not properly established but is likely to be a nucleation-growth process controlled by reactant diffusion [196, 199]. This was not studied further since the goal of the parametric study performed for this thesis was to identify a suitable set of parameters to obtain particles in the range 100-200 nm to ultimately favour the coupling of IR spectroscopy and electrochemistry. This was achieved by using the following procedure. In a typical experiment, 1.27 g of glucose (ACS reagent grade, Sigma-Aldrich) was added to distilled water (35 mL) in a PTFE-lined acid digestion vessel (45 mL, Parr Instrument Company). The closed vessel was then placed into an oven at 180 °C for 8 hours. The oven was then left

to cool down overnight before the sample consisting of the particles in a brown solution (with a 'caramel smell' noticed after opening the vessel) was collected. The particles were washed and centrifuged at least 5 times using distilled water and 5 times with ethanol (99.8 %, Fisher Scientific) for 10 to 15 minutes at 3100 × *g* per cycle (Hettich, Rotina 420R). Subsequently, the particles were left to dry overnight at 80 °C. Typical carbon particle yields were *ca.* 100 mg. The as-prepared particles lead to enzyme adsorption. However, it was found, in line with previous reports [200, 201], that the electrochemical response of materials prepared by this route can be improved by annealing the particles at high temperature. Therefore the particles were annealed at 1000 °C in argon (100 standard cubic centimetres per minute, sccm) for two hours. No effect on particle size distribution is observed after annealing while the graphitisation is changed (**Figure A2**), in agreement with previous experimental observations [202]. This change probably results from residual polymeric species on the carbon surface that are further converted to amorphous carbon materials upon heat treatment. This explanation is in agreement with the change in the colour of the particles from brown to black after annealing. Also in agreement with the literature [199], the relative standard deviation of the size of the particles assessed by TEM was around 10 %. The opportunity to obtain different type of particles and in particular hollow particles by this method was also achieved (**Table A2, Figure A3**). The benefit of hollow particles could be to minimise the amount of carbon in the material to facilitate the coupling of IR spectroscopy and electrochemistry. Unfortunately the final products did not bring any major advantage for the purpose of this study. They were not investigated further but these results illustrate the versatility of the technique.

2.2.3. Polymerisation-carbonisation: Si@C

Carbon particles with an IR transparent core of silicon are promising material to couple IR spectroscopy and electrochemistry for improved enzyme studies as suggested in

Section 1.2.3.3. Silicon core-carbon shell nanoparticles (Si@C) were generated through a polymerisation and carbonisation procedure reported by Gao *et al*. [203]. The particles were originally developed for batteries application and were shown to be conductive. Conductivity is an important property to develop enzyme electrodes. This is a strong argument to attempt to combine these particles not fully made of carbon with hydrogenase. Typically, 44 mg of 4,4'-sulfonyldiphenol (98 %, Aldrich, BPS), 20 mg of phosphonitrilic chloride trimer (99.95 %, Aldrich, HCCP) and 20 mg of silicon nanopowder (≥ 98 %, Aldrich) with an average particle diameter of *ca.* 100 nm were dispersed using an ultrasonic bath (Ultrawave, U1250D, 200 W, 40 kHz) for 20 hours in 30 mL of ethanol (99.8 %, Fisher Scientific) and tetrahydrofuran (anhydrous, ≥ 99.9 %, Sigma-Aldrich, THF) in a 1:1 mixture by volume to which 2 mL of triethylamine (≥ 99 %, Sigma-Aldrich, TEA) was added, **Figure 2.2a**.

The resulting silicon nanoparticles with a poly(cyclotriphosphazene-4,4'-sulfonildiphenol) [203] shell (PZS, **Figure 2.2b**), were washed 3 times with ethanol:tetrahydrofuran solution with centrifugation at 3100 × *g* (Hettich, Rotina 420R) to collect the particles. The particles were finally left to dry at 80 °C overnight prior to annealing under an argon atmosphere (100 sccm) at 900 °C for 2 hours. This is to form the carbon shell by annealing the polymer. A typical yield of final material is *ca.* 10-40 mg. This quantity is enough but relatively low for the purpose of enzyme studies by electrochemistry or spectroelectrochemistry. A process leading to *ca.* 100 mg of materials would be preferred to obtain enough material for several experiments to test the reproducibility of enzyme immobilisation on a same batch of material. The preparation method described was then successfully up-scaled in this thesis by multiplying all reactants and solvent quantities by 20 to obtain *ca.* 200 mg of Si@C particles.

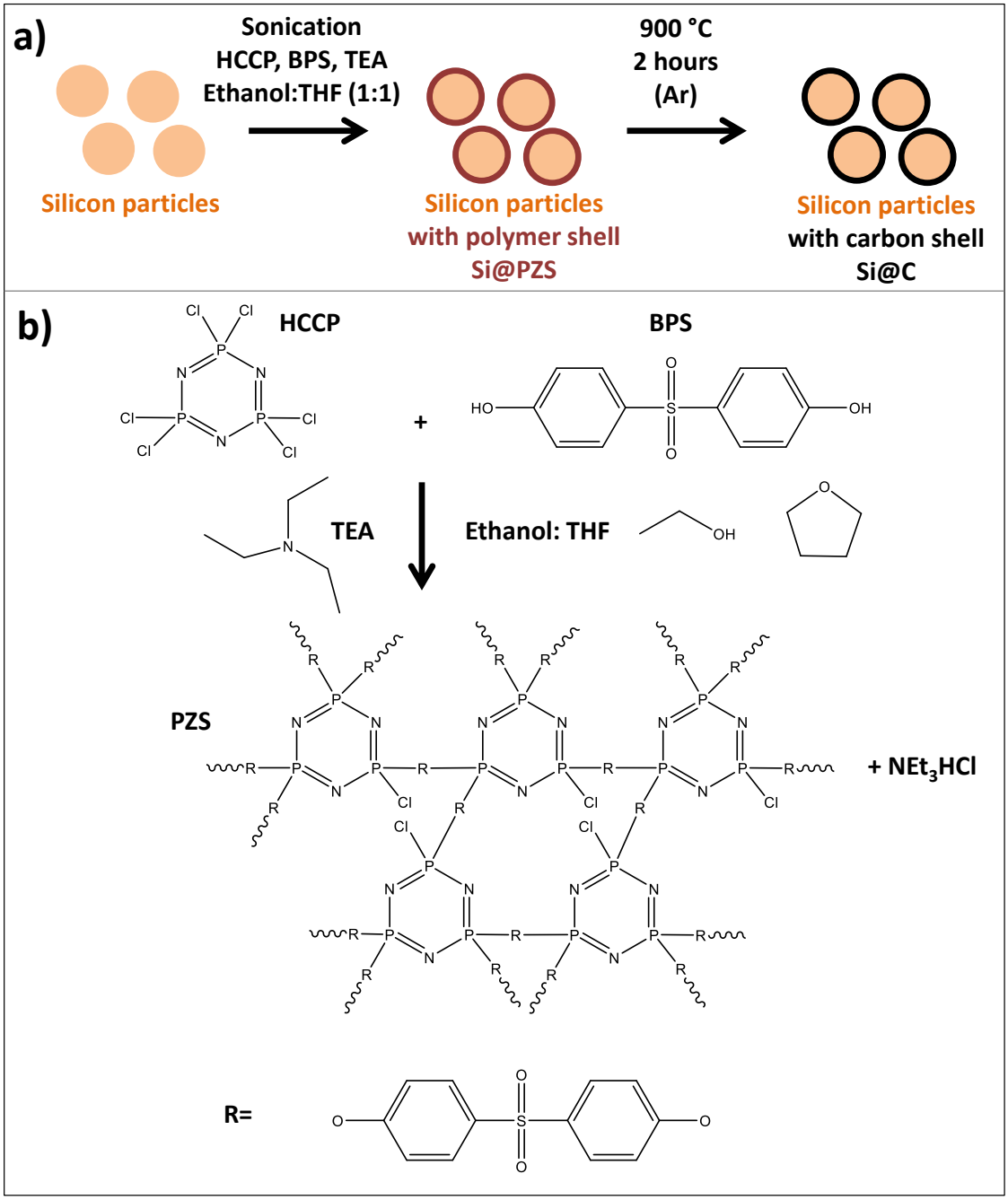

Figure 2.2. (a) Schematic representation of the synthesis of Si@C particles and (b) illustration of the formation of PZS.

2.2.4. AACVD synthesis of MWCNTs

MWCNTs have been intensively considered as electrode materials for hydrogenase immobilisation due to their high surface area and chemical stability (**Section 1.2.2.3**). MWCNTs were selected in this thesis in order to establish their benefits compared to other

carbon supports chosen to develop hydrogenase electrodes. MWCNTs synthesised in this report were obtained on a set up based on the AACVD technique reported previously [92, 191]. AACVD was selected due to the multiple advantages of the technique. (1) It is compatible with a range of liquid hydrocarbon precursors which gives control over several properties of the MWCNTs like length, chemical composition, oxidation resistance or graphitisation [92, 191]. Controlling these properties could be useful to control enzyme immobilisation. (2) In particular nitrogen-doped MWCNTs (N-MWCNTs) can be obtained by AACVD [92] to develop more defects and a different chemical structure compared to un-doped MWCNTs. This difference in structure and composition may be relevant to favour hydrogenase immobilisation [148]. (3) The AACVD technique consists of co-injection of catalyst and precursor which avoids substrate pre-treatment to grow MWCNT directly on substrate made of quartz or silicon. This property of AACVD will be exploited in **Chapter 4 and 5**. Finally, (5) AACVD is a technique that could be scaled up [192] and so the results obtained at a lab scale in this thesis could be directly relevant for industrial applications.

The general AACVD set up for used in this thesis is represented in **Figure 2.3** (pictured in **Figure A4**). A precursor made of a mixture of ferrocene used as catalyst and a liquid hydrocarbon (like toluene) is placed in a glass unit cell (**Figure A5**) at the bottom of which is a piezo-electric (RBI Pyrosol 7901). The cell is connected to a quartz tube of 21 mm inner diameter and the tube placed inside a furnace. The end of the system is connected to an acetone bubbler to exhaust gases and solid residues produced during synthesis, connected itself to a ventilation exhaust system. Adjusting the frequency and amplitude of the piezo makes it possible to develop conditions where a resonance is achieved in the cell and for which an aerosol is formed from the liquid mixture. By flowing a carrier gas (argon) to the system, the aerosol is injected into the quartz tube, playing the role of reactor. The argon flow carries the aerosol into the high temperature region of the furnace

where the ferrocene cracks down to lead to iron particles, **Figure 2.3**-1. These particles catalyse the growth of the MWCNTs. The solvent together with the carbon contained in the ferrocene provide the carbon source for this growth, **Figure 2.3**-2. After the synthesis, the whole internal surface of the quartz reactor is covered with vertically-aligned MWCNTs (**Section 1.2.2.3**). By scrapping the quartz reactor internal surfaces with a metal spatula, a powder of MWCNTs is collected for further use and characterisation. If substrates are placed within the quartz reactor during synthesis, they are also covered with forests of vertically-aligned MWCNTs as illustrated in **Figure 2.3**.

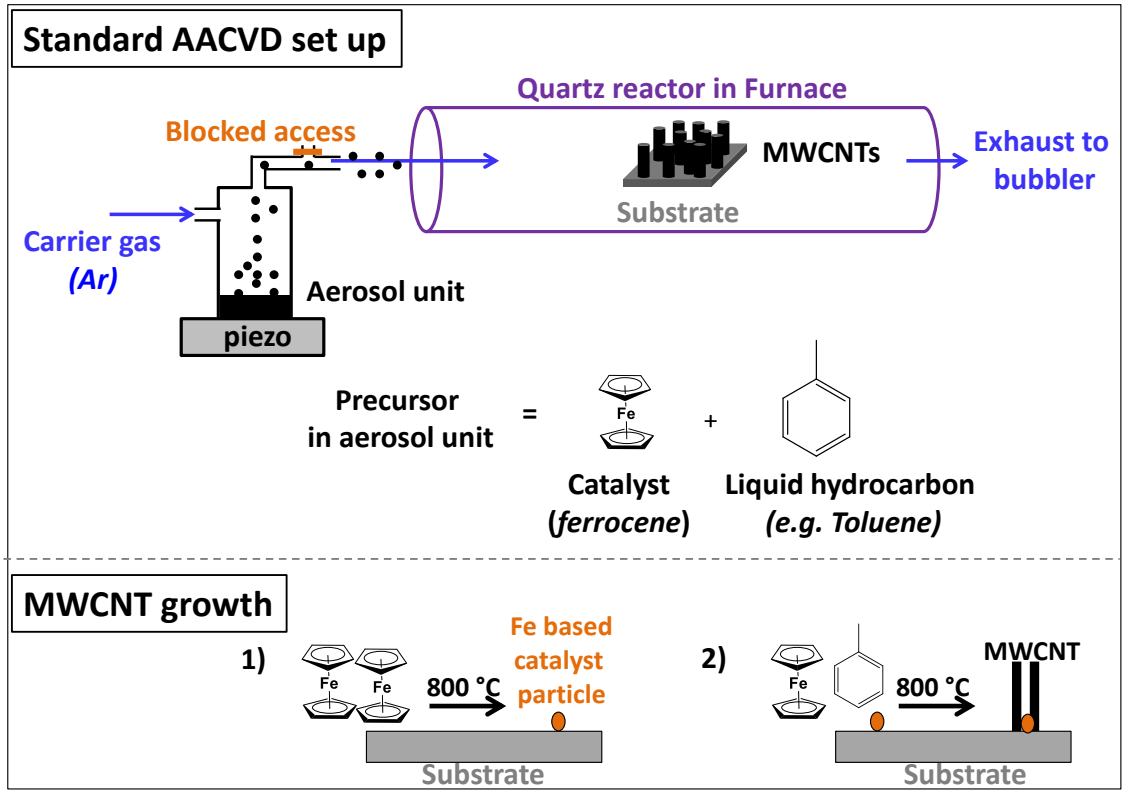

Figure 2.3. Schematic representation of AACVD synthesis set up used for the growth of vertically-aligned MWCNTs.

Unless otherwise specified, multi-wall carbon nanotubes (MWCNTs) and nitrogen-doped MWCNTs (N-MWCNTs) were synthesised using a mixture of 5 wt % ferrocene (98 %, Aldrich, purified through sublimation at 90 °C prior to use) and toluene (99.9 %, Fluka) for MWCNTs, or benzylamine (≥ 99 %, Fluka) for N-MWCNTs. The ultrasonic unit

was purged with argon for 10 minutes prior to heating up the furnace to avoid presence of oxygen in the system. Presence of oxygen in the system prevents the growth of MWCNTs and could be harmful at high temperature in the presence of hydrocarbons due to a risk of combustion and explosion. Experiments were performed at 800 °C under argon atmosphere (99.999%, BOC) with a flow of 2500 sccm unless otherwise specified. In **Chapter 3**, toluene was allowed to be carried to the furnace by the argon flow for 10 minutes to obtain MWCNTs and benzylamine for 20 minutes to obtain N-MWCNTs. The furnace was then left to cool down under argon atmosphere to < 300 °C before collecting the black MWCNT powder produced in the centre of the reactor. A typical yield for such experiments is *ca.* 500 mg per experiment. MWCNTs in **Chapter 4** and **Chapter 5** were obtained by modification of the general approach presented here. Since these modifications are part of the results of this thesis, they are detailed in the results chapters. Both MWCNTs and N-MWCNTs contained traces of iron-based impurities after synthesis, typically 5 wt % [191]. Purification of CNTs for instance with acid treatment is commonly performed to remove those impurities [24] but adds a step to the preparation of the material prior to immobilisation with the enzyme. Avoiding a purification steps considerably facilitates the use of CNTs as bio-electrode. In this thesis the purification of the MWCNTs was not necessary because the impurities did not affect the activity of the hydrogenases.

2.3. Carbon materials characterisation

2.3.1. Specific sample preparation

In the whole **Chapter 3**, powders made of the eleven carbon materials introduced in **Section 2.1 and 2.2** were used to develop enzyme electrodes. Therefore the same powders of materials were used for all characterisation techniques. In **Chapter 4 and 5** to overcome the challenging dispersion of MWCNTS (**Chapter 1**) a specific focus is given to MWCNT

forests (**Section 1.2.2.3**). MWCNT forests were characterised as-produced on substrates when the characterisation technique allows this specific geometry to be exploited. Since the substrate is part of the sample this confers several benefits. The first benefit is that the position of the MWCNT forest relative to the substrate is not lost, in contrast to the case of powders, which gives more information on the growth mechanism of the forest. Second, the same MWCNT forest on substrate can be characterised by several techniques after being placed in dedicated holders. For example it is then possible to collect SEM images, Raman spectra and EDS data (all techniques are detailed in the next paragraphs) from the same MWCNT forest. Since these techniques are not destructive the same sample can be further characterised by techniques requiring powders of the material (TEM or EELS, detailed in the next paragraphs) or for destructive characterisation like TGA (also detailed in the next paragraphs). Using the same sample for all characterisations facilitates the comparison, correlation and discussion of data obtained from different techniques. A more complete understanding of the nature and properties of the sample can then be achieved.

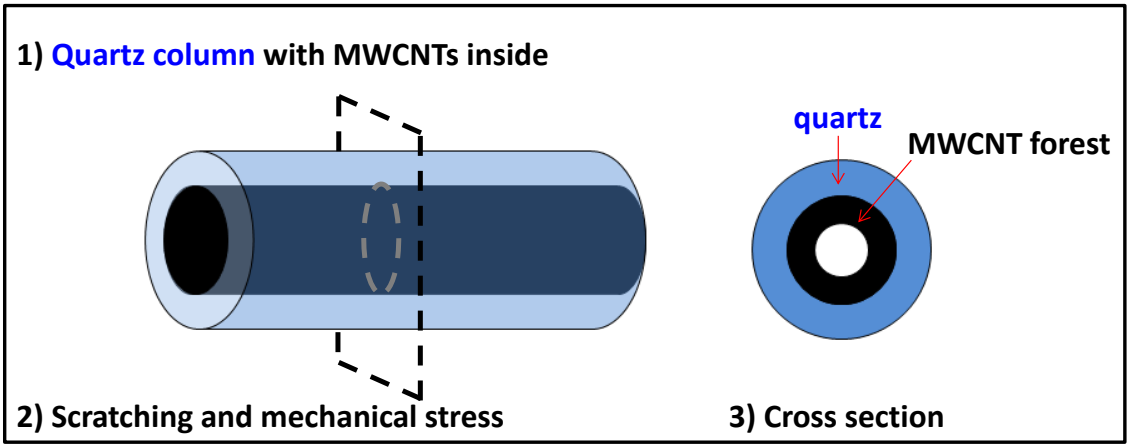

Figure 2.4. Schematic representation of the process to make cross-sections of quartz columns with vertically-aligned MWCNTs in it for confocal Raman microscopy, SEM and EDS measurements. Quartz is represented in blue and MWCNTs in dark.

The challenge to successfully perform various characterisations on the same sample comes with the need for specific sample preparation. In **Chapter 4**, to develop MWCNT

columns (**Section 1.2.4**) tubular quartz substrates were used. To characterise MWCNTs grown inside quartz columns of small inner diameter (1 or 2 mm), cross-sectioning of the columns was performed as illustrated in **Figure 2.4**. The columns (blue) with vertically-aligned MWCNTs (black) inside were scratched on the outer surface and a mechanical stress was applied with bare hands or tweezers. This process leads to neat cross sections, which makes the characterisation of the material grown inside the column relatively simple.

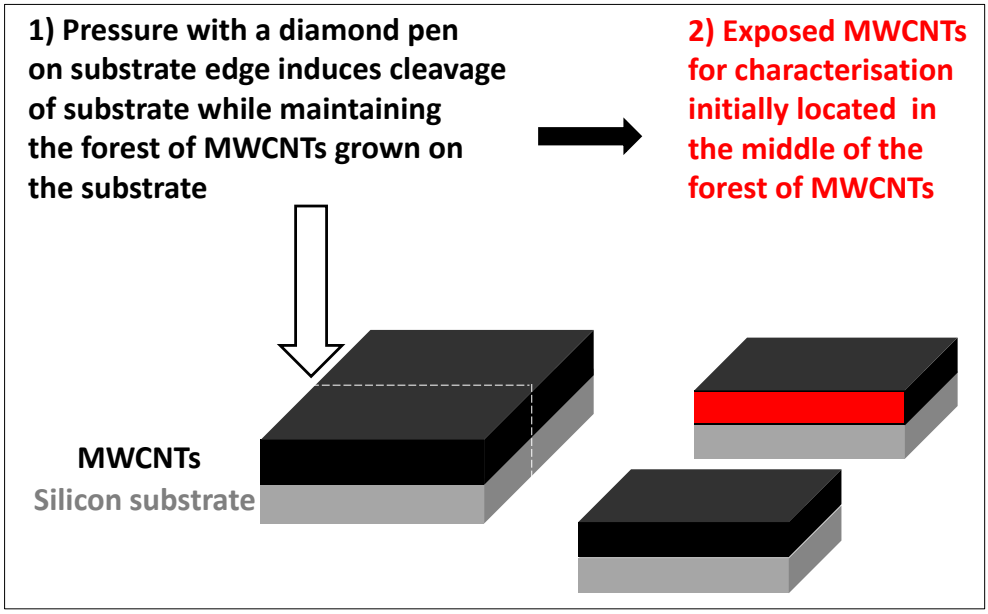

Figure 2.5. Schematic representation of samples preparation for confocal Raman microscopy, SEM and EDS measurements of as-synthesised MWCNT forests.

In **Chapter 5**, the substrates used were silicon wafers on which MWCNT forests were grown. Silicon was chosen because it is easy to cleave without damaging the forests as illustrated in **Figure 2.5**. The advantage of using a flat substrate is that the length of the forest can be easily assessed by looking at a section, in red in **Figure 2.5**. Then no information is lost regarding the position of the forests with respect to the substrate. This ultimately gives information on the growth mechanism that otherwise would be lost if MWCNT powders were used for characterisation. Since a cross-section is performed, a clear edge is obtained for analysis. This also provides an area to characterise, red in **Figure 2.5**,

more representative of the MWCNT forest because more MWCNTs are grown within the forest than on its edge. All SEM, EDS and Raman data of as-synthesised MWCNTs in **Chapter 5** are therefore associated with MWCNTs initially grown within the vertically-aligned forests. Just like for MWCNTs in a column, using a substrate makes it possible to acquire SEM, Raman or EDS data from the same sample.

2.3.2. Scanning electron microscopy

The different carbon nanomaterials powders (**Section 2.1 and 2.2**) selected to develop hydrogenase electrodes in this work are black and cannot be differentiated with the naked eyes or an optical microscope. To study their different morphology, scanning electron microscopy (SEM) images were then recorded with a Jeol 840F microscope operated at 5 kV using a secondary electron detector and a Zeiss NVision FIB microscope equipped with an in-lens and a backscattered electrons detector also operated at 5 kV.

A requirement to obtain images with SEM is to get conductive samples. SEM is then a relatively fast characterisation technique for carbon materials because all the carbon samples in this thesis are conductive, so no extensive preparation is required (*e.g.* no need for conductive coating). To obtain an image, the microscope beam interacts with the conductive sample surface to generate different emissions of electrons (**Figure A6**, **Table A3**). Low energy secondary electrons (*ca.* < 50 eV) are related to the very surface of the sample and give information on the topology of the sample as displayed in **Figure 2.6a**. In this figure is reported a SEM micrograph of a MWCNT forest with a compositional change, marked by a wavy MWCNT section (C) on top of a straight N-MWCNT (N) section (detailed further in **Chapter 5**). To achieve a higher resolution and investigate the interface between the two sections, an in-lens detector was necessary in this work. An in-lens detector more selectively collects with a magnetic field electrons with the lowest energy among the secondary electrons. This selects scattered electron from the very top few nanometres of a sample and

provides a higher resolution because the background contribution of higher energy secondary electrons is minimised. This leads to better quality images revealing features that could not be resolved with a secondary electron detector. For instance in **Figure 2.6**, 'broken' nanotubes with a pyramidal termination could be identified with the in-lens detector but not with a secondary electron detector due to the difference in resolution.

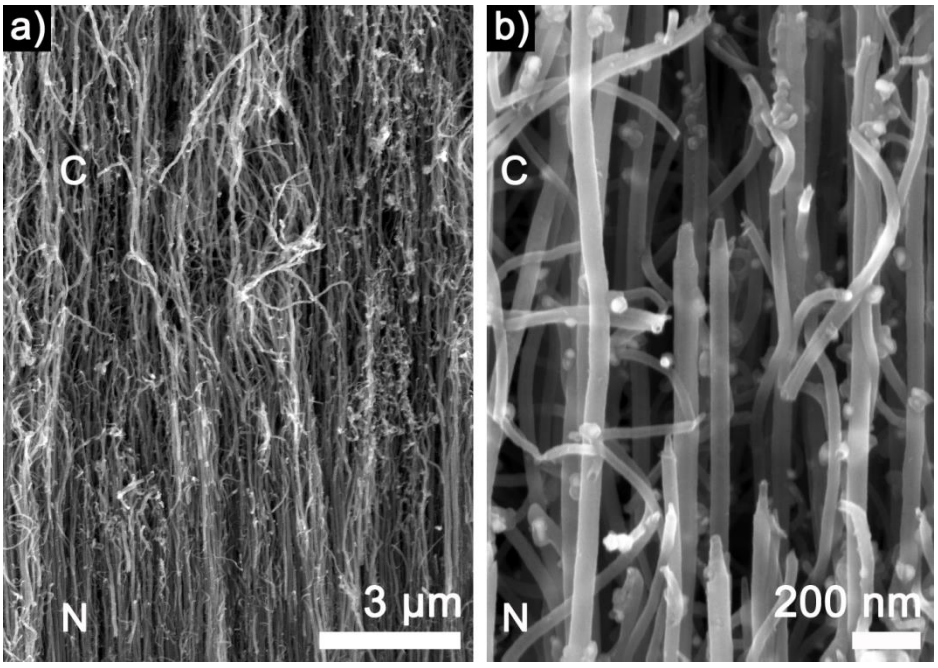

Figure 2.6. SEM micrographs of the same sample made of MWCNTs with a compositional change from MWCNT (C) to N-MWCNT (N) with (a) secondary electron detector and (b) with an in-lens detector.

Backscattered electrons are more energetic electrons and can originate from heavier elements in the sample. Platinum is a good element to illustrate the interest in exploiting backscattered electrons because its atomic number (78) is higher than carbon (6). Images based on backscattered electrons were used in this thesis to stress the influence of a change in composition in a MWCNT forest on platinum deposition (**Chapter 5**). In **Figure 2.7a-b** for instance, a difference in contrast in the grey scale image is observed between the sections made of MWCNTs (C, appearing darker) and N-MWCNTs (N, appearing brighter). The difference in contrast is more pronounced with the backscattered electron detector,

Figure 2.7b. The N-MWCNT section appears brighter, revealing a more uniform repartition of platinum on this section that the MWCNT section. A control image, **Figure 2.7c**, shows no difference in the greyscale image between N-MWCNT and MWCNT sections if no platinum is deposited. A backscattered electron detector is then suitable to assess the distribution of platinum on MWCNTs with a change in composition. This will be exploited for the first time in **Chapter 5** and the experimental procedure for deposition is fully detailed in **Section 2.7**.

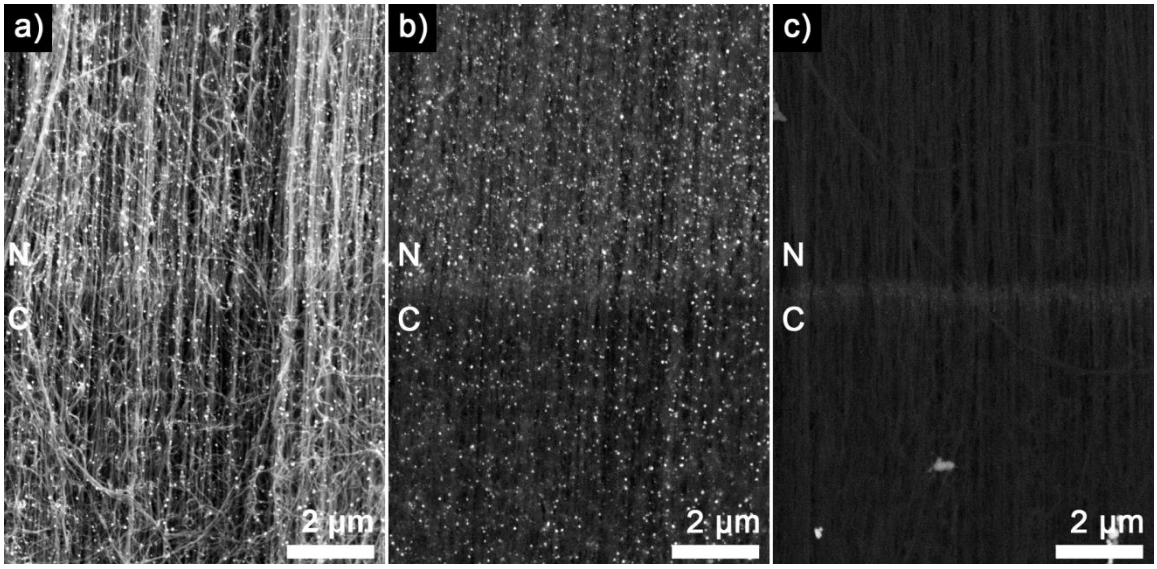

Figure 2.7. SEM micrographs of a same MWCNT forest with N/C junction after electrodeposition of platinum taken (a) with a secondary electron detector and (b) with a backscattered electron detector. (c) SEM micrograph (backscattered electron detector) of the same sample before platinum electrodeposition.

In **Chapter 3**, materials detailed in **Section 2.1 and 2.2** in the form of a powder were used for characterisation. They were deposited onto a conductive double-sided adhesive carbon disc sticking on one side to an SEM stub and supporting the powder sample on the other. In **Chapter 4 and 5**, the samples grown on substrates were prepared as detailed in **Section 2.3.1** and placed in dedicated holders to take images of the cross-sections.

2.3.3. Transmission electron microscopy

A sub-micrometre size for the carbon materials used in this thesis is important because nanomaterials are likely to develop suitable high surface area carbon electrodes for hydrogenase immobilisation (**Section 1.2.2.6**). Nanomaterials are also required to couple IR spectroscopy and electrochemistry (**Section 1.2.3**). To assess the structure of the materials at this scale, transmission electron microscopy (TEM) was chosen. A TEM image is based on the interactions of electrons with samples of thickness less than few hundreds of nanometres. The resolution achieved is usually higher than with most SEM equipment. TEM was then used to complement the characterisation of samples with features than could not be resolved by SEM. For instance, TEM was useful to establish the size distributions of carbon nanomaterials. The particle shape and size distribution was analysed from at least 10 different TEM images and at least 100 measurements on 100 individual particles.

A TEM image also gives information on the inner structure of materials whereas SEM gives only surface and topological information. TEM was then used to assess the hollow or core-shell structure of the nanomaterials. In addition, high-resolution TEM (HRTEM) was necessary to get information on the carbon plane orientation (*e.g.* basal or edge plane) within the materials: to characterise the graphitic structure at a scale relevant for the immobilisation of enzymes (*ca*. 5 nm in size). TEM images were taken with a Jeol 2000FX operated at 200 kV because at this voltage an optimal resolution was achieved with the equipment used and no damage of the samples could be noticed during the image acquisition. HRTEM images were recorded by Dr Antal A. Koós, Judy Britton or Vitaly Babenko (all Department of Materials, University of Oxford) with a Jeol 2010 operated at 200 kV. For measurements, few milligrams of carbon materials were dispersed in ethanol by sonication for a few seconds in an ultrasonic bath. The suspension was then drop-casted on to a Cu holey carbon TEM grid.

More specifically for this thesis, TEM was important to assess the differences between MWCNTs and N-MWCNTs in terms of general structures, inner diameter and size distribution. For instance, clear differences are observed between MWCNTs and N-MWCNTs in **Figure 2.8**: the MWCNTs have a tube-like structure with a hollow inner diameter (area of lighter contrast between the walls with darker contrast) whereas N-MWCNTs have a bamboo-like structure. TEM is also useful to identify residual catalyst-particles [191] within the nanotubes: features with a darker contrast inside the tubes, **Figure 2.8**. The difference in morphology and presence of catalyst particles can be observed in independent batches as detailed in **Chapter 3** or within a single MWCNT with a change in composition as explored in **Chapter 5.** The possibility to identify residual catalysts particles in the latter case was found to give information on the growth mechanism of MWCNT with compositional change as detailed in the related result chapter.

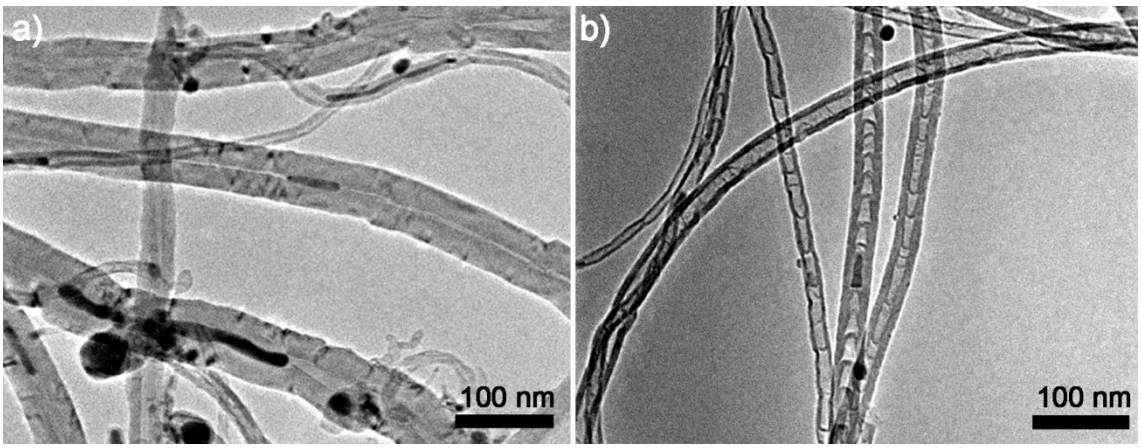

Figure 2.8. TEM micrographs of (a) a MWCNT and (b) a N-MWCNT sample. Catalyst-like particles are observed as objects with a darker contrast in the inner diameter of the nanotubes.

2.3.4. Raman spectroscopy

It has been suggested that the degree of graphitisation of carbon materials is an important parameter to control the immobilisation of hydrogenases (**Section 1.2.2**). To assess this property in the various carbon materials investigated, Raman spectroscopy is the most

suitable characterisation to complement HRTEM. Raman spectroscopy is indeed a simple, fast and sensitive technique and probably the most widely used to characterise carbon materials [189]. Raman data are acquired by simply placing a carbon material under a laser excitation to record different vibrational modes from the material. Carbon materials are typically characterised by the relative intensity of three peaks: D band (around 1340 cm^{-1}) and G band (around 1565 cm^{-1}) and 2D band (also called G′, around 2680 cm^{-1}). In simple terms, the G band arises from the graphitic network and extent of sp^2 hybridisation. It is related to C-C bond stretching in tangential vibrations of the graphitic carbon atoms respective to the axis of the tube [98, 189]. The D band intensity correlates with disordered amorphous carbon [98] in the sample and is linked to the extent of sp^3 and sp hybridisation. The 2D band corresponds to a two-phonon, second-order scattering process and is the second harmonic of the D mode [98]. It is then possible to differentiate carbon materials like diamond [189], amorphous carbon [189], graphene [189], s-SWCNT [189], m-SWCNT [189], or even MWCNTs obtained from different precursors [93, 191] with Raman spectroscopy by investigating their different graphitisation and Raman spectra.

The usual parameters used to compare carbon materials are the intensity (*I*) ratio of the various peaks [189]. Under the conditions of this study (532 nm excitation wavelength), if I_D/I_G is smaller than 1 the structures are considered to show a higher concentration of sp^2 hybridisation (*i.e.* extended graphitic character). If the ratio tends to 1 then the material is considered to have a more amorphous structure with a mixture of sp^2 and sp^3 hybridisation. Even in cases where I_D/I_G is close to 1, the presence of a 2D peak, more related to interactions between graphene-like planes, suggests a strong graphitic component. For all the carbon materials presented in **Section 2.1 and 2.2,** a powder made of the material was dispersed in ethanol by 5 minutes sonication prior to deposition on a microscope slide. The degree of graphitisation of the samples was then investigated using a JY Horiba Labram

Aramis imaging confocal Raman microscope with a 532 nm excitation, unless otherwise specified.

For the Raman microscope used, the spatial resolution to focus on a given area of the sample was about 1-2 µm in all cases for all samples. This resolution was more specifically exploited in **Chapter 4 and 5** to acquire local information along a MWCNT forest on a substrate. In **Chapter 4** this was done to acquire spectra of materials grown into quartz columns and sample preparation has been detailed in **Section 2.3.1**. In **Chapter 5**, MWCNTs with a compositional change were developed. An important experimental observation for further discussion and characterisation of these structures is that the change in composition leads to a change in morphology that can be assessed by SEM, **Figure 2.6** or **Figure 2.7.** This change can actually also be observed with a simple x50 optical lens. In **Figure 2.9a** for instance, an optical microscope image of a forest with change in composition after cross section (described in **Section 2.3.1**) is reported. The forest shows two sections with different contrast and these sections are made of MWCNTs (C, top-dark) and N-MWCNTs (N, bottom-grey). Confocal Raman microscopy makes it possible to record Raman spectra on each section. The Raman data associated with each section are shown in **Figure 2.9b** and differ from each other. The I_D/I_G value is inferior to 0.5 and a clear 2D peak is observed for the spectrum recorded on the top section. The I_D/I_G value is superior to 0.5 and a 2D peak with a relatively smaller intensity is observed for the spectrum recorded on the bottom section. Such spectra are usually associated with MWCNT and N-MWCNT batches respectively [93]. A higher I_D/I_G value together with the absence of a 2D peak can be explained by the influence of nitrogen doping introducing defects in the carbon lattice which accounts for a less ordered graphitic structure [204]. Observing these two typical signals within a same MWCNT forest is a good indication of a successful change in graphitisation associated with a change in composition and morphology *along* the forest.

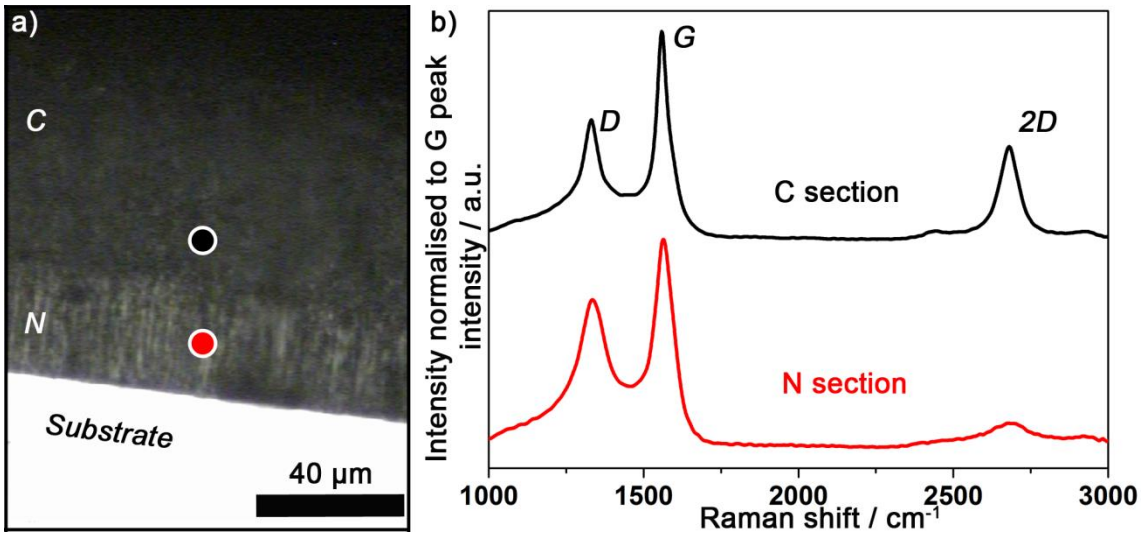

Figure 2.9. (a) Optical microscope image obtained with a x50 lens for a MWCNT forest with a change in composition. The forest shows a section of MWCNTs (C) on top of a section made of N-MWCNTs (N). (b) Associated Raman spectra taken in each sections in the areas represented in dark and red in (a).

Importantly here, the relative position of the different sections to the substrate is the same for optical microscope images in **Figure 2.9a** and SEM images in **Figure 2.6** or **Figure 2.7.** This is due to the specific sample preparation detailed in **Section 2.3.1**. Results from both SEM and Raman spectroscopy can then be directly and un-ambiguously correlated. These purely experimental observations first prove than Raman confocal microscopy has a spatial resolution suitable to characterise MWCNTs with a change in graphitisation. Second, Raman spectroscopy results can be correlated to complementary techniques. This is fully exploited in **Chapter 5** for comparison with other techniques such as EELS (**Section 2.3.6**), TGA (**Section 2.3.7**) and EDS (**Section 2.3.7**) to get for the first time a deep understanding of the influence of a compositional change on structure, morphology, graphitisation, oxidation resistance and functionalisation within a forest of MWCNTs with junctions.

2.3.5. Nitrogen adsorption porosimetry

To develop high surface area electrodes for hydrogenase immobilisation it is important to quantify the carbon surface area and the degree of porosity developed by the material. The preferred non-destructive technic to date to assess these properties is gas adsorption. The amount of gas adsorbed by mass of a sample and the associated isotherm gives information on surface area and porosity [205]. Nitrogen adsorption porosimetry was then performed using a Micromeritics Gemini V BET surface area analyser (nitrogen adsorption at 77 K). For data collection on the eleven materials described in **Section 2.1 and 2.2**, samples in the form of a powder made of each material were left at 200 °C in nitrogen overnight prior to the adsorption measurements. The data were analysed using the Brunauer–Emmett–Teller (BET) model [205] for relative pressure between 0.05 and 0.3. For BP, HNP and Si@C the Langmuir [205] model was more suitable as it gave a better fit to the data. For these materials both the BET and Langmuir surface areas were considered. The molecular cross sectional area of nitrogen was taken as 0.1620 nm^2. The Barrett-Joyner-Halenda (BJH) model was used to estimate pore characteristics [205]. Experiments were performed and data were interpreted with the help of Dr Frank Dillon (Prof Grobert's group, Department of Materials, University of Oxford). Results and interpretation are detailed in **Chapter 3**.

2.3.6. Energy electron loss spectroscopy

In **Chapter 5** of this thesis, MWCNTs with a compositional change were developed to possibly control hydrogenase immobilisation along a nanomaterial (as introduced in **Section 1.2.5**). More specifically, MWCNTs with junctions between un-doped MWCNT and N-MWCNT sections within a single MWCNT were developed. A MWCNT and a N-MWCNT differs by the presence of nitrogen atoms detected in the walls or in the hollow core of the N-MWCNT only [185]. To assess the expected change in composition along the

samples obtained in this thesis, energy electron loss spectroscopy (EELS) was used. EELS is an elemental analysis technique based on the measure of the kinetic energy loss of electrons after interaction with atoms present in a sample and gives information on the composition of a sample. Since the sensitivity to nitrogen (and light elements in general) with other techniques like EDS (detailed in the next section) is not high enough [206], EELS was the most suitable technique available for this work to assess a change in composition along a nanotube. Presence of nitrogen in the inner diameter or in the walls of CNTs was assessed in this thesis by EELS through the signal from gaseous nitrogen: N-K edge peak around 400 eV energy loss [185].

In **Figure 2.10a** for instance, experimental EELS spectra for a N-MWCNT (N) and a MWCNT without nitrogen doping (C) are reported. Spectra differ by the presence of a peak around 400 eV for the N-MWCNT which is absent for un-doped MWCNT. The presence of the peak at 400 eV is then a good indication to confirm nitrogen doping by assessing the presence of gaseous nitrogen. The presence or absence of this characteristic peak can be mapped along a MWCNT which is useful in this thesis to establish a compositional change along a single MWCNT as illustrated in **Figure 2.10b**. Areas of the sample where spectra showing a peak at 400 eV could be recorded are indicated by a letter ‘N’ on the scanning transmission electron microscope (STEM) image acquired in annular dark field (ADF) mode. Areas of the sample where a peak at 400 eV could not be observed are indicated by a letter ‘C’. The areas where a peak at 400 eV (N) could be observed are confined to one extremity of the tubes on the image. This shows that EELS signals characteristic of N-MWCNT or MWCNT can be found with a spatial confinement within a single carbon nanotube structure. EELS measurements confirm a change in composition along the nanotube and this is exploited and discussed further in **Chapter 5** to characterise MWCNTs with intratubular junctions.

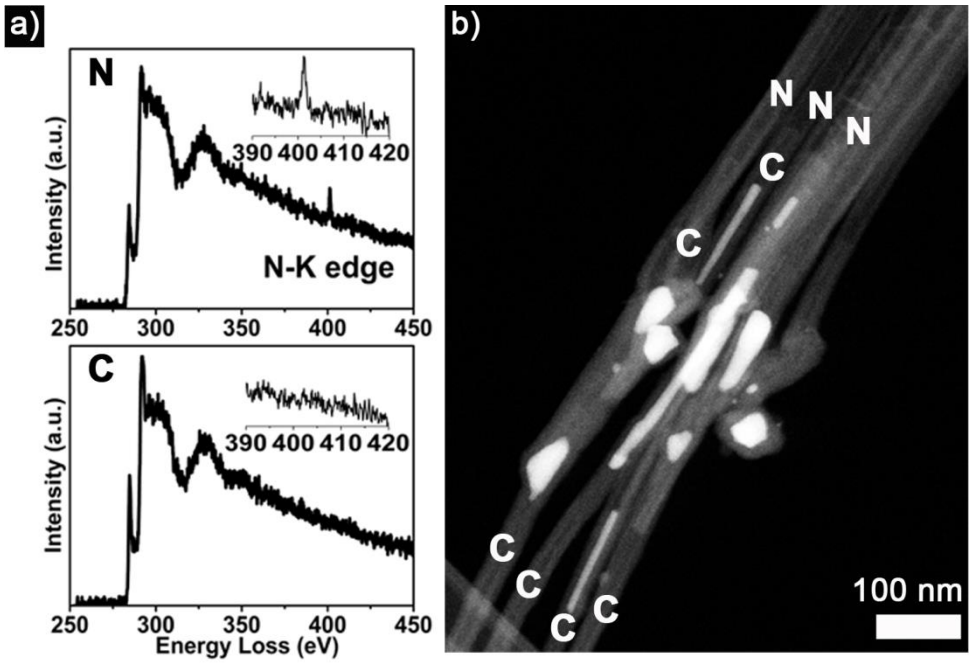

Figure 2.10. (a) Typical EELS spectra of N-MWCNT (N) and MWCNT (C). (b) STEM-ADF micrographs of MWCNT with a N/C junction. Letters N and C on the STEM images indicate area on the tubes where a peak at 400 eV related to presence of gaseous nitrogen could be observed (N) or not observed (C) in the EELS spectra acquired on these areas.

EELS measurements were performed at the University of Warwick with the help of Dr Rebecca Nicholls (due to refurbishment of the EM-suite at Oxford Materials). A Jeol ARM200F operated in STEM-ADF mode was used because the spatial resolution used in this mode is higher than with a TEM. The instrument was operated at 80 kV to reduce the knock-on damage caused by the beam [207]. Knock-on damage consists of removal of atoms from a sample under the electron beam. It happens only at energy higher than a threshold value which is higher than 80 kV for CNTs [207]. Operating below this threshold energy minimises damage to the sample. (Note that sample imaging for instance by TEM can be performed at higher voltage because the time needed for image acquisition is shorter than for spectroscopic data acquisition. Also the beam is more spread for TEM imaging so the electron dose transferred to the sample is not high enough to induce damage even at

200 kV). Samples were prepared as for TEM samples and data acquisition and analysis was performed by Dr Rebecca Nicholls (Department of Materials, University of Oxford).

2.3.7. Thermogravimetric analysis

Thermogravimetric analysis (TGA) assesses the mass loss occurring by combustion of a sample in a controlled oxygen atmosphere under an increasing temperature ramp. TGA was useful in this work to assess the difference in oxidation resistance from MWCNTs and N-MWCNTs [93]. The later have a lower oxidation resistance marked by a weight loss of material due to combustion happening at lower temperature than for MWCNTs. This is illustrated in **Figure 2.11** where the onset temperature - defined as the extrapolated temperature at which the weight loss begins - is 482 °C for N-MWCNTs and 612 °C for MWCNTs. This difference is due to more defects and a different composition in the N-MWCNT structure [92]. It can be expected that MWCNTs showing both a N-MWCNT and a MWCNT section due to a change in composition within the same MWCNT would show different oxidation behaviour on each section. For the first time this anticipated property was successfully investigated by TGA and results are detailed and discussed in **Chapter 5**. Measurements were performed with a Perkin Elmer Pyris Thermogravimetric Analyser from 100 ºC to 900 ºC at 5 ºC min^{-1} with the help of Dr Frank Dillon (Prof Grobert's group, Department of Materials, University of Oxford).

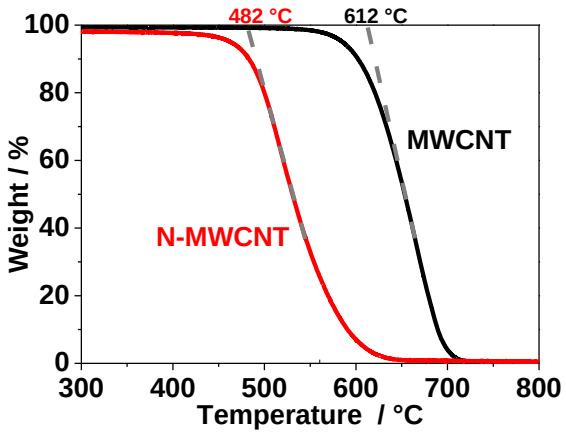

Figure 2.11. TGA analysis of N-MWCNT and MWCNT samples.

2.3.8. Energy dispersive X-ray spectroscopy

In this thesis, carbon materials with a change in composition are investigated to promote different reactivity and control the immobilisation of objects like enzymes along a MWCNT forest. However, enzymes used in this thesis have several drawbacks to prove that this control can be achieved by simple material design. First, hydrogenases have a limited availability. Second, their loading on carbon materials can be low [35]. Third, they are made of light atoms and so not easily detected on a surface. Fourth, electrochemistry is a simple method to characterise hydrogenase activity and immobilisation but electrochemistry with spatial resolution at the micro-nanoscale is not a standard technique and require specific equipment [208]. A proof of concept is then first established with platinum particles using deposition methods fully detailed in **Section 2.7**. One reason for using platinum is that it can be easily characterised by energy dispersive X-ray spectroscopy (EDS or EDX). When the sample is submitted to an electron beam, some electrons are extracted from the atoms in the material leaving holes. These holes can be filled by higher energy electron and X-rays are emitted during the process. The X-rays are characteristic of a given type of atom and so provide a probe to perform chemical analysis of a sample. For example platinum is characterised by a pronounced peak at 2.100 keV. The presence of this peak is illustrated in **Figure 2.12** and shows than platinum is not detected on as-synthesised MWCNTs (black) but is present after platinum deposition (red) on the MWCNTs. Presence of a characteristic peak from carbon in the EDS data comes from the MWCNT themselves, silicon comes from the substrate used, aluminium and lead come from the sample holder. Presence of iron is in agreement with residual iron-based catalyst particles present after AACVD synthesis of MWCNTs [191]. The opportunity to map the characteristic signal of platinum at 2.100 keV along a MWCNT forest is exploited in **Chapter 5.** This is useful to correlate a change in MWCNT structures (confirmed by Raman, SEM, TEM and/or EELS) to a change in the

loading and repartition of deposited platinum particles (assessed by SEM and EDS). EDS spectral acquisition was performed with a Jeol 840A SEM microscope operated at 10 kV and for EDS mapping and associated SEM backscattered imaging a Hitachi TM3000 table top SEM operated at 15 kV was used.

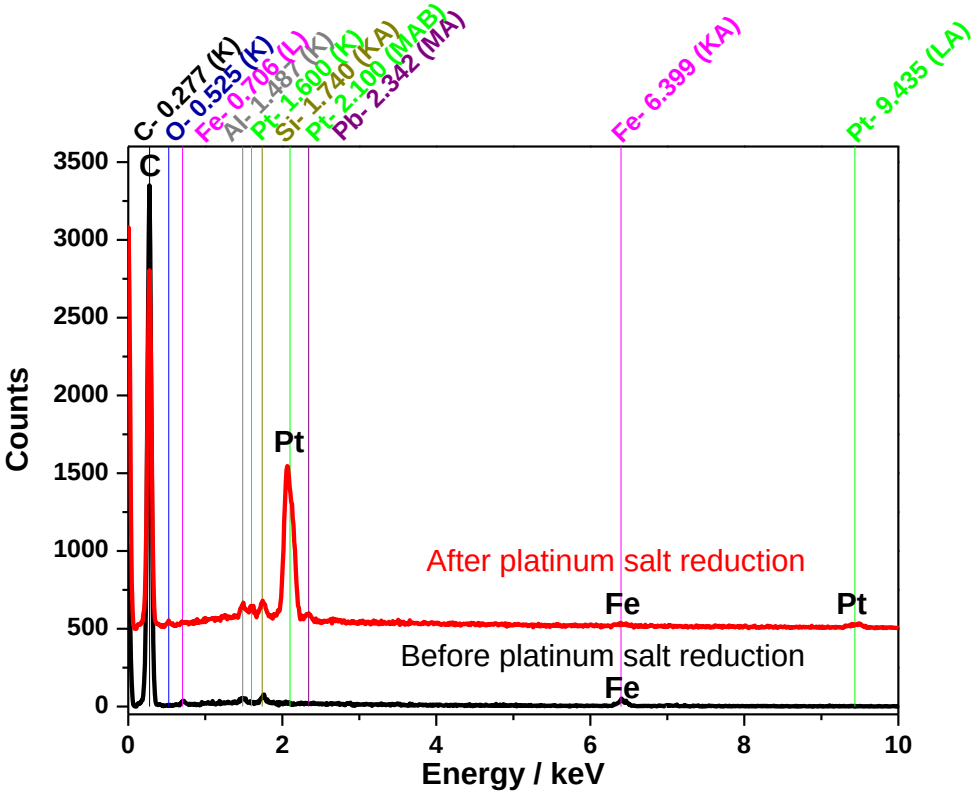

Figure 2.12. EDS analysis of MWCNTs before (black) and after (red) platinum deposition. Data after platinum deposition are reported with an offset of 500 counts for clarity.

2.4. Electrochemical measurements

2.4.1. Three-electrode measurements

Due to the electroactivity of the hydrogenases (**Section 1.2.1**), electrochemistry is an important characterisation technique in this thesis. The three-electrode set up used for electrochemical measurements is illustrated in **Figure 2.13**. The three-electrodes are a working electrode (WE), a counter electrode (CE) and a reference electrode (RE). All three are submerged into an electrolyte solution. A potentiostat (EcoChemie Autolab PGSTAT

128N) measures the electrochemical current between the WE and the CE and controls the voltage between the WE and the RE. The WE is the electrode of interest in this thesis and is made of carbon materials. The CE closes the electrochemical circuit and is made of platinum due to its relative inertness. The RE has a well-established and stable potential and is used to assess the electrochemical potential at which electrochemical phenomena happen. The reference electrodes used in this work are a saturated calomel electrode (SCE) from BAS, an homemade SCE or an homemade Ag:AgCl electrode. The potentials are reported against the standard hydrogen electrode which sets the standard of 0.000 V as the potential of the H^+/H_2 couple (for a proton activity of 1 at pH=0). Potentials are reported in volts (V) against the standard hydrogen electrode (SHE) using the relation E(SHE) = E(SCE) + 0.242 V at 25 °C [63, 209]. This conversion is adjusted by -0.67 mV for every one degree increase in temperature. For the Ag:AgCl electrode filled with a 3M NaCl aqueous solution the relation E(SHE) = E(Ag:AgCl, 3M NaCl) + 0.209 at 25 °C was used [209].

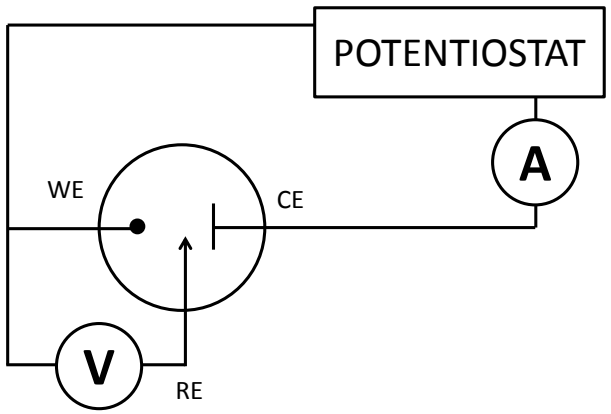

Figure 2.13. Schematic representation of the three-electrode set up used for electrochemical measurements. The potentiostat controls the voltage between the reference electrode (RE) and the working electrode (WE) while the current between the counter electrode (CE) and the WE is recorded.

2.4.2. Cyclic voltammetry

In cyclic voltammetry experiments, the potential applied in the electrochemical cell between the WE and the RE varies linearly as a function of time between two values. For instance from E_i to E_f between the time t_1 and t_0, therefore with a scan rate of $(E_f - E_i)/(t_1-t_o)$ as illustrated in **Figure 2.14a**. The current is recorded, **Figure 2.14b**, and the usual data presented is the current intensity as a function of potential, **Figure 2.14c**. The schematic representation in **Figure 2.14** corresponds to a case where no electro-active species is present in electrochemical contact with the WE: a 'blank'. If an electron exchange with the WE electrode happens at a given voltage due to a change in the redox state of the species, a higher absolute value of current is measured. This is due to electron exchange with the WE. Conventionally, oxidation processes are associated with positive current and reduction processes with negative current.

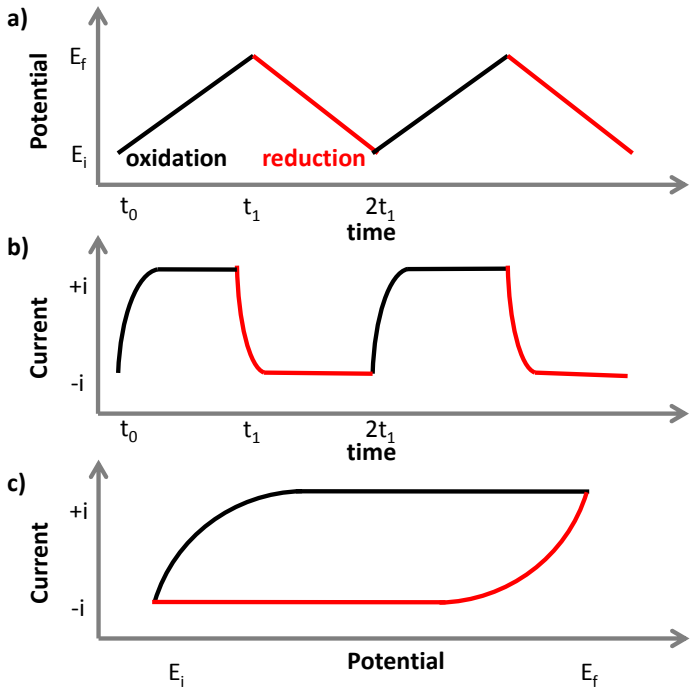

Figure 2.14. Schematic illustration of cyclic voltammetry. (a) The potential is cycled linearly over time. (b) Associated current response for a 'blank' electrode with no electro-active species in electrochemical contact with the working electrode. (c) Associated current response as a function of applied potential.

The main data of interest are then the voltage at which a redox phenomenon happens and the associated current. Controlling the voltage makes it possible to drive the species electrochemically connected to the WE into oxidised or reduced states. For instance, it makes it possible to control the enzyme in a range of potentials to establish how close to the thermodynamic potential the enzyme can operate [210]. The current reached in case of electrocatalysis gives information related to the kinetics and efficiency of the catalyst. This is because each catalytic cycle produces or consumes electrons. The flow of electrons, so the current measured, is then proportional to the number of catalytic active sites and their turnover frequency [100]. Cyclic voltammetry is then a useful technique to compare the activity of an enzyme on different carbon electrode and this is detailed further in **Chapter 3**.

2.4.3. Chronoamperometry

In the case of chronoamperometry the potential is fixed during the experiment and the current recorded as a function of time, **Figure 2.15**. If the current needs to be recorded for a succession of redox states of an electroactive species, a succession of potentials can be applied. Chronoamperometry can then be used to measure the activity of a redox species in an oxidised or a reduced state. The current recorded gives information on the number of electrons exchanged for a given time and so gives insight into the kinetics and efficiency of electrochemical processes. Chronoamperometry can also be used to evaluate the influence of a change in experimental parameters like concentration of reactants or temperature, by measuring associated changes in the current recorded at a given electrochemical potential. This technique will be relevant in particular for spectroelectrochemical measurements detailed in **Section 2.5**.

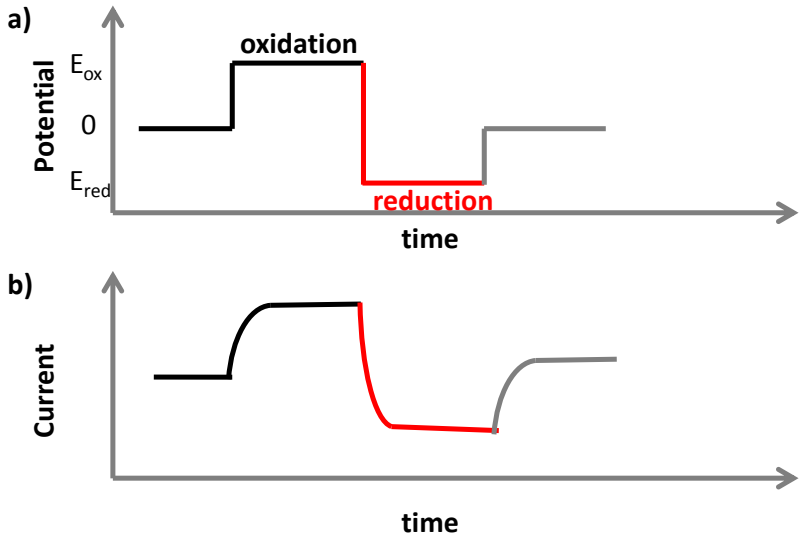

Figure 2.15. Schematic illustration of a chronoamperometry measurement. (a) the potential is varied between two potentials and (b) the current response recorded. The current response will strongly differ depending on the electrochemical process.

2.4.4. Electrochemical set up and sample preparation

The WE is the electrode of interest and the species to be investigated must be in electrochemical contact with its surface. The contact can be done by direct immobilisation on the WE surface, for instance by simple adsorption in the case of enzymes. It can also be done by drop-casting a dispersion of particles where the redox species has first been immobilised as illustrated in **Figure 2.16**. This is to develop high surface area electrodes (**Section 2.4.2**) to facilitate the acquisition of higher current related to the redox activity of the species. The WE in this work is a PG electrode with the 'edge' plane exposed (PGE) with geometrical area of 0.02 or 0.04 cm^2. The PGE electrode was polished with 1 µm α-alumina powder and cleaned by sonication in MilliQ water for at least one minute prior to all experiments and particle deposition.

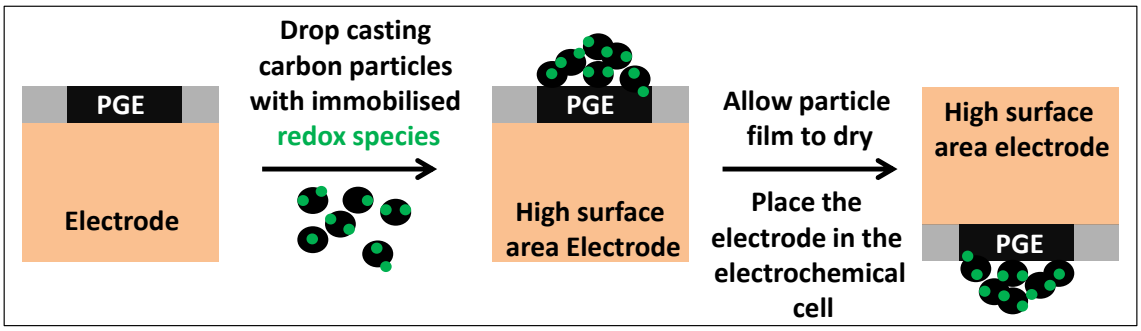

Figure 2.16. Schematic representation of the WE preparation for electrochemical investigation of immobilised redox species on carbon materials.

The WE is placed in an electrochemical cell presented in **Figure 2.17**. A rotator (EG&G model 636) control the rotation of the WE for rotating disc electrode (RDE) measurements to ensure that diffusion of the reactant (in this thesis: H_2) to the WE is not a limiting factor during electrocatalysis. The cell design has an inlet and outlet that allows a gas (for instance H_2) to pass above the cell solution to control the gas atmosphere. The enzyme activity and the potential of the reference electrodes depend on the temperature of the electrolyte. Therefore to ensure more reproducible results the cell is also water jacketed at 25 °C. The electrocatalytic activity of adsorbed species was assessed in an anaerobic N_2-filled glove box (<1 ppm O_2, Glove Box Technology Ltd.) to avoid traces of O_2 because it can inhibit the enzyme and O_2 reduction at the WE can complicate electrochemical data interpretation.

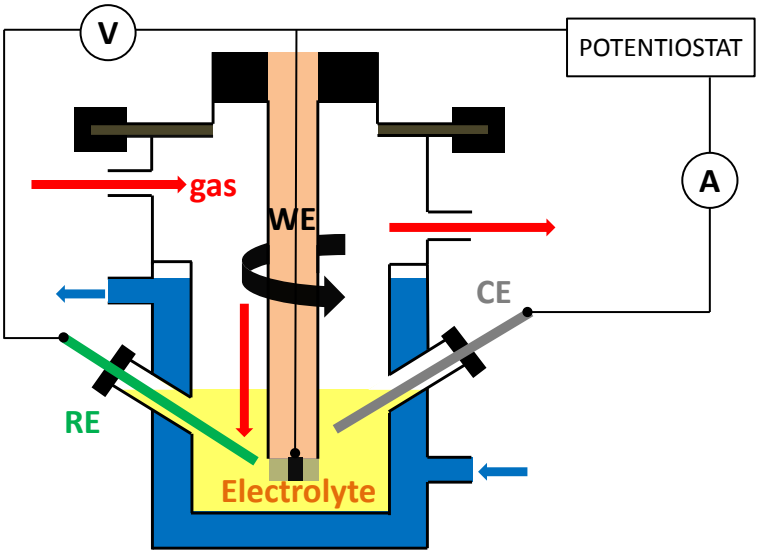

Figure 2.17. Schematic representation of the electrochemical cell used for electrochemical measurements. The electrolyte (yellow) containing cell is sealed (black) and the temperature is controlled by water circulation (blue). The RDE can be rotated which ensure gas (red) diffusion into the solution and to the working electrode (WE). The potentiostat controls the potential between the reference electrode (RE) and the (WE) while the current that passes between the counter electrode (CE) and the WE is recorded.

2.4.5. Hydrogenase electrocatalytic investigation

To study the influence of carbon materials on hydrogenase activity, hydrogenase 1 from *E. coli* (Hyd-1) was selected. Hyd-1 is a [NiFe] hydrogenase stable under a range of pH and temperature conditions, efficient in H_2 oxidation and tolerant to O_2 [33]. Hyd-1 is relatively robust and suitable for applications like enzyme fuels-cells [56]. The enzyme used in this thesis was purified from *E. coli* [211] following a published procedure [210] by Ricardo Hidalgo from Professor Vincent's group (Department of Chemistry, University of Oxford). It was used at a concentration of 20 µM unless otherwise specified. Each of the eleven carbon materials selected (**Section 2.1 and 2.2**) was dispersed at a loading of 20 mg mL^{-1} by sonication in ultra-high purity water (Millipore MilliQ, 18 MΩ cm). For adsorption of Hyd-1, a 5 µL aliquot of enzyme solution was added to 5 µL of each dispersed material the

mixture was left overnight at 4 °C to allow enzyme adsorption. Carbon materials were then washed in the glove box 3 times with 20 µL of potassium phosphate buffer (KPB, 100 mM, pH 6.0) prepared from potassium phosphate dibasic (≥ 98 %, Sigma-Aldrich) and monobasic (≥ 99 %, Sigma). The enzyme-modified carbon materials were then separated by centrifugation (7000 × *g*, MiniSpin from Eppendorf). To each sample, 5 µL of buffer was added to obtain a dispersion of materials with immobilised enzymes at 20 mg mL^{-1}.

The high surface area WE was then prepared by drop-casting 0.5 or 1 µL (as specified) of the various material dispersions with adsorbed Hyd-1 onto the surface of the PGE electrode (**Figure 2.16**). A flow of 1000 sccm H_2 (99.99 %, BOC) at 1 bar was introduced into the cell. The hydrogenase was activated for at least 5 minutes at -0.559 V *vs* SHE prior to measurements and further activated by sequences of 5 minutes at this same potential if the current recorded was noticed to significantly increase during successive scans of cyclic voltammetry. Current enhancement over time is indeed indicative of incomplete hydrogenase activation [63]. Voltammograms were acquired at a scan rate of 10 mV s^{-1} between -0.559 V and +0.241 V *vs* SHE. The absence of mediators [84] in all experiments means that the catalytic current arises solely from enzyme molecules adsorbed in an electro-active configuration on the material [212]. Measurements were conducted with the WE rotating at 2000 rotations per minute (rpm) unless otherwise stated. Steps to higher rotation rates were performed to see if the current could be increased. This would suggest a mass transport limited situation where the reactant is not provided fast enough to the catalyst. For each material, an electrode prepared without Hyd-1 showed no catalytic current response in the presence of H_2 over the potential window used for experiments in this study. Further examples and results relative to Hyd-1 activity are fully detailed in **Chapter 3**.

2.4.6. Flavin mononucleotide electrochemical investigation

Hyd-1 is a rather expensive to produce electro-active molecule with limited availability so a cheaper test molecule showing both electroactivity and IR characteristic signals was used for proof of concept experiments to couple IR spectroscopy and electrochemistry. This molecule is flavin mononucleotide (FMN, riboflavin 5'-phopshate sodium salt hydrate, from Sigma-Aldrich). In a similar way to the previously described procedure, FMN in MilliQ water at 10 mM was left to adsorb on the materials presented in **Section 2.1 and 2.2**. Adsorption was performed over one hour at 4 °C in the dark because FMN is light sensitive and its electrochemical properties are modified with long term exposure to daylight. In a typical experiment, 10 to 50 µL of a dispersion of material at a loading of 20 mg mL^{-1} in MilliQ water was mixed with an equal volume of FMN solution (10 mM). The particles were then thoroughly washed at least six times with several aliquots of MilliQ water and centrifuged to remove the washing solutions. A final volume of MilliQ water was added to the particles to give a final loading of *ca.* 20 mg mL^{-1}. Adsorbed FMN was first studied by electrochemistry and the experimental procedure for electrochemical measurements is the same as for Hyd-1 investigation unless otherwise specified. The difference is that no H_2 was used and no rotation of the electrode was required. This is because FMN undergoes a reversible 2 electron oxidation-reduction and only has redox properties without showing an electrocatalytic activity under the experimental conditions used.

2.5. ATR-IR spectroscopy under electrochemical control

2.5.1. Experimental set up

ATR-IR spectroscopy under electrochemical control is a technique that consists of coupling IR spectroscopy and electrochemistry. When fully developed this technique could lead to deep understanding of hydrogenase activity (**Section 1.2.3**). The principles for the electrochemical measurements are the same as previously described (**Section 2.4.1**). The electrochemical cell in an ATR configuration however differs from the RDE cell presented in **Figure 2.17.** The particles are now dropped onto a silicon prism as illustrated in **Figure 2.18a** and then pressed down below a piece of conductive carbon paper (TGP-H-030 from Toray) to create the WE. The design of the cell allows a RE and a CE to control the potential on the particle film, **Figure 2.18b**. The electro-active species, which are also IR active species, are now immobilised in direct contact with an optical prism. IR spectra can be collected while controlling the electrochemical potential, so while driving the species in a reduced or oxidised state. To assess the benefit of using nanomaterials to develop this technique (**Section 1.2.3**) the eleven carbon materials presented in **Section 2.1 and 2.2** with immobilised enzyme or FMN on it were used. The protocol to immobilise the redox species on the carbon materials is the same as described in **Section 2.4.5 and 2.4.6**. The volume of dispersion used for coupled IR spectroscopy and electrochemistry experiments was such that enough particles were deposited to fully cover the prism (typically 20 to 60 mg of material with immobilised enzyme or FMN). Spectra were obtained with a number of scans at least equal to 250 with a FTS- 7000 FTIR spectrometer or Varion 680-IR FTIR spectrometer.

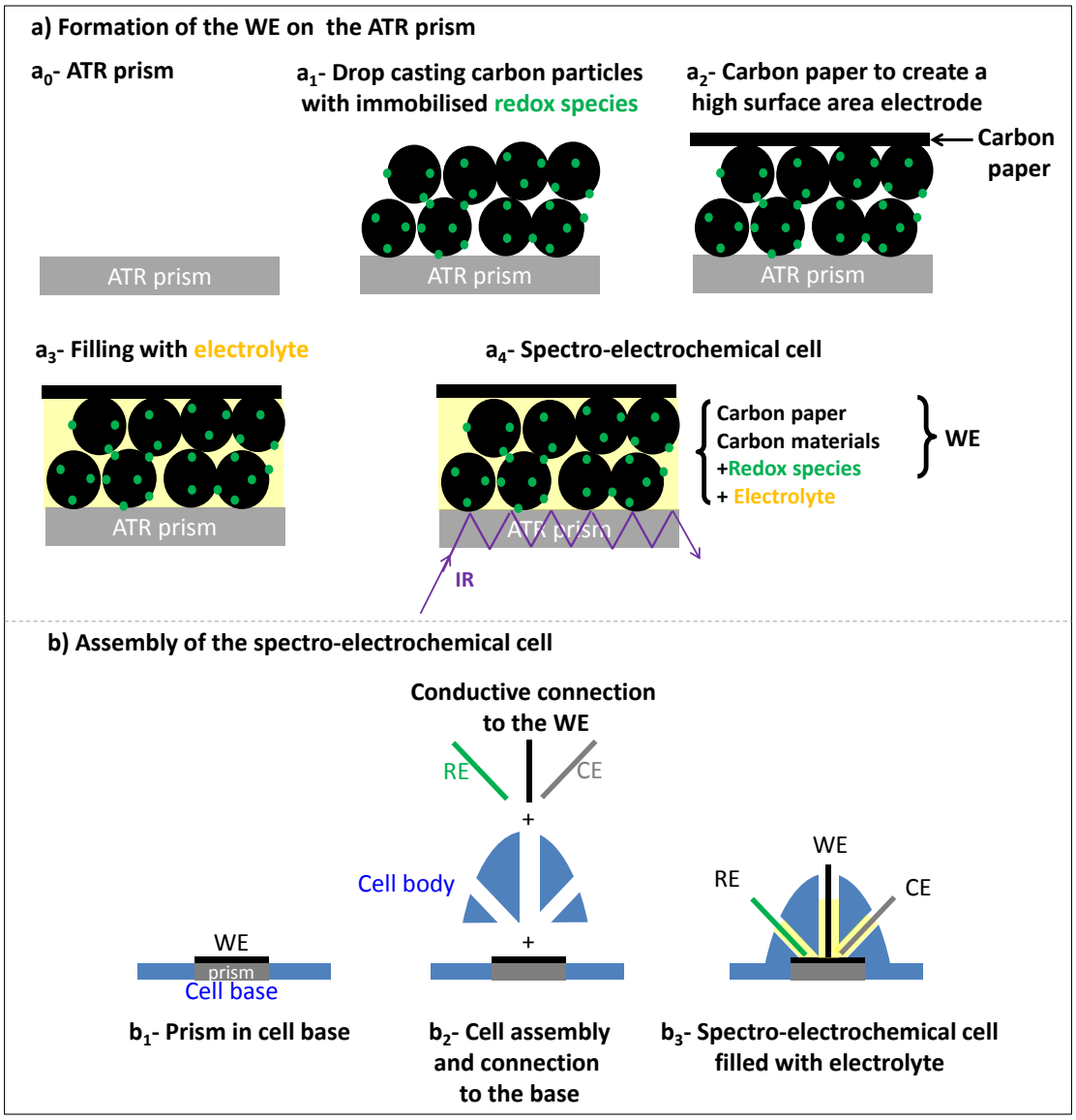

Figure 2.18. Schematic representation of (a) the formation of the working electrode (WE) for ATR-spectroelectrochemcial measurements and (b) assembly of the ATR- spectroelectrochemical cell with a WE, a reference electrode (RE) and a counter electrode (CE).

2.5.2. Data processing and presentation

Due to the specific technique of spectroelectrochemistry, some general understanding of the data acquisition and analysis is detailed in this section to facilitate further discussion in **Chapter 3**. The benefit of the ATR spectroelectrochemical cell is to control the adsorbed species on the carbon materials in reduced or oxidised states, for instance FMN absorbed on

BP (**Section 2.1**). FMN shows two distinct oxidised and reduced forms illustrated in **Figure 2.19a**. A cyclic voltammogram recorded in the spectroelectrochemical cell and displayed in **Figure 2.19b** shows two peaks at -0.20 and -0.25 V *vs* SHE. This corresponds to a two-electron transfer to respectively oxidise or reduce FMN, confirming that FMN adsorbed on the carbon material is under electrochemical control in the spectroelectrochemical cell. At potentials higher than -0.20 V *vs* SHE the FMN is in an oxidised state (FMN_{ox}), below -0.25 V *vs* SHE it is in a reduced state (FMN_{red}). Using chronoamperometry, **Figure 2.19c**, it is then possible to control the immobilised FMN in a reduced or oxidised sate while IR data are acquired.

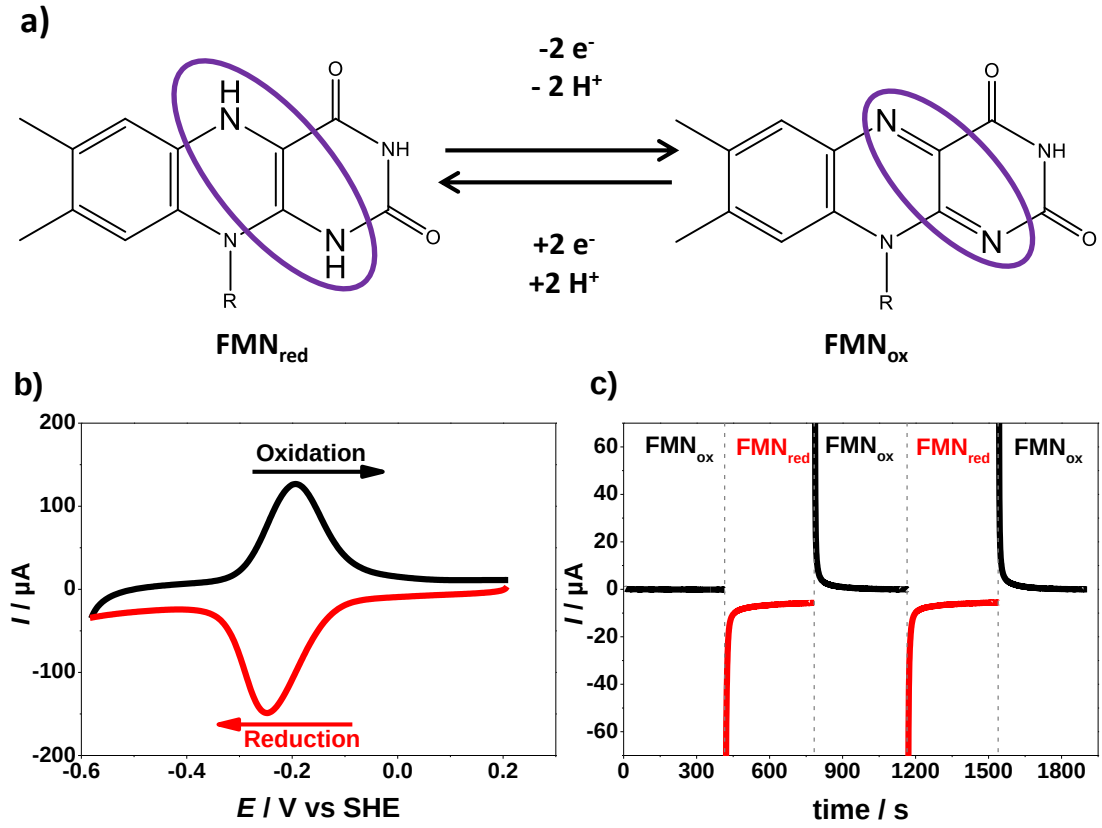

Figure 2.19. (a) Representation of the reduced (left) and oxidised (right) form of FMN [R=CH_2-$(HCOH)_3$-CH_2-$HPO_4^-Na^+$]. (b) Cyclic voltammogram and (c) chronoamperometry trace for FMN absorbed on BP recorded in the spectroelectrochemical cell. For the oxidised state (FMN_{ox}) the spectrum was recorded by controlling the potential at +0.2 V *vs* SHE and for the reduced state (FMN_{red}) the potential was controlled at -0.6 V *vs* SHE.

The differences in the molecular structures between FMN_{ox} and FMN_{red} forms should lead to different IR spectra depending on the potential applied in a spectroelectrochemical experiment. FMN_{ox} is expected if the potential applied is for instance +0.2 V *vs* SHE and FMN_{red} is expected if the potential applied is -0.6 V *vs* SHE. However, the as-acquired IR signal at those two potentials are dominated by the water absorbance of the electrolyte in the 3600–3000 and 1700–1600 cm^{-1} regions, and weaker absorption in the 2300–2000 cm^{-1} region, **Figure 2.20a-d**, simply because water is the main species present in the aqueous electrolyte in the spectroelectrochemical cell. Therefore the different features in IR signals expected FMN_{ox} or FMN_{red} forms are not observed directly. To observe distinct IR signals from oxidised or reduced forms of an electro-active species the spectroelectrochemical data are presented as *difference spectra*, **Figure 2.20e**. The subtraction reveals in particular a negative peak at 1539 cm^{-1} in the 'subtracted' spectrum (FMN_{ox}-FMN_{red}). The full significance of this peak will be covered in **Chapter 3**. Mathematically speaking, the positive peaks (pointing towards the top of the figure) in the subtracted spectrum correspond to IR features appearing in response to the potential step (*i.e.* the oxidised state of FMN) whereas negative peaks (pointing towards the bottom of the figure) are related to features present in the reduced state in **Figure 2.20e**. It must be understood for now that this is IR spectroscopic evidence that the adsorbed FMN has been controlled from an oxidised to a reduced state by the electrochemical potential applied. If there was no electrochemical control, applying a different potential to the FMN adsorbed on the electrode would not change the state of the FMN molecule. If the FMN remains in a same state (oxidised or reduced), it would have the same IR spectrum and so the subtracted spectrum in **Figure 2.20e** would be a flat featureless line. Data in **Figure 2.20** then show that coupling ATR-IR spectroscopy and electrochemistry of adsorbed species on a carbon electrode is

possible. The benefit of different carbon materials to perform the coupling is further discussed in **Chapter 3**.

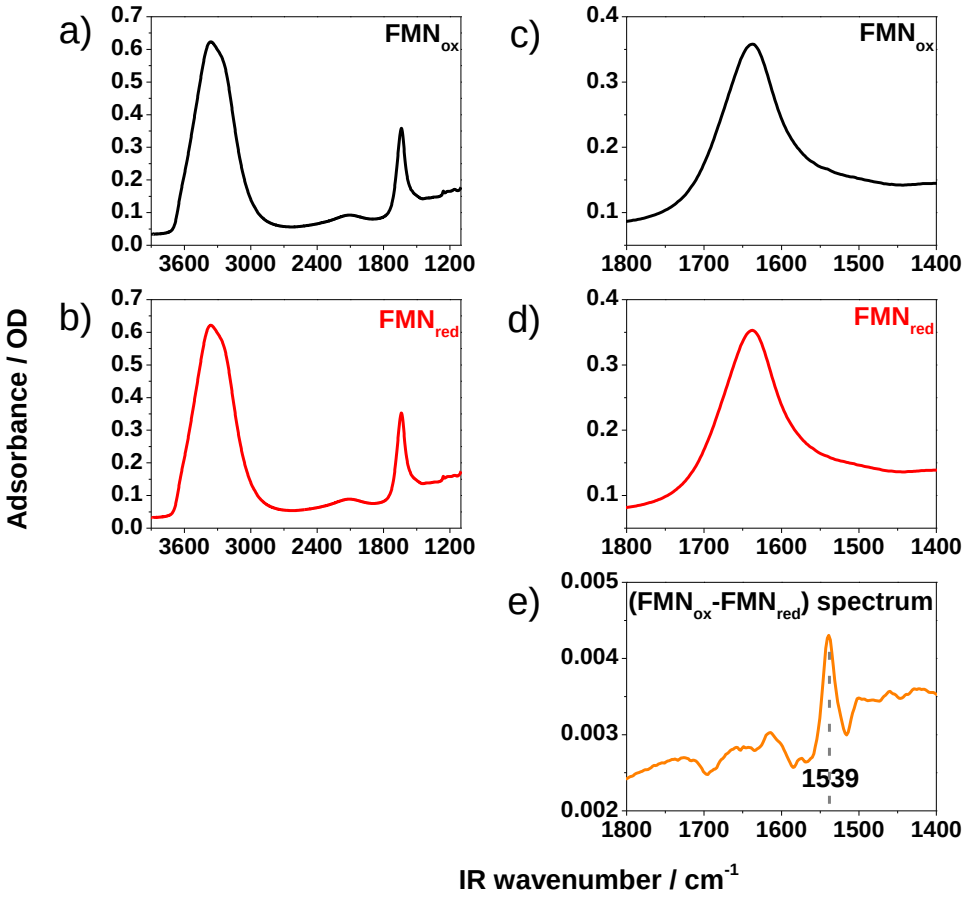

Figure 2.20. Spectra recorded at the different voltages applied during chronoamperometry for FMN adsorbed on BP. For the oxidised state (a, FMN_{ox}) the spectrum was recorded by controlling the potential at +0.2 V *vs* SHE and for the reduced state the potential was controlled at -0.6 V *vs* SHE (b, FMN_{red}). Enlargement of the wave number region where FMN has a strong signal are represented in (b) and (c) for FMN_{ox} and FMN_{red} respectively. The subtracted spectrum (e, FMN_{ox}-FMN_{red}) corresponds to the subtraction of the FMN_{red} spectrum from the FMN_{ox} spectrum.

2.6. Chemical reaction assessment

In **Chapter 4**, MWCNT scaffolds are developed to support bio-electrocatalysis and chemical synthesis in a flow reactor configuration. To follow the completion of the chemical transformations occurring and detailed in **Section 1.2.4.2**, UV-vis and high-performance liquid chromatography were needed.

2.6.1. UV-vis spectroscopy

A first step in the successful implementation of the enzyme recycling system presented in **Section 1.2.4.2** is to perform the *in situ* formation of the cofactor NADH from NAD^+, **Figure 2.21**. To follow the formation of this molecule, UV-vis spectroscopy was performed by Dr Holly Reeve (Prof Vincent's group, Department of Chemistry University of Oxford) according to her protocols and calibrations. The Beer-Lambert law links the measured absorbance (A) of a molecule at a particular wavelength to the concentration of the molecules (c), the extinction coefficient at this wavelength and the path length (l) by:

$$A=\varepsilon.c.l \qquad (\mathbf{B})$$

The amount of NADH formed is quantified by following the absorption at 340 nm because at this wavelength NADH absorbs whereas NAD^+ does not [213] due to the presence of a pyridine group in the NADH form only [214]. For UV-vis measurements a Cary 60 UV-vis spectrophotometer (Agilent) was used with a UV-vis cuvette of path length 1 cm.

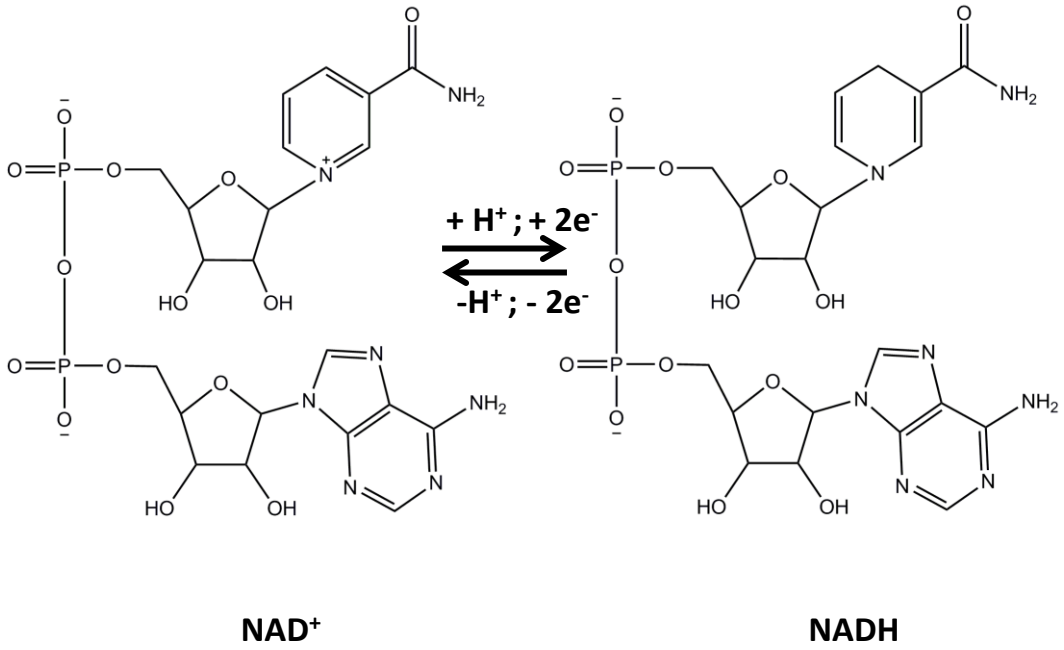

Figure 2.21. NAD^+/NADH redox couple.

2.6.2. High-performance liquid chromatography

To specifically follow the conversion of a reactant to a product, high-performance liquid chromatography (HPLC) was performed by Dr Holly Reeve (Prof Vincent's group, Department of Chemistry University of Oxford) according to her protocols and calibrations. This was done to separate, identify and quantify the conversion of acetophenone to 1-phenylethanol, **Figure 2.22**, by the enzyme cascade described in **Section 1.2.4.2.** Separation is possible due to different interactions of the molecules with the stationary phase, leading to different retention times. A Shimadzu Prominence equipped with a system controller (CBM-20), a superior solvent delivery system (LC-20AD), a high-throughput autosampler (SIL-20A), a column oven (CTO-10AS) and UV-vis absorbance detector (SPD-20A) was used running on LabSolutions software. The mobile phase was a mixture of 80 % water and 20 % acetonitrile running at 1 mL min^{-1}, the Chromolith® Performance 100-3 mm column (Merck) used was maintained at a temperature of 40 ^oC. The absorbance

at 210 nm and 260 nm (aromatic ring absorbance) were monitored for detection of acetophenone and 1-phenylethanol.

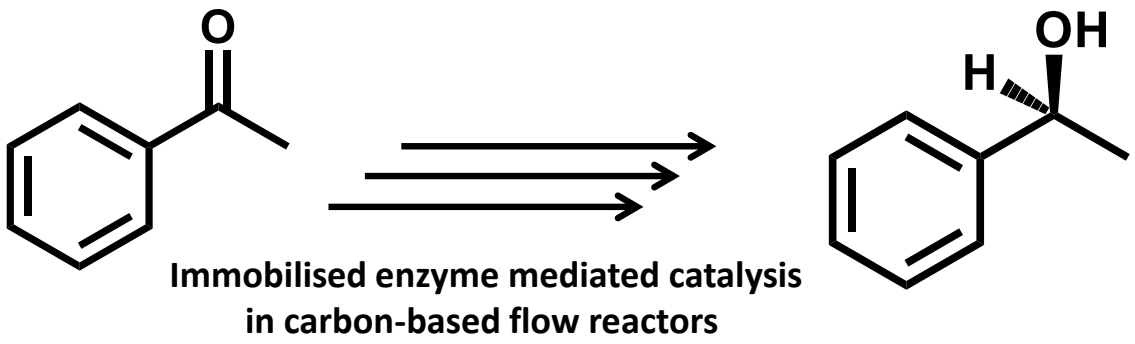

Figure 2.22. Hydrogenation of acetophenone to 1-phenylethanol.

2.7. Platinum deposition on MWCNTs

In this thesis, MWCNT forests with a change in composition are investigated to promote and control different reactivity and functionalisation along the forest (**Chapter 5**). Hydrogenases are however not suitable to prove for the first time that controlled immobilisation of nano-objects on these forests can be achieved. Hydrogenases have limited availability, a low loading on carbon surfaces (about 1 pmol.cm^{-2}) [35], and there is no simple technique to assess their localised immobilisation. Electrochemistry is a convenient tool for their bulk investigation but developing a technique to map the immobilisation of electro-active objects on nanomaterials is still an area of research under development. It requires specific equipment like scanning electrochemical microscopes that could not be accessed for this thesis [95, 96]. Platinum particles were then preferred for a proof of concept. This is first because platinum deposition is reported to be sensitive to the nature of the MWCNTs they are deposited on. For instance different platinum particles size and coverage are reported on MWCNTs compared to N-MWCNTs [164]. Second, deposition of platinum on the forests is simple to characterise by SEM but also by chemical analysis like EDS. Third, platinum

particle deposition is simple to perform by different bulk methods that do not induce a localised immobilisation. If any difference in platinum repartition is observed it then comes from different properties of the support used for immobilisation - in this work a MWCNT forest with a change in composition - and not from the process used to deposit the particles.

2.7.1. Electrochemical reduction of platinum salts

Electrochemistry is a first technique to immobilise platinum particles onto conductive materials [72]. Platinum particles were electrodeposited using the three-electrode set up described in **Section 2.4.3**. The WE was the MWCNT forest on a silicon wafer simply clipped with a crocodile clamp; CE was a platinum wire; RE was a SCE. An Autolab128N potentiostat (EcoChemie, Netherlands) was used and experiments were performed in an anaerobic glove box (MBraun, <1 ppm O_2). Pre-treatment consists of scanning the samples 10 times at a scan rate of 50 mV s^{-1} in H_2SO_4 (0.1 M, obtained after dilution from 98 % sulphuric acid from Fisher Scientific) between -0.06 and +1.54 V *vs* SHE to improve the wettability and hydrophilicity of the MWCNT forest. Platinum electrodeposition was performed with a solution of $H_2PtCl_6.6H_2O$ (5 mM) in KPB (50 mM, pH 7) or KCl (50 mM) electrolyte by cycling the potential 3 to 30 times between -0.54 and +0.46 V *vs* SHE at a scan rate of 50 mV s^{-1}. Different electrolytes and numbers of scans were used to make sure that the platinum immobilisation is not dependent on a specific electrolyte or number of scans.

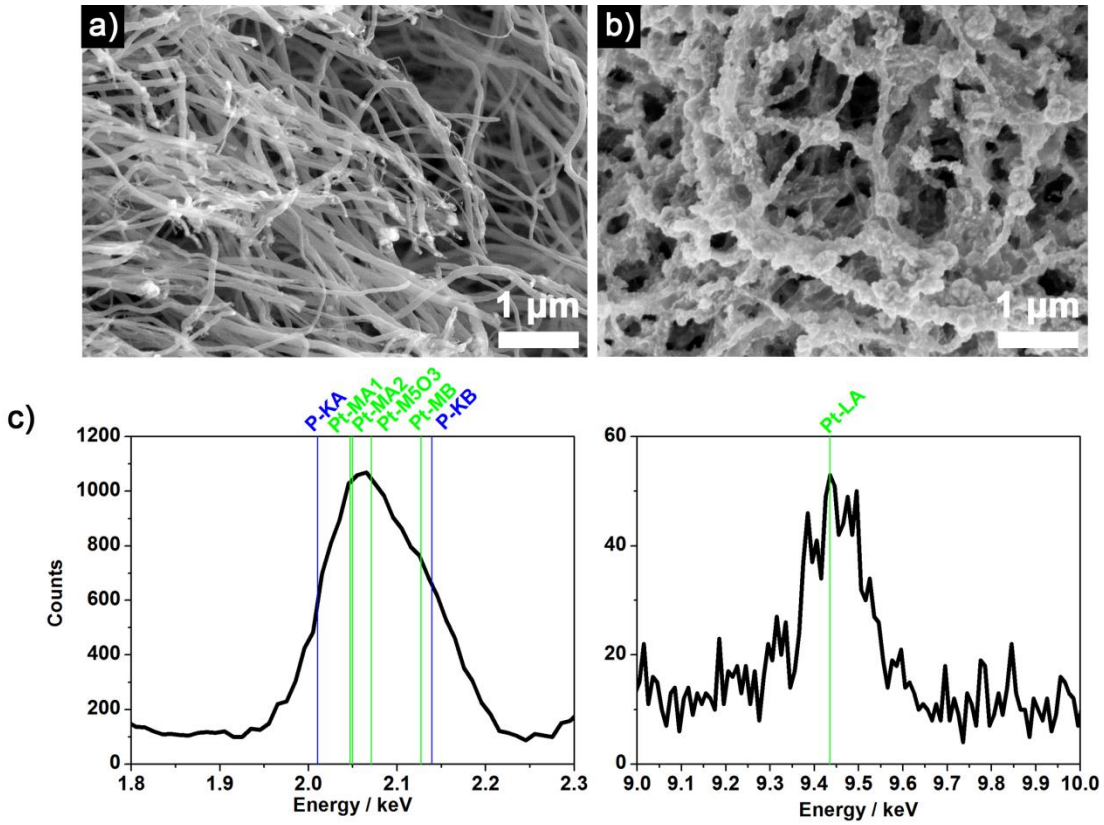

Figure 2.23. (a) SEM images of MWCNTs (a) before and (b) after electrodeposition of platinum particles. (c) Presence of the platinum characteristic peaks in EDS analysis confirm deposition of platinum on the MWCNTs.

Electro-deposition is confirmed by SEM as presented in **Figure 2.23**: presence of conductive round particle-like features with a bright contrast on the SEM image, **Figure 2.23b**. These features are not observed before platinum deposition, **Figure 2.23a**. Backscattered electrons images (**Figure 2.7**) and EDS, **Figure 2.23b**, also confirm the presence of platinum after electro-deposition only. The benefit of electro-deposition is to show that the MWCNTs network is conductive: without conductivity no electro-deposition could be possible. It also provides a way to functionalise MWCNTs by a bulk deposition method to identify the influence of a local change in composition or graphitic structure along the forests.

2.7.2. Chemical reduction of platinum salts

Alternatively, platinum deposition was performed by chemical reduction with formic acid (98 %, Fluka) at room temperature and in air by dropping the MWCNT forests grown on silicon wafers into a solution of $H_2PtCl_6.6H_2O$ (1.5 mM) prepared in a mixture of H_2O:HCOOH (20:1, v:v). Samples were left into the solution for 3 to 8 hours. Samples were subsequently thoroughly washed with water and dried at room temperature. This last approach efficiently covers carbon surfaces like amorphous carbon [215], MWCNTs [216] or N-MWCNTs [217] with platinum. The deposition of platinum is confirmed by SEM and EDS in this thesis just like for the case of electrochemical deposition. The benefit of chemical reduction is to avoid the need for an electrochemical set up for MWCNTs functionalisation. It is performed with simple chemicals at room temperature and ambient air, by simply dropping the MWCNT forest in an aqueous solution. Chemical reduction is also a bulk deposition method, suitable to assess the influence of a change in chemical composition or graphitisation along MWCNT forest on the platinum nucleation and deposition.

Chapter 3: Comparison of carbon electrodes for hydrogenase immobilisation towards coupling ATR-IR spectroscopy and electrochemistry

"Science, my lad, is made up of mistakes,
but they are mistakes which it is useful to make,
because they lead little by little to the truth."
Jules Verne

A specific thank you to Dr Frank Dillon (Department of Materials, University of Oxford) for running the nitrogen adsorption porosimetry experiments and to Dr Philip A. Ash (Department of Chemistry, University of Oxford) for fruitful discussion about coupling ATR-IR spectroscopy with electrochemistry. A warm thank you to Ricardo Hidalgo (Department of Chemistry, University of Oxford) for help and support and co-working with me on the Hyd-1 and FMN studies. An important part of the results presented in this Chapter 3 was published in Ref [193] and reproduced by permission of the Royal Society of Chemistry.

3.1. Introduction

Due to their electrocatalytic activity and efficiency in splitting or producing dihydrogen, hydrogenases are promising bio-electrocatalysts for a range of energy devices like enzyme fuel cells (**Section 1.2.1**). To exploit or study the catalytic activity of hydrogenases, one approach is their immobilisation on conductive supports to create electrodes. A widely used material for hydrogenase immobilisation is pyrolytic graphite (PG) because simple and robust adsorption of the enzyme is achieved on the surface of this carbon material (**Section 1.2.2**). PG can be used as a planar electrode or as particles to create a 'high surface area' electrode (**Section 2.4**) after deposition on a conductive support. The benefit of a higher surface area electrode is to lead to higher electrocatalytic current from the adsorbed enzymes, which is directly relevant to develop enzyme fuel cells. Unfortunately PG particles have several drawbacks. The material is usually prepared freshly by abrasion just prior to enzyme adsorption which is not suitable for large scale production. The material also has a relatively large size about 5-10 µm with a relatively low specific surface area (about 40 m^2 g^{-1}) [62] compared to other materials. To improve applications of hydrogenases,

electrodes leading to a higher current than the PG-based-electrodes are required. This can be achieved with a higher surface area electrode and a range of nanomaterials with specific surface areas expected to be higher than 100 m^2 g^{-1} [98, 201] have then been investigated as alternative electrode materials to PG in recent years (**Section 1.2.2.5**). However, the surface area developed by these materials is not always fully quantified in these studies. In addition, these alternative materials have not been assessed with the same hydrogenase or under comparable conditions. It is then challenging to firmly establish the properties that are important to consider in the selection of a carbon material to develop hydrogenase-based devices. This issue is then addressed in this thesis.

In **Chapter 3**, the hydrogenase Hyd-1 from *E. coli*, was adsorbed on different electrodes made of different carbon materials. A systematic study under equivalent experimental conditions was performed to identify the most suitable materials for enzyme adsorption. This was assessed by the electrocatalytic current achieved from the hydrogenase electrode but also by how efficiently the carbon surface available was used by the enzyme. Eleven carbon materials presented in **Section 3.2** were selected for their different properties. These are for instance a higher surface area than PG particles, different degree of graphitisation and different morphologies assessed in **Section 3.3.1**. These properties have been suggested to favour hydrogenase loading and help in achieving high current output at a hydrogenase electrode in enzyme-fuel cells. The electro-activity of Hyd-1 on the eleven different materials is compared in **Section 3.3.2**. A high surface area is shown to be important to improve the electrocatalytic current whereas a high degree of graphitisation favours a better use of the carbon surface available by the hydrogenase.

Controlling the properties of carbon materials at the nanoscale is relevant to develop enzyme electrodes for devices. This thesis also shows how the careful consideration of materials used can contribute to the development of new techniques to study the

hydrogenase active site chemistry. This is illustrated with the design of carbon materials to develop electrodes that facilitate the IR spectroscopy investigation of enzymes under electrochemical control (**Section 1.2.3**). This technique consists of coupling electrochemistry and IR spectroscopy in an ATR configuration and is based on IR evanescent waves. These waves have a limited penetration depth into the volume of sample to probe. For the experimental conditions used in this study (**Section 1.2.3**), the penetration depth of the IR waves is about 1 micrometre. The volume probed is made of carbon materials where electro-active species like enzymes are immobilised. To characterise hydrogenase activity with the spectroelectrochemical technique, a high loading of hydrogenase in the probed volume is required and this can be achieved with high surface area materials with a sub-micrometre size. The PG beads with a typical dimension around 5-10 µm are then bigger than the expected penetration depth of the evanescent waves and so not suitable to perform the coupling. The alternative materials developed for hydrogenase electrodes presented in **Section 3.2** are nanomaterials. They are then promising candidates to improve the coupling of ATR-IR spectroscopy and electrochemistry. Thanks to the careful design of materials at the nanoscale, ATR-IR spectroscopic studies of molecules under electrochemical control directly adsorbed on carbon materials is proven for the first time in **Section 3.3.3**. This marks a milestone in the development of a technique which can now be employed in experiments designed to give a better fundamental understanding of hydrogenase activity and reactions.

3.2. Selection criteria for the carbon materials

To develop high surface area electrodes with alternative material to PG particles and to favour direct adsorption of hydrogenases on these materials, eleven carbon materials were selected to present different properties. These are for instance different shape, size, degree of graphitisation, porosity and surface area. To favour the coupling of ATR-IR spectroscopy

and electrochemistry, the materials were also selected to show a micro or nanoscale. They were finally chosen because they are commercially available or are straightforward to obtain in most modern laboratories by the techniques and protocols covered in **Chapter 2**. Materials that require as little processing as possible simplify the development of enzyme electrodes. Therefore further additional treatments like chemical functionalisation of the materials [33, 82, 84] to achieve better enzyme loading are beyond the scope of the present work.

Due to the success demonstrated for pyrolytic graphite 'edge' surfaces in hydrogenase electrocatalysis [35], several materials with ordered graphitic character were investigated. Abraded pyrolytic graphite (APG, **Section 2.1**) was selected because it is a material reported to develop high surface area electrodes for hydrogenase immobilisation [62, 63]. It will be used as a reference material in this study. As an alternative to APG, micron-sized graphite particles (MG, **Section 2.2.1**) were prepared by a simple exfoliation route with the intention of developing a higher specific surface area than APG and increasing the proportion of 'edge' sites. Commercial graphite platelet nanofibers (GNF, **Section 2.1**), consisting of stacked graphitic layers perpendicular to the fibre axis were selected due to the prevalence of graphitic 'edge' surface.

In order to assess the suitability of rather amorphous carbon materials, four commercially-available carbon blacks already used in fuel cell catalysis [57] were selected (**Section 2.1**): Mogul L (ML), Vulcan XC72R (VX), Black Pearls 2000 (BP) and a carbon nanopowder (CNP). In addition to the commercially available carbon black materials, carbon particles prepared by hydrothermal synthesis (HNP, **Section 2.2.2**) from a glucose precursor [196] were tested. This material and this synthesis technique were selected because the well-established hydrothermal synthetic approach is a relatively green synthesis method and can be adapted to obtain various carbon-based materials (**Section 2.2.2**). Therefore it could be a

useful approach to potentially tune carbon materials as required for specific applications. In addition, to test the applicability of composite materials, particles with a thin carbon shell surrounding a silicon core were prepared by polymerisation followed by carbonisation (Si@C, **Section 2.2.3**) [203]. Since the silicon core is IR transparent, this could give a material suitable for coupling ATR-IR spectroscopy and electrochemistry as detailed in **Section 1.2.3**.

Finally, MWCNTs were selected because they have been previously suggested as conductive networks for high surface area electrodes for hydrogenase immobilisation [84]. Their synthesis requires more specific equipment than the other materials. However, home-made synthesis by AACVD (**Section 2.2.3**) makes it possible to control the properties of the MWCNTs. For instance the possibility to cover substrates with MWCNT forests can be exploited. Also the chemical composition of the tubes can be controlled to obtain nitrogen-doped MWCNTs (N-MWCNTs) [92]. Alteration of the carbon lattice by nitrogen doping confers defects and heteroatom sites [92] which may improve hydrophilicity and provide anchor sites for protein attachment. N-MWCNTs were then combined for the first time with a hydrogenase.

3.3. Results and discussion

For the eleven carbon materials selected, commercial (APG, ML, VX, BP, CNP and GNF) or produced in-house following established recipes (MG, MWCNT, N-MWCNT, HNP and Si@C), several properties were investigated. These are the size and shape of the materials assessed by SEM and TEM. Their graphitic structure assessed by HRTEM and Raman spectroscopy. Their surface area and their mesoporosity (pore size between 2 and 50 nm, a scale relevant for enzyme adsorption) assessed by nitrogen adsorption. The characteristics of each material are detailed in **Section 3.3.1** and gathered in **Table 3.1**. The properties were found to be in agreement with data from suppliers or

previously reported [31, 62, 92, 195, 196, 203, 218-220]. In **Section 3.3.2**, all materials were tested for adsorption of Hyd-1 in a configuration suitable for direct electronic transfer with the carbon electrode [35]. The influence of the carbon materials on Hyd-1 activity was assessed by measuring the enzyme electrocatalytic activity for H_2 oxidation. Due to their nano-size the carbon materials were further considered in **Section 3.3.3** to couple ATR-IR spectroscopy and electrochemistry.

Table 3.1. Characteristics of carbon materials investigated.

Material	Abbreviation	Source	Typical size	Raman I_D/I_G	Model used for specific surface area	Specific surface area ($m^2 g^{-1}$)	Pore diameter[a] (nm)	Pore volume[b] ($cm^3 g^{-1}$)
Abraded Pyrolytic Graphite	APG	Abrasion	*D*: 3-5 µm *t* > 500 nm	0.17 ±0.04	BET	35 .2±0.1	4.6	0.05
Micron-sized Graphite	MG	Exfoliation	*D*: 500 nm-1µm *t* < 300 nm	0.19 ±0.05	BET	52.5 ±0.5	5.9	0.11
Graphite platelet NanoFibers	GNF	Sigma-Aldrich	*D*: 20-250 nm *L* < 3 µm	1.20 ±0.11	BET	81.0 ±0.4	5.7	0.14
Multi-wall Carbon Nanotube	MWCNT	AACVD	*D*: 50-100 nm *L*: 50-150 µm	0.36 ±0.04	BET	60.0 ±0.6	6.1	0.12
Nitrogen-doped Multi-wall Carbon Nanotube	N-MWCNT	AACVD	*D*: 50-100 nm *L*: 40-120 µm	0.89 ±0.11	BET	57.1 ±0.2	7.2	0.14
Hydrothermal Nanoparticles	HNP	Hydrothermal synthesis	*D*: 100-120 nm	1.08 ±0.01	Langmuir BET	816 ±4 550 ±14	3.6	0.34
Carbon NanoPowder	CNP	Aldrich	*D*: 30-50 nm	0.94 ±0.08	BET	198.0 ±0.5	6.9	0.45
Mogul L	ML	Cabot Corporation	*D*: 25-40 nm	0.96 ±0.05	BET	127.6 ±0.4	8.7	0.34
Vulcan XC72R	VX	Cabot Corporation	*D*: 12-63 nm	1.06 ±0.05	BET	237 ±3	5.1	0.28
Black Pearls 2000	BP	Cabot Corporation	*D*: 17-31 nm	1.18 ±0.03	Langmuir BET	2053 ±24 1332 ±22	4.7	1.36
Silicon Core Carbon Shell Nanoparticles	Si@C	Polymerisation and Carbonisation	Core *D*: 50-150 nm Shell *D*: 10-20 nm	1.05 ±0.03	Langmuir BET	328.9 ±0.8 221 ±5	3.8	0.13

a: average pore diameter estimated by BJH desorption ($4V/A$); b: single point measurement at relative pressure 0.95 for pores less than 40 nm; *t*: thickness; *L*: length; *D*: diameter. In the case where the Langmuir model gives a better fit to the data than the BET model, values obtained with the Langmuir model are specified in addition to the results obtained using the BET model.

3.3.1. Carbon materials characterisation

3.3.1.1. SEM/TEM characterisation: size and morphology

Figure 3.1 shows SEM images of materials which can be classed as plate-like (APG and MG) or fibre-like (MWCNT, N-MWCNT and GNF) according to their general morphology. Images presented in the left hand panel were recorded at the same magnification and are presented to show differences in the overall morphology of the samples, **Figure 3.1a, c, e, g, i**. Images presented in the right hand panel show magnifications selected to highlight more specific aspects of the material like shapes and sizes, **Figure 3.1b, d, f, h, j**. The diameter of the flat surface of the APG plates is in the range 3-5 µm whereas the MG plates are smaller, falling mostly in the range 0.5-1 µm. A rough estimate of the thickness (*t*) of the plates (**Table 3.1**) was also evaluated from examination of the SEM images. The MG plates are thinner (< 300 nm) than APG (> 500 nm). These observations confirm that exfoliation of graphite flakes is a relevant synthetic route to obtain small-size graphite plate-like materials (MG). MWCNTs and N-MWCNTs have typical diameters below 100 nm and a length up to 150 µm and 120 µm respectively. TEM images in **Figure 3.2** confirm that they are both hollow materials and qualify as tubes. The hollow nature of the N-MWCNT can also be observed by looking at the catalyst-free tips of a N-MWCNT at high magnification SEM images: circular features in **Figure 3.1h**. In agreement with the literature, MWCNTs, **Figure 3.2a**, have thick wall and a small inner diameter. N-MWCNTs, **Figure 3.2b**, have thinner walls and a larger inner diameter [92]. The typical bamboo-structure [92] with compartments is observed within the N-MWCNTs as well as ‘kinks’ along the wall, **Figure 3.2b**. In contrast GNF are not hollow and consist of stacked layers (discussed further in **Section 3.3.1.2**) with diameters in the range 20-250 nm, and are typically shorter than 3 µm.

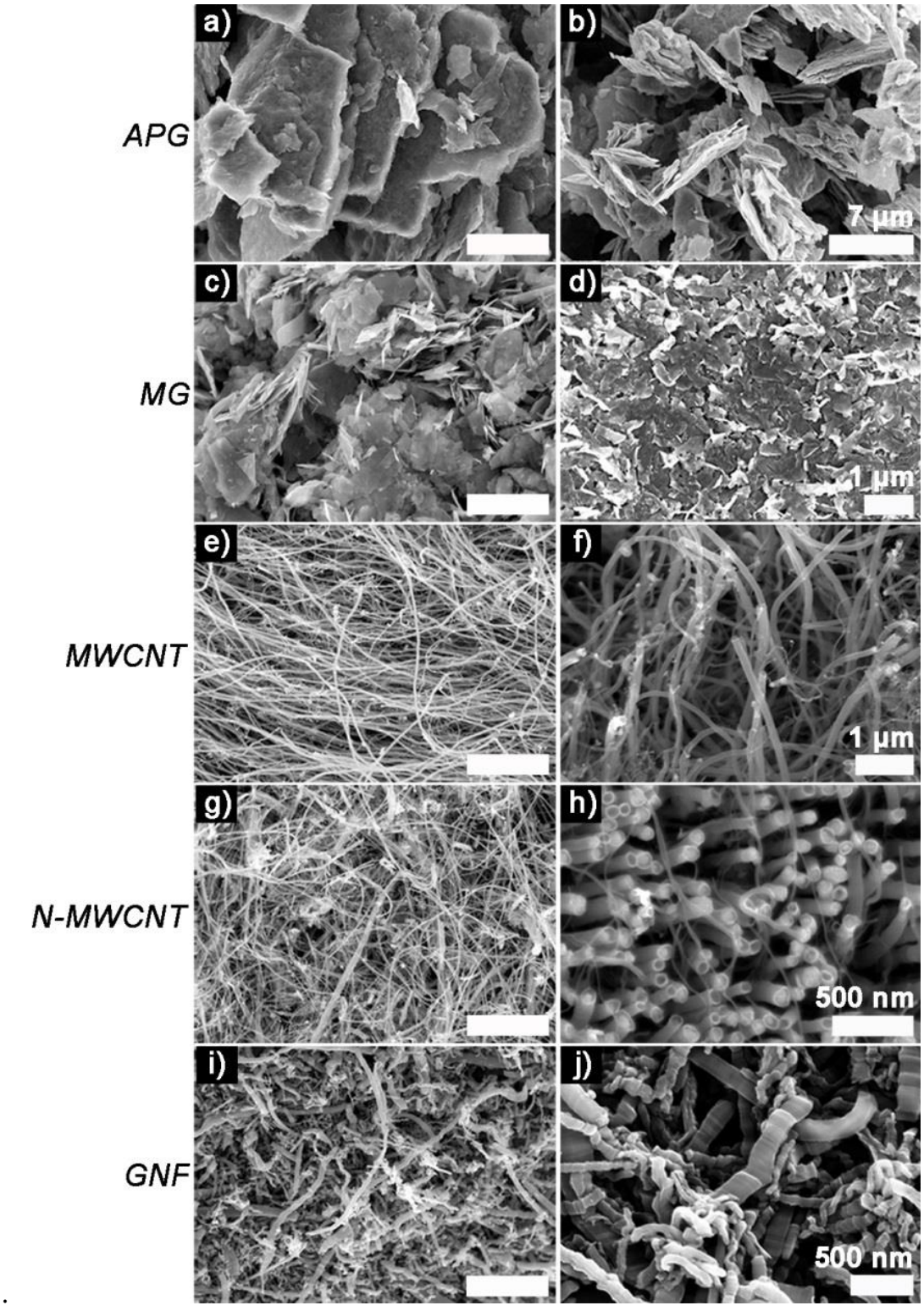

Figure 3.1. SEM micrographs of plate-like and fibre-like carbon materials. Images taken at the same magnification (a, c, e, g, i; scale bars = 3 µm) reveal the overall morphology. In order to highlight specific morphological features of each material, images were also taken at different magnifications (b, d, f, h, j; scale as indicated).

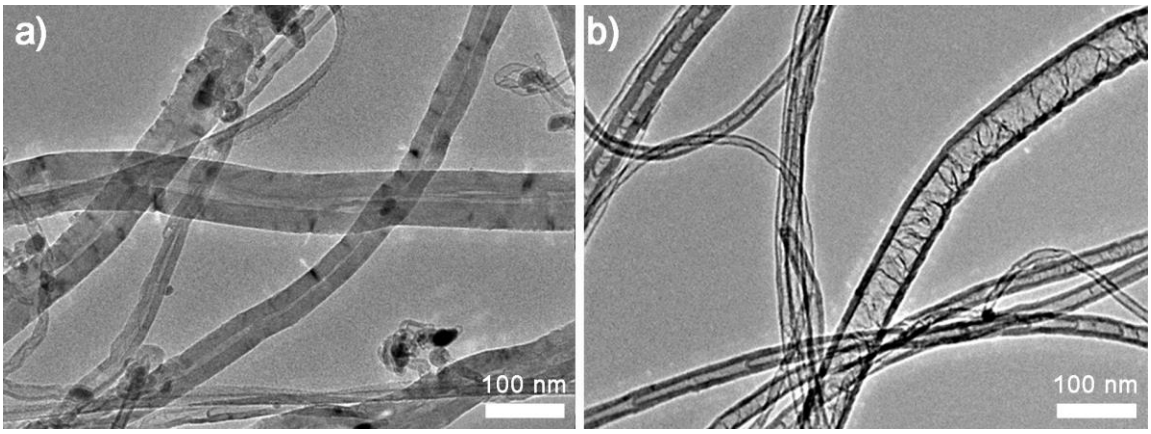

Figure 3.2. TEM micrograph of (a) MWCNTs and (b) N-MWCNTs.

Images of the materials having particle-like morphologies (CNP, ML, VX, BP, HNP and Si@C) are displayed in **Figure 3.3** which is split into SEM images in the left-hand panel (**Figure 3.3a, c, e, g, i and k**) and TEM images in the right-hand panel (**Figure 3.3b, d, f , h, j and l**). The electron microscopy studies showed that all the commercially available materials (CNP, ML, VX, BP) possess an average particle size less than 50 nm (**Table 3.1**). The particle size for in-house synthesised HNP ranged between 100 nm and 120 nm. TEM images of the Si@C particles are consistent with a silicon core (50-150 nm) coated with a thin carbon shell (10-20 nm). The core-shell structure of the Si@C particles was indicated by the difference in contrast in the TEM images. Also HRTEM images in **Figure 3.4** confirm a change in the structure of the material from highly periodic atomic structure in the core (attributed to silicon) and more amorphous materials for the shell (carbon). Finally, the presence of the amorphous carbon shell was confirmed by Raman analysis (see **Section 3.3.1.2**).

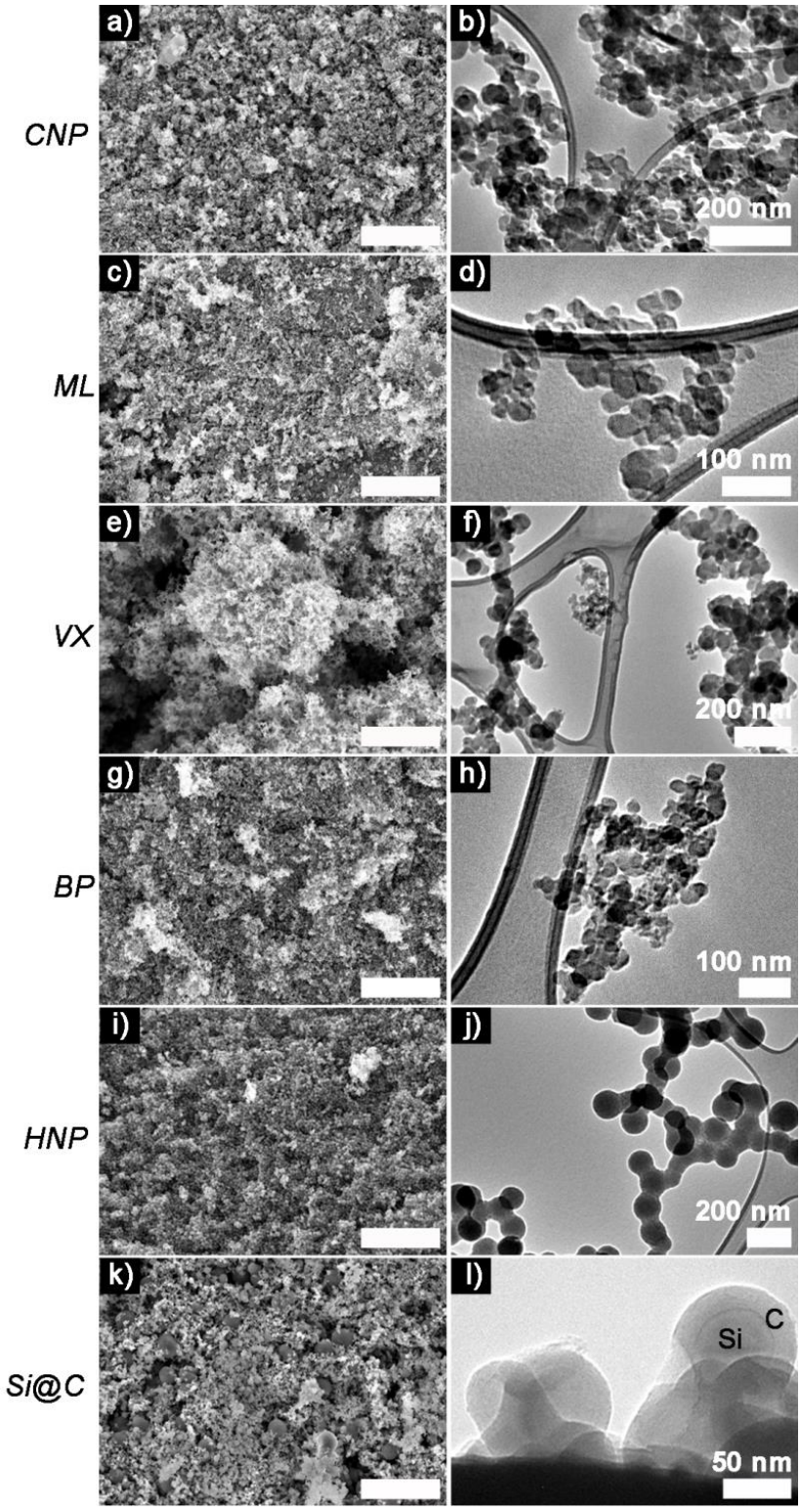

Figure 3.3. SEM and TEM micrographs of particle-like materials. Images taken at the same magnification (a, c, e, g, i, k; scale bars = 3 µm) reveal the overall morphology. In order to highlight specific morphological features of each material, images were also taken at higher magnifications (b, d, f, h, j, l; scale as indicated).

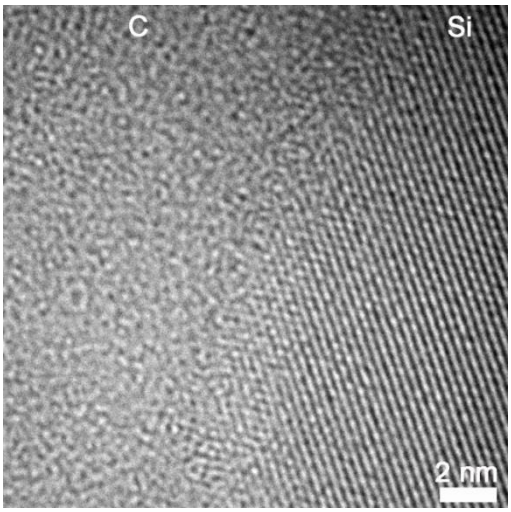

Figure 3.4. HRTEM of a Si@C particle where the shell is on the left of the image and the core on the right. ***With the courtesy of Vitaly Babenko, Department of Materials, University of Oxford.***

3.3.1.2. Raman spectroscopy and HRTEM: graphitic structure

Raman spectra for each material are shown in **Figure 3.5**, and I_D/I_G values are summarised in **Table 3.1**. Three main peaks in the Raman spectrum were considered in order to assess the degree of graphitisation in the materials: the D, G and 2D peaks at *ca.* 1340, 1565 and 2680 cm^{-1} respectively (discussed in **Section 2.3.4**). APG and MG display I_D/I_G less than 1 and show a strong 2D peak. This confirms that the materials both show graphitic structure (sp^2 network). Similarly, the I_D/I_G of the MWCNTs is less than 1 and the spectrum also shows a strong 2D peak. A HRTEM image of the wall of a MWCNT confirms an ordered graphitic structure, **Figure 3.6a**. It can be seen in this image that the carbon planes, appearing as lines of atoms making up the walls, are relatively straight. This illustrates that the majority of the exposed MWCNT surface is then basal-plane type carbon. The presence of 'edge'-like structures can be expected at the open end of the tube only (**Section 1.2.2**) and are therefore not likely to be abundant in the material [221].

N-MWCNTs show I_D/I_G close to 1 and the presence of a 2D peak. Production of

nitrogen-doped carbon nanotubes is known to introduce defects in the graphitic carbon network [93, 162]. This is consistent with the increase in I_D/I_G and smaller 2D peak compared to a MWCNT sample. A HRTEM image of a N-MWCNT confirms that this material has a less ordered graphic structured compared to the MWCNT, **Figure 3.6b**. It can be seen in this image that the carbon planes appearing as lines of atoms making up the walls are less straight than for a MWCNT, **Figure 3.6a**. This is in agreement with presence of nitrogen in the carbon walls modifying the carbon structure and introducing defects [92]. The Raman spectrum of GNF shows I_D/I_G greater than 1 and a 2D peak confirming graphitic character. In contrast to a MWCNT, HRTEM study of GNF shows the predominance of graphitic 'edge'-like features making up the majority of the GNF surface, **Figure 3.6c**. The Raman spectrum of GNF also displays a D′ peak: shoulder on the D peak, see inset in **Figure 3.5**. This is also related to an abundance a micro-sized sp^2 domains and is consistent with the stacked platelets making up the fibre with their edges oriented perpendicular to the fibre axis [31]. This is expected since the GNF can be seen as a superposition of several graphene plates on top of each other forming a tubular structure with presence of 'edge'-like features along the fibre surface.

The remaining materials (CNP, ML, VX, BP, HNP, Si@C) have a Raman spectrum with I_D/I_G close to 1 and no 2D peak. This is indicative of a rather amorphous structure without extended crystalline domains. For instance an HRTEM image of the BP particles in **Figure 3.6d** confirms that these particles do not exhibit obvious 'edge'-like character [219].

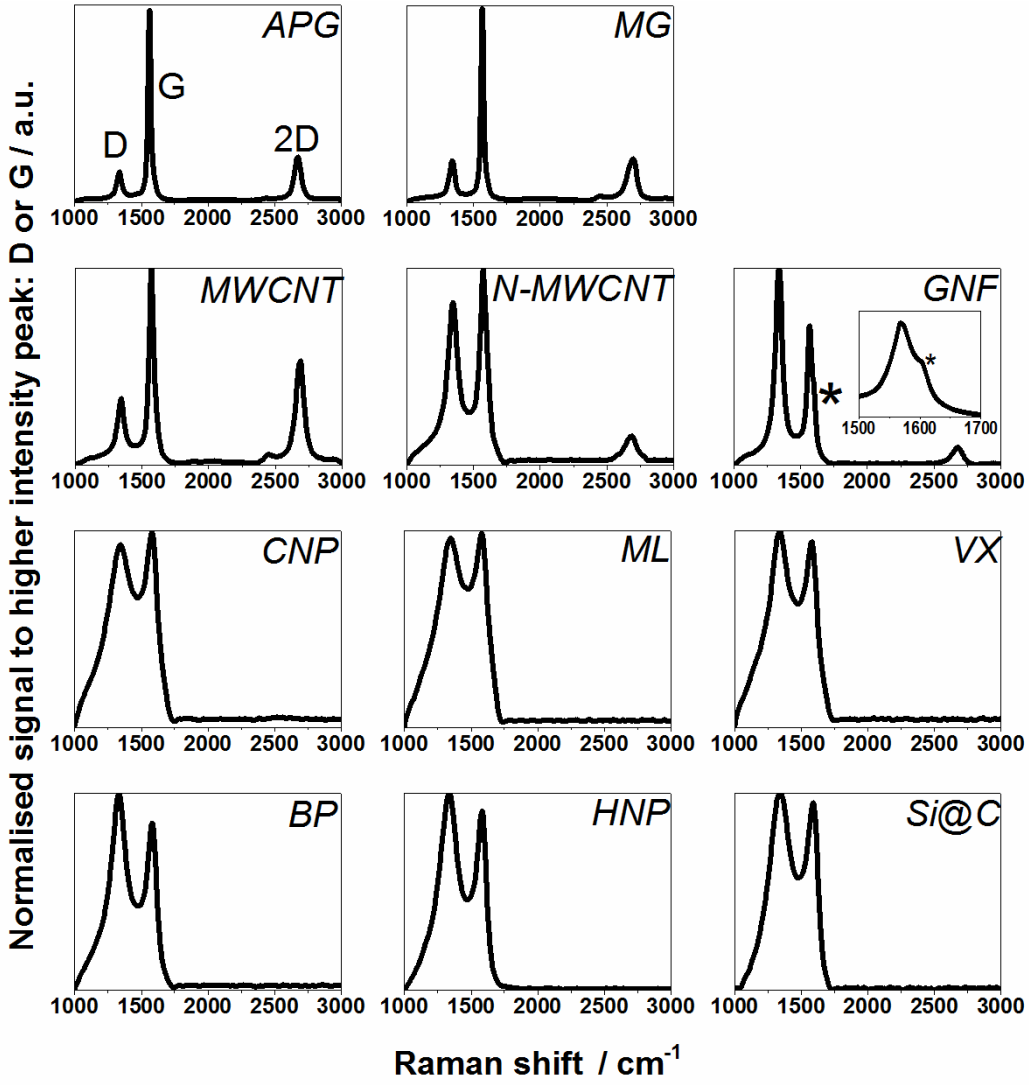

Figure 3.5. Raman spectra of all 11 carbon samples investigated confirming the graphitic and rather amorphous nature of individual materials respectively. The * marks the D′ shoulder on GNF (see also the inset).

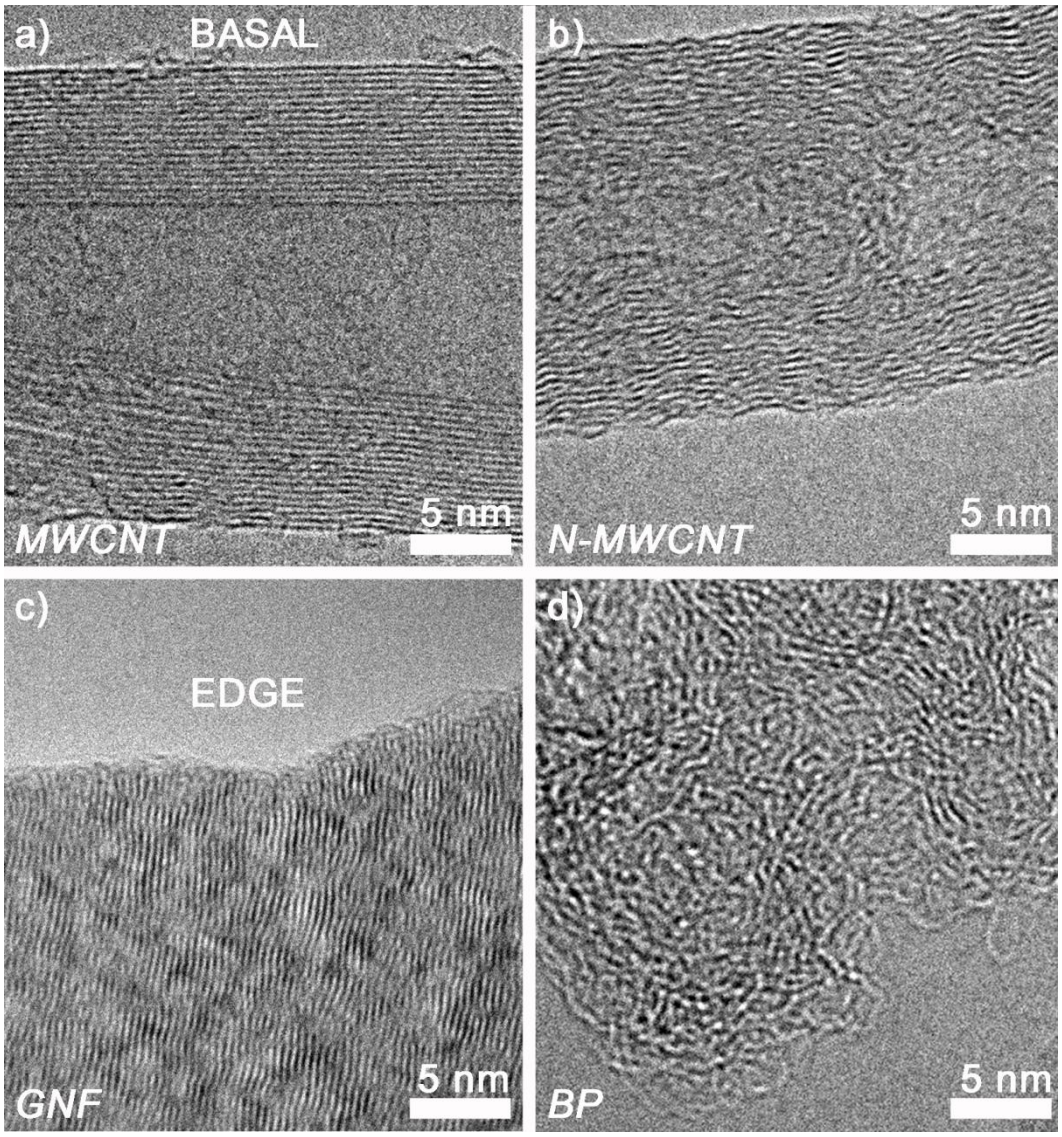

Figure 3.6. HRTEM images revealing the surface morphologies of (a) MWCNT, (b) N-MWCNT, (c) GNF and (d) BP. ***With the courtesy of Antal A. Koós, Department of Materials, University of Oxford.***

3.3.1.3. Nitrogen adsorption porosimetry: porosity and surface area

The surface area and porosity of the materials were assessed by nitrogen adsorption [205]. Results are shown in **Figure 3.7** and summarised in **Table 3.1**. The observed porosity results from two factors: the surface properties of the material itself but also from aggregation of the carbon particles leading to porous networks in the material powder. APG, MG, MWCNT, N-MWCNT, GNF, CNP, ML and VX all display a type II

isotherm. This is an isotherm concave to the pressure axis, since at relative pressure 0 the volume of gas adsorbed must be 0. The isotherms also display a B point [205] marking the beginning of a linear relationship between adsorption and relative pressure. The presence of the type II isotherm is indicative of predominance of rather large pores: macropores with diameter greater than 50 nm. Pores in this size range are likely to be due to aggregation of the materials which can also be seen in the SEM and TEM images in **Figure 3.1** and **Figure 3.3**. Fitting the isotherms according to the BET model gives a specific surface area lower than 100 m^2 g^{-1} for APG, MG, MWCNT, N-MWCNT and GNF. In contrast, CNP, ML and VX have a specific surface area between 100 and 250 m^2 g^{-1}. Thus the plate-like and fibre-like particles fall into a lower surface-area range, consistent with the larger sizes of these materials. APG displays a pronounced H3 hysteresis: the desorption isotherm does not follow exactly the adsorption isotherm at high relative pressure, **Figure 3.7a**. GNF and CNP show a less pronounced H3 hysteresis, as evident from the enlargement of part of the isotherm in **Figure 3.7b**. The combination of a type II isotherm and presence of H3 hysteresis is designated as a type II(b) isotherm [205]. A type II(b) isotherm is usually observed in powders and aggregates, and thus is consistent with the nature of these materials.

The nitrogen adsorption isotherm for BP, HNP and Si@C differs slightly from the previously described type II isotherms. A more pronounced plateau at high relative pressure is observed. This is indicative of a type I isotherm reflecting the presence of micropores (pore diameter less than 2 nm). The Langmuir model is more suitable to fit the data for materials with micropores than the BET model [205]. For the three materials the better fit of the Langmuir model to the data is then consistent with the presence of micropores. The specific surface area of these materials is greater than 300 m^2 g^{-1} (as determined from the Langmuir model). Values obtained from the BET model are also

included in **Table 3.1** for comparison. HNP and Si@C show evidence of H4 hysteresis as shown in **Figure 3.7b**. This behaviour is usually associated with activated carbons and materials displaying slit-shaped pores especially in the micropore range [205]. This is also consistent with the better fit of the Langmuir model for data from HNP and Si@C.

The previous type II and I isotherms do not indicate a strong mesoporous structure. However, all materials have some degree of mesoporosity. Overall, apart from Si@C, all materials have a more pronounced mesoporous structure than APG as observed on the pore size distribution reported in **Figure 3.8**. Most of the porosity in the range 2-20 nm is due to pores of size larger than 5 nm. Also, for APG, MWCNT, N-MWCNT, MG, GNF, CNP, BP and Si@C, a portion of pores with size slightly lower than 5 nm accounts for a slightly higher population of pores. To simply quantify the mesoporosity of the materials, a convenient estimation of the average size of pores in a material can be inferred by dividing the pore volume (V) in the material by the surface area (A) of the material. Assuming the pores can be modelled by perfect cylinders, the average pore diameter is equal to $4V/A$ [205]. All materials have to some extent a mesoporous structures and mesoporous volume (**Table 3.1**). For all materials considered in this study, the average mesopore size is within the range 3.5 to 9 nm, although pores of smaller and larger diameter can also be found in the materials. This is a range that should be accessible to hydrogenase molecules which are *ca.* 5 nm in diameter. The materials with smallest average pore size (< 4 nm) are the synthesised materials HNP and Si@C.

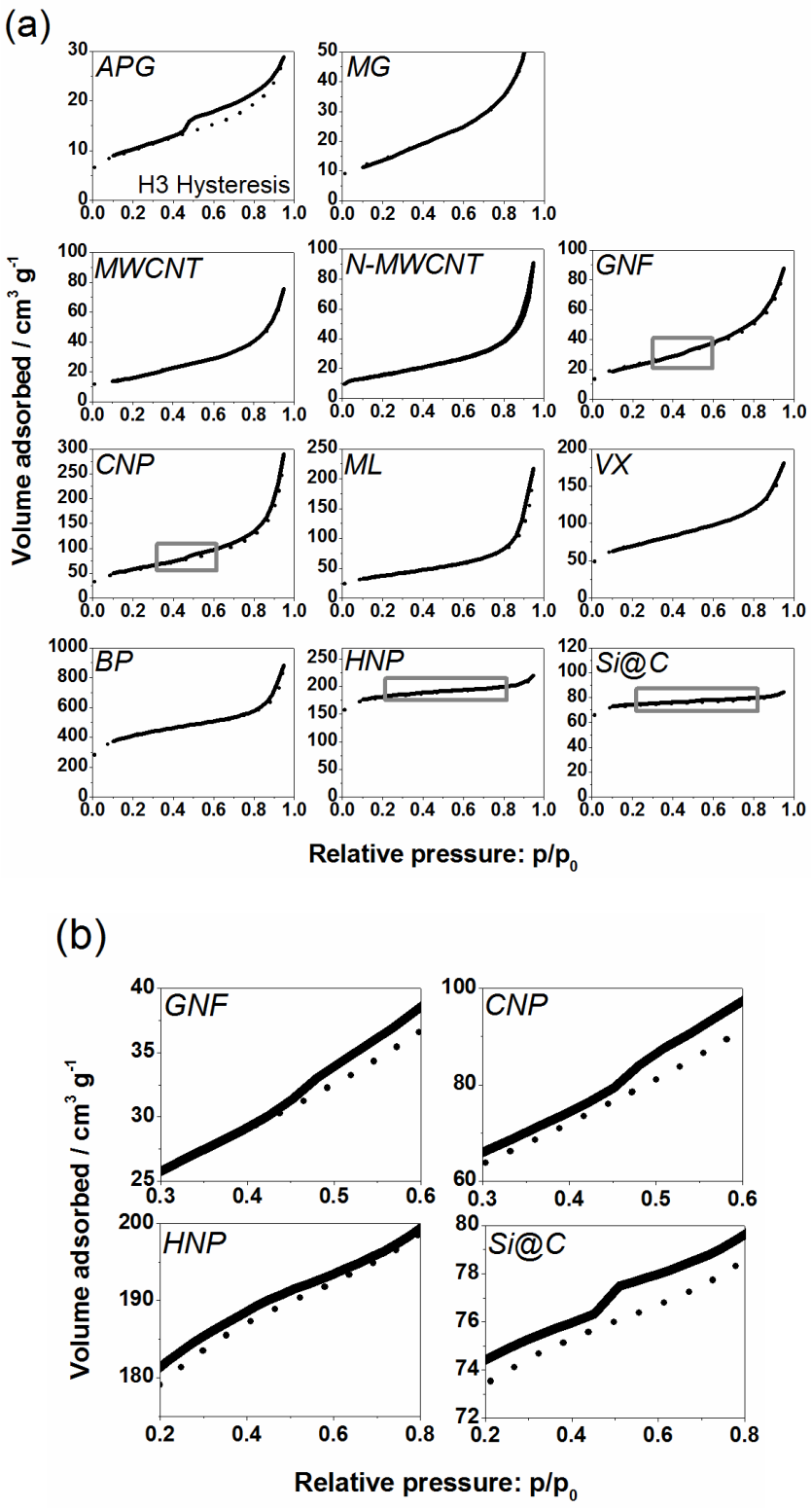

Figure 3.7. (a) Nitrogen adsorption (dotted) and desorption (solid) isotherms at 77 K for each carbon material investigated. Grey boxes indicate the part of the isotherm which is enlarged in panel (b) for GNF, CNP, HNP and Si@C to highlight the H3 hysteresis for GNF, CNP, and the H4 hysteresis observed in the HNP and Si@C samples.

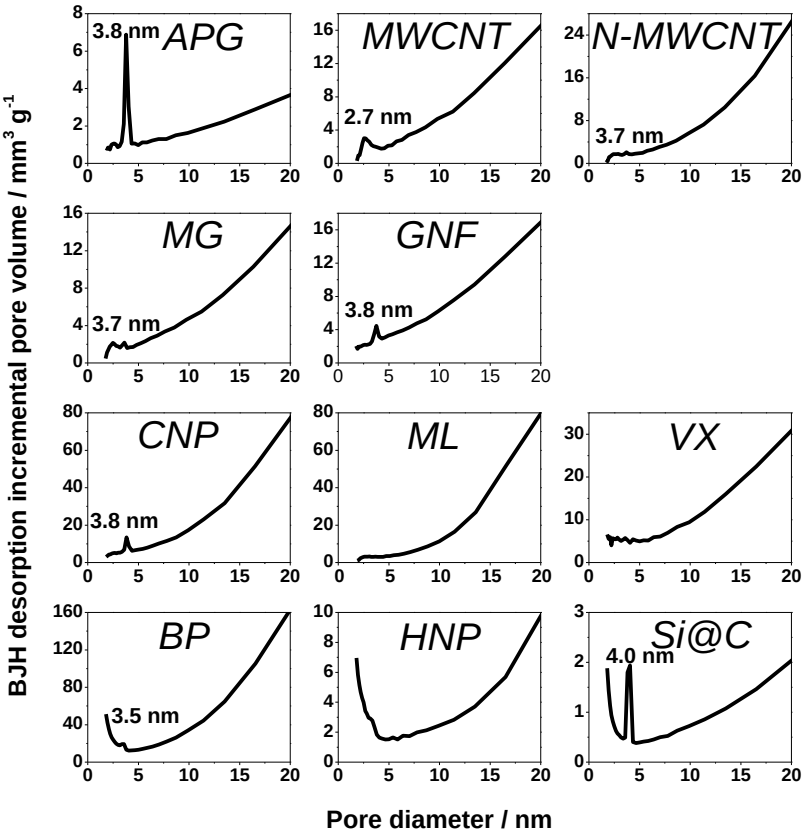

Figure 3.8. Pore size incremental pore volume obtained from nitrogen desorption isotherms at 77 K for each carbon material investigated.

3.3.2. Immobilised hydrogenase electrocatalytic activity on various carbon electrodes

The materials characterised in **Section 3.3.1** have a higher specific surface area than APG and a more pronounced mesoporous structure (**Table 3.1**). They were then investigated to develop high surface area electrodes for Hyd-1 immobilisation. The electrochemical set up used, protocol for enzyme immobilisation and electrochemical measurements performed are detailed in **Section 2.4**. Since hydrogenases are biological catalysts, there are sensitive to various parameters like temperature or pH. These parameters were controlled during electrochemical assessment by using buffers and a water jacketed electrochemical cell. However, the activity of hydrogenases can also vary from a batch of enzyme to another and from one day to another as an enzyme sample

ages. To ensure the observations made are reproducible, 6 sets of experiments were performed on different days. Each day, all materials were assessed using a same batch of hydrogenase. The results presented summarise the trends confirmed with these 6 sets of experiments.

3.3.2.1. Hydrogenase electro-activity on various carbon materials

A typical cyclic voltammogram for Hyd-1 adsorbed onto a rotating disc electrode (RDE) made of pyrolytic graphite with the edge surface exposed (PGE) is reported in **Figure 3.9a**. This represents the relation between electrochemical current and potential during cyclic voltammetry experiments. For these experiments the electrochemical potential is varied as a linear function of time while the current from the electrocatalytic activity of the enzyme is recorded (**Section 2.4**). The electrode is immersed in buffered aqueous solution (pH 6.0) equilibrated with 1 bar H_2 (*ca.* 0.8 mM). Hyd-1 does not show significant activity for proton reduction under a H_2 atmosphere [210], so no catalytic current is observed at potentials more negative than -0.3 V *vs* SHE: the current with (black) or without (grey) enzyme is the same below -0.3 V in **Figure 3.9a**. At higher potentials a clear oxidative catalytic wave is observed in the presence of the enzyme only. This corresponds to the oxidation of H_2 to H^+ catalyse by the immobilised hydrogenase. A current of *ca.* 0.095 mA cm^{-2} is reached around +0.24 V *vs* SHE. No catalytic current is observed under H_2 for a bare electrode (grey) without enzyme adsorbed and no current is observed for an electrode with immobilised enzyme without H_2. Each cycle of catalytic turnover by a molecule of hydrogenase leads to electron flow into the electrode. Therefore the catalytic current is directly proportional to the number of electro-active enzyme molecules, provided that the current is not limited by availability of H_2 to the enzyme [100]. The electrode is rotated rapidly (2000 rpm) to maintain the H_2 concentration at the electrode surface close to that in the bulk solution.

Hyd-1 exhibits an onset potential for H_2 oxidation just positive of -0.3 V. This is consistent with the slight overpotential requirement (50-60 mV) of this enzyme relative to the $E(H^+/H_2)$ potential at 1 bar H_2 [210]. The thermodynamic potential for $E(H^+/H_2)$ under the experimental conditions is indicated by a vertical line in **Figure 3.9**. The residual slope in the cyclic voltammogram at higher potentials is characteristic of immobilised enzyme electrocatalysts engaged in a direct electron transfer with the electrode (DET, **Section 1.2.2.2**). This has been explained by a dispersion of orientations of the enzyme on the electrode leading to a range of electron transfer rates [47]. A similar waveshape, although with higher electrocatalytic current of about 0.35 mA cm^{-2} at +0.24 V *vs* SHE, is obtained for Hyd-1 adsorbed on plate-like APG particles deposited onto the RDE, **Figure 3.9b**. This is consistent with an earlier report in which Hyd-1 on APG was deposited on a RDE in a Nafion binder [63]. By achieving a higher electrocatalytic current than on the PGE-RDE, this illustrates the advantage in developing 'high surface area' electrodes made of high specific surface area carbon materials. It is also shown that using a binder is not necessary.

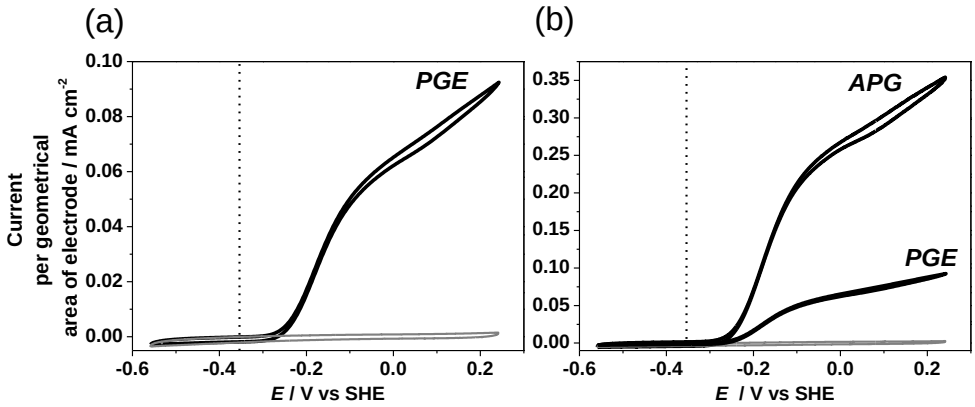

Figure 3.9. Cyclic voltammograms of Hyd-1 (a) adsorbed directly on a PGE-RDE and (b) on APG deposited on the RDE. The results presented in (a) are also reported in (b) for comparison. The electrode was rotated at 2000 rpm in pH 6.0, 100 mM KPB under 1 bar H_2 at 25 °C. The dotted vertical lines mark the thermodynamic potential of H^+/H_2 couple under the conditions of the experiment. The grey voltammograms are obtained under identical conditions with no hydrogenase deposited on the RDE.

In order to assess the benefit of alternative materials to APG an equal amount of each material, modified with Hyd-1, was deposited onto a PGE-RDE. The associated catalytic current in solution equilibrated with H_2 was recorded by cyclic voltammetry and results are reported in **Figure 3.10**. Electrodes were prepared by drop-casting 0.5 µL of a 20 mg mL^{-1} dispersion of the hydrogenase-modified particles onto a PGE-RDE of surface area 0.02 cm^2. Thus the current per geometric area of electrode is directly proportional to the current per gram of material. All of the carbon materials give an increase in catalytic current per geometrical area of the electrode relative to Hyd-1 on a bare pyrolytic graphite electrode, **Figure 3.9a**. A significant increase in current is observed for the commercially available carbons, BP, VX, ML and CNP which have a high surface area and more pronounced mesoporosity (**Table 3.1**). However, in each case the shape of the cyclic voltammogram for those materials yields a plateau at high potentials. This is characteristic of a film in which H_2 is not efficiently provided to the enzyme. The current is then severely mass transport limited. BP is the material with the highest specific surface area and with the most pronounced mesoporous structure in this study. It is demonstrated with this material that mass transport can be improved slightly by increasing the electrode rotation rate at 5000 rpm: see the dashed line in **Figure 3.10** for BP. However the plateau remains and further increase in rotation rate to 7000 rpm (not shown) provides negligible improvement in current since the plateau shape is still present. This suggests that fast rotation fails to provide efficient mass transport *through* the particle film to buried hydrogenase molecules. The mesopores, with an average diameter in the range 3.5 – 9 nm (**Table 3.1**) for all materials used in this study, are of similar dimension to Hyd-1 which has a diameter of roughly 5 nm. This is advantageous since the mesoporous network should be accessible to Hyd-1. Enzyme molecules inside the pores are likely to be almost completely surrounded by carbon. This favours hydrogenase immobilisation so that the majority of

molecules have a good contact with the carbon surface and can thus engage in DET (**Section 1.2.2**). Unfortunately these films of particles are mass transport limited. In parallel to the increasing use of nanomaterials to develop hydrogenase electrode, mass transport limitation at mesoporous carbon electrodes modified with hydrogenase has been stressed recently in the literature [85]. This severe limitation to fully exploit the electrocatalytic activity of hydrogenase is further addressed in a later section.

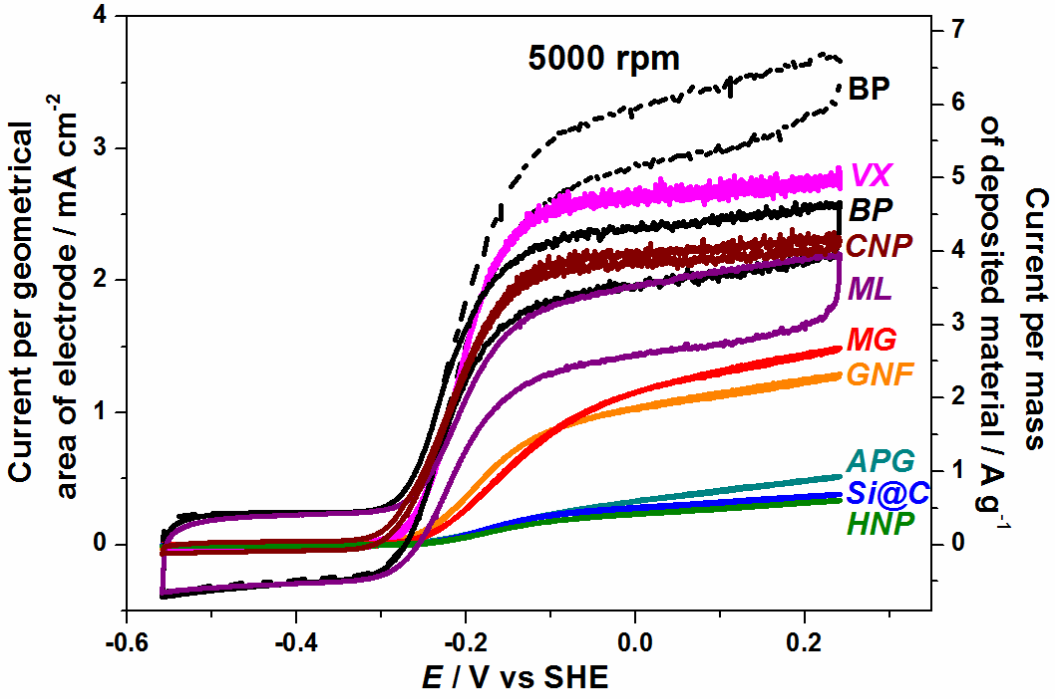

Figure 3.10. Cyclic voltammograms of Hyd-1 adsorbed on various carbon materials in 100 mM KPB, pH 6.0, 25 °C, equilibrated with 1 bar H_2. Materials were deposited on a 0.02 cm^2 PGE-RDE, and the electrode was rotated at 2000 rpm. The left hand axis shows the current normalised to the geometric area of electrode and the right hand axis indicates the current per gram of deposited carbon material. In all cases 0.5 µL of 20 mg mL^{-1} dispersion of carbon material with adsorbed enzyme were deposited on the RDE. The current associated with BP material is reported at 2000 rpm (BP solid line) and 5000 rpm (BP dashed line).

Before addressing the limitation in the electrocatalytic current achieved due to ineffective mass-transport, it is important to establish first that the carbon materials do not impair or alter the hydrogenase activity. This requires comparing the hydrogenase electro-activity under non-mass transport limited conditions for all materials. For CNP, VX, ML and BP, to obtain conditions that are not limited by mass transport at the PGE-RDE, the particle dispersions were diluted to 5 mg mL^{-1}, applying 0.5 µL to the PGE-RDE. Results are shown in **Figure 3.11**. Also shown on this figure are MWCNT and N-MWCNT samples modified with Hyd-1. The difficulty in dispersing the relatively hydrophobic nanotubes in water means that the mass of nanotubes deposited cannot be controlled reliably. Therefore the absolute current is not comparable with the other materials. However the shape of the cyclic voltammograms still indicates whether the hydrogenase can be immobilised on the materials. The catalytic waveshapes in voltammograms recorded under conditions where mass transport is not significantly limiting, **Figure 3.11**, are very similar to the well-characterised waveshape reported for Hyd-1 adsorbed on a PGE electrode, **Figure 3.9a**. Importantly, the onset potential for H_2 oxidation is independent of material, showing that interfacial electron transfer to and from hydrogenase molecules is effective on each carbon material. The residual slope in the electrocatalytic voltammogram at high potential is similar for each material, **Figure 3.11**. This suggests that there are not significant differences in the distribution of orientations of Hyd-1 [47]. The results demonstrate that the eleven carbon materials selected in this study are suitable for adsorption of Hyd-1 in an electro-active configuration. This suggests that most conductive carbon-based materials are likely to be a relevant candidate to develop an electrode for hydrogenase studies or applications.

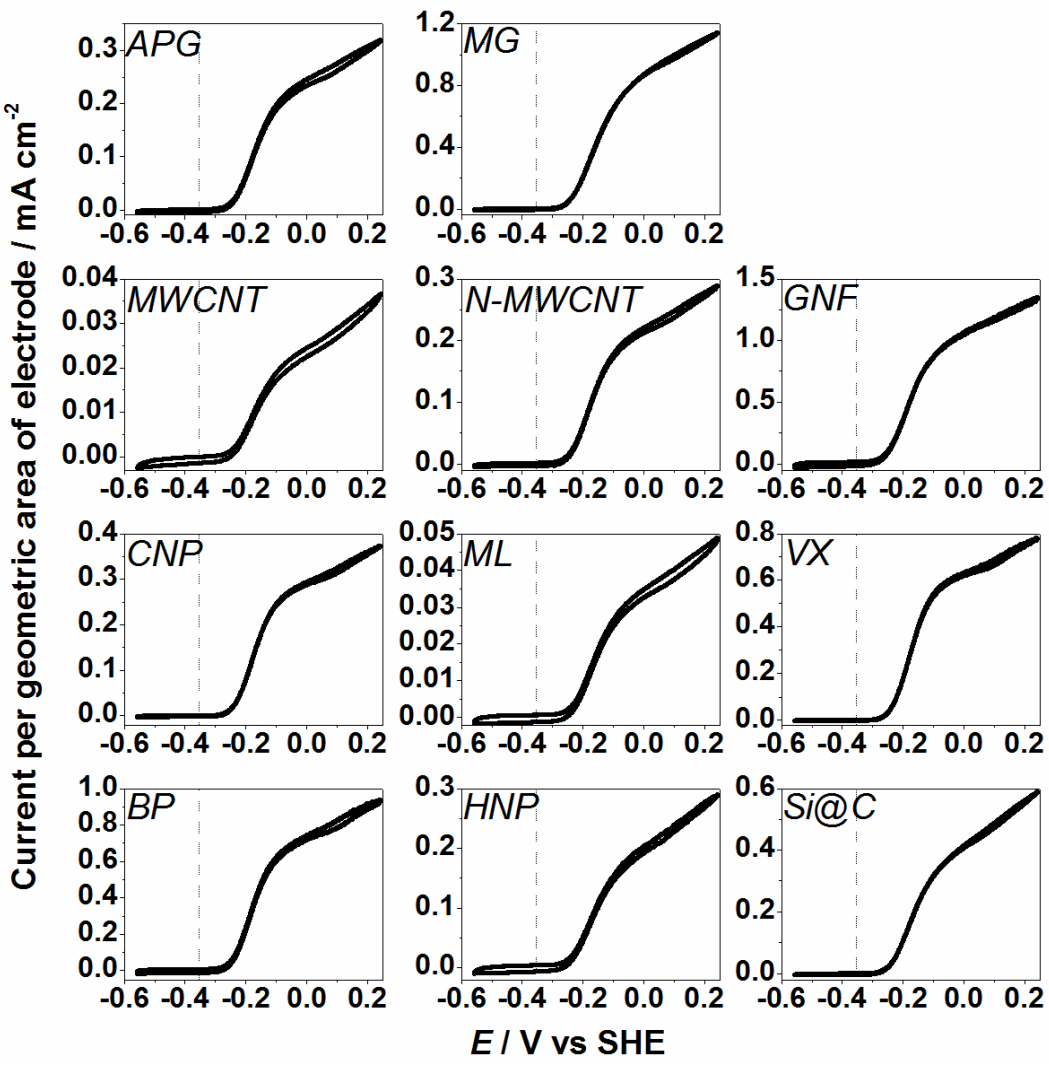

Figure 3.11. Cyclic voltammograms of adsorbed Hyd-1 on the various carbon materials deposited onto a PGE-RDE, in 100 mM KPB, pH 6.0, 25 °C, equilibrated with 1 bar H_2. Dilution of the dispersion of certain particles (CNP, ML, VX and BP, see text) means that currents are not significantly mass-transport limited. The dotted lines mark the thermodynamic potential of the H^+/ H_2 couple under the experimental conditions.

3.3.2.2. Overcoming mass transport limitation

It is now established that on all the carbon materials selected the hydrogenase can be adsorbed in a configuration that allows DET. The advantage conferred by using one material compared to another to develop high surface area electrodes can then be investigated further. High currents per gram of material with Hyd-1 adsorbed on

commercial carbon blacks (BP, VX, ML and CNP) are promising for fuel cells. However, the mass transport limitation observed for CNP, ML, VX and BP in **Figure 3.10** is likely to be a problem for realistic applications of hydrogenase electrocatalysis. The current reached could be higher provided that mass transport can be addressed. Hyd-1 activity on BP was therefore investigated in a flow electrochemical cell configuration where mass transport can be improved. The flow cell used is equivalent to the spectroelectrochemical cell described in **Section 2.5**. The electrolyte is continuously flowed through the cell at approximately 2000 cell volumes per second which ensures non-mass transport limited conditions. In **Figure 3.12**, scans (a) and (b) were recorded at a PGE-RDE, whereas scan (c) was recorded with the same amount of material in the flow-cell. At high potentials a higher current is reached in the flow-cell and the plateau is absent. This suggests that mass transport to enzyme molecules in the particle film is no longer significantly limiting the current. The hydrogenase adsorption was performed with a 0.02 mM solution of Hyd-1 and incubated with the particle overnight at 4 °C (**Section 2.4.5**). In order to test whether enzyme loading on BP could be improved by longer adsorption times from more concentrated enzyme solution, an electrode was prepared in the flow-cell using particles that had been incubated with 0.2 mM Hyd-1 for 48 hours at 4 ^{o}C, scan (d). In this case an improved current per mass of material of 12 A g^{-1} (at +0.24 V *vs* SHE) was recorded. This is about twice the current recorded at the same potential in the flow cell configuration with less concentrated enzyme and shorter incubation time (c).

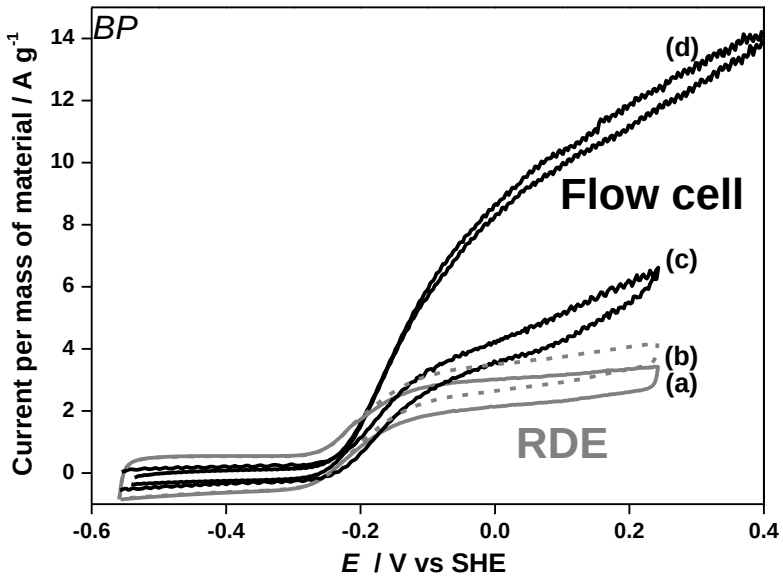

Figure 3.12. Cyclic voltammograms of Hyd-1 adsorbed on BP assessed on a PGE-RDE (grey) at (a) 2000 rpm or (b) 5000 rpm; and cyclic voltammograms for the same quantity of BP studied in a flow cell configuration (with H_2-saturated solution flowing at 50 mL min^{-1}) for (c) the same set of particles as (a) and (b); and (d) for particles prepared with longer adsorption time (48 hours) from more concentrated Hyd-1 solution (0.2 mM). All were prepared by deposition of BP (1 µL) from a 20 mg mL^{-1} suspension.

Slow diffusion of Hyd-1 into the mesoporous network of BP will lead to very long equilibration times for adsorption of the enzyme. Restricted or hindered diffusion of macromolecules through pores of a similar diameter is a well-documented phenomenon [222] and is the basis of size exclusion chromatography. Hyd-1 is a particularly robust hydrogenase, and for some biological electrocatalysts it would be unfeasible to allow such long adsorption times due to protein degradation. An important observation is that the electrocatalytic current for BP in the flow cell with longer adsorption time for Hyd-1 exceeds that obtained for the initial particle preparation at all potentials during H_2 oxidation, **Figure 3.12**. This implies that a significant amount of enzyme can adsorb within the mesopores of the material where efficient mass transport of H_2 becomes

particularly important for efficient catalysis. Templated ordered mesoporous carbons and other inorganic materials have been developed specifically for the adsorption of enzymes in biotechnology. However they usually involve a sacrificial template, multi-step synthesis, and may display relatively poor conductivity [223, 224]. The success of Hyd-1 adsorption on BP shows that it is possible to make use of readily available carbons with some degree of mesoporosity for enzyme electrocatalysis. Once mass transport limitation is addressed, BP which is the material with the highest specific surface area in the panel of materials selected, is the material leading to the highest recorded electrocatalytic current in this study.

3.3.2.3. Promoting higher hydrogenase loading with graphitic materials

An important parameter to consider after the magnitude of the electrocatalytic current is how efficiently the material accommodates the hydrogenase. Assessing how much of the surface available is actually used by the enzyme is important to establish in order to further optimise hydrogenase electrodes. In the voltammograms of **Figure 3.10**, electrodes formed from larger or less mesoporous particles, such as APG, MG and GNF show less evidence of mass transport limitation. The relative currents per mass of material are also lower. **Figure 3.13** shows the voltammetric data from **Figure 3.10** recalculated to show the current density with respect to the BET surface area of each electrode made of the various materials. **Figure 3.13** then gives an indication of how effectively the total surface area of each electrode is being used for electrocatalysis. In this case the highest current densities occur for electrodes made of materials with larger size or with lower specific surface area.

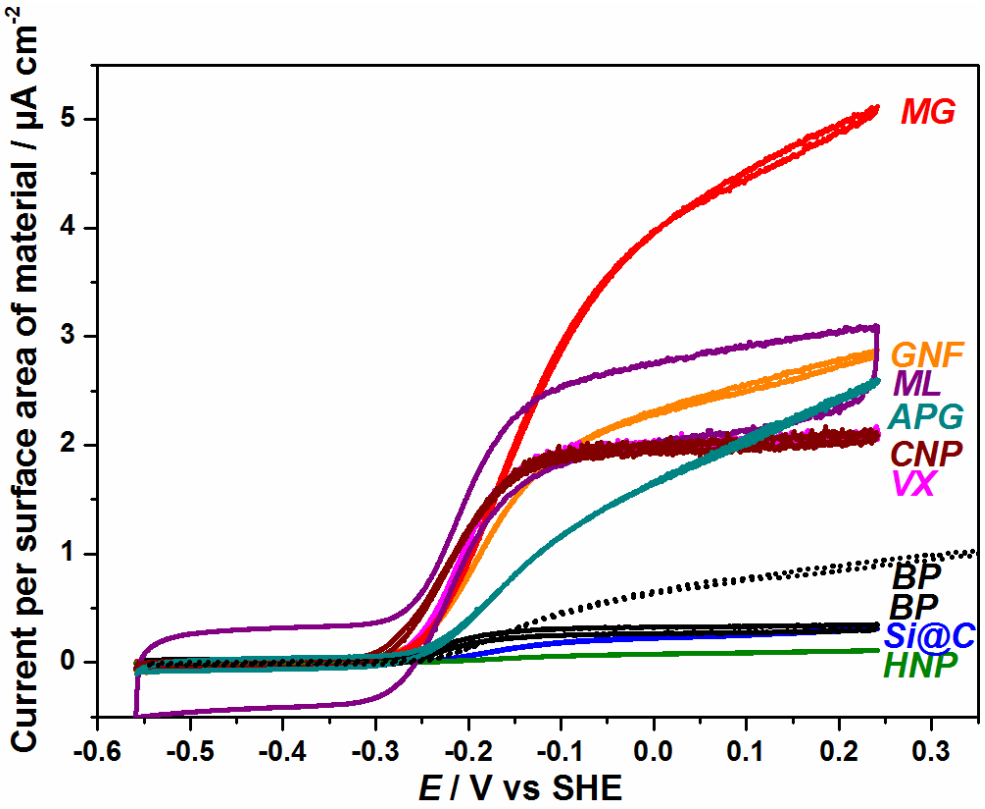

Figure 3.13. Voltammetric data from Figure 3.10 reported as current per surface area (BET) of material. For comparison, the scan obtained in the flow-cell configuration cell from Figure 3.12(d) is also reported (dotted BP voltammogram).

It is noted than even after improving mass transport to Hyd-1 on BP by use of a flow cell, the high surface area of the material is clearly being under-utilised compared to other materials. This is displayed as a dashed line in **Figure 3.13**: only a current per surface area of material of 0.9 µA cm^{-2} (at +0.24 V *vs* SHE) was obtained with BP in a flow cell configuration, whereas MG gives a current of 5.1 µA cm^{-2} (at +0.24 V *vs* SHE). Also APG and GNF, despite a lower surface area and lower degree of mesoporosity relative to BP, compare more favourably with the other materials when evaluated on the basis of current per surface area of material used to develop the electrode. This suggests that the surface of these materials is used more efficiently for electrocatalysis. This is probably due to a more graphitic structure (**Figure 3.5**) and the presence of graphitic 'edge' surfaces in MG, APG and GNF. This observation is in line with the successful use

of PGE electrodes for protein film electrochemistry on a range of proteins [35]. As stressed in **Section 1.2.2**, materials tailored to express edge-like surface as such as carbon nanofibers, have been reported only recently by Lojou and co-workers in view of improving enzyme loading [85]. The counterpart of this material in the present study is GNF. The data provided in the report by Lojou and co-workers makes it possible to estimate a maximal current density of *ca.* 3 µA cm^{-2} for the hydrogenase electrocatalytic current per surface area of electrode made of carbon nanofibres. This is comparable with the value obtained here with the commercially available GNF at +0.24 V *vs* SHE. However the results reported by Lojou's group were obtained with a different enzyme, experiments were run at 60 °C and the material was thermally treated to increase its surface area [85]. This makes any detailed comparison between the material used by Lojou and co-workers and the as-received GNF used here difficult. This is a common difficulty in comparing results from one study with another in the literature. It is then challenging to conclude on the benefit of one carbon electrode compared to another (**Section 1.2.2.6**). The benefit of the present study is to compare the same enzyme on different materials under equivalent experimental conditions. With this approach, it can be firmly established that among all the materials selected, MG gives higher current per surface area of material than GNF and all other materials. MG appears as the material in this study for which the carbon surface of the electrode is used the most efficiently by Hyd-1. This is an important result. It stresses that a simple sonication method (**Section 2.2.1**) leads to a material with a micron size and with improved enzyme loading. This is important to further develop efficient high surface area electrodes in devices like enzyme fuels-cells.

Another option to compare the results presented in this thesis to the literature would have been to assess Hyd-1 electrocatalytic activity under the experimental conditions used by Lojou and co-workers for instance. To attempt this, Hyd-1 was assessed at 60 °C. It was

surprisingly observed that currents up to eight times higher (**Figure A7**, **Figure A8**) than the one presented in this study performed at 25 °C could be achieved with different carbon material used as electrodes. Also the enzyme is stable for time of at least 10 hours under continuous operation at 60 °C. This unexpected behaviour stresses that Hyd-1 is temperature resistant. These results are not detailed further in this thesis because Hyd-1 is in fact so stable that the nature of the carbon material does not seem to influence the temperature resistance. This observation put the result presented in the context of realistic applications in enzyme fuel cells. This also stresses the need for a better understanding of the hydrogenase activity. To understand this unexpected behaviour, the coupling of IR spectroscopy and electrochemistry is a useful technique to develop. This can be done by careful carbon material design as detailed in **Section 3.3.3**.

3.3.2.4. The specific case of MWCNTs

CNTs have been intensively used in the development of hydrogenase electrodes [8]. Attractive features of MWCNTs or N-MWCNTs are the opportunity to develop relatively high surface area electrodes with a mesoporous network (**Table 3.1**, **Figure 3.1**). It is established here that direct adsorption of Hyd-1 is possible on MWCNTs and for the first time on N-MWCNTs, **Figure 3.11**, but their dispersion in aqueous solution is challenging due to their intrinsic hydrophobicity. A slight improvement in dispersion is observed with N-MWCNTs compared to MWCNTs. However it is still difficult to make accurate comparisons of electrocatalytic current per mass of material used as electrode. It might be expected that the defects and heteroatom sites brought by nitrogen incorporation within the carbon lattice in N-MWCNTs (**Figure 3.6b**) should offer anchor-points for specific attachment of enzymes. However, this is beyond the scope of the present study. A common concern on the use of MWCNTs for biology-related applications is the presence of residual iron impurities in the samples [24]. Interestingly,

despite presence of iron impurities in the MWCNTs and N-MWCNTs samples obtained by AACVD [191], no further treatment of the as-produced nanotubes was necessary in this study. This is because presence of iron did not impair the electro-activity of the hydrogenase and did not lead to complication in the interpretation of the electrochemical behaviour of the enzyme, **Figure 3.11**. It can be concluded that as-synthesised CNTs are then suitable for hydrogenase adsorption. This observation is encouraging to use as-synthesised MWCNT forests rather than dispersed MWCNTs. First, using MWCNT forests avoid the challenging dispersion of MWCNTs in aqueous solutions. Second, direct growth of MWCNTs on substrates offer opportunities to design scaffolds for enzyme catalysis that none of the other materials studied could offer. This will be fully exploited in **Chapter 4** and **Chapter 5**.

3.3.2.5. Tailored carbon materials for specific hydrogenase applications

The results presented also show that the successful adsorption of hydrogenase is not limited to commercially available materials. This opens the scope of applications of hydrogenase to areas where dedicated carbon supports are required. HNP and Si@C are examples of materials that can be tailored to accommodate hydrogenases for specific purposes, despite having a microporosity rather than mesoporosity (**Table 3.1**). HNP material can be obtained by the versatile and simple hydrothermal synthesis: a green synthetic route using glucose (a renewable feedstock) as starting material. It requires readily-available laboratory equipment (**Section 2.2.2**) to obtain materials as diverse as particles [225], hollow spheres [198], graphitic plates [226], porous carbon networks [227] and nanoporous structures [228]. The HNP with a high specific surface-area (816 m^2 g^{-1} according to the Langmuir model results, **Table 3.1**) has also been demonstrated in various electrochemical devices [201, 229]. It is then a promising platform for further bio-electrocatalysis. Si@C particles have an IR transparent silicon core but a sufficiently

conductive outer carbon shell (10 to 20 nm) to support enzyme adsorption and electrocatalysis. Therefore Si@C may have interesting applications as an electrode material for coupling *in situ* ATR-IR spectroscopy and electrochemistry as discussed below.

3.3.3. Towards an efficient coupling of electrochemistry and ATR-IR spectroscopy for study of immobilised redox species on carbon materials

Promising results were obtained in **Section 3.3.2** to guide the development of high surface area electrodes for hydrogenase immobilisation. If the material used as electrode has a high specific surface area, high electrocatalytic current from the immobilised enzymes can be obtained. If the materials show a high degree of graphitisation, the hydrogenase loading on the electrode made of this material can be improved. In this section, another property is more specifically exploited: the size of the carbon materials. For a better understanding of the function of hydrogenases, new techniques of investigation are required and coupling IR spectroscopy to protein film electrochemistry (detailed in **Section 1.2.3**) is a promising tool to develop [105]. The coupling can be achieved in an ATR configuration by building an electrochemical cell on top of a silicon prism (detailed in **Section 2.5.1**). This allows control over the electrochemical activity of the hydrogenase, at the same time IR spectroscopic data can be acquired. Previously, promising results have been obtained with this approach on carbon materials like APG and VX to study hydrogenase activity [103, 104]. However the enzyme was immobilised with a polymer binder in the particle network. This does not guarantee that the signal recorded was obtained from truly adsorbed enzymes. It could come from enzyme in solution or trapped into the conductive binder.

To investigate only immobilised species in direct electrochemical control and discard any influence of the binder in the results, carbon only electrode must be developed for this

technique. The challenge comes from the use of evanescent waves to acquire IR data from species adsorbed on carbon materials in an ATR configuration. These evanescent waves have a limited penetration depth of roughly 1 µm into the sample for the experimental conditions of this study (**Section 1.2.3**). To acquire a stronger IR signal from species under electrochemical control immobilised on carbon materials, a large amount of these species should ideally sit within 1 µm of the prism surface. The coupling of ATR-IR spectroscopy and electrochemistry is then expected to be facilitated by using sub-micrometre materials to create the carbon electrode. A range of nanomaterials were shown to effectively immobilise hydrogenase in **Section 3.3.2**. They were then investigated to perform IR spectroscopy of immobilised species under electrochemical control. The test molecule flavin mononucleotide (FMN) which is cheaper and easier to obtain than Hyd-1, was first used as proof of concept before moving to hydrogenase studies. A milestone would be to record data from directly adsorbed redox species on carbon materials.

3.3.3.1. Flavin mononucleotide as a test molecule

Flavin mononucleotide (FMN) is a molecule found in enzymes and biological structures, **Figure 3.14**. Therefore FMN, and other flavin based compounds, have been considered for bio-related applications [230]. However it is selected for this study for other reasons. First it is electrochemically active with clearly defined oxidised and reduced forms [231]. Second, it adsorbs strongly on carbon materials. Third, it has distinct IR spectra in the oxidised and reduced form with a pronounced feature around 1540 cm^{-1} in the oxidised state [230]. FMN is then a suitable test molecule for IR investigation of an adsorbed species under electrochemical control. FMN was adsorbed on all the eleven carbon materials presented in **Section 3.3.1** according to the procedure detailed in **Section 2.4.6**. To confirm that FMN adsorbs on the eleven carbon materials, electrochemical measurements and IR measurements in an ATR configuration without electrochemical control and without electrolyte (‘dry

particles') were performed. Presence of FMN was proved in all cases and for all materials as illustrated in **Figure 3.14** for HNP. In the absence of adsorbed FMN no redox behaviour (flat lines) was observed for either the PGE electrode (grey line) or HNP deposited on the PGE electrode (dashed line). After deposition of HNP with adsorbed FMN on the PGE electrode, the oxidation peak around -0.22 V *vs* SHE (positive current) corresponds to loss of 2 electrons and 2 protons from the reduced form of FMN to lead to the oxidised form. The reduction peak around -0.28 V *vs* SHE (negative current) corresponds to reversible reduction. A band around 1543 cm^{-1} in particular confirms by IR spectroscopy the presence of FMN on the dry particles after adsorption (inset of **Figure 3.14**). Similar results are obtained on the other materials. This is illustrated in **Figure 3.15** for electrochemical measurements on electrodes made of plate-like (APG and MG), tube-like (GNF) and particle like (Si@C) materials.

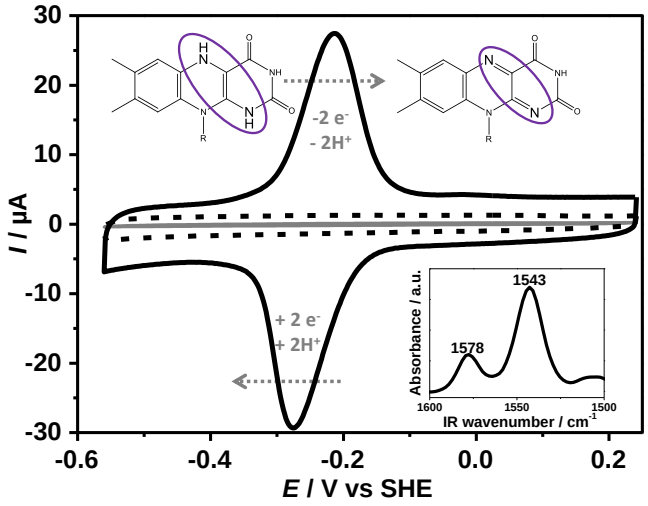

Figure 3.14. Cyclic voltammogram of FMN adsorbed on HNP (plain dark) deposited on a PGE electrode and associated molecular structure of the reduced and oxidised forms of FMN [R=CH_2-$(HCOH)_3$-CH_2-$HPO_4^-Na^+$]. Measurement performed in KPB 100 mM, pH 7, at a scan rate of 10 mV s^{-1}. Cyclic voltammograms of the bare electrode (plain grey) and HNP without adsorbed FMN (dashed dark) recorded under equivalent conditions are also reported. The IR signal from FMN adsorbed on dry HNP is reported in the inset: the peak at 1543 cm^{-1} in particular is characteristic of FMN.

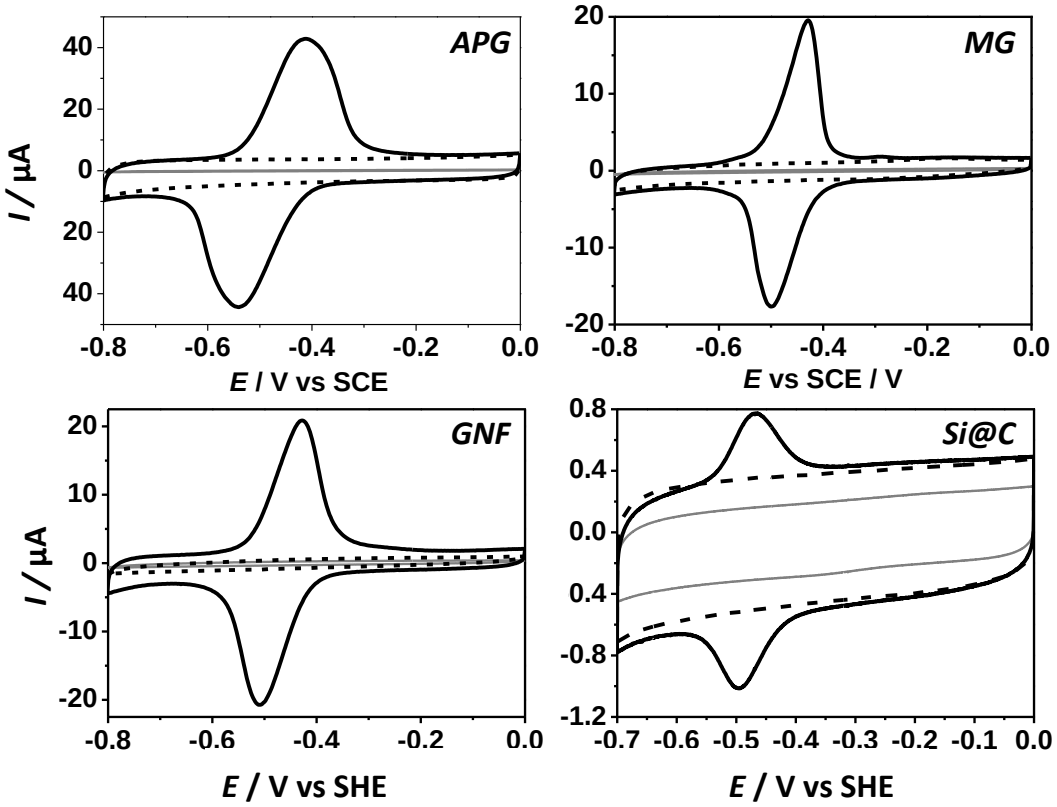

Figure 3.15. Cyclic voltammograms of FMN adsorbed on APG, MG, GNF and Si@C materials deposited on a PGE electrode (plain dark). Cyclic voltammograms for HNP without adsorbed FMN (dashed dark) and the bare electrode (plain grey) under equivalent conditions are also reported. Measurement performed in KPB (100 mM, pH 7) at a scan rate of 10 mV s^{-1}.

The oxidised and reduced forms of FMN have different bonds, circled in the isoalloxazine rings represented in **Figure 3.14**. In particular a C=C bond in the reduced form is not present in the oxidised form. These different bonds are characterised by different adsorption in the IR [232]. It should then be possible to observe a difference in the IR signal recorded for the oxidised or the reduced form of FMN. Transforming the adsorbed FMN into an oxidised or a reduced state is possible by chronoamperometry (**Section 2.4.3**). The spectroelectrochemical set up described in **Section 2.5** was used to assess if a change in IR signal between oxidised and reduced states could be observed. However, the experimental conditions to allow electrochemical control required an aqueous electrolyte. Therefore most

of the as-recorded IR spectrum is dominated by absorbance from water molecules. A possible way to overcome this issue is to report a *difference* of spectra taken at different potentials, which mathematically remove the water signal. It makes it possible to observe IR features that are changed by the electrochemical control. As-acquired spectra and the data processing are detailed in **Figure 2.20** in the experimental methods section. In **Figure 3.16**, the difference between IR spectra of FMN recorded in an oxidised state and spectra recorded in a reduced state are reported for a plate-like (MG), a tube-like (GNF) and a particle-like (HNP) material (**Section 3.3.1**). Negative features are IR signals related to the reduced form of FMN whereas positive features are related to the oxidised form (see **Section 2.5** for more details). Since the difference spectra are not flat, the results show that all types of materials studied allow the acquisition of IR spectra for adsorbed FMN under electrochemical control. However these results differ from one material to another as detailed in the next section.

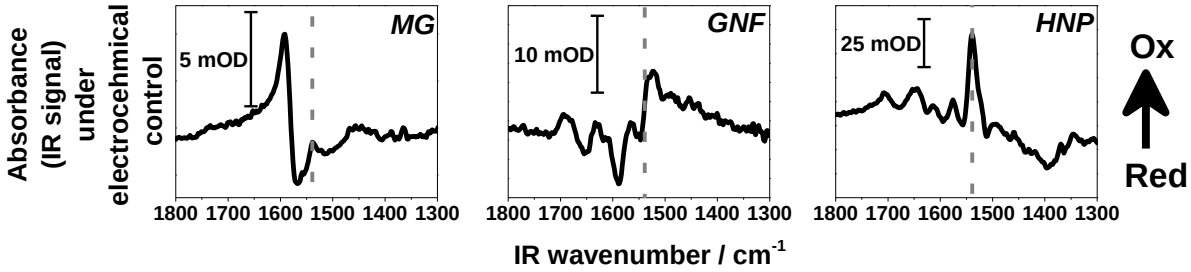

Figure 3.16. IR oxidised-*minus*-reduced difference spectra of FMN adsorbed on MG, GNF and HNP under electrochemical control. The reference (reduced) spectrum was taken at a potential of -0.49 V *vs* SHE. The most oxidising potential applied was +0.21 V *vs* SHE. The vertical grey-dashed line marks 1539 cm^{-1}.

Observing a signal from a difference spectrum is a first step to couple ATR-IR spectroscopy and electrochemistry of adsorbed species on carbon materials. To identify an optimal material other parameters are important. A second criterion is the reproducibility of the results. This was assessed by performing at least three independent experiments. A third criterion is to achieve a reversible electrochemical control. This should be the case with

FMN because the FMN redox couple is reversible as highlighted in **Figure 3.14**. Reversibility in the IR spectroelectrochemical experiments is confirmed by reporting several spectra on a same Figure, like in **Figure 3.17** which shows IR data for FMN adsorbed on MG under electrochemical control. A spectrum was taken at a reference potential: -0.49 V *vs* SHE. Another spectrum was taken at the same potential and is displayed at the bottom of the Figure in black. This spectrum is featureless confirming than no changes in the IR signal occurred which is consistent with the fact that the potential was not changed. This spectrum is then used as reference. A succession of potential steps was then performed by chronoamperometry and IR spectra recorded for each of the steps. The spectra recorded for each potential step are displayed offset from each other. The data acquired at the most oxidising potential compared to the potential used for reference are represented in red: +.0.21 V *vs* SHE in **Figure 3.17**. The sequence of electrochemical potentials was then performed in reverse order from this most oxidising potential (red) until reaching the first applied potential (reference potential, black). The succession of spectra from bottom to top in each Figure then corresponds to the chronological order of spectral acquisition. The spectrum displayed at the top of the Figure corresponds to a spectrum acquired at the final potential applied. This potential is the same as the one used as reference (-0.49 V *vs* SHE) and used to acquire the spectrum displayed at the bottom of the Figure. The bottom spectrum (first spectrum in black) and the top spectrum (last spectrum in black) should be the same, featureless reference signal in the case of a reversible electrochemical phenomenon under electrochemical control, as it is observed in **Figure 3.17**. Fourth, by doing small potential steps the experiments can be as long as 6 hours. The stability and reversibility of the signal with time is then also assessed to make sure the carbon material is not subject to modification that could impair the data interpretation. These longer experiments also

illustrate the robustness of the method. Detailed potentials steps for each image are given in **Table A4** and in all cases the electrolyte used was KPB, 100 mM, pH 7.

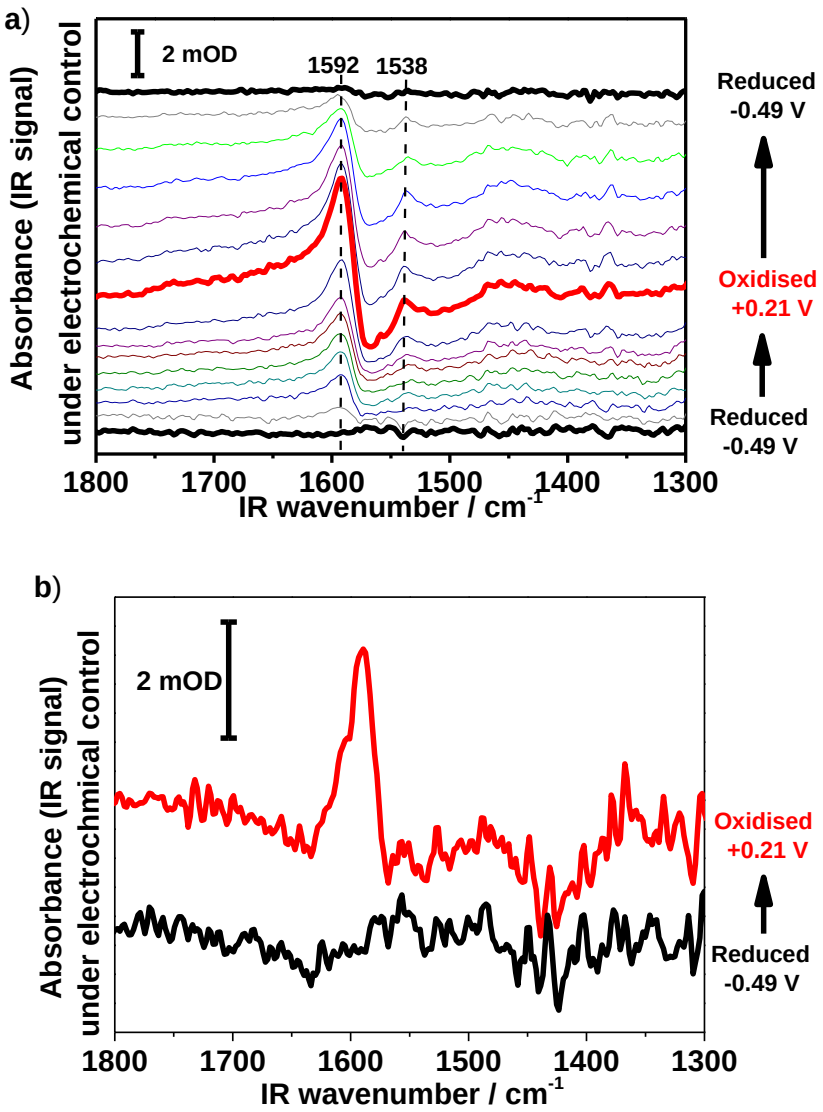

Figure 3.17. IR spectra of FMN adsorbed on MG particles under electrochemical control recorded at different voltages. The reference spectrum was taken at -0.49 V *vs* SHE (black). The most oxidising potential applied was +0.21 V *vs* SHE (red). Each spectrum corresponds to a different potential applied. (a) MG with adsorbed FMN, (b) MG without FMN.

3.3.3.2. Plate-like materials

APG is a suitable material for FMN immobilisation and is suitable for hydrogenase electrodes (**Section 3.3.2.1**). The first attempts to develop the coupling of ATR-IR

spectroscopy and electrochemistry for studies of adsorbed species directly under electrochemical control were then performed with APG. However, no signal of FMN under electrochemical control could be recorded. This is because to obtain a sufficient signal/noise ratio in the ATR configuration used, the redox species immobilised on carbon materials need to be as close to the prism as possible (**Section 1.2.3.3**). The APG beads have a size bigger than 5 µm and so are not suitable electrode materials because they are bigger than the expected penetration depth (around 1 µm) of the evanescent waves. An obvious strategy to give sufficient surface area to improve the signal is to minimise the size of the graphitic flakes. This makes MG, with a smaller size than APG (**Table 3.1**), an ideal candidate.

IR spectroelectrochemical measurements performed with FMN adsorbed on MG are reported in **Figure 3.17a.** A peak at 1538 cm^{-1} appears at oxidative potential (+0.21 V *vs* SHE). This is a good hint that it is possible to obtain IR data for adsorbed FMN under electrochemical control because a peak around 1540 cm^{-1} corresponds to a reversible change in the FMN isoalloxazine ring (circled in **Figure 3.14**). This peak also disappears under potential control: the top and bottom spectra acquired at the same reductive potential (-0.49 V *vs* SHE) lead to the same flat signal. However this result was difficult to reproduce and so MG does not appear as a fully optimised material for the development of the technique. In particular another band at1592 cm^{-1} could be observed. This band is not related to FMN because it can be observed on the raw material without adsorbed FMN, **Figure 3.17b**. For the voltage range scanned no electrochemical signal could be observed from the material itself (**Figure 3.15**). Therefore, this reversible appearance of the peak at 1592 cm^{-1} in **Figure 3**.17**b** cannot be attributed to electro-active species on the carbon surface, although it depends on the potential applied. This peak could however result from changes in the vibrational features of functional groups on the carbon surface (like ketone, acid or other oxygen-containing groups) due for instance to different protonation state. The

different protonation state could result from different local pH induced with the applied potential by polarisation of water molecules in the vicinity of the carbon surface. Last, but important for future discussion, the intensity of the signal attributed to FMN is relatively low and about1 mOD.

3.3.3.3. Tube-like materials

Due to their strong IR absorption and difficult dispersion in aqueous solvents, no satisfying results were obtained in this study with dispersed MWCNTs or N-MWCNTs. Using GNF, easier to disperse in aqueous solution, a spectroelectrochemical response from adsorbed FMN was observed as reported in **Figure 3.18**. A first observation is that the material itself gives potential-dependent IR signals. This is for instance observed with two negative peaks around 1650 and 1600 cm^{-1}, appearing in the red spectrum in **Figure 3.18a**. However no redox signal from the material itself for the potential range considered can be observed in the cyclic voltammogram (**Figure 3.15**). In a similar case to MG, this potential dependent IR signal is likely to be related to (de)protonation of oxygen containing groups on the carbon surface. In the presence of adsorbed FMN, additional reversible features are observed 1400-1520 cm^{-1}, in particular a peak around 1523 cm^{-1}: GNF + FMN curves in **Figure 3.18a**. These extra peaks are present only after FMN adsorption and so can be attributed to potential-dependent changes in adsorbed FMN. The intensity of the signal related to FMN is about 5 mOD, **Figure 3.18a**, which is a higher signal than in the case of MG. The fact that the peak attributed to FMN does not appear at 1539 cm^{-1} as in the case of MG is probably a result of different FMN-carbon interaction. The adsorbed FMN may interact differently with a material showing mainly edge-plane like structure like GNF (**Section 3.3.1**) compared to MG because the latter still shows some basal plane features. The potential-dependent behaviour of GNF with or without FMN adsorbed on it is easily reproducible. It can be repeatedly observed by holding the FMN at reducing

(black spectra) or oxidative (red spectra) potentials and switching several times the potential, **Figure 3.18a**. In particular, reversibility was achieved with GNF even for long experiments (*ca.* 3 to 6 hours) including several potential steps, going from reduced to oxidised, **Figure 3.18b**, or oxidised to reduced conditions, **Figure 3.19**. Since GNF has a typical size smaller than MF, this confirms that scaling down the size of the materials is promising to achieve the coupling of ATR-IR spectroscopy and electrochemistry.

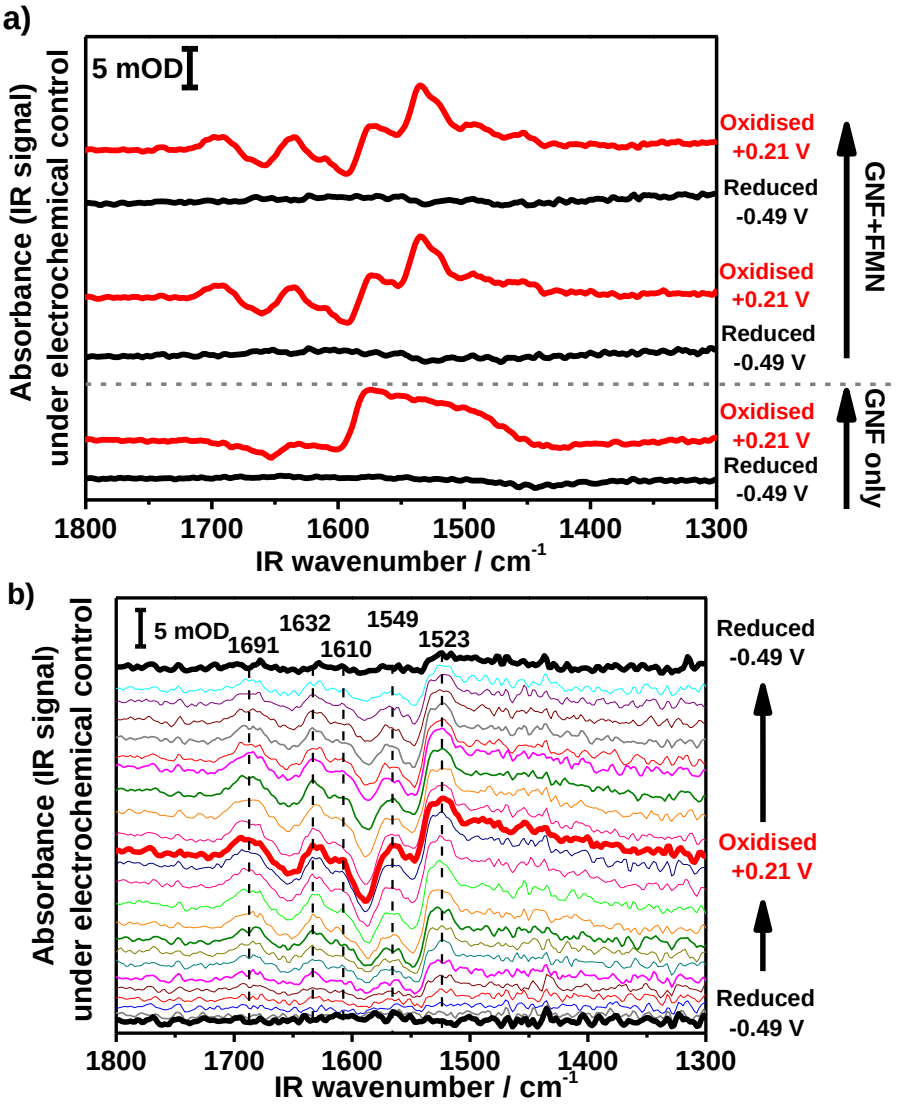

Figure 3.18. IR spectra of GNF particles under electrochemical control recorded at different voltages (a) with or without adsorbed FMN and (b) with adsorbed FMN for several electrochemical steps. The reference spectrum was taken at -0.49 V *vs* SHE (black). The most oxidising potential applied was +0.21 V *vs* SHE (red). Each spectrum corresponds to a different applied potential.

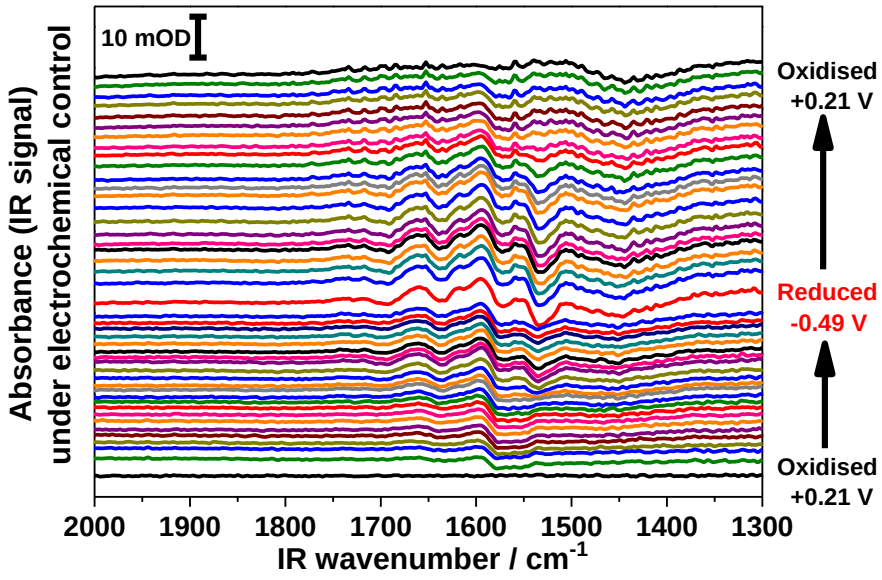

Figure 3.19. IR spectra of FMN adsorbed on GNF particles under electrochemical control recorded at different voltages. The reference spectrum was taken at +0.21 V *vs* SHE (black) and the most reduced potential in red is -0.49 V *vs* SHE (red). Each spectrum corresponds to a different applied potential.

These encouraging results suggest that MWCNTs with a similar size to GNF (**Table 3.1**) should also facilitate the coupling of ATR-IR spectroscopy and electrochemistry. This is possible only if their challenging dispersion can be addressed. This can be done by directly growing MWCNTs on the silicon prism used for IR spectroscopic data acquisition. The synthesis of MWCNTs was performed using AACVD as described in **Section 2.2.4**. The optical prism was used as substrate and n-propylbenzene as precursor with 5 wt% ferrocene. This is because this precursor gives slower growth rate [179] for the MWCNT forest, so it is easier to control the growth of the MWCNT to a sub-micrometre length. MWCNT growth was performed for 3 minutes and a MWCNT network directly in contact with the prism with a total length less than 1 µm can be developed. This is confirmed by SEM images reported in **Figure 3.20.** FMN adsorption was then performed by dipping the prism with MWCNT forest on it into an aqueous solution of FMN. After several washes in MilliQ water to remove unadsorbed FMN, a hint of adsorbed FMN under electrochemical

control could be observed around 1534 cm^{-1} as illustrated in **Figure 3.20**. However this approach does not lead to satisfying results. First the signal attributed to FMN was difficult to observe in most experiments and so results are not easily reproduced. Second, growing MWCNT forests for coupling ATR-IR spectroscopy and electrochemistry is a complicated approach. Particles dispersion (like MG or GNF) can be used on a daily basis for several experiments. They are simply used by deposition of a particle film on the prism. In contrast, growing MWCNTs on the prism requires a day to day MWCNT synthesis for each experiment. This involves intensive cleaning of the prism for example in concentrated acids after each use and prior to any new synthesis of MWCNTs. Therefore this approach consisting of growing a MWCNT forest on a prism was not considered as a convenient route for further development of the technique.

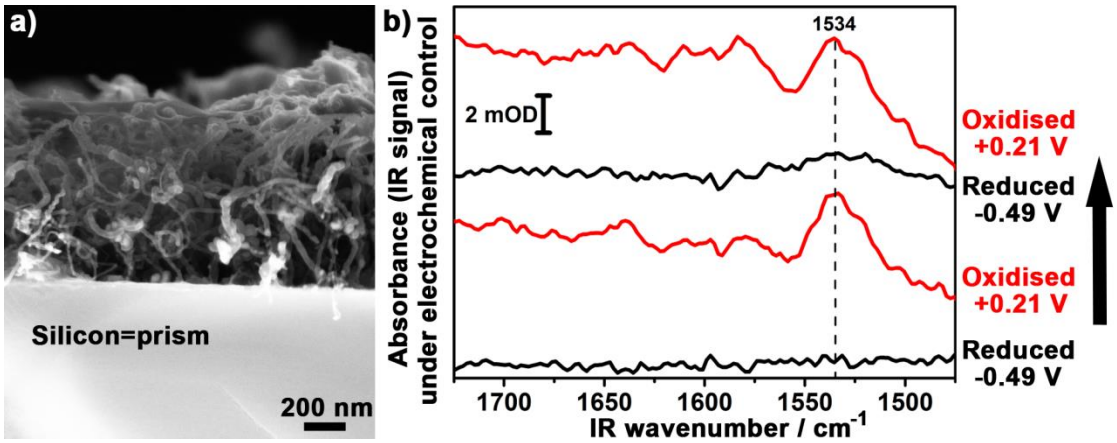

Figure 3.20. (a) SEM micrograph of MWCNTs directly grown on a silicon wafer. When similar structures are grown on the optical prism used for the IR experiment and electrochemical control is achieved a hint of FMN signal can be observed: (b) control over the peak at 1534 cm^{-1} with applied potential. The reference spectrum was taken at -0.49 V *vs* SHE.

3.3.3.4. Nanoparticle materials

GNF is a promising material to couple ATR-IR spectroscopy and electrochemistry. However the material has a relatively large size (diameter about 20-250 nm, **Table 3.1**) compared to

other materials. For instance the carbon nanoparticles characterised in **Section 3.3.1** have a diameter lower than 100 nm. Improved coupling and reproducibility can be expected by using these particle-like materials. This is illustrated with HNP in **Figure 3.21**. The first advantage of using HNP compared to the previous cases of MG, MWCNT and GNF, is that the signal for the peak at 1539 cm^{-1} attributed to the oxidised form of FMN under electrochemical control has an intensity about 50 mOD. This is about 10 times higher than with GNF which facilitates the interpretation of the data. Also additional positive peaks are observed at 1707, 1648, 1614, 1576 and 1497 cm^{-1} for the oxidised form of adsorbed FMN, **Figure 3.21**. Precise band assignment is complicated by a lack of consistency of assignment in the literature, both experimentally and computationally. Oxidised FMN in solution exhibits C=O bands at *ca.* 1712 and 1660 cm^{-1}, and bands due to the isoalloxazine ring at roughly 1626, 1580, 1547 and 1506 cm^{-1} [232]. These vibrations can be seen as positive contributions to the difference spectra reported in **Figure 3.21**. They are observed at slightly lower wavenumber for immobilised FMN than FMN in solution. This is probably due to the interaction with the carbon electrode and/or interaction between several FMN molecules upon adsorption which modifies the vibrational modes of FMN. The negative peaks observed correspond to the reduced FMN. For instance contributions from the isoalloxazine ring at *ca.* 1595, 1556 and 1512 cm^{-1}. Broad negative features are also present around 1400 cm^{-1}. These can be attributed to the N-H bond deformations that are not present for the oxidised form. Even for long experiments (*ca.* 3 to 6 hours), stability and reversibility of the FMN signal could be observed whether from reduced to oxidised, **Figure 3.21a**, or oxidised to the reduced form, **Figure 3.21b**. No clear signal under electrochemical control for the particle-like materials themselves could be observed as opposed to the previous materials. This also makes the peak assignment to the adsorbed FMN more reliable on the particle-like materials. Similar conclusive results were obtained with the commercially available BP

(**Figure 2.19**), VX, ML and CNP. The results presented are a milestone in the development of the technique showing the possibility to perform IR investigation under direct electrochemical control of molecules directly adsorbed on carbon materials.

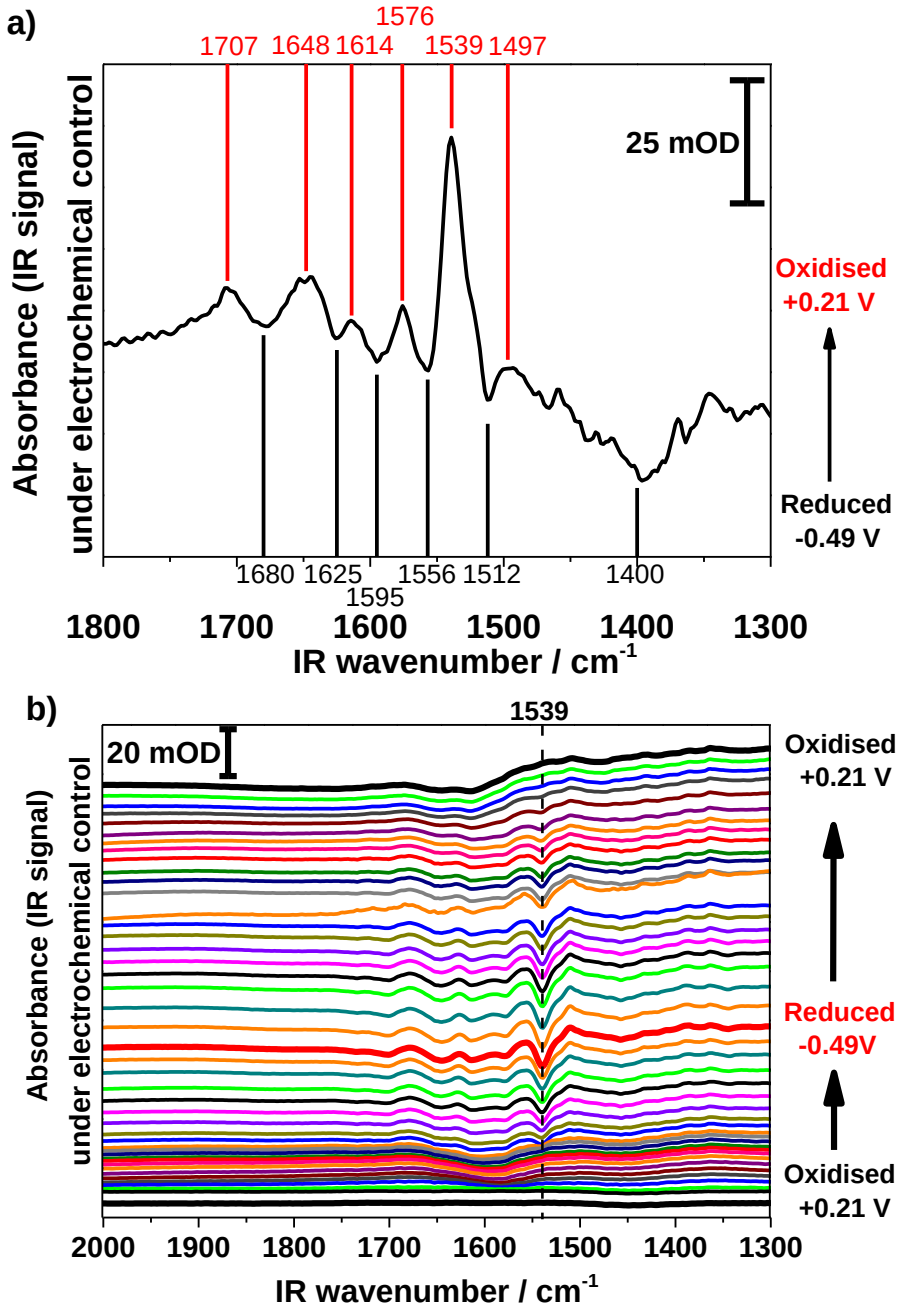

Figure 3.21. (a) IR oxidised (+0.21 V vs SHE) *minus* reduced (-0.49 V *vs* SHE) difference spectra of FMN adsorbed on HNP. (b) IR spectra of FMN adsorbed on HNP under electrochemical control recorded at different voltages. The reference spectrum was taken at +0.21 V *vs* SHE (black). The most reduced potential is -0.49 V *vs* SHE (red). Each spectrum corresponds to a different applied potential.

For Si@C particles, the amount of electrochemically active FMN immobilised on the material was low compared to the other materials. Low loading is indeed consistent with the lower current (less than 1 µA, **Figure 3.15**) associated with the redox properties of FMN observed on Si@C compared on other materials like GNF (up to 20 µA, **Figure 3.15**). No IR spectroelectrochemical data related to FMN could be recorded and it was concluded that Si@C did not lead to satisfying results for FMN studies. However the Si@C particles were successfully used for IR spectroelectrochemical studies of Hyd-1 as detailed below.

3.3.3.5. IR spectroscopy under electrochemical control of hydrogenase

Spectroelectrochemical data for Hyd-1 adsorbed on Si@C particles are reported in **Figure 3.22**. The peaks observed correspond to the vibration of the CO ligand at the active site of the enzyme (**Figure 1.14**). The vibration of CO is sensitive to the redox state of the active site. The positive peaks correspond to features appearing with the oxidised state of the immobilised hydrogenase (Ni-B state) whereas the negative peaks correspond to the loss of features that were present in the reduced states (NiR_{III} and NiR_{II} bands). This is because the spectrum presented is the difference between a spectrum taken in the oxidised state subtracted by a spectrum taken in the reduced state. This is an exciting result because for the first time IR signals related to the active site of a hydrogenase can be recorded under direct electrochemical control. Similar results were obtained on the commercially available BP for hydrogenase study. This last material has been taken forward as the core material for coupled ATR-IR spectroscopy and electrochemistry for enzyme studies in Prof Vincent's group.

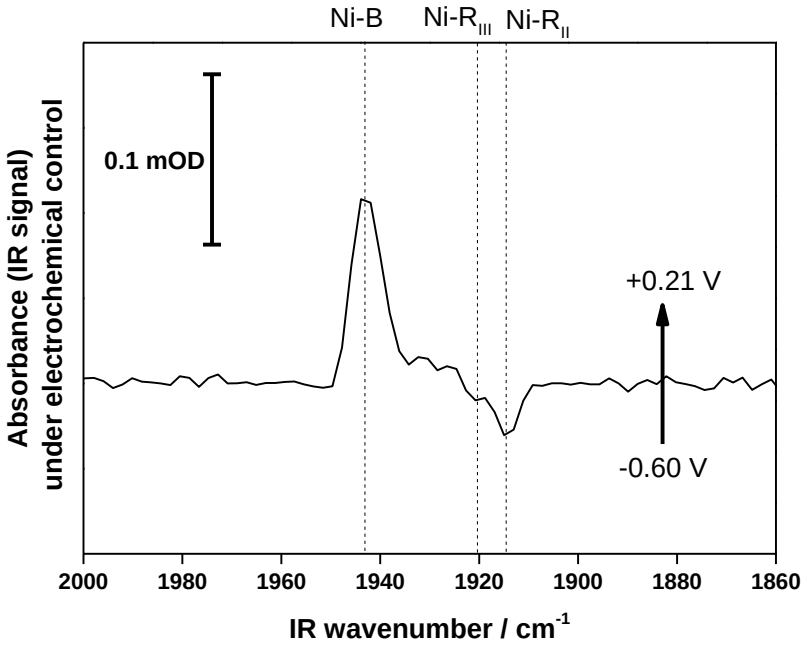

Figure 3.22. IR spectrum of the *ν*(CO) region for Hyd-1 immobilised on Si@C particles. Spectrum reported is the difference spectrum between spectrum recorded at +0.21 V *vs* SHE and spectrum recorded at -0.60 V *vs* SHE. *With the assistance of Ricardo Hidalgo, Department of Chemistry, University of Oxford.*

3.4. Conclusions

Eleven different carbon materials with different properties were selected and characterised to develop enzyme electrodes. The hydrogenase Hyd-1 from *E. coli* was adsorbed on all these carbon materials. For the first time, the unified study of the same hydrogenase under equivalent experimental conditions is performed. It is then possible to establish the advantages conferred by selecting one material compared to another to develop high surface area enzyme electrodes. It is first shown that all of the eleven carbon materials are relevant for hydrogenase adsorption. In order to optimise the electrocatalytic current from enzyme electrodes, materials with high specific surface area and a relatively pronounced mesoporosity are the most suitable materials. The catalytic

current per mass of materials achieved, for instance 12 A g^{-1} at +0.24 V *vs* SHE with the commercial material BP 2000 (BP), is promising and the materials could be considered for scale up in applications like fuel cells. In particular high electrocatalytic current can be achieved if mass transport limitation through the porous network is properly addressed *via* careful cell design. In this study, BP was found to be the best material to achieve high electrocatalytic current. However the total surface area available is not fully used by the hydrogenase. A better hydrogenase loading per surface area of electrode material is achieved with more graphitic materials. In particular the simple preparation of exfoliated graphite (MG) with size less than 1 µm gives a material for which the available surface area is best used by the hydrogenase in this study. These results suggest that an optimal material to develop electrode for applications of hydrogenases - and possibly other enzyme - should combine a high surface area and a pronounced 'edge' structure. This material is still to be identified.

It is also established in this chapter and for the first time that performing ATR-IR spectroscopic investigations of species directly immobilised on carbon electrodes is possible. This constitutes a milestone in the development of the technique. The coupling is successfully achieved by selecting and designing carbon materials with a nanoscale. Various carbon nanomaterials, like graphite nanofibers (GNF) and carbon particles like hydrothermal nanoparticles (HNP), were used to record IR spectroscopic data related to the biologically relevant molecule FMN under direct electrochemical control. Also IR spectroelectroscopic data related to Hyd-1 were obtained on silicon core carbon shell particles (Si@C). The results show the compatibility of different carbon materials with the spectroelectrochemical measurements. The different results obtained on GNF and HNP for FMN studies suggest that future IR spectroelectrochemical studies to identify the influence of the carbon material used as electrode on the activity or stability of bio-electrocatalysts are now possible.

Finally, MWCNTs and N-MWCNTs are difficult to disperse in aqueous buffers and are challenging to use for electrochemical or spectroelectrochemical investigation in this thesis. The direct growth of MWCNT forests directly on a silicon prism overcomes their challenging dispersion. Unfortunately this approach is difficult to implement for spectroelectrochemical experiments. Using powders made of carbon nanomaterials further dispersed in aqueous solutions and drop-casted on the prism is much simpler. Nevertheless, the next chapter of this thesis shows that developing MWCNT forests directly on a substrate can be a more relevant strategy than using dispersed materials. In particular to tailor carbon scaffolds for emerging applications of immobilised hydrogenases in flow-bio-redox catalysis.

Chapter 4: MWCNT columns for flow-bio-redox catalysis

"Try and fail, but don't fail to try"
John Quincy Adams

Thank you to Thomas F. Bottein who worked under my supervision for three months and contributed intensively to the synthesis and characterisation of the MWCNT columns (CNCs); to Dr Seyyed Shayan Meysami (Department of Materials, University of Oxford) for performing the HF treatment of the columns; to Dr Antal A. Koós (Department of Materials, University of Oxford) for his doubts about the possibility to develop CNCs by the proposed approach. These doubts gave me will to try and succeed. A warm thank you to Holly A. Reeve (Department of Chemistry, University of Oxford) for concretising in terms of catalysis my ideas behind the CNCs, or 'TiTs'(Tubes in Tubes) as they are sometimes informally called.

4.1. Introduction

Powders made of the carbon materials characterised in **Chapter 3** are suitable to develop high surface area hydrogenase electrodes. These electrodes are relevant for enzyme fuel cells or to develop the coupling of IR spectroscopy and electrochemistry. However, powdered carbon materials may not be optimal for emerging hydrogenase applications that could benefit from novel carbon scaffolds (detailed in **Section 1.2.4**). Enzymes are increasingly considered in chemical synthesis [10] due to their high selectivity, biodegradability and ability to operate under mild conditions of temperature and pressure. These properties are advantageous to reduce costs in production of chemicals. However some redox enzymes require a stoichiometric amount of a cofactor molecule to operate. Recycling this expensive cofactor can be extremely difficult and costly. It has been shown that a cascade of enzymes including a hydrogenase offers the opportunity to recycle cofactors *in-situ* using H_2 as reductant without producing waste or by-products [20]. A major requirement is for the redox enzymes to be in electronic contact with each other through a conductive carbon support. To facilitate the implementation of this promising new system to industrial production, flow chemistry (also detailed in **Section 1.2.4**) could be exploited. Flow chemistry [113, 115, 233] offers multiple benefits compared to batch processing, including continuous production, possibility to work with small volumes and higher concentrations, minimal waste and

minimal energy requirement. These advantages all contribute to reducing costs for production of chemicals [10]. To develop sustainable and simple industrial production methods of chemicals, it would be relevant to combine the enzyme-based cofactor regeneration system mentioned above with flow catalysis. However this combination is challenging due to the lack of simple conductive scaffolds compatible with flow systems for enzyme immobilisation.

In **Section 1.2.4**, a column filled with a material on which catalysts are immobilised is identified as a simple flow reactor. However, this reactor configuration is complex to achieve if the catalyst support used is a powder made of (nano)material because high pressure [129, 130] and/or fillers [132] are required to pack or stabilise the column. Direct *in situ* synthesis of the materials used as support in the column would simplify the reactor design [144]. This direct growth is possible with CNT forests (**Section 1.2.2.3**). Advantageously, CNTs have already been demonstrated as support for a plethora of catalysts [24, 75, 135, 164] due to their high surface area, high mechanical, thermal and chemical stability. In addition, they are electrically conductive and hydrogenases can be immobilised on CNTs as confirmed in **Chapter 3**. This combination of properties makes CNT forests ideal candidates to transpose the enzyme-mediated cofactor regeneration system [20] to a flow reactor. Unfortunately, developing CNT flow reactors is not a simple task. When they are used as forests, for membranes [143], filtration [140] or chromatography [141, 142], several steps are required to get from the CNT synthesis to the design of the flow device. Templates [135], etching steps [135] and building the flow system around the CNT forest after synthesis [69] are required. The process is simplified by direct *in situ* growth of CNT forests in a column, as has been reported for development of chromatographic devices [140, 141, 145, 146] but then only one column can be obtained at a time. The limited availability of these columns with their inner diameter filled with CNT forests is a bottleneck. The

implementation of CNT forests for flow (bio) catalytic systems is then limited [69, 76, 128, 135, 136]. A simpler route to obtain CNT scaffolds compatible with flow applications would be beneficial.

Chapter 4 details a method to obtain conductive carbon scaffolds compatible with flow devices and further demonstrates the suitability of these supports for bio-redox-catalysis in a flow configuration. The approach proposed is extremely simple, yet it addresses several challenges at the same time. First, to work around the difficulty in using powders made of carbon material in flow systems, the direct growth of vertically-aligned MWCNTs by AACVD in quartz columns of small inner diameter is investigated in **Section 4.3.1**. Second, the limited production of MWCNT columns is overcome. Control over the MWCNT filling in the column can be achieved and several columns can be obtained in a single experiment. This is shown in **Section 4.3.2** where experimental parameters like time of experiments, value of carrier gas flow rate, length and inner diameter of the quartz column are investigated to establish their influence on the MWCNT forest thickness profile in the column. In **Section 4.3.3**, the flow rate of carrier gas is more specifically established as a key synthesis parameter. This study leads to optimised MWCNT scaffolds for possible applications in flow systems. Third, the direct relevance of the scaffolds for flow systems and flow catalysis is proven in **Section 4.3.4**. This is simply achieved due to the geometry of the quartz columns used, without need for chemical or thermal treatment after MWCNT synthesis. Fourth, flow-bio-redox catalysis is demonstrated in the as-synthesised MWCNT columns in **Section 4.3.5** by transposing the modular enzyme cascade described in **Section 1.2.4.1** to a flow system. For the first time, the biocatalytic hydrogenation of acetophenone to 1-phenylethanol is investigated in a flow configuration by exploiting the conductivity of the MWCNTs and the ability of enzymes to operate at room temperature and low pressure. The results presented prove that the MWCNT columns

(CNCs) developed are simple and extremely promising platforms not only for bio-redox-catalysis but also flow catalysis in general. The properties illustrated within this chapter that make the CNCs a versatile scaffold for flow devices are summarised in **Section 4.4**.

4.2. Experimental

The general materials and methods relevant to this chapter have been covered in **Chapter 2**. This experimental section gives specific information related to the development of MWCNT columns: CNCs. MWCNTs were synthesised with the AACVD set up described in **Section 2.2.4** following reported experimental conditions [92, 191]. A mixture of toluene and 5 wt % ferrocene was used as precursor, argon as the carrier gas and all experiments run at 800 °C. Experiments were performed for times longer than 60 minutes, so an ultrasonic unit with a water-cooling system was used to avoid overheating the solution and the equipment during the continuous operation of the piezo-electric device for long period of time. Quartz tubes with inner diameter (ID): 1, 2 or 4 mm (outer diameter 8, 4 and 6 mm respectively, from Robson Scientific) were used as substrate to develop the carbon scaffolds. They are referred to as ‘columns’ and not tubes in this thesis by analogy with the terminology for chromatographic devices [142] and flow systems [114]. When the column inner diameter is filled with MWCNTs it leads to ‘MWCNT columns’ abbreviated CNCs. The range of size for the inner channel of the column was selected to develop mini flow systems: inner diameter defining the channel size between 0.5 and 2 mm [114], for reasons detailed later in this chapter. As-received columns were cleaned by sonication in ethanol for few minutes prior to use. Without other pre-treatment, they were placed at various distances in a quartz tube reactor (21 mm ID) placed itself in a furnace, as illustrated in **Figure 4.1**. For instance the column placed at 17 cm relative to the beginning of the furnace, has one end at 17 cm and the rest of the column between distance 17 cm and 23 cm.

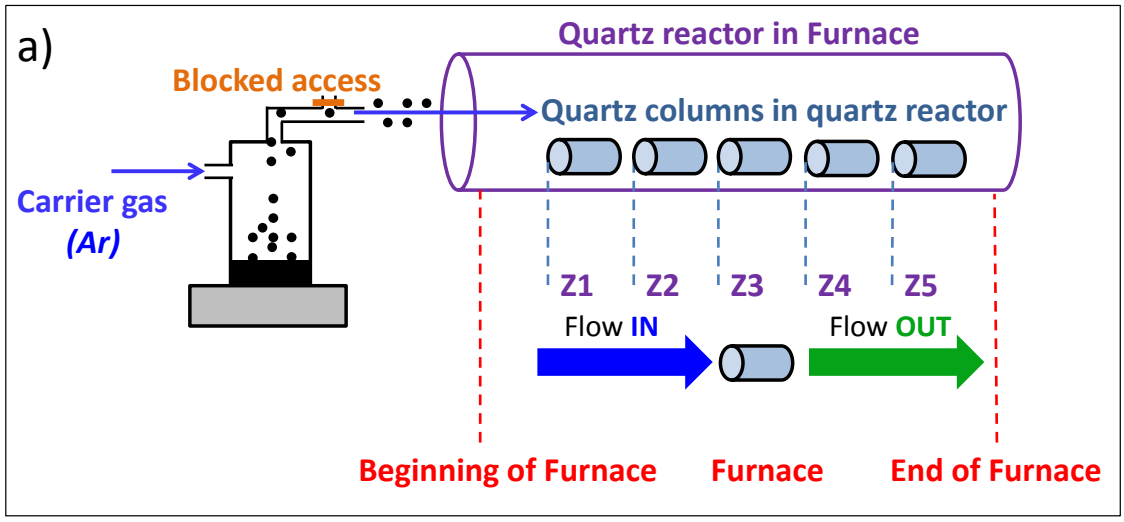

Figure 4.1. Schematic representation of the synthesis set up and carrier gas flow progression during the experiment. A 21 mm ID quartz tube is used as a reactor and divided into different zones where substrates (quartz columns) are placed. Typically Z1=17 cm, Z2=23 cm, Z3=29 cm, Z4=39 cm, Z5=45 cm, values correspond to distances into the furnace which was 55 cm long.

For optical microscope, SEM, Raman and EDS data acquisition, the method to obtain cross sections cut of the columns is described in **Section 2.3.1**. Raman intensity ratios were obtained as an average of at least 6 spectra on the same cross section. Thickness of the MWCNT forest was assessed using an optical microscope (VMS-004 Deluxe microscope, with a x10 objective or confocal microscope of a JY Horiba Labram Aramis Raman microscope with a x50 objective) with at least 4 measurements on the same cross section. Positions in the columns are expressed relative to the entrance of the column. The position 0 cm, referred to as IN, corresponds to the end of the column directly facing the carrier gas flow during synthesis, **Figure 4.1**. The opposite end is referred to as OUT. Controlling the position of the column relative to the flow during synthesis is important to understand the growth of MWCNTs. This position can un-ambiguously be established by marking one extremity of the outer surface of the column with a diamond pen. After removing the

MWCNTs grown during synthesis and covering the mark, the relative position of the column to the carrier gas flow during synthesis can be established.

4.3. Results and discussion

4.3.1. AACVD synthesis of CNCs and characterisation

4.3.1.1. Towards production of CNCs by AACVD

The first challenge to develop CNCs by AACVD is to prove that a MWCNT forest can grow within the inner channel of tubular substrates. MWCNT growth in a quartz tube with relatively large inner diameter, for example 21 mm ID is well established [191]. It is also established than growing CNTs in small inner diameter columns (*e.g.* 0.5 mm ID) is possible when the hydrocarbon flow needed is forced to pass through the column during synthesis [140, 141, 145, 146]. Growing MWCNTs into small diameter columns as schematised in **Figure 4.1** is not guaranteed. The columns are placed into a bigger inner diameter quartz tube playing the role of reactor. It is uncertain whether the hydrocarbon flow required for the growth of MWCNTs will penetrate through the smaller inner diameter columns because it is not forced to do so. This thesis shows that it is actually straightforward to grow a black material inside quartz columns of 1 mm ID or more by AACVD with the approach proposed. In **Figure 4.2**, a schematic representation and photos of the column before, **Figure 4.2a**, and after synthesis, **Figure 4.2b,** are reported. After synthesis, MWCNTs are observed on the outside surface of the columns as a black deposit. These MWCNTs are not of interest for developing flow catalytic scaffolds and are easily removed by simply scrapping the outer surface of the columns with a blade, **Figure 4.2c**. After this step, the inner diameter of the column is observed to be black while some columns have a hollow core with a black deposit that can be seen-through.

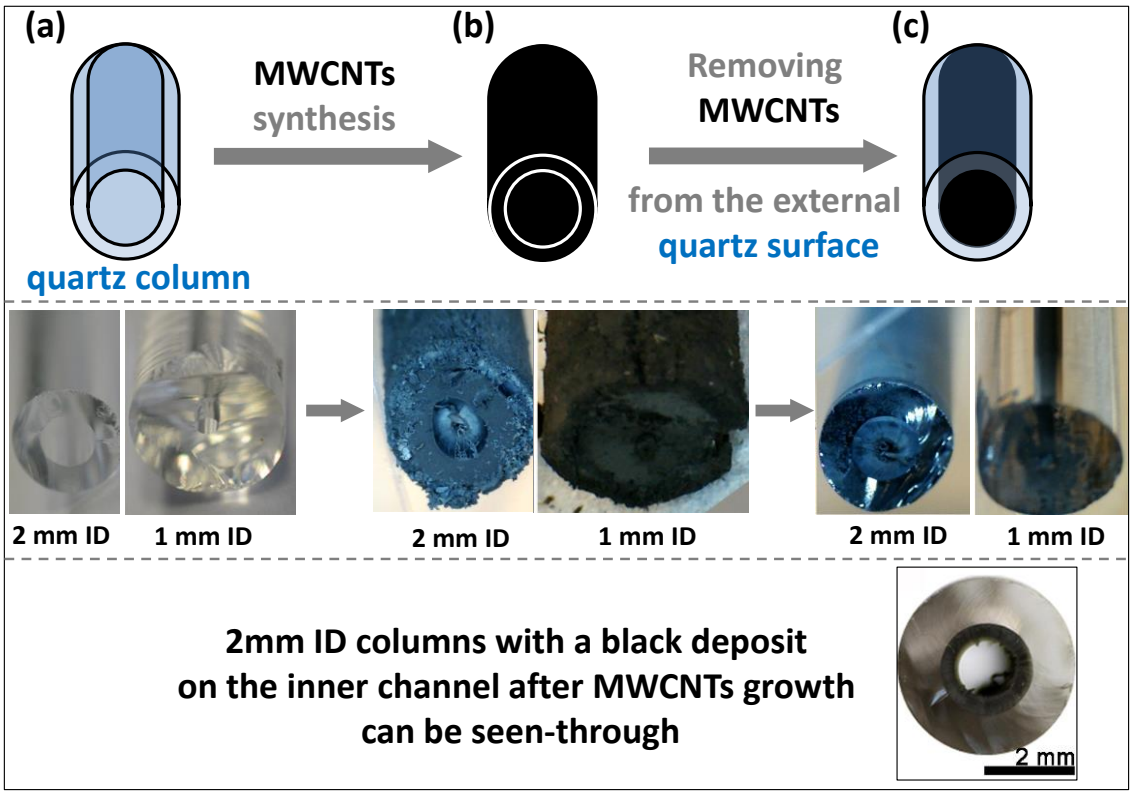

Figure 4.2. Schematic representation and photos of columns with 2 mm and 1 mm ID (4 mm and 8 mm outer diameter respectively): (a) before MWCNT synthesis, (b) as-produced after synthesis, (c) after synthesis and after removing the MWCNTs grown on the external surfaces of the columns. Some columns are seen-through with a black deposit on the inner wall after synthesis.

4.3.1.2. Characterisation of CNCs

The black deposit inside the columns is consistent with growth of MWCNT forests. This deposit is further characterised by several techniques and results are shown in **Figure 4.3**. **Figure 4.3a** shows a schematic representation of cross and longitudinal sections of the column after MWNT growth. In **Figure 4.3b** and **Figure 4.3c** are displayed SEM micrographs of the material grown in the middle of a column, after respectively cross and longitudinal section cuts. The typical forest geometry for MWCNTs grown by AACVD is observed, with the nanotube axis perpendicular to the inner diameter surface of the quartz column they are grown on. The quartz column appears as a white background in the SEM

cross section in **Figure 4.3b** whereas the MWCNT forest is grey. A dark circular section in the middle of the image corresponds to a hollow core without material also observed in **Figure 4.3c** as an inner channel. This inner channel is formed because the MWCNTs are not grown long enough to fill the column of 2 mm ID. Nevertheless, there is no part of the column surface without MWCNTs, *i.e.* a full coverage of the quartz column inner wall is achieved. The full coverage but partial filling is consistent with the ability to see-through the columns despite MWCNT deposition (**Figure 4.2**). A SEM micrograph acquired at higher magnification is displayed in **Figure 4.3d**, confirming that the inner channel of the quartz column is covered with a tubular nanomaterial. A typical Raman spectrum acquired on a cross section is displayed in **Figure 4.3e**. The three expected characteristic Raman peaks of MWCNTs [93] around 1340 cm^{-1} (D peak), 1565 cm^{-1} (G peak) and 2680 cm^{-1} (2D peak) are observed. A TEM micrograph of the materials collected within a column is shown in **Figure 4.3f**. The image obtained is characteristic of MWCNTs (as detailed in **Chapter 3**) and confirms that hollow tube-like nanomaterials are synthesized in the column. Analysis of 10 TEM images with 100 measurements in total indicate that the tubes show an inner diameter between 8 and 20 nm, with thick outer walls leading to an outer diameter in the range 25-60 nm. All together, these results confirm full coverage of the column inner channel with a vertically-aligned MWCNT forest.

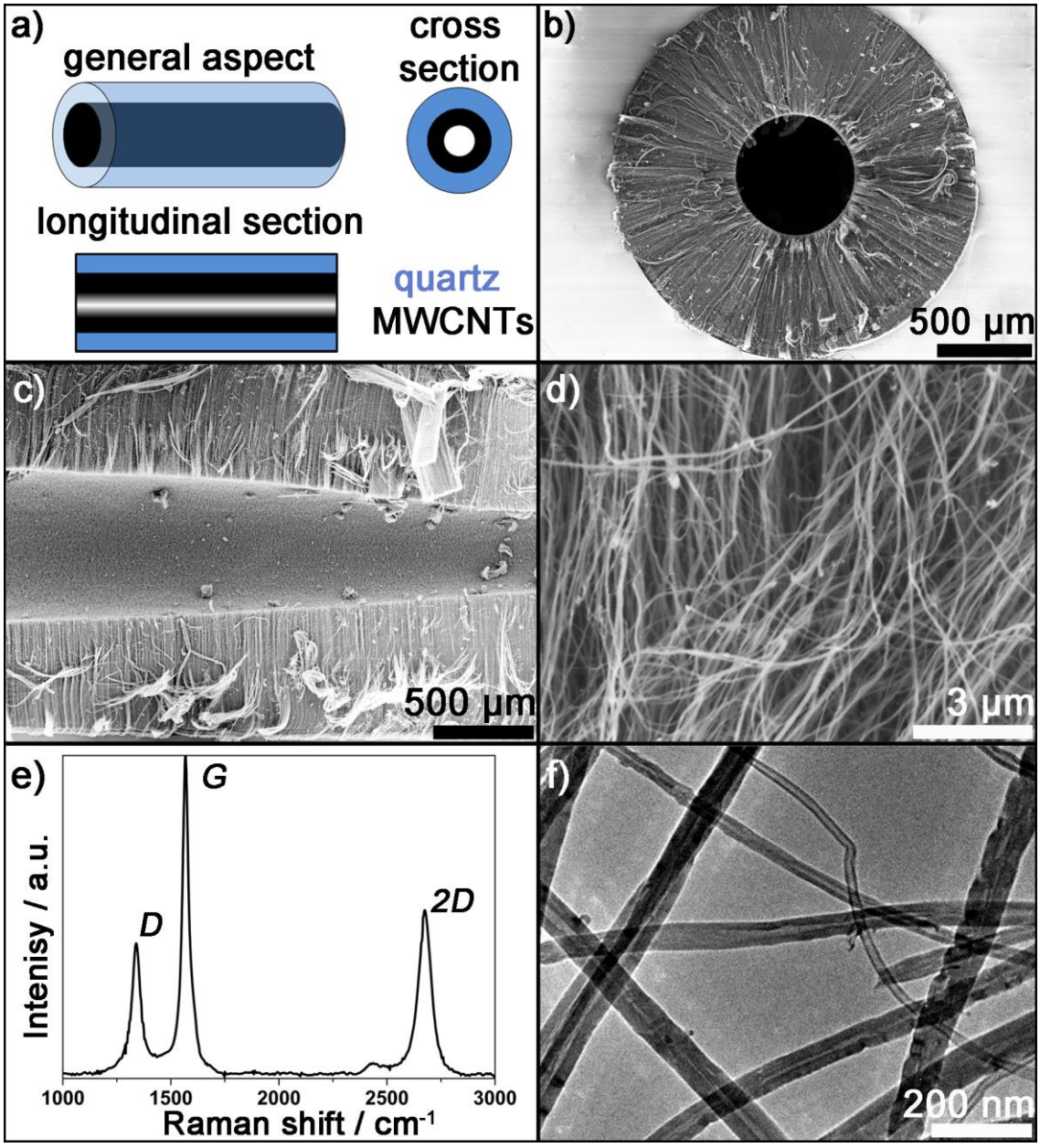

Figure 4.3. (a) Schematic representation of the CNC and associated sections. (b) SEM micrographs of a cross section performed in the middle of CNC showing vertically-aligned MWCNTs. The quartz surface appears as a white background, the MWCNTs are in grey and the inner channel formed by the partial filling of the column in dark. (c) SEM micrographs of a longitudinal section of a CNC showing an inner channel free of MWCNTs. (d) Higher magnification SEM micrograph. (e) Raman spectrum and (f) TEM micrograph of MWCNTs grown in the CNC.

4.3.1.3. Benefits of CNCs

The mass of MWCNTs deposited in the column was up to 10 mg for a 2mm ID and 2 cm long column and for synthesis time of 90 minutes. Assuming a specific surface area of about 60 m^2 g^{-1} for the MWCNTs as characterised in **Chapter 3**, the expected surface of carbon in the column is around 6000 cm^2 whereas the quartz surface in the column is 1.256 cm^2 based on geometrical consideration. It means that the surface area after growing the MWCNTs increased by a factor up to 4800 compared to a column without MWCNTs. A first benefit of the CNCs is then to develop a high surface area of carbon material within the column.

A second benefit is the geometry compatible with a flow device (**Figure 1.24**) that can be connected to tubing easily and this will be exploited later in this chapter.

A third benefit is to provide more mechanical protection to the MWCNTs. MWCNTs grown on a flat substrate or on the outer surface of the column after synthesis can easily be scraped from the substrate (**Figure 4.2b-c**). In contrast, MWCNTs into the column are protected by the quartz shell. For instance one can step on the column without damaging the structure or losing the MWCNTs.

Also cross sections of the CNCs can be performed without loss of the MWCNTs and the forest is maintained after sonication. This suggests a fourth benefit which is a relatively strong mechanical link between the MWCNT forests and the column. All these benefits encourage further investigation of CNCs for applications in flow systems.

4.3.2. Control over the filling of quartz column with MWCNTs: parametric study

4.3.2.1. Assessment of quartz column filling with MWCNTs

To make the most of the CNCs, control over the MWCNT forest is required. The influence of experimental parameters on the thickness of the forest in the column was studied to achieve an optimal filling with MWCNTs. The parameters investigated are the distance of

the columns within the reactor, the inner diameter of columns, the duration of the experiment, the length of columns and the flow rate value of carrier gas because they are all likely to strongly influence MWCNT growth in the CNC. To evaluate the effect of these parameters on the column filling with MWCNTs several measurements can be performed.

An optimised filling corresponds to a high surface area of carbon developed. Nitrogen porosimetry should be a preferred measurement to evaluate the carbon surface area (**Section 2.3.5**). However the characterisation is limited to one or two samples per day and can be subject to access restriction like training, booking or maintenance. Nitrogen porosimetry was not considered as a time and cost efficient characterisation for the parametric study presented in this thesis since more than 345 samples had to be analysed. An optimised carbon surface and optimised filling also corresponds to a dense and thick MWCNT forest. The MWCNT density (number of MWCNTs per surface area of support) and forest thickness can be evaluated by SEM. However similar practical training, booking and time restrictions (about 1 sample per hour and booking only possible for up to 10 hours a week) apply to this technique.

A simpler approach is proposed and preferred in this thesis to evaluate the column filling by considering only the forest thickness. It is found that a simple optical microscope can be used for this purpose. Compared to alternative techniques, optical microscopy is faster and less subject to booking restriction and training on the equipment is completed in half an hour. The sample preparation is minimal: the CNC just need to be placed under a lens. The technique is simple and fast since up to 20 samples were characterised in a day. It is also a reliable technique and the spatial precision of *ca.* 5 µm achieved was enough for the purpose of this study. Finally, the forest thickness can be evaluated along a column after performing cross sections cuts. This method of investigation gave deep insight into MWCNT properties and growth process. In this thesis, a maximal and uniform forest thickness across

the column assessed by optical microscopy is then considered desirable to optimise the surface of carbon material available for enzyme and catalyst immobilisation.

4.3.2.2. Influence of column inner diameter and distance into the furnace

The growth of MWCNTs was possible in columns with 1, 2 or 4 mm ID. Within the scope of this investigation, the inner diameter is not a limiting factor to grow MWCNTs as it will be illustrated along this chapter. A detailed study is performed on columns with 1 and 2 mm ID to develop mini reactors [114]. Compared to micro systems (channel of size less than 0.5 mm) [114], mini flow systems facilitate the synthesis of MWCNTs directly into the inner channel. Mini devices are also easy to implement in flow systems, to replace if needed, suitable to work with small volumes of solvent at a time and also small quantities of catalysts like enzymes. Their compatibility with flow systems still offers the benefits of flow reactors (*e.g.* the possibility to upscale the production of chemicals [114]). For the final end application of flow catalysis in this thesis, it is also easier to flow a liquid through a micro reactor compared to reactors with smaller inner diameter due to lower pressure drop.

Meysami *et al.* recently investigated the influence of the distance of flat quartz substrates within a furnace on the AACVD synthesis of MWCNTs [191]. The study showed that the distance within the furnace has an influence on the MWCNT properties like length and graphitic structure due to different growth conditions along the furnace. A similar study was performed for the present columns (tubular substrates). The distances where the forest thickness in the columns was the easiest to control were located between 23 and 29 cm within the furnace in most cases and regardless of the furnace used. Results could change from one furnace to another due to slightly different temperature profile but the influence of a different furnace was not observed with the three furnaces used. A specific focus was then given to the columns located between 23 and 29 cm in the furnace during synthesis (**Figure 4.1**) as discussed later in the chapter.

4.3.2.3. Influence of the duration of synthesis on the average thickness of the MWCNT forest in a CNC

A rough estimation of the uniformity of a MWCNT forest in a column is evaluated by considering the difference between the maximum and minimum thickness. Rather than reporting an average thickness or a range of thicknesses, the uniformity is better pictured by reporting a profile along the column. In **Figure 4.4** for instance, the data presented are then the average thickness of the MWCNT forest estimated at different positions along one column. The uncertainty on the thickness at a given position corresponds to at least four measurements performed on a single column for a given set of experimental parameters. The Y axis shows the maximal range of thickness possible for the column considered: 1000 µm for a 2 mm ID column. In **Figure 4.4**, the thickness of the MWCNT forests developed along 2 mm ID columns is investigated as a function of the duration of synthesis. A clear trend is observed: a longer synthesis time leads to longer MWCNTs and so to an overall thicker forest in the column. A longer synthesis time corresponds to a longer time when the precursor is pushed by the carrier gas into the hot region of the furnace, so a longer time for the growth leading to longer MWCNTs. This explanation is consistent with results obtained on flat substrates [92]. For synthesis time shorter than 30 minutes, the forest thickness along the column is rather uniform as there is not much difference between the maximum and minimum thickness along one column, **Figure 4.4**. For time of experiment longer than 30 minutes, the forest thickness is less uniform: especially clear by comparing the position 0 and 2 cm with respective forest thickness 270 and 700 µm for 90 minutes of synthesis in **Figure 4.4a**. It is important to note with this example that the data presentation proposed takes into account the fact that one end of the column is facing a flow of carrier gas and hydrocarbon during synthesis (0 cm, IN position) and the other end is not (2 cm, OUT position). These positions are not equivalent and this influences the forest thickness as it will be extensively discussed in **Section 4.3.3**.

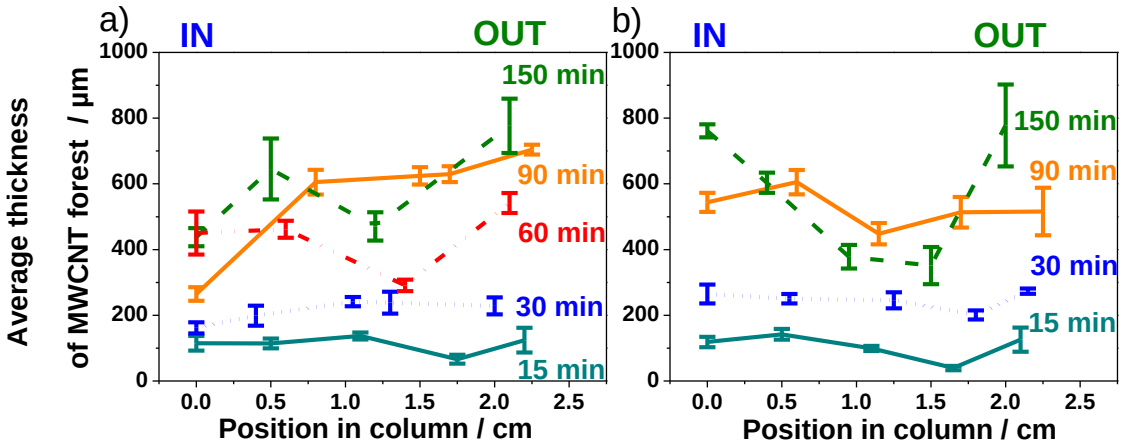

Figure 4.4. Average thickness of the MWCNT forest grown into a 2 cm long column with 2 mm ID as a function of the position in the column and as a function of the duration of synthesis. Carrier gas flow rate was 2500 sccm and columns placed (a) 23 cm and (b) 29 cm within the furnace.

For synthesis longer than 150 minutes, MWCNTs can be grown long enough to block the column. The MWCNTs are too long to fit in the column inner channel and 'spill' outside, **Figure 4.5**. These blocked columns are not desirable in the scope of this thesis because they are not compatible with flow catalysis at low pressure (detailed in **Section 4.3.4**). Regardless of the time of experiment considered, the overall MWCNT forest thickness is not much improved for experiments longer than 90 minute. Indeed obtaining a thickness of the MWCNT forest equal to the inner radius of the column from position IN to position OUT could not be achieved, **Figure 4.4**. In conclusion 90 minutes was considered enough time to achieve an optimal filling as most of the column inner channel is then covered with a forest thicker than 500 µm. More than 75 % of the volume of the inner channel of the quartz column is then filled with MWCNTs. This provides a column functionalised with carbon materials relevant for immobilisation of enzymes and especially hydrogenases (**Section 1.2.2.3**).

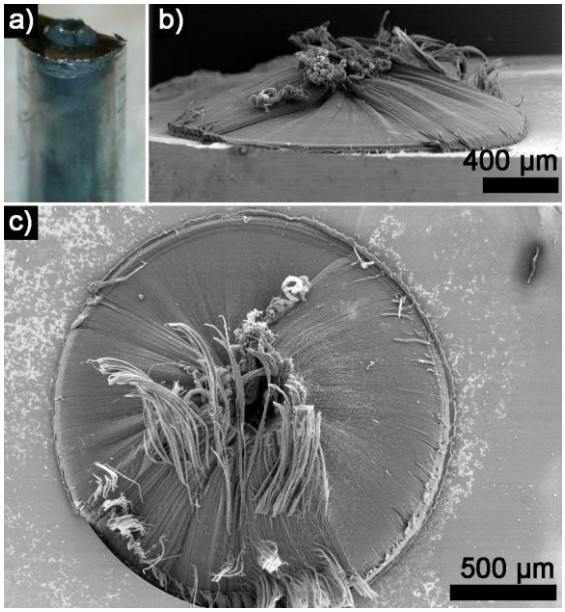

Figure 4.5. (a) Photo of a CNC where MWCNTs spill outside the column at the OUT position. The ID of the column is 2 mm. (b) and (c) are SEM micrographs of the same.

The same study on 1 mm ID columns indicates a strongly non-uniform filling, **Figure 4.6**. Data are presented with the Y axis showing the maximal range of thickness possible for a 1 mm ID column: 500 µm. The thickness of the forest in the middle of the column is typically about half of the thickness at the IN (0 cm) or OUT (2 cm) positions. IN and OUT positions are usually completely filled for time of experiments of 90 minutes or more: forest thickness about 500 µm. In rare cases a complete filling was observed with 1 mm ID columns, like for 150 minutes synthesis in **Figure 4.6a**. The systematic blockage of the ends of the column for time of synthesis longer than 90 minutes is due in these cases to the small ID. MWCNTs can grow long enough to connect with the MWCNTs grown diametrically opposed as illustrated in **Figure 4.7**. It is also observed on this image that the commercial 1 mm ID columns have a non-spherical inner channel. This accounts for the blocked column and the difficulty in reproducing the results with this inner diameter value. In all cases the MWCNTs partially or fully blocking the column are not suitable for flow catalysis at low pressure (**Section 4.3.4**). It is concluded that the optimal ID for the column to develop flow mini rectors is 2 mm.

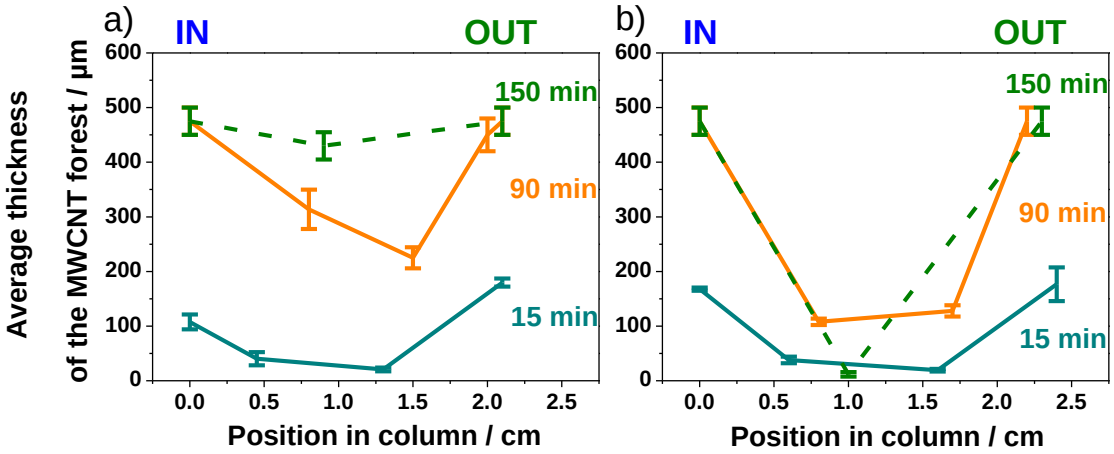

Figure 4.6. Average thickness of the MWCNT forest grown into a column as a function of the position in the column and as a function of the duration of synthesis. The columns were 2 cm long with 1 mm ID. Carrier gas flow rate was 2500 sccm and columns placed (a) 23 cm and (b) 29 cm within the furnace.

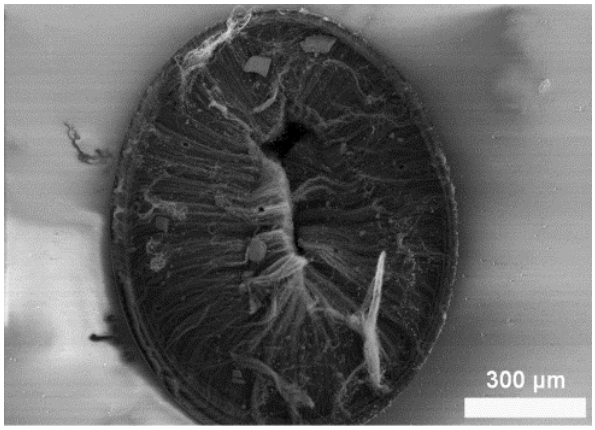

Figure 4.7. SEM micrograph of a 1 mm ID column completely blocked with MWCNTs tangentially-aligned to the column inner diameter surface.

4.3.2.4. Influence of column length on the average thickness of the MWCNT forest in a CNC

To achieve a uniform filling with MWCNTs, the influence of the column length was investigated. Filling columns less than 2 cm long is possible. However it is difficult to accurately investigate the forest thickness profile since cross sections cuts of these are challenging to perform. With 2 mm ID columns, as the column is longer, a greater variation in the average thickness profile is observed. This trend is illustrated in **Figure 4.8** where a

4 cm long column shows thicker maximum thickness (position 4 cm, 750 µm) but also thinner minimum thickness (position 2 cm, 120 µm) compared to a 2 cm long column (thickness between 450 and 600 µm). As a conclusion, 2 cm long columns give a more uniform filling for 2 mm ID columns under the experimental conditions selected. For CNCs of 1 mm ID, filling is usually inhomogeneous and extremities of the columns are usually more filled than the middle of the column, **Figure 4.9**. This has been observed for a number of experiments with various experimental conditions as illustrated along this report. This stresses that 1 mm ID is not an ideal value to develop CNCs. Columns with 2 mm inner diameter and 2 cm long are recommended.

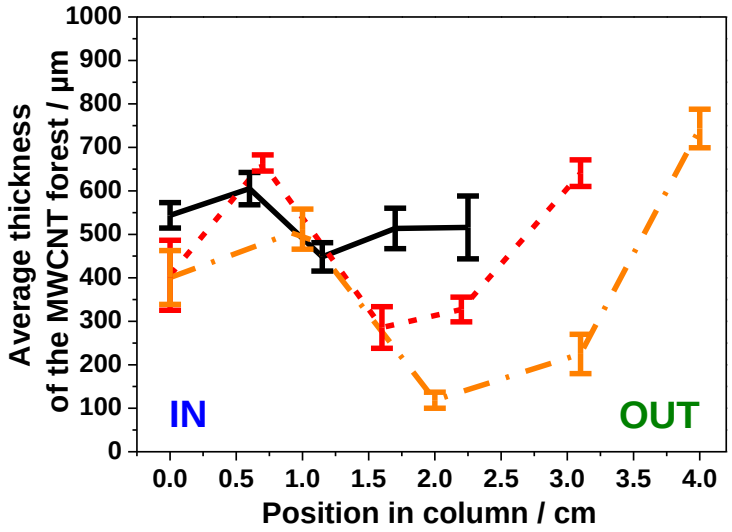

Figure 4.8. Average thickness of the MWCNT forest grown into the column as a function of the position in the column for 2 (plain-black line), 3 (dashed-red line) and 4 cm (dot-and-dashed-orange line) long columns with 2 mm ID. Carrier gas flow rate was 2500 sccm and the duration of synthesis was 90 minutes. All columns were located between 23 and 29 cm within the furnace.

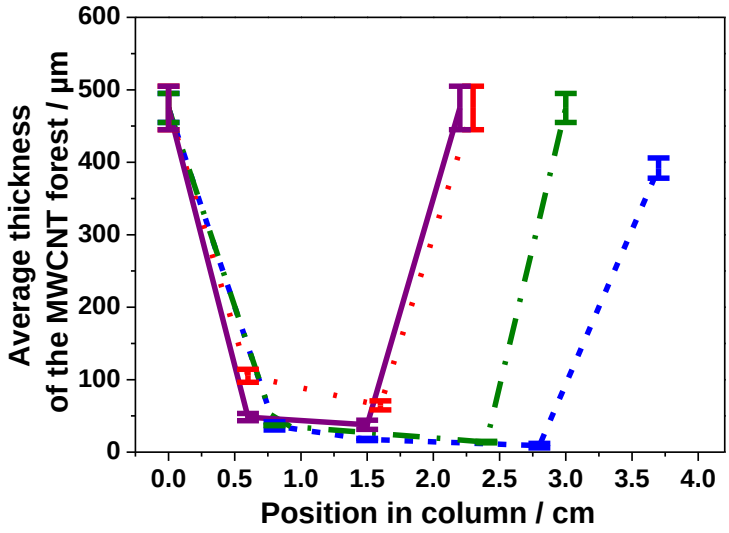

Figure 4.9. Average thickness of the MWCNT forest grown into columns as a function of the position in the column for 2 (dotted-red and plain-purple lines), 3 (dash-and-dotted green line) and 4 (dashed-blue line) cm long column with 1 mm ID. Carrier gas flow rate was 1000 sccm and the duration of the synthesis was 150 minutes for 2 cm long columns and 90 minutes for 3 and 4 cm long columns. All columns were placed between 23 and 29 cm within the furnace.

In **Figure 4.8** and **Figure 4.9** the IN or OUT positions tend to show thicker forest than the rest of the column. This has been observed in twenty two independent experiments for columns of various length and diameter. Also for experiments performed with a flow rate of carrier gas of 2500 sccm, the forest thickness at the IN position was usually thinner than at the OUT position for 2 mm ID columns. This is more pronounced for longer CNCs as displayed in **Figure 4.8**: about 400 µm forest thickness at the IN position and 750 µm at the OUT position for a 4 cm long column. This observation will be explained in a later section.

4.3.2.5. Influence of flow rate of carrier gas on the average thickness of the MWCNT forest in a CNC

The influence of the flow rate of carrier gas on quartz column filling was investigated and three different flows rate values were considered: 1000, 2500 and 5000 sccm. 1000 and

2500 sccm are commonly used and can be considered as optimal for the growth of MWCNTs in AACVD synthesis [92, 191]. 5000 sccm is the maximum value that could be safely reached with the experimental set up used. A high carrier gas flow rate was selected to promote the flow of hydrocarbon to penetrate through the small inner diameter columns. This choice was based on the hypothesis that the inhomogeneous filling in different samples (see **Figure 4.4**, **Figure 4.6**, **Figure 4.8**, **Figure 4.9**) is due to a flow of carrier gas not being efficient in penetrating through the small inner diameter columns during synthesis.

In **Figure 4.10**, for the case of 2500 sccm (plain lines) a better global filling is achieved compared to the case of 1000 sccm (dashed lines). This is especially clear for 2 mm ID columns (a and b) because the forest is thicker for 2500 sccm than for 1000 sccm for all position in the column except at position 0 cm. The forest is also more uniform across the column. This effect is not so pronounced for 1 mm ID (c and d). For experiments performed at 2500 sccm, the forest at the IN position (0 cm) is generally thinner than at the OUT position (**Figure 4.4**, **Figure 4.6**, **Figure 4.8** and plain lines in **Figure 4.10**). This is especially clear for 2 mm ID columns that are 3 or 4 cm long in **Figure 4.10b** (plain lines). The opposite occurs for a carrier gas flow rate of 1000 sccm (dashed lines in **Figure 4.10a,b**) where the IN extremity of the column tends to show a thicker forest that the OUT extremity, all other experimental parameters being identical otherwise. This observation gives information on the growth mechanism of MWCNTs and will be further explained in a dedicated section in parallel to Raman analysis (**Section 4.3.3**).

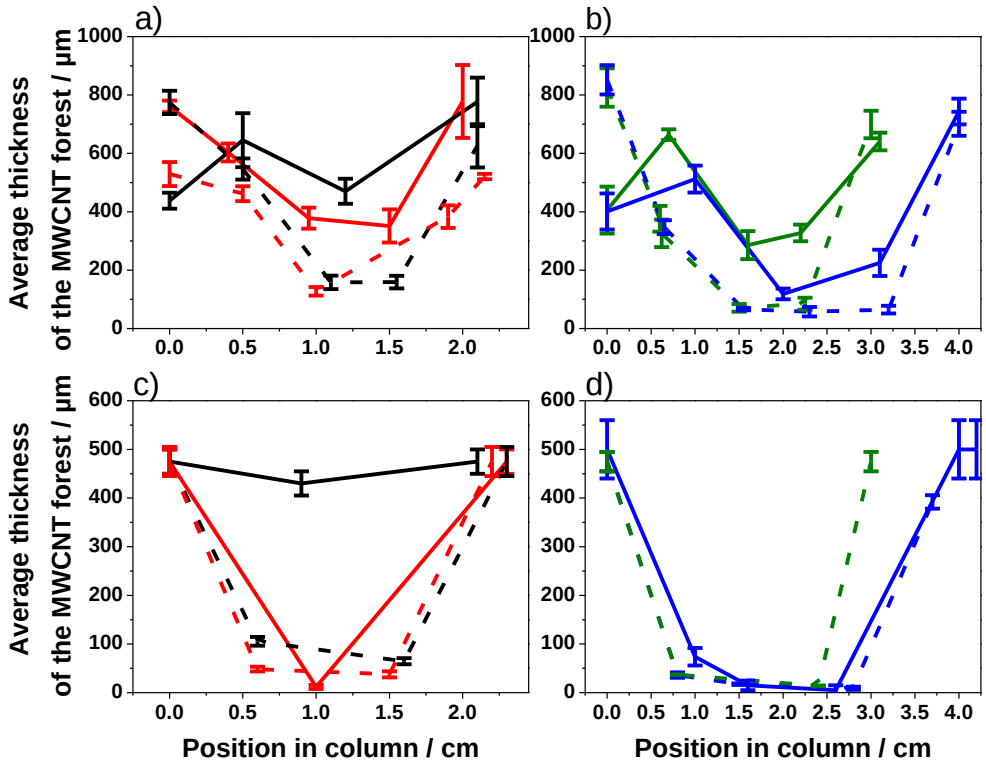

Figure 4.10. Average thickness of the MWCNT forest grown into the column as a function of the position in columns with (a and b) 2 mm and (c and d) 1 mm ID. Carrier gas flow rate was 2500 sccm (plain lines) or 1000 sccm (dashed lines) and results obtained for a column placed at 23 (black lines in a and c), 27 (blue lines and green lines in b and d) and 29 (red lines in a and c) cm within the furnace. Experiment duration was (a and c) 150 minutes or (b and d) 90 minutes.

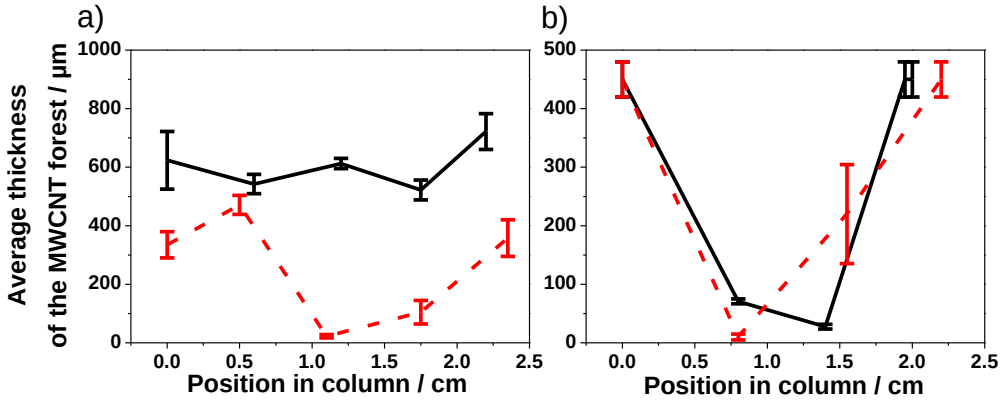

Figure 4.11. Average thickness of the MWCNT forest grown into a column as a function of the position in the column for 2 cm long column with (a) 2 mm and (b) 1 mm ID. Carrier gas flow rate was 5000 sccm and results obtained for a column placed at 39 (plain-black lines) and 45 cm (dashed-red lines) into the furnace. The duration of synthesis was 90 minutes.

Using 5000 sccm does not bring any advantage compared to the other flow rates investigated, **Figure 4.11**. First, a more uniform filling is now achieved for columns placed at 39 and 45 cm in the furnace. This is because for higher flow rate the time of residence of the hydrocarbon precursor is shorter in the reactor. The place in the furnace where an efficient MWCNT production happens is changed compared to the cases of 1000 and 2500 sccm. Second, for a same time of experiment more hydrocarbon precursor is consumed during the experiments at higher flow rate because a higher quantity of aerosol is pushed into the furnace. Third, the filling is not improved in terms of forest thickness and uniformity along the column compared to results obtained with 1000 sccm or 25000 sccm (**Figure 4.10**). For these reasons, 5000 sccm was not considered as a value worth investigating further.

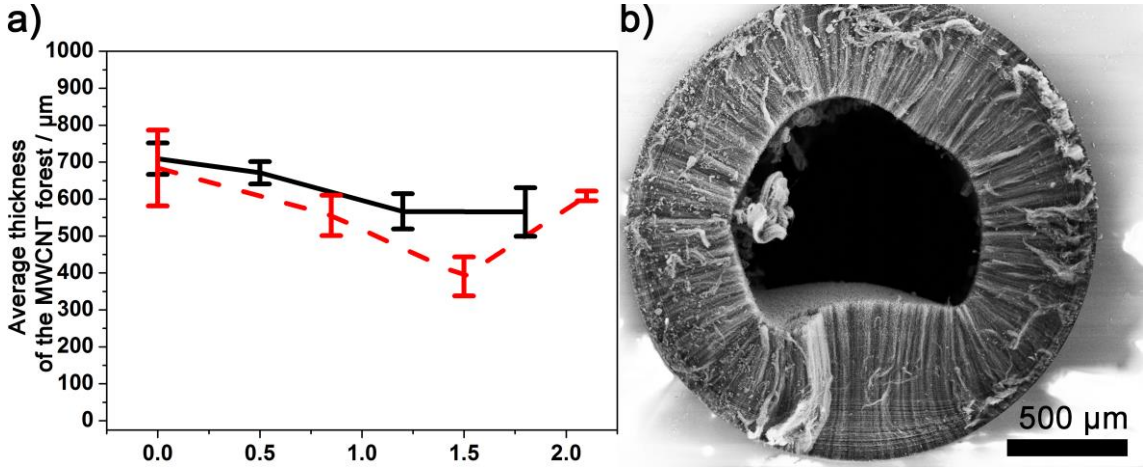

Figure 4.12. (a) Average thickness of the MWCNT forest grown into a 2 cm long with 2 mm ID column as a function of the position in the column. A change of carrier gas flow rate was performed during synthesis. Experiments were carried out over 20 minutes at 2500 sccm followed by 100 minutes at 1000 sccm. Samples were placed at 23 cm (plain-black line) or 29 cm (dashed-red line) in the furnace. (b) SEM micrograph of a cross section micrograph of a 2 mm ID CNC obtained during a synthesis where the flow rate is changed from 2500 to 1000 sccm.

The carrier gas flow rate values leading to a reasonable filling of the quartz columns are 2500 sccm and 1000 sccm. To investigate further the influence of the carrier gas flow value, experiments where the carrier gas flow rate was changed after a period of time *during* a single synthesis were performed. The aim was to minimise the amount of precursor used to develop a more cost-effective approach. Therefore only changes from 2500 sccm to 1000 sccm were investigated, **Figure 4.12**. With a 2 mm ID and 2 cm long column, the forest thickness is slightly more uniform along the column with a flow decrease during synthesis compared to the cases of a fixed value for the carrier gas flow rate, **Figure 4.12a** (to be compared with **Figure 4.10a** for instance). Similar observations are made for longer columns, **Figure 4.13a** (compared with **Figure 4.10b**). No improvements occurred for 1 mm ID, **Figure 4.13c-d**. A major change with a decrease in the flow of carrier gas *during* synthesis, *i.e. 'as'* the MWCNTs are growing, is that the MWCNT forest becomes non-concentric with the column axis of symmetry: **Figure 4.12b** (compared to **Figure 4.3b**). This new forest geometry probably results from different growth rate and adds evidence to the importance of the flow rate of carrier gas for controlling the filling of small inner diameter quartz columns with MWCNT forests. The flow change approach leads to more complex data interpretation but also a more complex synthesis procedure because there is a need to modify experimental parameters *during* the synthesis. As a consequence the flow change approach was not considered optimal to develop CNCs and was not investigated further. In particular the effect of a flow increase during synthesis was not explored.

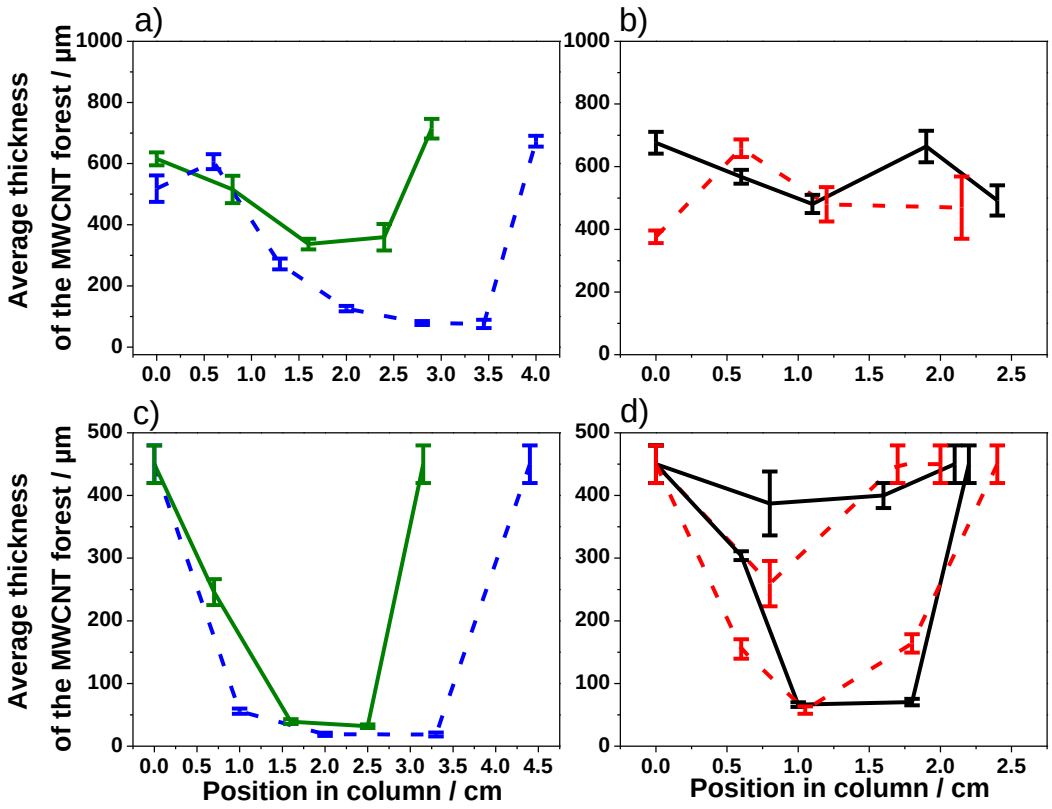

Figure 4.13. Average thickness of the MWCNT forest grown into CNCs with (a and b) 2 mm and (c and d) 1mm ID column as a function of the position in the column. A change of carrier gas flow rate was performed during synthesis. Experiments were carried with synthesis time of (a and c) 15 minutes at 2500 sccm continued for 75 minutes at 1000 sccm or (b and d) 20 minutes at 2500 sccm and 100 minutes at 1000 sccm. Samples were placed 23 (plain-black lines in b and d), 27 (blue and green lines in a and c) and 29 cm (dashed-red lines in b and d) within the furnace. Reproducibility of results displayed in Figure 4.12 is reported in (b).

4.3.2.6. Optimised AACVD synthesis of CNCs

Different parameters influence the direct growth of MWCNTs by AACVD into quartz columns of small ID. The uniformity of the filling with MWCNTs is mainly controlled by the flow rate or carrier gas, with 2500 sccm suitable to achieve an optimal filling. The uniformity is also controlled by the length and inner diameter of the column, with a length of 2 cm and an ID of 2 mm optimal. The duration of synthesis is the main parameter to control the forest thickness and 90 minutes was considered optimal to achieve maximal filling. The

position in the furnace also influences the filling and thicker forests were obtained between 23 and 29 cm for 2500 sccm. These parameters considered as optimal to produce CNCs are summarised in **Table 4.1**.

Table 4.1. Selected parameters to obtain CNCs with an optimised filling with MWCNTs.

Parameters	Value
Inner diameter of columns	2 mm
Length of columns	2 cm
Duration of synthesis	90 minutes
Flow rate of carrier gas (Ar)	2500 sccm
Zone in the furnace	23-29 cm into the furnace

The thickness profiles presented in this work are consistent and relatively well reproduced to fill columns of 2 mm ID with MWCNTs, even in the case of flow rate change during synthesis. For instance, the results presented in **Figure 4.13b** are obtained under the same conditions as the results presented in **Figure 4.12a**. In both cases the MWCNT forest average thickness is between 400 and 700 µm. However results are generally less reproducible for 1 mm ID column. In **Figure 4.13d** for instance the set of data in plain black correspond to two independent experiments. In one case, the minimum forests thickness is round 400 µm whereas it is around 50 µm in the other.

An important achievement is also the preparation of multiple CNCs by stacking columns on top of each other at the same position. For instance eight columns were placed at 23 cm and eight other at 29 cm during a same experiment performed with the optimal parameters identified in **Table 4.1**. The mass of MWCNTs deposited per column was 4.2 ± 0.8 mg at 23 cm and 8.5 ± 1.6 mg at 29 cm. Assuming a consumption rate of precursor of 8 mg s^{-1} for the experimental conditions used [234] this gives an overall conversion yield of 0.23 %. This is extremely low but most of the reactor as well as the outside of the small inner diameter quartz column are also covered with MWCNTs. These MWCNTs can be collected and use for other purposes but this thesis gives an exclusive focus to the MWCNTs

grown within the columns. The associated profiles for the forests thickness are similar for the eight columns at 23 cm or the eight columns at 29 cm, **Figure 4.14**. All columns show a consistent MWCNT filling: similar mass of deposited MWCNTs, equivalent forests thickness and profile. Forest thickness is however slightly thinner than in **Figure 4.4** for similar experimental conditions but with only one column used. This suggests that putting several columns at the same position may modify the flow distribution around each column. Nevertheless it proves that preparing multiple CNCs, up to 16 in the present study, with MWCNT forests thicker than 100 µm in each is possible in a single experiment. Despite the fact that the hydrocarbon flow is not forced to penetrate through the column as in other reports [140], this makes the AACVD approach proposed a simple method to obtain several CNCs at a time. The ability to produce and provide multiple CNCs is an important achievement to facilitate their investigation in flow catalysis in this thesis and broaden their applications in the long term.

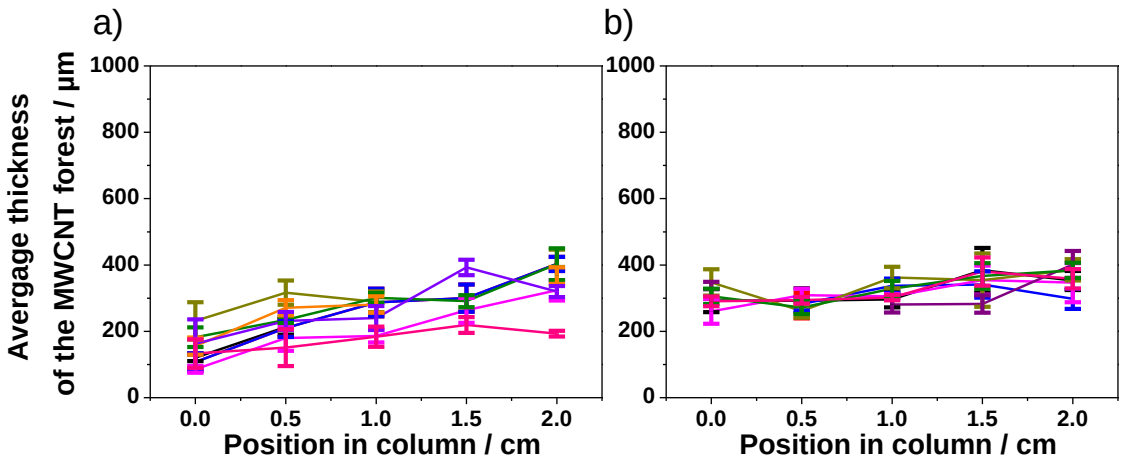

Figure 4.14. Average thickness of the MWCNT forest grown into CNCs with 2 mm ID and 2 cm long as a function of the position in the column. Experiments were carried with a duration of experiment of 90 minutes at 2500 sccm. Eight samples were placed (a) 23 and eight other samples at (b) 29 cm within the furnace. Data from each sample are represented in a different colour.

4.3.3. Control over MWCNT properties in a CNC

The differences observed between IN and OUT positions in terms of thickness of the MWCNT forest (**Figure 4.4**, **Figure 4.6**, **Figure 4.8** and **Figure 4.10**) deserve more investigation. During synthesis the hydrocarbon flow is likely to penetrate into the column, pass through the column and finally exit the column (**Figure 4.1**). Change in velocity and distribution of carrier gas flow at different locations may account for the differences in forest thickness and potentially control other properties like graphitisation along the column. In this section the differences in forest thickness are correlated with a Raman spectroscopy study of the MWCNTs. This gives information to further control MWCNT properties and to understand MWCNT growth in CNC.

4.3.3.1. Systematic Raman study of MWCNTs in a CNC

Raman is a simple and fast characterisation technique, sensitive to the graphitic structure of MWCNTs (**Section 2.3.4**). Raman can easily be performed on MWCNTs grown in a CNC after cross sections are cut. A systematic Raman study of the MWCNTs grown in CNCs was performed to assess the homogeneity of the graphitic structure of the MWCNTs obtained. The three different ratios of the three main Raman peaks observed in MWCNTs (**Section 2.3.6**) were calculated. A small I_D/I_G intensity ratio indicates a low defect MWCNT. The I_{2D}/I_G ratio can be a measure of the sp^2 hybridisation of the material in a similar way to I_D/I_G, except that I_{2D}/I_G will be of higher value if the MWCNT has low defect density. The I_{2D}/I_D ratio can be interpreted as another measure of sp^2 hybridisation to defects and should be of higher value when the defect density is lower. After removing the MWCNTs grown on the external walls of the columns (**Figure 4.2**) the various Raman intensity ratios measured at the IN and OUT positions display a lower standard deviation (**Figure A9**). It is then possible to systematically record and compare Raman spectra at the IN and OUT positions. By doing so for a number of experimental conditions (including

different ID), it was found that the I_D/I_G ratio is statistically different at these two positions for the same column. The other ratios: I_{2D}/I_G and I_{2D}/I_D were in most cases significantly different as well between IN and OUT positions (**Figure A10-A16**). However, the intensity ratios obtained on cross-sections of the columns (*i.e.* for MWCNTs grown *in* the column) were however not significantly different from IN or OUT positions and so were not investigated further (**Figure A12-A13**).

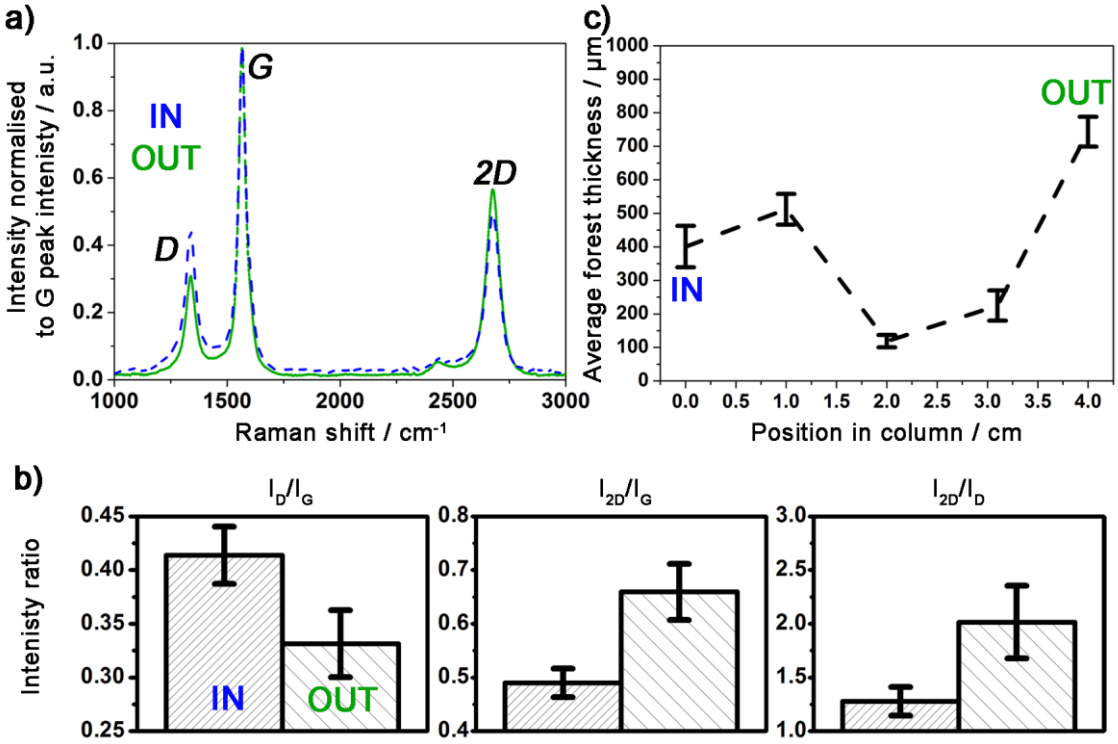

Figure 4.15. (a) Raman spectra for MWCNTs grown directly at the entrance of the columns (IN, dashed-blue line) or directly at the exit (OUT, plain-green line) of a 4 cm long column with 2 mm ID. Synthesis was performed with a carrier gas flow rate of 2500 sccm for 90 minutes. Substrate was placed 27 cm within the furnace. (b) Raman intensity ratios at the IN (dense stripes) and OUT (sparse stripes) positions of the column. (c) Profile of the average MWCNT forest thickness along the column.

The difference in Raman intensity ratio, and so the difference in graphitic structure of the MWCNTs grown at the IN and OUT positions, is best illustrated in **Figure 4.15** with the case of a 4 cm long and 2 mm ID column. Raman spectra at the IN position show a relatively

higher D peak intensity and smaller 2D peak intensity compared to the spectra recorded at the OUT position, **Figure 4.15a**. The I_D/I_G value is significantly smaller at the OUT that the IN, **Figure 4.15b**, and the two other ratios are also statistically different between the two positions. This observation can be correlated to the difference in forest thickness of MWCNTs at the IN and OUT position for this same column highlighted in **Figure 4.15c**. The thickness of MWCNT forest is significantly longer at the OUT than the IN position. This combination of lower I_D/I_G value and longer MWCNTs at the OUT positions, compared to higher I_D/I_G value and shorter MWCNTs at the IN position, was observed for flow rate of 2500 sccm for various other experimental parameters (**Figure A10-A15**). The difference in Raman intensity ratio between IN and OUT extremities was possible to observe on 2 cm long columns with 2 mm ID, **Figure 4.16**, but was more pronounced on columns longer than 2 cm with 2 mm ID or with column of 1 mm ID (**Figure A14**). In contrast, for a flow rate of 1000 sccm the inverse trend was noticed: MWCNTs have a smaller I_D/I_G value at the IN rather than the OUT of the CNC, while MWCNTs are now longer at the IN than the OUT position. This is quite pronounced even with columns of 2 cm long as illustrated in **Figure 4.16**. This was also observed on column with 1 mm ID (**Figure A14**). Therefore, by changing the flow rate of carrier gas used in an experiment at 1000 sccm to 2500 sccm in another experiment, it changes the end of the column where longer MWCNTs together with a more graphitic structure (smaller I_D/I_G ratio) are observed (**Figure 4.16**). A flow rate of 5000 sccm did not lead to any significant difference in the I_D/I_G ratio (**Figure A16**).

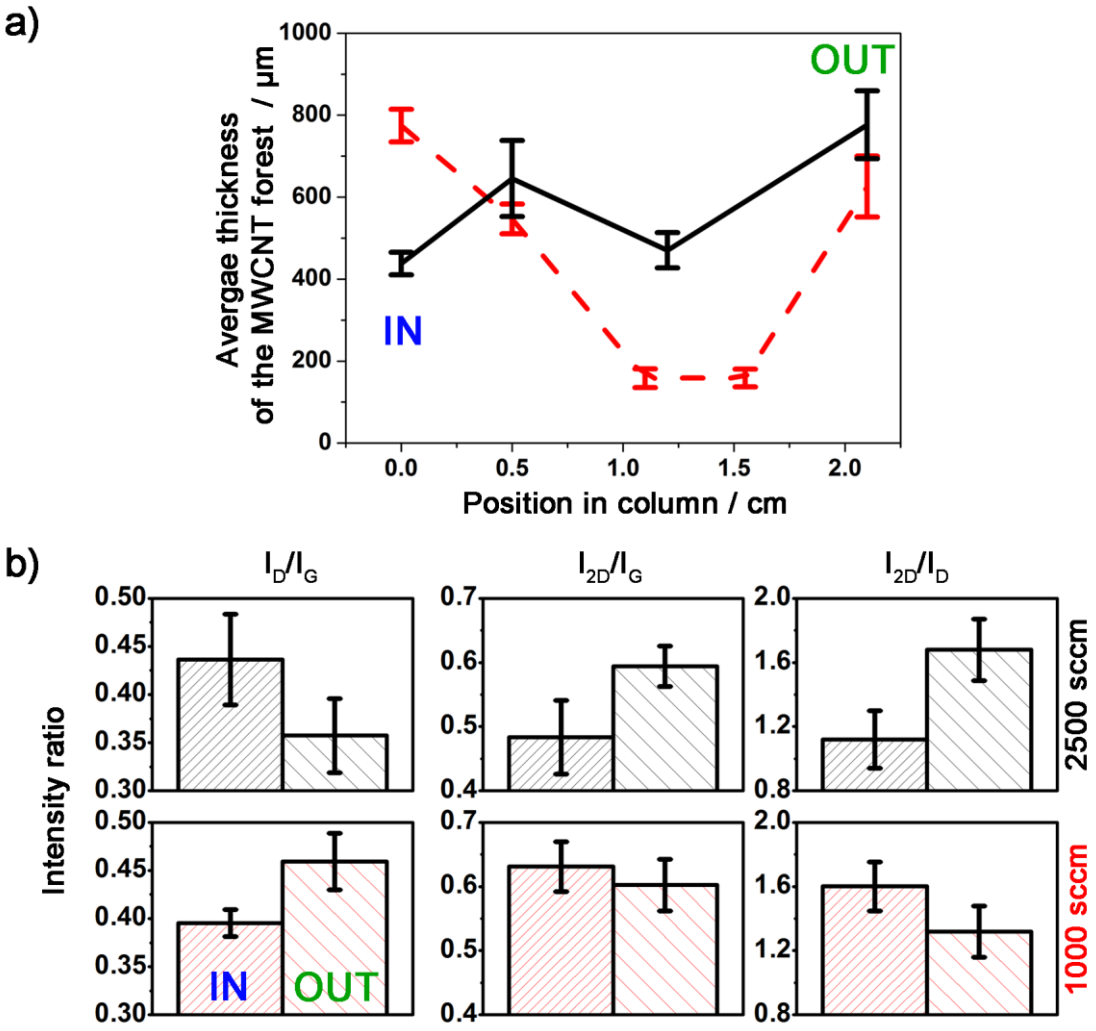

Figure 4.16. Effect of the carrier gas flow rate on (a) the MWCNT forest thickness profile in a column and (b) Raman intensity ratios at the IN (dense stripes) and OUT (sparse stripes) positions of a single CNC. The carrier gas flow rate was 2500 sccm (black line) or 1000 sccm (red line). All other experimental parameters were identical: the columns were 2 cm long with 2 mm ID, placed at 23 cm in the furnace during synthesis for a synthesis time of 150 minutes.

4.3.3.2. Control over MWCNT properties along a CNC: influence of carrier gas flow rate

The thickness of the forest in a CNC at IN and OUT positions together with its graphitic structures can be controlled by the flow rate of carrier gas (**Section 4.3.3.1**). This suggests that the flow velocity is an important parameter to control the filling of columns with

MWCNTs. It is likely that different flow regimes are developed on different sections of the column. This leads to different growth conditions for the MWCNTs and so could explain the different properties observed. The anisotropy of the flow around the column is likely to account for the different flow regimes. This anisotropy exists because the substrates are placed in the reactor with their cross section perpendicular to the flow of carrier gas during synthesis as illustrated in **Figure 4.17a**. Breaking the preferential orientation of the column to the flow may give a more uniform filling with MWCNTs. Columns may be placed as illustrated in **Figure 4.17b-c.** With the orientations (b) and (c) in the reactor, full coverage of the column internal wall with MWCNTs was possible. However the length of the column is limited to 15 mm by the quartz tube reactor of 21 mm ID. Also maintaining columns in position is challenging which makes the process less reproducible and more difficult to achieve. It was concluded that breaking the flow anisotropy in this study was not possible in a controlled way to improve the column filling with MWCNTs.

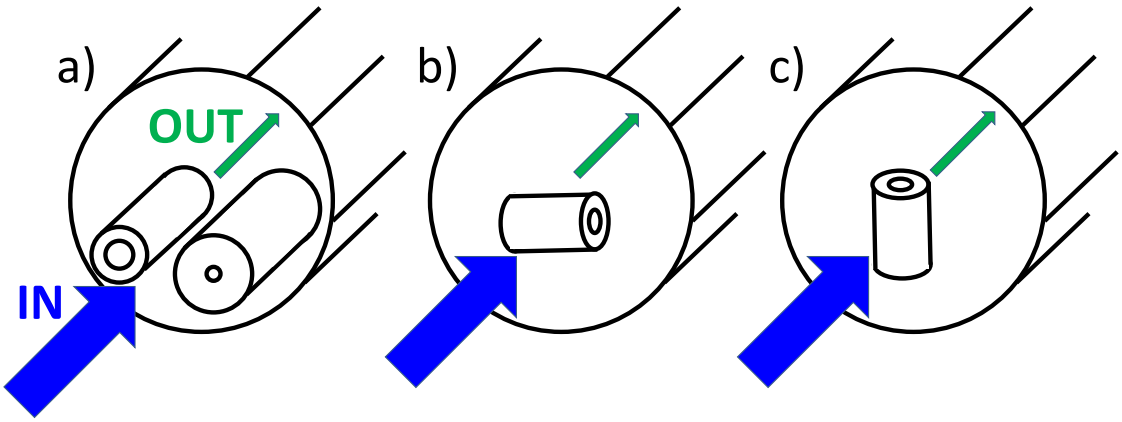

Figure 4.17. (a) Schematic representation of position of columns in the reactor during a standard synthesis: cross section facing the flow. (b) and (c) represent alternative column positions.

Instead, the anisotropy in the flow distribution can be enhanced. This is first done to investigate the hypothesis that different flow regimes are created around the quartz column during synthesis. At the same time, this is also done to confirm two trends reported in this study in terms of forest thickness achieved and difference in Raman intensity ratio at IN and

OUT positions. First, the forest thickness profile tends to be less homogeneous as the length of the column increases (**Figure 4.8**, **Figure 4.9**, **Figure 4.10** and **Figure 4.13**). Second, the difference in forest thickness and graphitic structures is more marked for longer columns and/or smaller inner diameter columns (**Figure 4.15**, **Figure 4.16** and **Figure A14**). An experiment was then performed with a 10 cm long column with 1 mm ID and a flow rate of 2500 sccm, **Figure 4.18**. As expected for this column longer than 2 cm and for this small inner diameter, most of the column was unfilled after synthesis. Most of the forest has a thickness smaller than 40 µm in the column. This result suggests that most of the hydrocarbon flow does not go through the column efficiently, thus preventing catalyst particle deposition and MWCNT growth. The growth of MWCNTs at the OUT position however occurs with an average forest thickness of 550 µm, thicker than the 200 µm at the IN position. This also means longer MWCNTs than the radius of the column channel which leads to a blocked column at the OUT position (**Figure 4.7**). As expected for 2500 sccm of carrier gas (**Section 4.3.3.1**), the I_D/I_G value is lower at OUT than IN positions, other peak intensity ratios are also significantly different. These observations confirm the trends reported in this study. In addition, it gives information on a possible growth mechanism. The OUT position is not directly facing the hydrocarbon flow during synthesis (**Figure 4.17a**). A possible explanation for the MWCNT growth is then some ‘back flow’ phenomenon through a turbulent regime to allow catalyst particles deposition and MWCNT growth at this location.

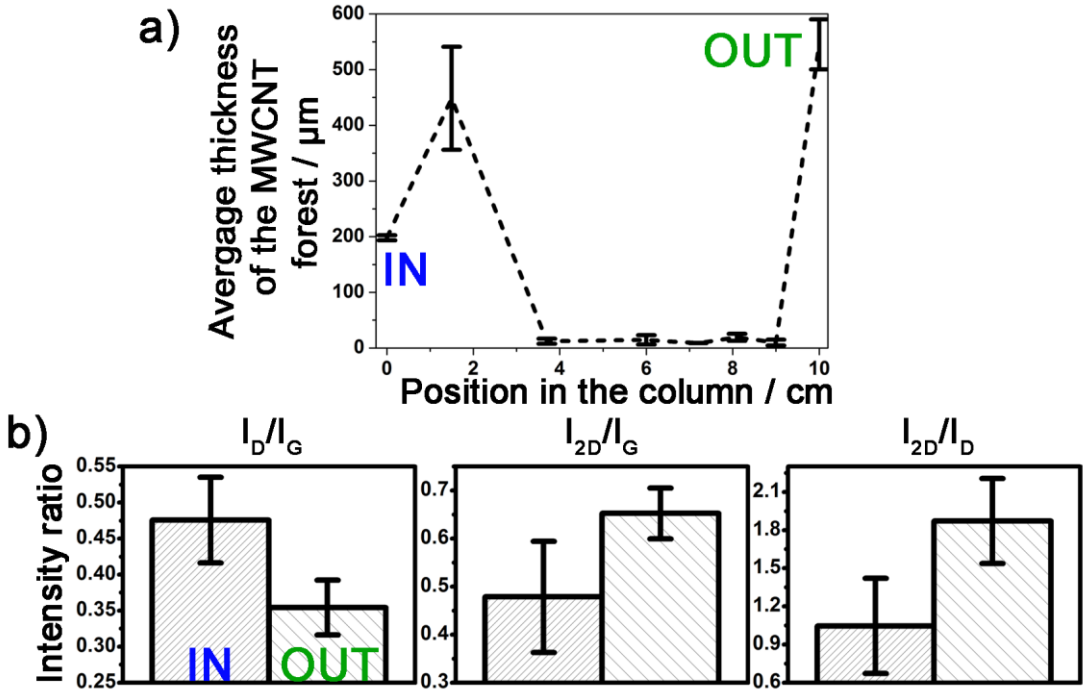

Figure 4.18. (a) Thickness profile of the MWCNT forest grown into a 10 cm long and 1 mm ID column as a function of the position in the column. Carrier gas flow rate was 2500 sccm and the duration of the synthesis was 90 minutes. Substrate was placed at 27 cm within the furnace. (b) Raman intensity ratio at the IN (dense stripes) and OUT (sparse stripes) positions for this same column.

4.3.3.3. Possible mechanism for the growth of MWCNTs in a CNC

Based on the observations reported, a general growth mechanism for the MWCNTs in a CNC can be suggested, **Figure 4.19**. The difference in forest thickness and I_D/I_G value at the IN and OUT positions and the un-complete filling with MWCNTs in the CNCs can be explained by the influence of the flow rate of carrier gas. Depending on the carrier gas flow value (2500 or 1000 sccm), different conditions for the formation of the catalyst particles from ferrocene and responsible for MWCNT growth are likely to be induced at the IN and OUT positions. Roughly, at the IN position the carrier gas flow and so the precursor carried by this flow, can directly access the inner channel where the MWCNT growth happens, **Figure 4.19a**. The carrier gas flow is however not going through the column efficiently and this accounts for shorter MWCNTs so a lower thickness of MWCNT forests, **Figure 4.19b**.

The growth of MWCNTs at the OUT position, which is not directly facing the carrier gas flow, can be explained by turbulences possibly induced at this position. This could generate a 'back flow', **Figure 4.19c**. The different flow regime also leads to different growth conditions, resulting in different properties of the MWCNTs grown at these different locations.

To attempt to further detail this observation the Reynold number [235] of the system can be estimated. The Reynold number is defined as:

$$\mathrm{Re} = \frac{\mathrm{Lu}}{\mathrm{v}} = \frac{\mathrm{L\,F}}{\mathrm{v}\,\pi\mathrm{R}^2} \qquad (\mathbf{B})$$

u is the velocity of the gas (in m s^{-1}), L is a typical distance in the system (in m), and v the kinematic viscosity of the gas used as carrier gas (in m^2 s^{-1}), F is the flow of carrier gas (in m^3 s^{-1}) and R the radius of the quartz tube used as reactor (in m). The estimation of the highest value for Re for the system is obtained taking L as 0.55 m (length of the furnace), F as 2500 sccm so 4.1 10^{-5} m^3 s^{-1} and v as 1.26 10^{-5} m^2 s^{-1} for argon at 25 °C. This gives Re of ca. 1200 at 25 °C. Since v decreases as the temperature increases it can be concluded that Re at 800 °C is inferior to 1200 which corresponds to a laminar flow. For F being 1000 sccm the value of Re will be even less. For both cases of a flow of carrier gas equal to 2500 sccm or 1000 sccm it can be expected, in a rough approach, that the flow regime will be laminar (Re < 2000). Therefore estimating Re does not give much insight into the growth mechanism of the MWCNTs in the proposed approach. However the rough estimation proposed does not take into account the specific geometry of the tubes and the possible fast change in temperature at the entrance of the furnace.

In a similar way the Knudsen number [235] can be estimated assuming a Boltzmann gas:

$$\mathrm{Kn} = \frac{\lambda}{\mathrm{L}} = \frac{\mathrm{k_B T}}{\sqrt{2}\,\pi\,\mathrm{L\,P\,d^2}} \qquad (\mathbf{C})$$

With λ the mean free path of the argon molecules (in m) and L a typical length scale in the system (in m), k_B is the Boltzmann constant (in J K^{-1}), T is the temperature (in K), P is the pressure in the system (in Pa), d is the particle hard shell diameter (in m). Using k_B as 1.38 10^{-23} J K^{-1}, T as 1073 K, d in the range of 10^{-10} or 10^{-9} m, P close to atmospheric pressure for the system considered so ca. 10^6 Pa and L about 0.002 m this gives Kn inferior to 10^{-3}. This suggests that the mean free path of the molecules of catalysts and hydrocarbon is much smaller than the typical size of the small inner diameter column used. Therefore the growth conditions with the small inner diameter columns should not be different from the growth conditions in usual CVD systems. In that case again the Knudsen number does not give much insight into the growth mechanism in the mini-reactors.

More detailed flow modelling taking into account the effect of the tubular geometry of the column would certainly give more detailed inside into the influence of the flow. This is however beyond the scope of this study. Nevertheless the simple explanation proposed can also account for the different MWCNT filling obtained with a flow rate change during synthesis (**Figure 4.12**). Changing the flow rate of carrier gas promotes different growth conditions along the column *while* the MWCNTs are formed. This could explain the slightly more homogenous filling along the column but also the difference in forest thickness in a single cross section (**Figure 4.12b**).

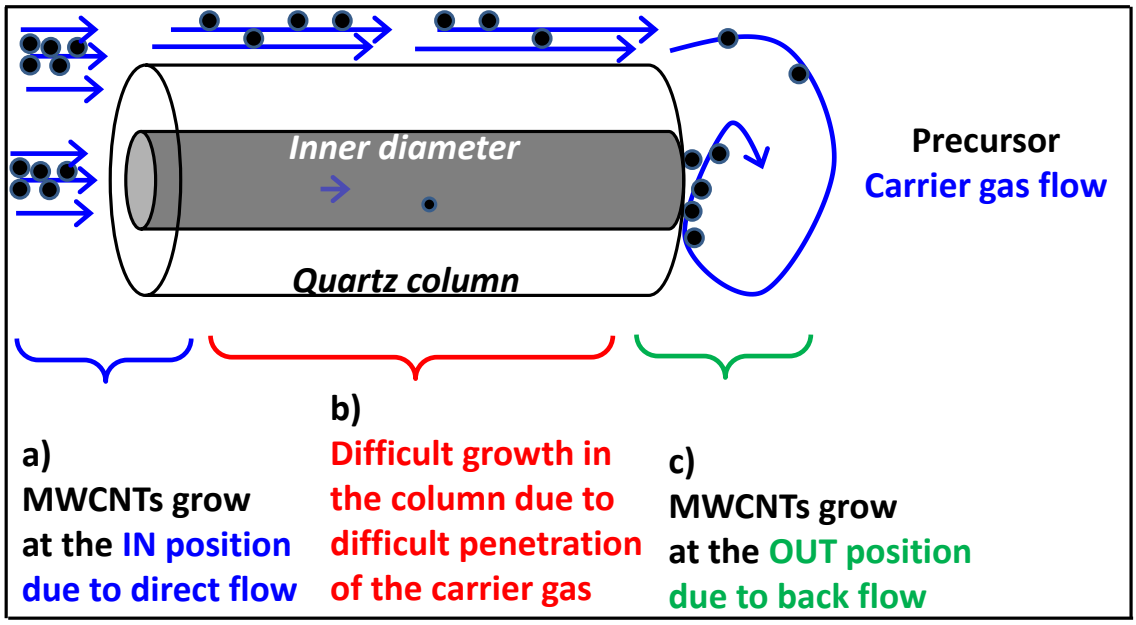

Figure 4.19. Schematic representation of a possible mechanism to explain the growth of MWCNTs in CNCs.

4.3.3.4. Control over MWCNT reactivity with oxygen along a CNC

Using columns as substrates and controlling the flow rate of carrier gas gives control over forest thickness and graphitic structures in a CNC. The oxidation resistance is also important to control to operate the CNC under conditions where the MWCNTs are not damaged by oxidation, for instance in the context of high-temperature flow catalysis. Assessing the oxidation resistance of the MWCNTs is not directly relevant for the scope of biocatalysis performed at room temperature or under mild conditions but is important to illustrate the versatility of the CNCs.

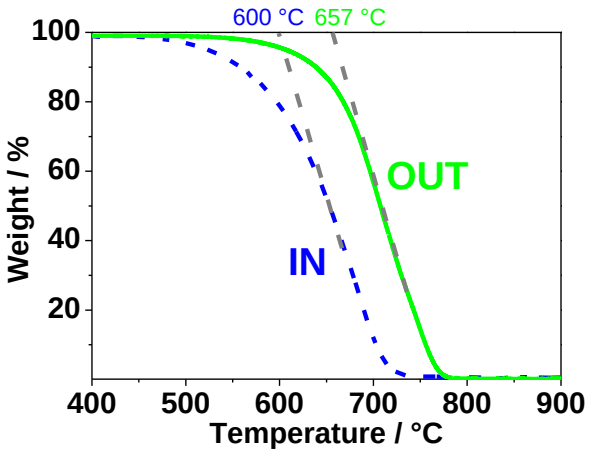

Figure 4.20. Thermogravimetric analysis of MWCNTs collected at the IN (dotted-blue line) and OUT (plain-green line) position for a CNC of 2 mm ID obtained with a flow rate of argon at 2500 sccm with a synthesis time of 90 minutes and located at 23 cm in the furnace.

The TGA analysis (**Section 2.3.7**) of MWCNTs collected in CNCs shows that MWCNTs react with oxygen at temperatures higher than 500 °C only (start of mass loss), **Figure 4.20**. This indicates that the CNCs are stable at high temperature (< 500 °C) in an oxygen environment. However, MWCNTs collected at the IN and OUT position have different oxidation resistance: onset temperature of 600 °C and 657 °C respectively. In the case of a carrier gas flow rate of 2500 sccm, 10 % of the MWCNTs grown closer to the IN position (plain-green) have reacted with oxygen at 560 °C. The same amount of MWCNTs reacts only at 640 °C if the MWCNTs are grown closer to the OUT position (dashed-blue). This means than the MWCNTs at the OUT position have a higher oxidation resistance than the MWCNTs grown at the IN position. This is consistent with the difference in thickness and graphitic structure observed because more graphitic materials usually have a higher oxidation resistance due to the strong structure-properties relationship within a MWCNT [92, 93]. This is an important side observation in the broader context of improving the production of MWCNTs by AACVD. These results show that forest thickness, graphitic structure and oxidation resistance of MWCNTs obtained by AACVD can be simply

controlled by considering the geometry of the substrate used and the flow rate of carrier gas during synthesis.

4.3.3.5. Investigating the robustness of the MWCNT forest

To be suitable for enzyme immobilisation, the MWCNT network must be robust and interconnected. The main focus of this work is on the MWCNTs grown within the columns which are not simple to investigate because they are surrounded by a quartz shell. However, vertically-aligned forests pictured in **Figure 4.21a-b** are grown perpendicular to the IN and OUT surfaces of the column as schematised in **Figure 4.21c**. MWCNTs grown on these surfaces lead to 'ring-like' structures visible in **Figure 4.21b**. When MWCNTs are grown long enough, they can be removed with tweezers leading to free-standing rings of MWCNTs, **Figure 4.21d-f**. In the photos in **Figure 4.21d-e** the MWCNTs are perpendicular to the plane of the support where the MWCNT forests are placed. This is schematised in the 'top view' presented in **Figure 4.21f**. If the flow of hydrocarbon was forced through the columns, these structures could not be obtained since the column external surfaces (blue in **Figure 4.21c**) would not be accessible for MWCNTs growth. These rings illustrate the cohesion of the MWCNT creating a solid and free-standing forest. This strongly suggests that an interconnected carbon network is also developed within the columns.

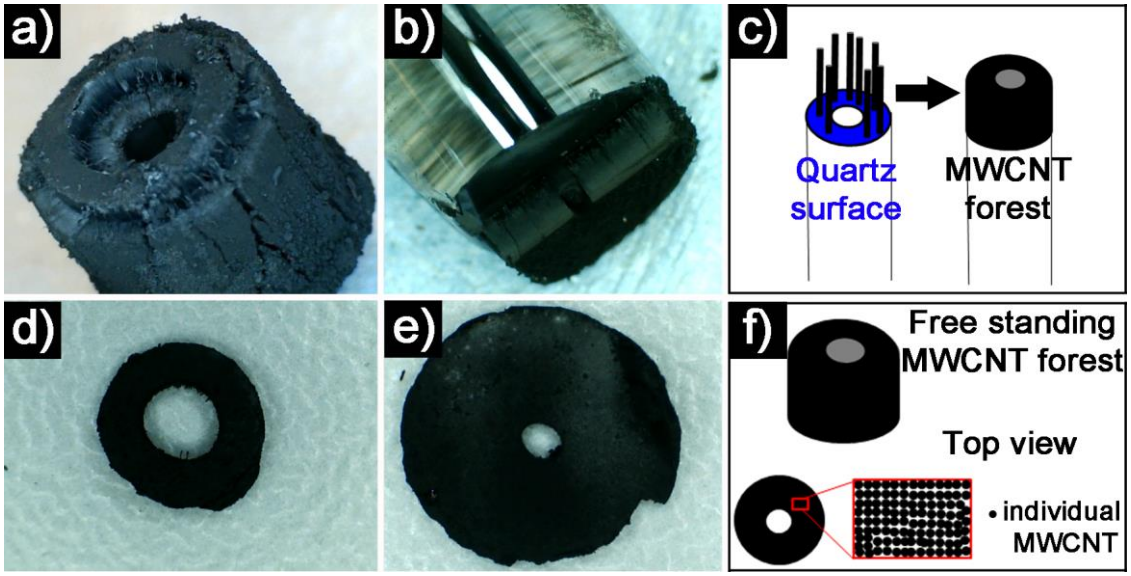

Figure 4.21. Photos of: (a) 2mm ID column fully covered with MWCNTs on all the outside surface of the column. (b) 1mm ID column after removing the MWCNTs grown on the outer surface. Half of a ring-like MWCNT forest is still visible. (c) Schematic representation of the formation of the ring-like MWCNT forests. (d) and (e) show the rings obtained from 2 mm and 1 mm ID columns respectively, once the ring has been removed from the column. The MWCNTs in (d) and (e) are perpendicular to the support as illustrated in the schematised 'top view' in (f). The red square is an enlargement of the top view of the MWCNT ring. A black dot in this red square represents an individual MWCNT.

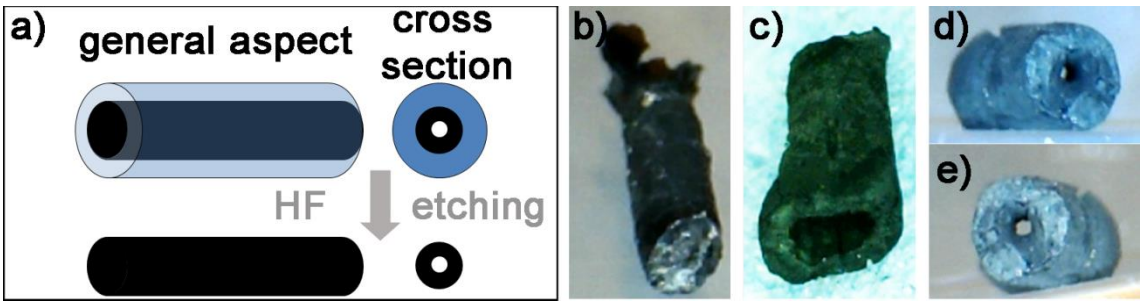

Figure 4.22. (a) Schematic representation of the quartz shell (blue) removal to get free-standing CNCs (black) after HF treatment. Photos of the free-standing CNCs obtained from (b) 1 mm ID and (c-e) 2 mm ID columns.

To assess the robustness of the inner MWCNT forest, free-standing CNCs can be obtained after removing the quartz column, **Figure 4.22a**. This can be done by HF etching: CNCs were placed in a solution of 10 or 20 % HF in water and sonication was performed for 5 to 10 minutes; followed by intensive washing with water. The free-standing columns of MWCNTs (without quartz shell), **Figure 4.22b-e**, could be relevant for filtration devices as already reported in the literature [140]. However, the mechanical stability achieved in this thesis is not high enough to connect the free-standing columns to any tubing. A specific focus is then given in the next sections to flow catalysis avoiding the hazardous HF treatment. This is to take advantage of the mechanical link between the MWCNT forest and the quartz as well as the high surface area carbon network developed in the column. The robust carbon network developed should be suitable for enzyme immobilisation without need for chemical or thermal treatment, so no need for binder or fillers are required to stabilise the column.

4.3.4. Towards continuous flow catalysis using CNCs

AACVD is a simple technique to obtain several CNCs in a single experiment (**Section 4.3.2**) while controlling the column filling and MWCNT properties (**Section 4.3.3**). Due to their geometry, CNCs are promising scaffolds for flow catalysis and their compatibility with flow applications involving redox processes is investigated in this section.

4.3.4.1. Compatibility of CNCs with a solution flow

An important step towards application of CNCs to flow devices is the ability for the column to support a stream of solvent without removing the MWCNTs. This was assessed by flushing water with a syringe barrel attached to a CNC as displayed in **Figure 4.23a**. Alternatively, a peristaltic pump was used to pass a flow of water through the column. In both cases the flow is passed without noticeable loss of the MWCNTs and with relatively

low pressure. Low pressure minimises hazard and cost compared to several-bar pressure required in other flow devices based on packed-bed columns [129, 130], chromatographic columns [140, 141, 145, 146], flow reactors and micro-reactors [110, 113], or other monolithic structures for flow catalysis [135]. The low pressure needed can be explained by the CNC design, **Figure 4.23b**. The columns are partially filled (**Figure 4.2**, **Figure 4.3b-c**) which could facilitate a flow of water through the column despite a hydrophobic network. MWCNTs are not agglomerated but individualised due to their alignment (**Figure 4.3d**) which has been suggested to promote wettability [144] and to enhance the flow distribution within the carbon scaffold [69, 139]. For 'blocked-core' columns (**Figure 4.5**), it was not possible to get any liquid through the CNC by applying pressure with a syringe, **Figure 4.23b**. This observation indicates that CNCs stand some pressure without loss of the MWCNTs and could be relevant for water purification or filtration. These possible applications were not investigated further to focus on flow redox catalysis in this thesis.

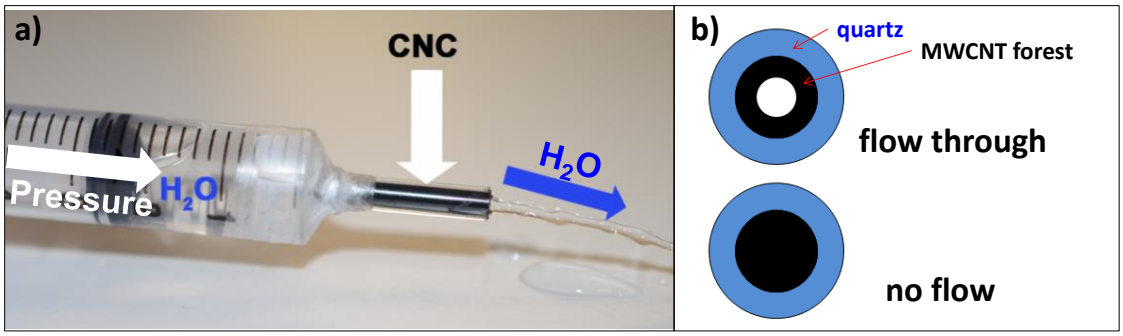

Figure 4.23. (a) Photo of a stream of water going through the CNC under moderate pressure applied with a syringe. The CNC (2 mm ID, 2 cm long) is used as a needle. (b) Schematic representation of a cross section of hollow and blocked core CNCs where a flow can respectively be passed and not.

4.3.4.2. Conductivity of CNCs for flow-redox catalysis

An important requirement for the CNC to be compatible with the enzyme cascade described in **Section 1.2.4** is to achieve conductivity across the CNC. In order to assess the conductivity of the MWCNT network, an electrode was made out of a CNC. This was done

by connecting carbon yarn with conductive epoxy glue at one end of the column, **Figure 4.24a**. The other end was dipped into an aqueous solution of a platinum IV complex salt, yellow in **Figure 4.24a**, and electrodeposition of platinum was performed as described in **Section 2.7**. The CNC was used as working electrode and the potential was cycled up to 50 times between -0.54 and +0.46 V *vs* SHE at a scan rate of 50 mV s^{-1} to deposit platinum by electroreduction. **Figure 4.24b** is an SEM micrograph showing after electrodeposition the extremity of the column that was dipped in the platinum salt solution. Structures appearing in white in the SEM micrograph were not present before electrodeposition (**Figure 4.3d**) and cover the MWCNTs. EDS confirms that they are made of platinum (**Section 2.7**). The formation of these structures is only possible because the electrons travel *through* the CNC, meaning the MWCNT network is conductive. These results also illustrate a first approach to functionalise CNCs.

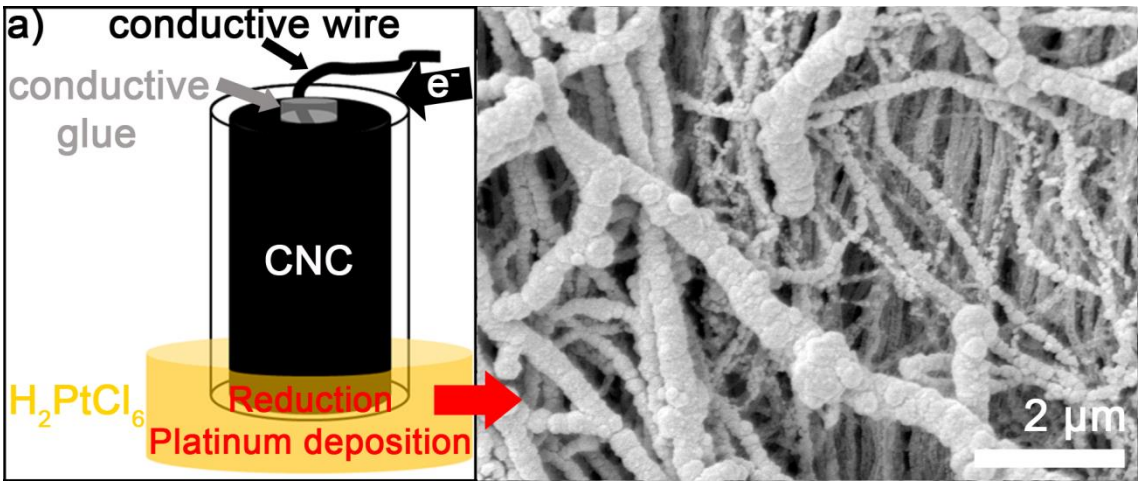

Figure 4.24. (a) Schematic representation of an electrode made of a CNC for platinum electrodeposition. (b) SEM micrographs of the extremity of a CNC dipped into a solution of platinum salt after electrodeposition.

4.3.4.3. Immobilisation of molecules and particles in CNCs

To use CNCs for biocatalyst immobilisation it is important to show that molecules and/or particles can be immobilised in the MWCNT network. In order to establish if the carbon network in a CNC could accommodate immobilised or trapped species, aqueous solutions of

the Raman active molecule fluoresceinamine, **Figure 4.25**, were left to adsorb within the CNC. Adsorption of fluorescein-based molecules is expected by π-stacking on CNT surface [236] and the presence of this species can be assessed by Raman spectroscopy. A saturated aqueous solution of fluoresceinamine (6-aminoafluoresceine, ≥ 90 %, Aldrich) was obtained in MilliQ water. The solution was flushed into a CNC by successive uptakes of solution with a syringe as illustrated in **Section 4.3.4.1**. The column was then left overnight in the solution. This step favours solution uptake into the MWCNT network by capillary force. The column was then thoroughly washed with MilliQ water and left to dry at room temperature in air prior to Raman measurements.

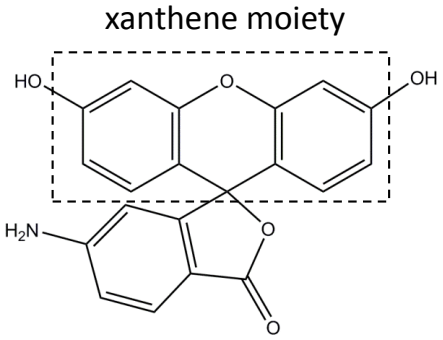

Figure 4.25. Molecular structure of fluoresceinamine.

Raman spectra acquired on a CNC after adsorption of fluoresceinamine are displayed in **Figure 4.26a**. The peaks at 1340 and 1565 cm^{-1} are mainly the characteristic D and G peaks from the MWCNTs. Additional peaks at 1179, 1414, 1474, 1504 and 1634 cm^{-1} correspond to vibrations in the xanthene moiety of fluoresceinamine [237, 238], **Figure 4.25**. These peaks confirm immobilisation of fluoresceinaine in the CNC carbon network. The characteristic peaks of the probe molecule are especially clear at the extremity of the column in direct contact with the solution during overnight adsorption: fine-green line in **Figure 4.26a**. These peaks were also observed after cross sections cut in the middle of the column: bold-red line in **Figure 4.26a**. A schematic representation and photos of the

exposed extremities and the cross section cut after fluoresceinamine adsorption are represented in green and red respectively in **Figure 4.26b**.

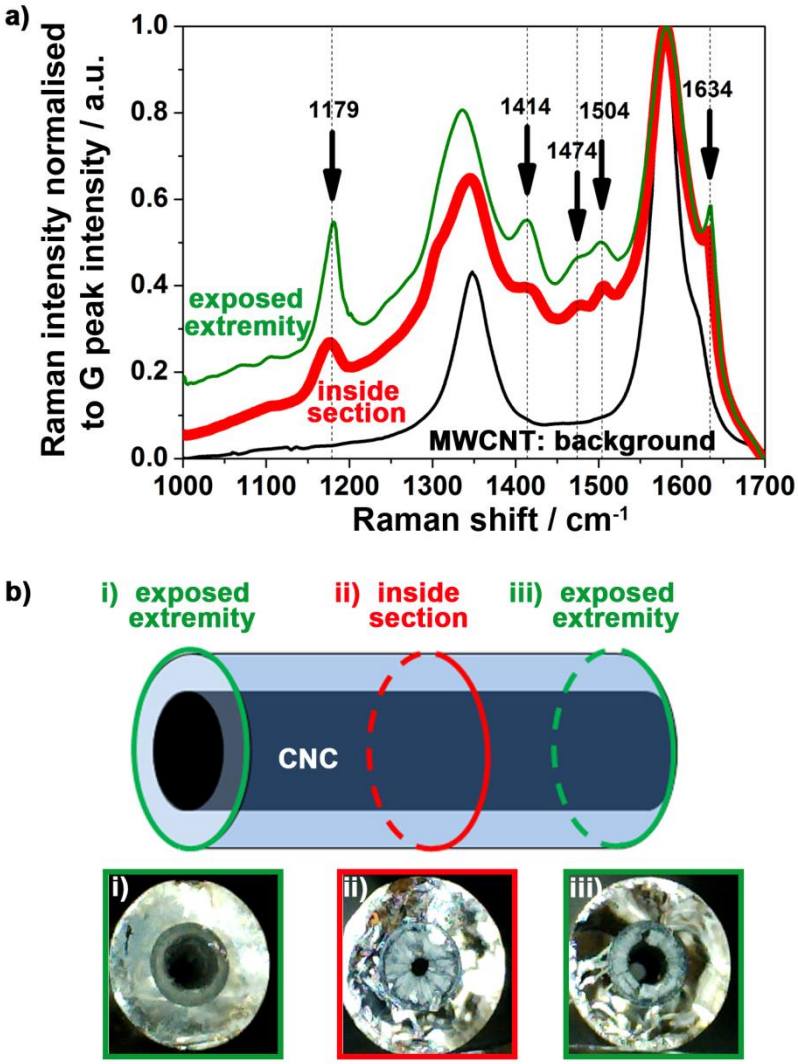

Figure 4.26. (a) Raman spectra of MWCNTs in a 2mm ID CNC after fluoresceinamine adsorption. Spectra were recorded at the extremity of the column (fine-green line) or inside the column after cross section (bold-red line) as illustrated in (b). A MWCNT spectrum without fluoresceinamine under identical acquisition parameters is reported in fine-black line as the background signal. (b) Schematic representation and photos of the two extremities (i and iii) of the CNC used and a section in the middle of the column (ii). In the photos the quartz surface appears in white, the MWCNTs in grey and the inner channel free of MWCNTs in dark.

The photos show that the MWCNT network is not altered by the protocol for fluoresceinamine adsorption and the middle of the column had a relatively thick MWCNT forest. Without further optimisation, the signal from fluoresceinamine was recorded up to 20-40 µm from the top of this thick MWCNT forest in the CNC. Similar results with columns of different length or alternative probe molecules were obtained (**Figure A17** and **Figure A18**). Raman spectra reveal peaks characteristic of the probe molecule in all cases. These results show that it is possible to simply adsorb various species into the MWCNT network from aqueous solutions and despite the hydrophobicity of the MWCNTs.

In order to illustrate the versatility of the CNC it is also important to show that catalyst particles can be immobilised within the CNC network. Platinum particles were used because they are simple to identify by SEM and EDS (**Chapter 2**). An as-synthesised CNC was left for 1day in concentrated sulphuric acid (98 %) to improve the hydrophilicity of the MWCNT network. This acid treatment did not remove the MWCNT network. The CNC was then thoroughly washed with MilliQ water. The CNC was left for another day in 10 mL of an aqueous solution of $H_2PtCl_6.6H_2O$ (21 mM) to impregnate the forest. After a day, 0.5 mL of HCOOH was added to chemically reduce the salt to form platinum particles. After 12 hours, the sample was thoroughly washed with ultra-high purity water. During all steps the solution was stirred. Cross section cut in the middle of the CNC was then performed for imaging and analysis. The SEM micrograph displayed in **Figure 4.27a** represents the MWCNTs on the cross section performed. Presence of white, conductive dots on the SEM image is indicative of a successful chemical reduction of the platinum salt within the CNC. Formation of platinum particles is further confirmed by EDS analysis in **Figure 4.27b** with a characteristic peak at 2.100 keV for platinum in the EDS spectrum (**Section 2.3.8**).

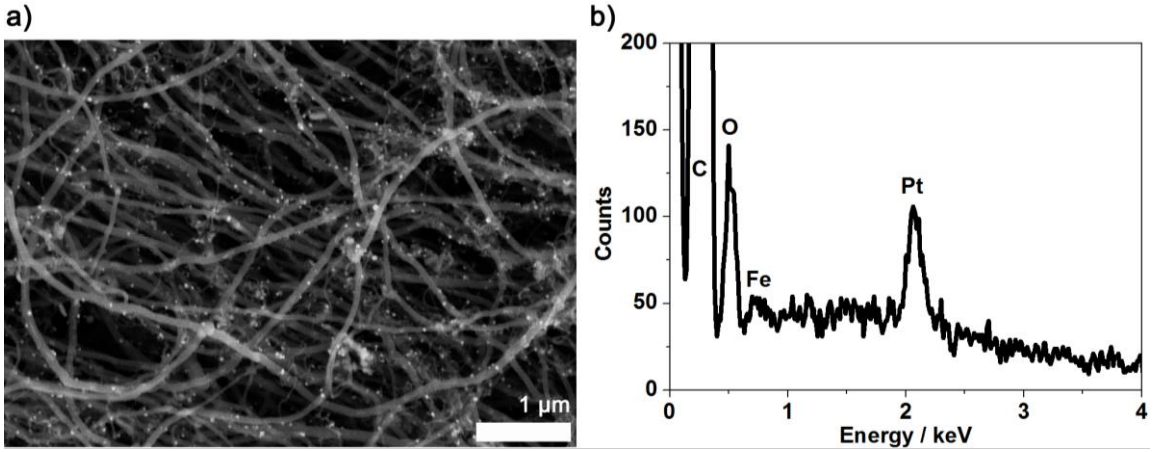

Figure 4.27. a) SEM micrograph of a cross section from the middle of a 2 cm long CNC after chemical reduction of platinum IV reveals the presence of conductive particles: white dots on the MWCNTs. (b) EDS analysis confirms the presence of platinum-based species on this cross section only after chemical reduction.

These results suggest that a variety of metal particles and metal catalysts could be immobilised in the CNC, for instance by a simple chemical reduction as for the platinum particles in this thesis. Immobilisation of metal catalyst in a vertically-aligned MWCNT forest has already been exploited in flow catalysis (**Section 1.2.4**). However several bar pressure [135] or temperature higher than 100 °C [69] were required to operate the flow system or to functionalise the CNTs. The CNTs in those reports were selected to provide a high surface area. The present thesis gives for the first time a specific focus to flow biocatalysis at room temperature and low pressure with immobilisation of the catalyst by simple adsorption in order to minimise the energy requirement to perform catalysis. Furthermore, the conductivity of the MWCNT forest is also exploited in this thesis.

4.3.5. Flow catalysis with CNCs: hydrogenase as a case study

The enzyme cascade catalysed chemical synthesis detailed in **Section 1.2.4.2** is relevant for production of fine chemicals [20]. Transposing this cascade to a flow system would be

beneficial for industrial applications. For the first time, combining flow catalysis and bio-redox-catalysis *via* the use of vertically-aligned MWCNTs is addressed with the CNCs designed. As a demonstration, an enzyme cascade made of an hydrogenase, a NAD^+-reductase and an NADH dependent enzyme (an alcohol dehydrogenase, ADH) co-immobilised within a CNC is used in a flow configuration to convert acetophenone to 1-phenylethanol, a product used in the perfume industry [239].

4.3.5.1. Towards *in situ* NAD^+/NADH recycling in a CNC

Efficient cofactor generation performed by an enzyme cascade in the CNC relies on the *in situ* formation of NADH from NAD^+ by the NAD^+-reductase as illustrated in **Figure 4.28**. The biotransformation is possible due to the efficient oxidation of H_2 by the hydrogenase to provide the required electrons (**Section 1.2.4.1**). This means that the two enzymes must be electronically connected through the carbon network.

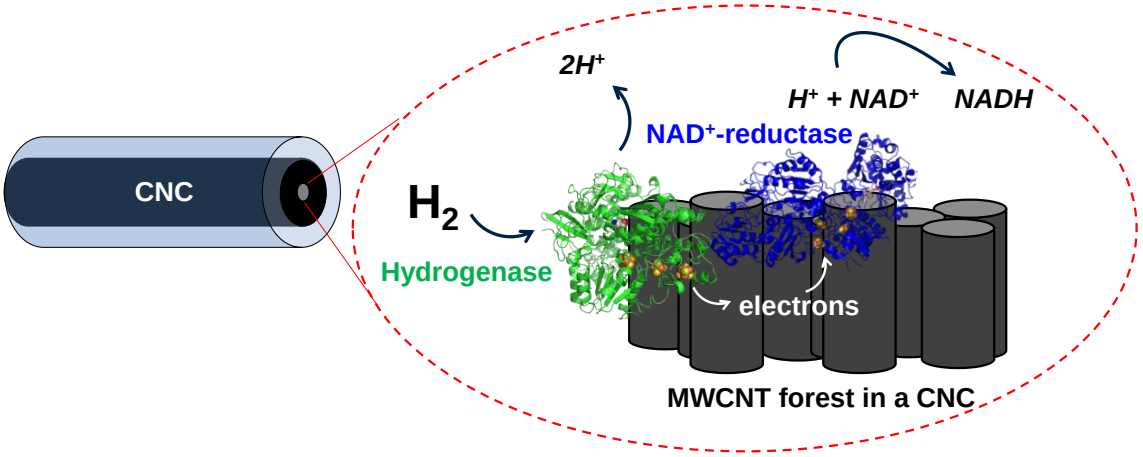

Figure 4.28. Schematic representation of enzyme-catalysed H_2-driven NADH generation in a CNC. The electrons from H_2 are passed from the hydrogenase to the NAD^+-reductase through the conductive MWCNT network in the CNC.

A CNC obtained with parameters highlighted in **Table 4.1** was used as-produced, without any other treatment, to support the adsorption of the two required enzymes. A hydrogenase (*D. vulgaris*, 35 µg, provided by Prof Wolfgang Lubitz, *Max Planck Institute*

for Chemical Energy Conversion) and an NAD^+-reductase (40 µg, provided by Dr Oliver Lenz, *Technische Universitaet Berlin Institute of Chemistry*) were adsorbed at 4 °C for 30 minutes in the CNC. The CNC was then rinsed with 5 mL of bis-tris buffer (≥ 98 %, Sigma, pH 6, 10 mM) to remove un-adsorbed enzyme and used for H_2-driven NADH generation. A H_2-saturated solution (total volume 1.2 mL) containing NAD^+ (0.5 mM, from Melford Laboratories Ltd) was cycled at *ca.* 25 µL min^{-1} through the CNC into a UV-vis cuvette and UV-vis spectra were recorded at hour intervals. The solution was continuously flushed with 1 bar H_2 in the UV-vis cuvette headspace to ensure the reaction solution was saturated with H_2. Advantageously the conversion of NAD^+ to NADH can be monitored *in line* using UV-vis spectroscopy with NADH having an absorbance at 340 nm [213]. This is exploited to assess NADH generation in a flow set-up as schematised in **Figure 4.29**.

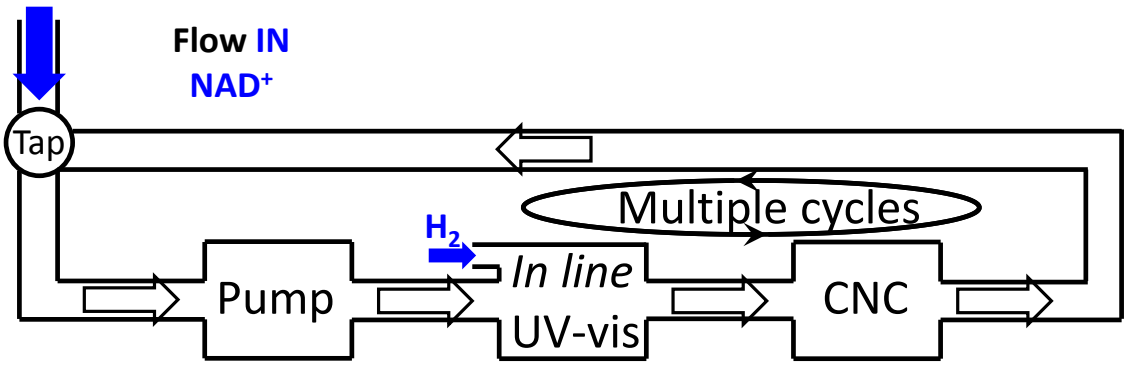

Figure 4.29. Schematic representation of the set up used to assess the formation of NAD^+ using a hydrogenase and a NAD^+-reductase co-immobilised in a CNC.

The UV-vis spectra in **Figure 4.30a** show a clear increase in absorbance at 340 nm over time, indicating formation of NADH (**Section 2.6.1**). The NAD^+-reductase cannot catalyse the oxidation of H_2. The electrons required for the formation of NADH from NAD^+ necessarily come from the splitting of H_2 by the hydrogenase which demonstrates that the hydrogenase and NAD^+-reductase are able to exchange electrons with each other via the conductive MWCNT network. Electron exchange is consistent with the results showing conductivity through the carbon network detailed in **Section 4.3.4.2**. It is also consistent with

the possibility to immobilise species in the MWCNT network detailed in **Section 4.3.4.3**. After 21 hours and multiple cycles, 40 % conversion of NAD^+ to NADH was achieved. The data from the first 21 hours is not shown because there was a significant lag phase due to the hydrogenase requiring activation. The data in **Figure 4.30b** correspond to hours 21 to 28 after addition of fresh NAD^+ solution. The enzyme modified CNC is still generating NADH at an appreciable rate after addition of fresh NAD^+ solution. Although multiple cycles through the CNC were required, a significant amount of NADH was made. Operation of the system after several hours indicates a promising long term stability of the enzyme regeneration system in the CNC. Successful H_2-driven NADH generation in a flow configuration is therefore demonstrated. This reaction could be further extended to supply NADH to a third enzyme for a specific reduction reaction to selectively convert a reactant to a product.

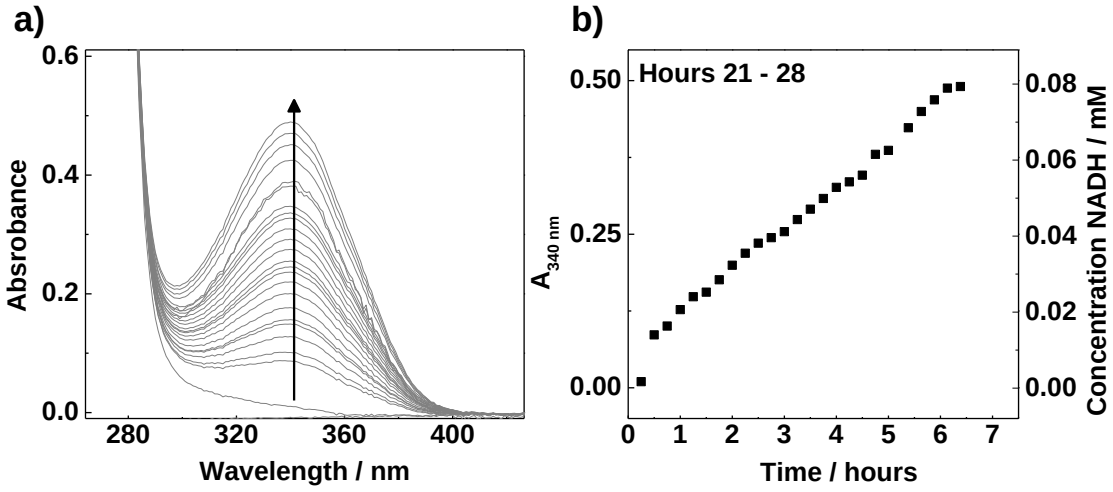

Figure 4.30. (a) UV-vis spectra showing an increase in absorbance at 340 nm and therefore (b) an increase of NADH concentration over time. A H_2-saturated solution containing NAD^+ was cycled through a CNC modified with hydrogenase and NAD^+-reductase into a UV-vis cuvette. Experiment performed in 10 mM bis-tris buffer, pH 6 at 22 °C. *With the assistance of Dr Holly A. Reeve, Department of Chemistry, University of Oxford* [122].

4.3.5.2. Enzyme-mediated catalysis in a CNC

In order to assess the relevance of the CNCs for H_2-driven NADH-dependent chemical synthesis, a third enzyme was added to the system as schematised in **Figure 4.31**. It is expected that the ADH will be able to consume the NADH formed *in situ* to perform the hydrogenation of acetophenone to 1-phenylethanol.

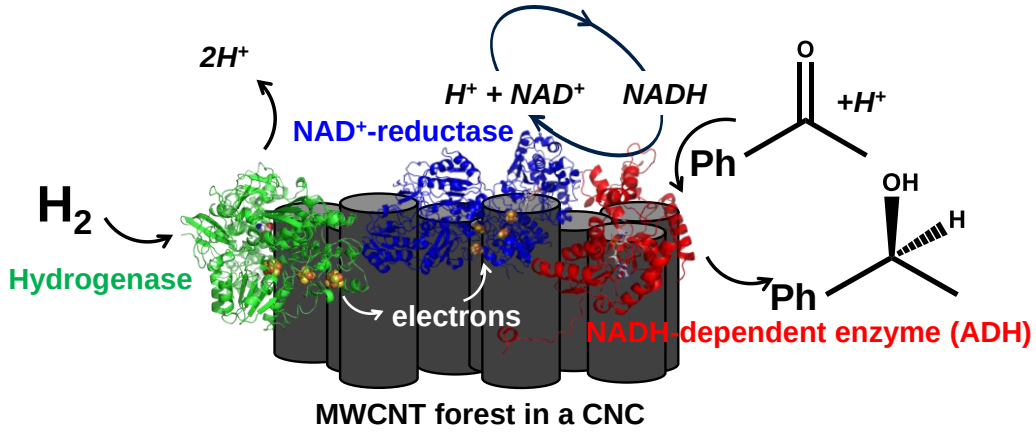

Figure 4.31. Schematic representation of enzyme-catalysed H_2-driven ketone reduction in a CNC. ***Adapted from Dr Holly Reeve's DPhil thesis, Department of Chemistry, University of Oxford*** **[122].**

A CNC with adsorbed hydrogenase (Hyd-1, 27 µg), NAD^+-reductase (15 µg) and an ADH (1.2 mg, supplied by Johnson Matthey) during 30 minutes at 4 °C was used for H_2-driven NADH supply and conversion of acetophenone to 1-phenylethanol. The CNC was rinsed with clean buffer to ensure that no un-adsorbed enzyme was left in the CNC. The ADH uses NADH as a reducing equivalent for acetophenone reduction and does not need to be immobilised. However, rinsing the CNC means that un-adsorbed ADH does not contribute to catalysis and that the entire H_2-driven system uses adsorbed enzymes, thus minimising enzyme contamination in the final product and minimising the amount of ADH required. A H_2 saturated solution (5 mL) containing NAD^+ (1 mM) and acetophenone (8.3 mM) in bis-tris buffer 10 mM at pH 8 was cycled through the enzyme-modified CNC at *ca.* 25 µL min^{-1}. A continuous flow of 1 bar H_2 was maintained to ensure saturation with H_2

throughout the experiment, **Figure 4.32**. No UV-vis measurements were performed in this case and the conversion of acetophenone to phenylethanol after 22 hours of continuous cycling was more accurately assessed by HPLC (**Section 2.6.2**).

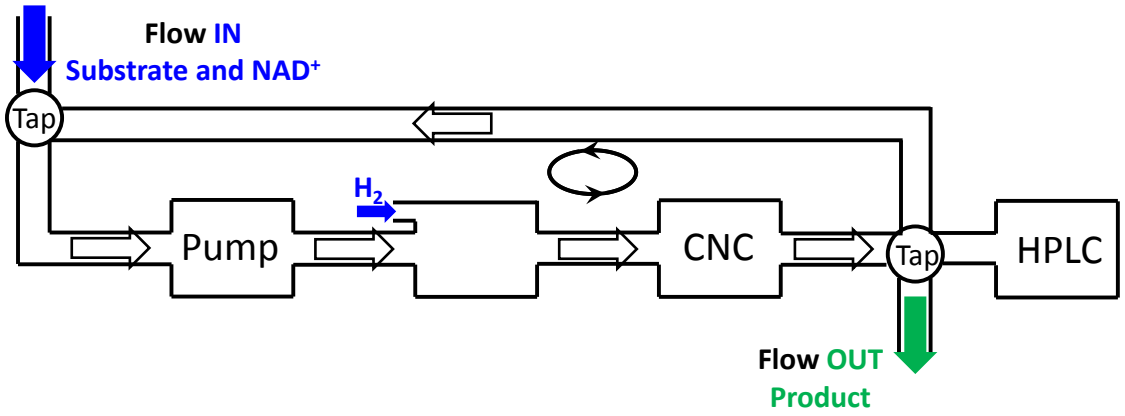

Figure 4.32. Schematic representation of the set up used to assess the conversion of acetophenone to 1-phenylethanol using a CNC modified with a hydrogenase, a NAD^+-reductase and an alcohol dehydrogenase.

An HPLC trace of the final solution in **Figure 4.33** shows that phenylethanol has been generated at a final concentration of 2 mM after 22 hours (25 % conversion). This equates to a total turnover number of > 54,000 NADH per NAD^+-reductase enzyme. This total turnover number is lower than value obtained on batch processes with enzymes immobilised on particles [122] but it likely to be an underestimation because all the enzyme molecules may not have adsorbed in the CNC. The HPLC results show that the desired catalytic conversion is successful. Purification or treatment of the MWCNTs is not necessary and as-synthesised CNCs can be readily used for enzyme-mediated synthesis of chemicals.

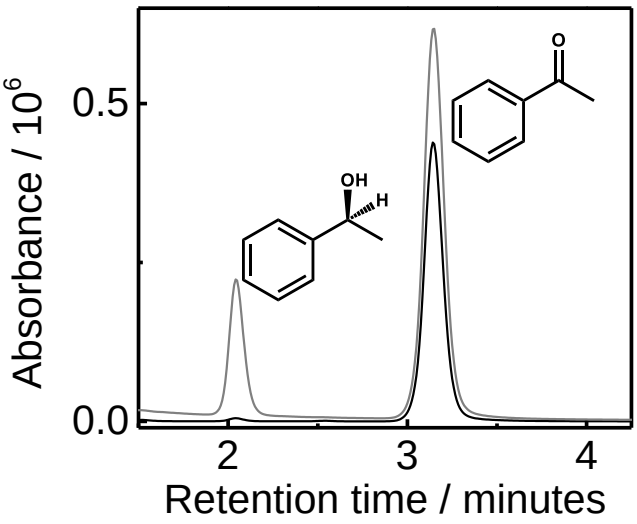

Figure 4.33. HPLC traces confirming production of phenylethanol (2.1 minutes) from acetophenone (3.2 minutes). A H_2-saturated solution containing NAD^+ (1 mM) and acetophenone (20 mM) was cycled through a CNC modified with hydrogenase, NAD^+-reductase and ADH. An aliquot of the final solution after 22 hours was analysed using HPLC. Experiment performed in 10 mM, bis-tris buffer, pH 8 at 22 °C with continuous bubbling of 1 bar H_2 over the reaction headspace. The absorbances at 210 nm (grey line) and 260 nm (black line) are shown. *With the assistance of Dr Holly A. Reeve, Department of Chemistry, University of Oxford* [122].

In conclusion, these results demonstrate for the first time how to simply exploit vertically-aligned MWCNTs for bio-redox-catalysis and biochemical synthesis in a flow configuration by using the designed CNCs. Optimisation of the results presented in terms of yields, time of experiments re-use of the functionalised CNC was not attempted due to the limited availability of enzyme and time restriction for equipment and co-workers. Since the thickness of the MWCNT forest in CNCs can be controlled, **Section 4.3.2**, future optimisation of the proof of concept established could be to study the effect of MWCNT filling on the efficiency of the flow-bio-redox catalytic system presented.

4.4. Summary and benefits of CNCs

CNCs obtained by AACVD in this thesis are shown to be versatile scaffolds for synthesis of chemicals using biocatalysts. More broadly they offer a set of properties that are relevant for a wider range of applications in flow systems.

1) *Simplicity*. CNCs are obtained by AACVD with a template-free approach with no need to treat the columns before synthesis. Several columns can be obtained per experiment. No chemical or thermal treatment is required after synthesis prior to use of the CNCs to support, for instance for enzyme-mediated catalysis and synthesis.

2) *Alleviate dispersion of MWCNTs*. The use of CNCs completely avoids the challenging dispersion of MWCNTs. The limited number of steps between MWCNT synthesis and device fabrication facilitates the integration of MWCNTs in flow systems.

3) *Mechanical stability*. MWCNTs are protected within the column: mechanical stress does not damage the MWCNT forest. This is a strong benefit in comparison to cases where the MWCNTs are grown on a flat substrate or after an etching step to get free-standing MWCNT forests.

4) *Catalyst and electrocatalyst immobilisation*. Various species (molecules, particles, enzymes) and catalysts can be immobilised in the high surface area, porous, conductive MWCNT network of a CNC. The catalyst is simply recovered by recovering the CNC. This avoids filtration steps to separate catalysts and MWCNTs from the products. Immobilisation methods of catalysts, including enzymes on MWCNTs [117], which have been previously reported [24, 33, 137] could be transferred for further functionalisation of the CNCs.

5) *Tolerance to chemicals*. CNCs can be used with aqueous solutions, despite the hydrophobicity of MWCNTs. CNCs are compatible with a range of chemicals and organic solvents too like ethanol or isopropanol.

6) *Flow chemistry*. CNCs are easily handled or connected to tubing and can be dipped into solution and removed. CNCs are readily compatible with flow devices for possibly scaling up the production of chemicals with continuous or semi-continuous processes. *In line* characterisation (UV-vis) or separation/purification (chromatography) is possible.

7) *Operation at low pressure*. The vertical alignment of MWCNTs in the column gives an orientation that could not be achieved with dispersed MWCNTs in a packed-column configuration. Together with the control over column filling with MWCNTs, this may contribute to a better solution flow within the column [139]. This accounts for the low pressure required to pass a liquid through the mini reactor. A lower pressure means a less hazardous process but also low energy requirement to perform chemical transformations.

8) *Thermal stability*. CNCs are demonstrated here for room temperature synthesis but MWCNTs are known to have good heat transfer properties [135]. The use of a quartz column together with the high oxidation resistance of MWCNTs up to 500 °C in air, should confer to the CNCs compatibility with high temperature (flow) catalysis.

9) *Possible further applications*. The observations reported in this thesis suggest that further control over filling with MWCNTs of quartz columns could lead to applications in filtration devices. The simple CNC design is promising to combine filtration/purification with (bio-redox) catalytic reactions performed in a flow configuration.

10) *Simple building block for flow systems*. The opportunity to produce several columns at a time makes it possible to connect different columns in series or parallel for different chemical steps to take place in each column. The CNCs could be a versatile building block for catalyst cascades.

11) *Combination of the previous*. These different benefits could be jointly exploited to optimise flow catalytic systems. For instance, the cofactor regeneration step presented

could be performed in a first column put in series with a second column where a NADH-dependent enzyme could be immobilised. This should work since the NADH is efficiently released in the flow as confirmed by *in line* UV-vis measurements. This could allow independent optimisation of immobilisation strategies for the various enzymes/catalysts in various columns. Alternatively, it allows independent optimisation of synthesis parameters like temperature for each column. This approach is not limited to series of two columns and the facile production of CNCs makes it possible to explore more complex enzyme cascade configurations. This potentially leads to an extremely modular overall system not only on the catalysts, solvents and catalytic reactions considered but the design of the flow system itself.

4.5. Conclusions

A simple and versatile AACVD synthesis of MWCNT columns (CNCs) is established. CNCs can be seen as quartz columns with their inner diameter covered with MWCNTs. The MWCNTs are obtained with a precursor made of toluene and 5 wt % ferrocene and synthesis performed at 800 °C. The influence of various experimental parameters is detailed. The most uniform filling is achieved with 2 cm long, 2 mm ID columns for 90 minutes of synthesis with a carrier gas flow rate of 2500 sccm and for columns placed between 23 and 29 cm in the furnace. The carrier gas flow rate has a strong influence on the structures grown in the quartz columns and can be controlled to optimise the general filling with MWCNTs. Controlling MWCNT properties on different parts of the same CNC, such as forest thickness and graphitisation at the different ends of the CNCs is also achieved. Importantly several columns can be obtained at a time, all showing similar filling with MWCNTs. Alongside the specific focus of developing columns compatible with flow catalysis, unusual structures can

be obtained like blocked-core columns and first evidence is given for their relevance in alternative applications like filtration.

Due to the particular geometry of the substrate on which the MWCNTs are grown the CNCs are ideal scaffolds for flow catalysis devices. Without any treatment required, aligned MWCNTs in the column provide a conductive, porous, interconnected carbon network suitable to support electrocatalytic reactions in a flow reactor configuration. For instance, H_2-driven cofactor regeneration was successfully mediated by enzymes immobilised in a CNC. This was further exploited to perform the conversion of acetophenone to 1-phenylethanol in a flow set up. The overall concept of flow-bio-redox catalysis proved for the first time in this chapter due to the design of CNCs is better summarised in **Figure 4.34**. This concept and could be extended to other chemical transformations with different substrates and enzymes or metal catalysts to obtain different products.

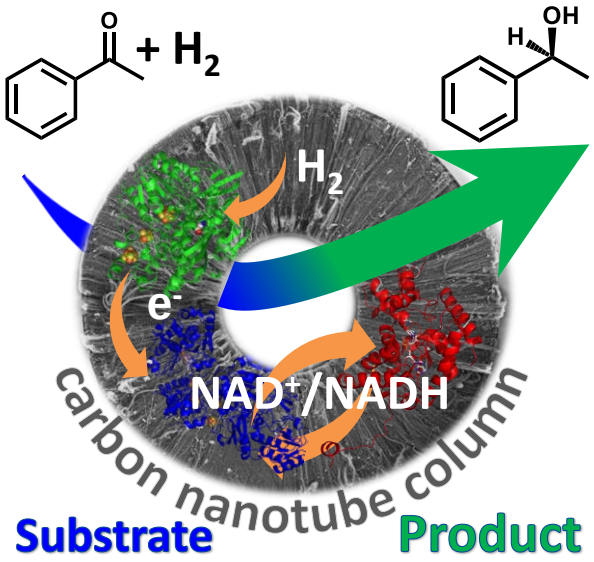

Figure 4.34. Carbon nanotube column: a simple carbon scaffold to perform hydrogenase H_2-driven cofactor regeneration for enzyme-mediated catalysis in a flow reactor configuration.

The overall approach presented in **Chapter 4** covers design, synthesis, characterisation and application of MWCNT scaffolds for flow-bio-redox catalysis. It leads to an extremely versatile platform relevant for devices well beyond the scope of the present study for flow systems. However the enzymes are immobilised within the MWCNT forest without control on the exact location where they are adsorbed in the carbon network. In view to possibly improve catalytic processes, a complementary degree of nanomaterial design is addressed in the next chapter to achieve a spatial control on the immobilisation of objects within a MWCNT forest.

Chapter 5: AACVD synthesis of MWCNT forests with intratubular junctions and new applications

"The most exciting phrase to hear in science,
the one that heralds new discoveries,
is not 'Eureka!' but 'That's funny...'"
Isaac Asimov

A specific thank goes to Dr Frank Dillon for running the TGA experiments, Dr Rebecca J. Nicholls for her help in the EELS data acquisition and analysis and Dr Antal A. Koós for fruitful discussions (all three are from the Department of Materials, University of Oxford).

5.1. Introduction

Forests [90] or powders made of CNTs [75] are promising supports for catalysts like particles, molecules or enzymes [24, 69, 75] due to their high surface area, their chemical, thermal and mechanical stability [69]. However, once immobilised on the material or in the forest, the catalysts are randomly distributed on the carbon surface and there is no or little control over the location where the immobilisation occurs. It can be hypothesised that a spatial control over immobilisation of objects and reactivity along a nanomaterial could improve the performances of future devices. For instance, it may help to improve the enzyme cascade investigated in **Chapter 4.** Achieving a spatial control over the co-immobilisation of two groups of enzymes with redox properties on a same nanomaterial could hypothetically bring novel properties by creating directional current flow (**Section 1.2.5**). However, testing this hypothesis is challenging. To date, a localised immobilisation is difficult because the local control at the nano/micro-scale to obtain asymmetric functionalisation of nanomaterials is not a simple task. In most cases, the asymmetric functionalisation is achieved by a method that is asymmetric itself, for instance using masks or templates [158-160]. The localised immobilisation of species is then limited to specific techniques and specific processes. To achieve a broader control of the immobilisation of objects on nanomaterials, developing

CNTs with intratubular junctions is a new conceptual approach presented in **Section 1.2.5**. The idea is to tailor different compositions and thus different structures and properties with a nano/micro-scale control along a CNT or a CNT forest. Inducing different properties should give a simple spatial control at the nano/micro-scale over the reactivity and the functionalisation along the nanomaterials. The main difference between the approach proposed compared to previous approaches is that the controlled functionalisation is induced by the material design. There is no need to locally modify the material after it has been synthesised. Most bulk modification techniques already reported for the functionalisation of CNTs should then 'spontaneously' lead to an asymmetric functionalisation.

Using CNTs with junctions to obtain asymmetric functionalisation of nanomaterials has never been explored. So far, CNTs with junctions have been exclusively considered for electronic applications (**Section 1.2.5**). This restriction can be explained by a limited production and limited length achieved to date for CNTs with junctions. Broadening their scope of applications to the facile creation of asymmetric structures then requires several challenges to be adressed. First, the production of MWCNTs with junctions must be improved. To do so the ACCVD synthesis of MWCNTs with continuous junctions is studied for the first time in **Section 5.3.1**. A specific focus is given to junctions between nitrogen-doped and un-doped sections in MWCNTs because they have been identified in this thesis as suitable platforms for localised immobilisation of enzymes (**Section 1.2.5**). Also N-MWCNTs [162] have been extensively compared to their un-doped counterparts [71, 92, 240] . Nitrogen doping brings different surfaces properties, reactivity, oxidation resistance, conductivity and catalytic properties to the MWCNTs. Developing sections with nitrogen doping in a MWCNT with junctions is then a promising option for simple identification of the influence of a change in composition along a nanomaterial. In **Section 5.3.2**, a combination of AACVD using liquid precursors and CVD using gaseous precursors is

identified as a robust and suitable approach to obtain large quantities of materials. A variety of sharp and continuous simple or multiple junctions along a single MWCNT forest are obtained. In parallel to this achievement, a second challenge is addressed regarding the characterisation of the junctions. Characterisation is important to prove that a change in composition, morphology or graphitisation is successfully induced along a single MWCNT. Junctions are first characterised by electron microscopy techniques: SEM, TEM and EELS because these techniques are suitable and commonly used to characterise MWCNTs with junction (**Section 1.2.5**). However, optical microscopy combined with Raman spectroscopy is a technique more rarely considered to characterise these MWCNTs [176, 186] and has probably been overlooked. Since the yield of materials achieved is higher in this thesis than in most previous reports, Raman microscopy is shown to be fast and simple but also extremely reliable to characterise junctions of various natures. The relatively large production of MWCNT with junctions also makes it possible to address another challenge: there is no information to date on the oxidation resistance of MWCNT with junctions. An achievement in this thesis is to present in **Section 5.3.3** the first TGA analysis of MWCNTs with junctions. The results complete the characterisation of the structures and suggest that different localised oxidation behaviour can be controlled along a MWCNT forest.

The unprecedented characterisation of MWCNTs with junction by TGA leads to another achievement detailed in **Section 5.3.4**. For the first time, controlled and localised oxidation along MWCNTs with junctions is achieved and confirmed by SEM and Raman analysis. The development of a junction between nitrogen-doped and an un-doped sections in a single MWCNT forest is exploited even further in this thesis: for the first time the localised and spontaneous immobilisation of species along a MWCNT forest is proved. This spontaneous localised immobilisation is not demonstrated with hydrogenase or other enzymes for practical reasons. The complete novelty of the approach proposed in this thesis

to obtain asymmetrically functionalised nanomaterial requires a solid proof of concept. Due to the low loading achieved with hydrogenase, the localised immobilisation of enzymes is difficult to assess with the characterisation techniques available for this project. Rather than enzymes, platinum particles were chosen because their localised immobilisation on MWCNT forests can easily be assessed by SEM and EDS measurements (**Chapter 2**). Moreover, methods to deposit platinum are extremely simple. Platinum particles can be deposited by mixing the CNTs with a platinum salt solution to further achieve chemical reduction of the salt [216] or electrodeposition [72]. Deposition of platinum particles is then performed on MWCNT forests with junctions in **Section 5.3.5** with these bulk methods. For first time, *via* careful MWCNT design, it is proved that an asymmetric deposition of particles can be spontaneously achieved preferentially on one section of a MWCNT forest compared to another.

5.2. Experimental

The general materials and methods relevant to this chapter have been covered in **Chapter 2**. This experimental section gives specific information related to the development of MWCNTs with junctions. As detailed in this chapter, the MWCNTs with junctions were obtained by modifications of the AACVD set up presented in **Section 2.2.4**. AACVD was chosen for the multiple benefits of the technique (**Section 1.2.5.6**). First is the possibility to use different liquid hydrocarbons to control the structures and properties of the MWCNTs, in particular un-doped and N-MWCNTs. Second, vertically-aligned forests of materials are obtained on substrate without need for pre-treatment of the substrate since catalyst and hydrocarbon source for MWCNT growth are co-injected. Third, it is a technique that could be scaled up in the long term for large scale production of MWCNTs.

By analogy with previously reported synthesis routes (**Section 1.2.5.4** and **Table 1.2**), obtaining MWCNTs with an intratubular junction by AACVD requires switching

hydrocarbon precursor sources during the synthesis. In the following, the MWCNT section grown before the switch will be referred to as '1'and the section grown after the switch as '2'. To simplify further discussion, the nature of the MWCNT sections is referred as 'C' for a non-doped section (MWCNT) and 'N' for a nitrogen-doped section (N-MWCNT). Combinations of liquid and gaseous precursors are investigated. The section grown from a liquid or gaseous precursor will be indexed as 'liq' and 'gas' respectively. As an example, a '$N_{1\text{-}liq}/C_{2\text{-}gas}$' structure will refer to MWCNTs obtained by growing first an N-MWCNT section from a liquid precursor followed by growth of an un-doped MWCNT section from a gaseous precursor. All chemicals: ethanol (CH_3OH, 99.8 %, Fisher Scientific), benzylamine ($C_6H_5CH_2NH_2$, ≥ 99.0 %, Fluka), toluene ($C_6H_5CH_3$, 99.9 %, Sigma-Aldrich) were used as received. Ferrocene ($C_{10}H_{10}Fe$, 98 %, Aldrich) was resublimed at 90 ºC prior to use. Gases: argon (Ar, 99.999 %), dihydrogen (H_2, ≥ 99,995 %), ammonia (NH_3, ≥ 99,98 %) and acetylene (C_2H_2, industrial grade) were obtained from BOC.

To fully understand the growth of MWCNT forests with junctions, silicon substrates (from Sibert) cleaned by sonication for 5 minutes in ethanol prior to experiments were used. The MWCNT forest obtained after synthesis were characterised on the substrate as detailed in **Section 2.3.1**. The position of the MWCNTs with respect to the substrate is then maintained after synthesis which is useful to get a deeper insight into the growth mechanism compared to previous reports. The same sample can be characterised using several non-destructive techniques like SEM, Raman and EDS. After characterisation, the same sample could be used for TEM, EELS and TGA which require collecting MWCNTs from the forest. This strategy gives a more complete understanding of the structure and properties of the materials. Characterisation was preferentially performed on samples placed in the reactor in such a way that they were located at *ca.* 30 cm in the furnace during synthesis.

This location was found to lead to more reproducible results in terms of length of MWCNTs. Also the longer MWCNTs were usually obtained in this region of the furnace.

5.3. Results and discussion

5.3.1. Synthesis of MWCNT forests with intratubular junctions

In this section different synthesis approaches based on AACVD are compared to identify a synthesis method giving sharp and continuous junctions between un-doped and nitrogen-doped MWCNTs.

5.3.1.1. Synthesis of C_1/N_2 and N_1/C_2 junctions with a liq/liq approach

The first option to grow MWCNTs with intratubular junction by AACVD is to simply switch the nature of the liquid precursor during growth. A small adaptation of the set up described in **Figure 2.3** is required: a Y-shape connection was used to connect two aerosol units before the quartz tube used as reactor, **Figure 5.1**. Since two liquid precursors are needed, this approach is referred to as liq/liq approach. The precursors used were toluene for the C section of the MWCNTs or benzylamine for N section of the MWCNTs, with ferrocene (5 wt %) acting as a catalyst source. The mixture of liquid precursors and catalyst was introduced with argon as a carrier gas at a constant flow rate of 2500 sccm. The first precursor was introduced in the furnace at 800 °C for typically 5 minutes before switching to the second liquid precursor which was introduced for typically 10 minutes. These parameters were chosen because they are suitable to obtain MWCNTs and N-MWCNTs with lengths of about 20 µm, as demonstrated previously by studying the growth of MWCNTs and N-MWCNTs separately [92]. Each N and C section in the expected MWCNT forest with a junction should then be long enough to be identified by SEM. Instantaneously switching from one liquid precursor to another was not possible experimentally since the aerosol

formed requires about 30 seconds to reach the furnace after it has been allowed to flow. An interval of at least 1 minute had to be left for the two precursors to mingle.

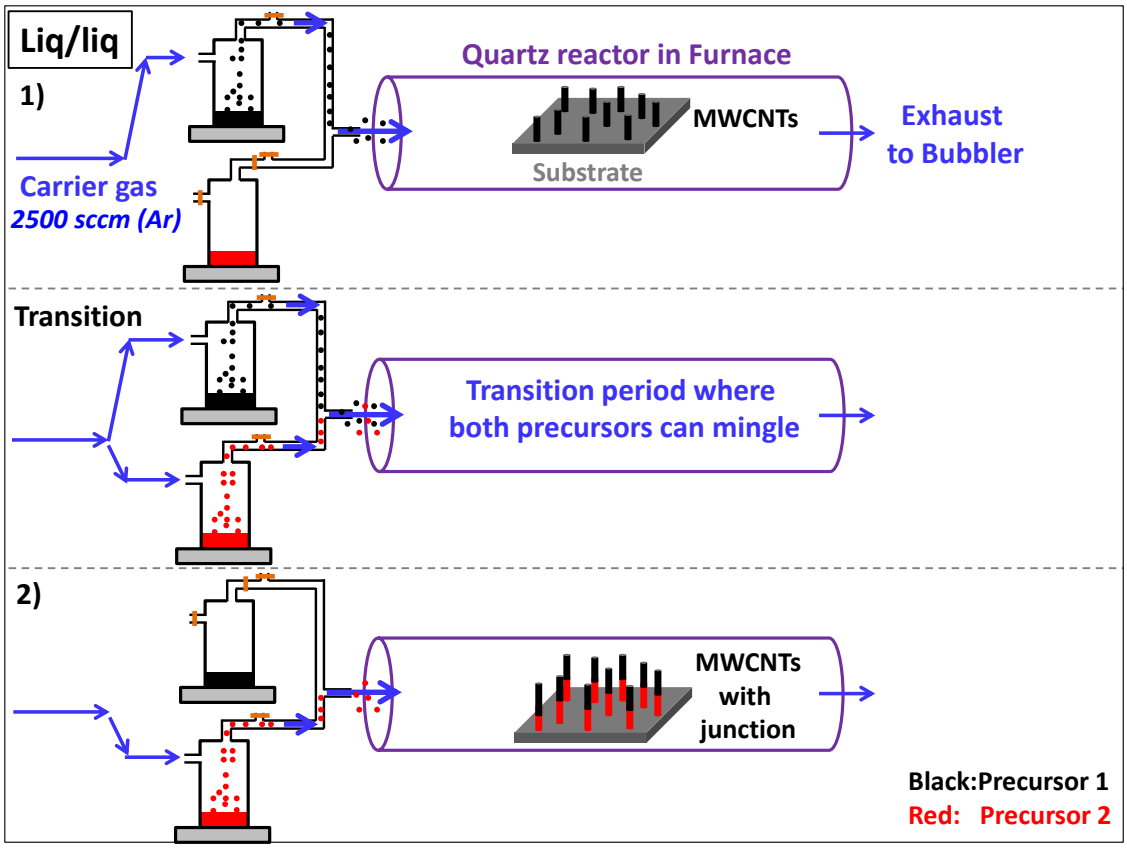

Figure 5.1. Schematic representation of the various step required for the liq/liq approach. MWCNTs growth on the silicon wafer used as substrate is illustrated and follows a root-growth mechanism detailed in the text.

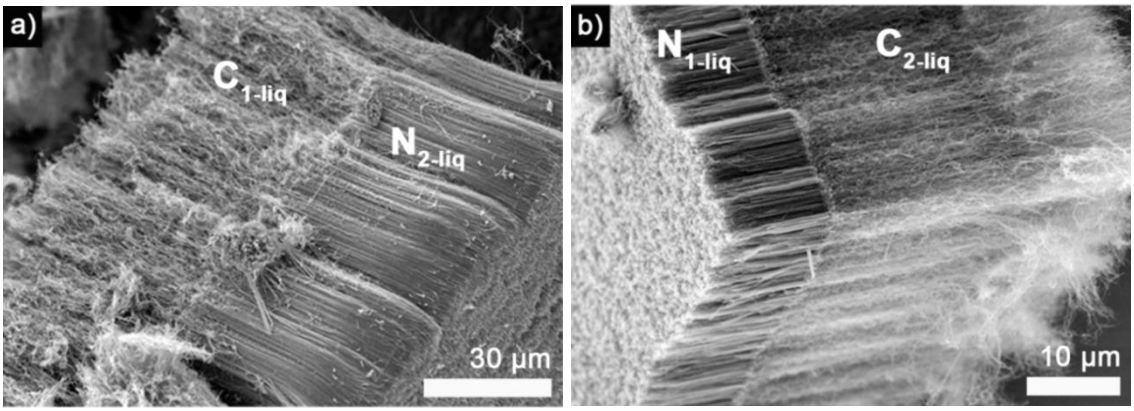

Figure 5.2. SEM micrographs (a) $N_{1\text{-liq}}/C_{2\text{-liq}}$ and (b) $C_{1\text{-liq}}/N_{2\text{-liq}}$ structures not supported on substrate.

SEM micrographs of $C_{1\text{-liq}}/N_{2\text{-liq}}$ and $N_{1\text{-liq}}/C_{2\text{-liq}}$ structures obtained are shown in **Figure 5.2** and **Figure 5.3** together with Raman data in **Figure 5.3**. For both C_1/N_2 and N_1/C_2 structures, one side of the MWCNT forest is straight and the other is wavy. This is consistent with a change in composition because N-MWCNTs obtained by AACVD are straighter that un-doped MWCNTs [92]. Raman spectra acquired along the MWCT forests are also displayed in **Figure 5.3**. The straight sections show a I_D/I_G value about 1 and a nearly non-existent 2D peak. On more wavy MWCNTs the I_D/I_G value is less than 1 and a marked 2D peak is observed. These are exactly the signals expected from N-MWCNTs and un-doped MWCNTs respectively (**Section 3.3.1.2**). These results confirm the presence of N and C sections in the MWCNTs.

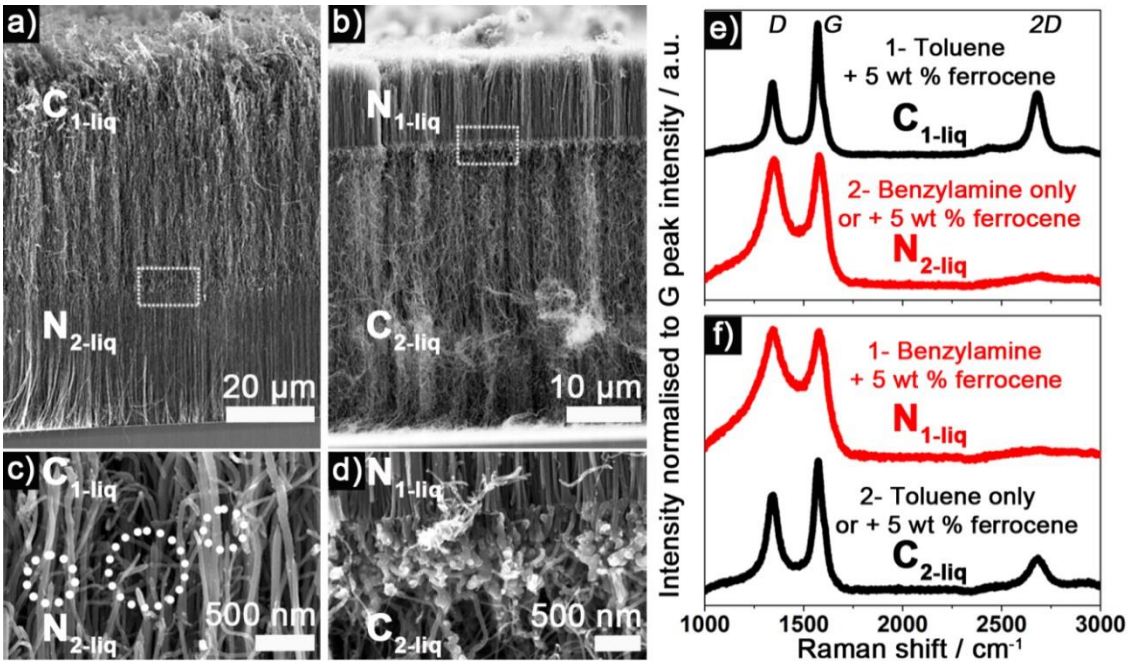

Figure 5.3. SEM micrographs of (a) $C_{1\text{-liq}}/N_{2\text{-liq}}$ and (b) $N_{1\text{-liq}}/C_{2\text{-liq}}$ MWCNT forests on silicon wafers (at the bottom of the micrographs). Higher resolution images for the interface between N and C sections identified by the square boxes in (a) and (b) are displayed in (c) and (d) respectively. 'Broken' MWCNTs are observed at the C_1/N_2 interface and are highlighted in dotted circles in (c). Raman spectra of each section for each of the structures are displayed in (e) for a $C_{1\text{-liq}}/N_{2\text{-liq}}$ and (f) for a $N_{1\text{-liq}}/C_{2\text{-liq}}$.

To gain deeper insight into the growth mechanism, the forests were studied grown on silicon substrates (**Section 2.3.1**). The superposition of sections relative to the substrate in **Figure 5.3** can be related to the order of precursor injections, confirming in all cases that MWCNT growth proceeds by a root-growth mechanism. This means that the nature of the first precursor used (precursor 1) drives the properties of the top section of the MWCNTs (relative to the substrate) and the second precursor (precursor 2) drives the bottom section. For instance if a toluene precursor is used first, a section made of wavy nanotubes with a I_D/I_G smaller than 1 and intense 2D peak is developed further away from the substrate, **Figure 5.3a,e**. Using benzylamine as second precursor leads to a straighter section with a I_D/I_G about 1 and nearly no 2D peak observed in contact with the substrate. The opposite is achieved if the order of precursor injection is changed, **Figure 5.3b,f**. A root-growth mechanism is consistent with previous reports where the mechanism has been established by more complex routes mainly based on isotope labelling [241, 242]. The growth sequence related to the precursor injection is illustrated in **Figure 5.1**. The symbolic colour of each section of the MWCNTs is matching the symbolic colour of the precursors responsible for the growth of that same section. This growth mechanism is also illustrated in **Figure 5.4a,b**. In this figure an un-doped MWCNT is represented by tubes with thick walls and small inner diameter and a N-MWCNT by a larger inner diameter, thinner walls and a bamboo structure. This schematic representation is in agreement with the TEM analysis performed in **Chapter 3** for un-doped and nitrogen-doped MWCNT. The catalyst particles required for MWCNT growth are located on a substrate, at the root of the CNT. The newly synthesised section of the MWCNT is formed at this root location. It will be important for the following discussion to note that MWCNTs with sections of different composition can be obtained if the second precursor is a mixture of liquid hydrocarbon and ferrocene or a liquid precursor without ferrocene, **Figure 5.3**.

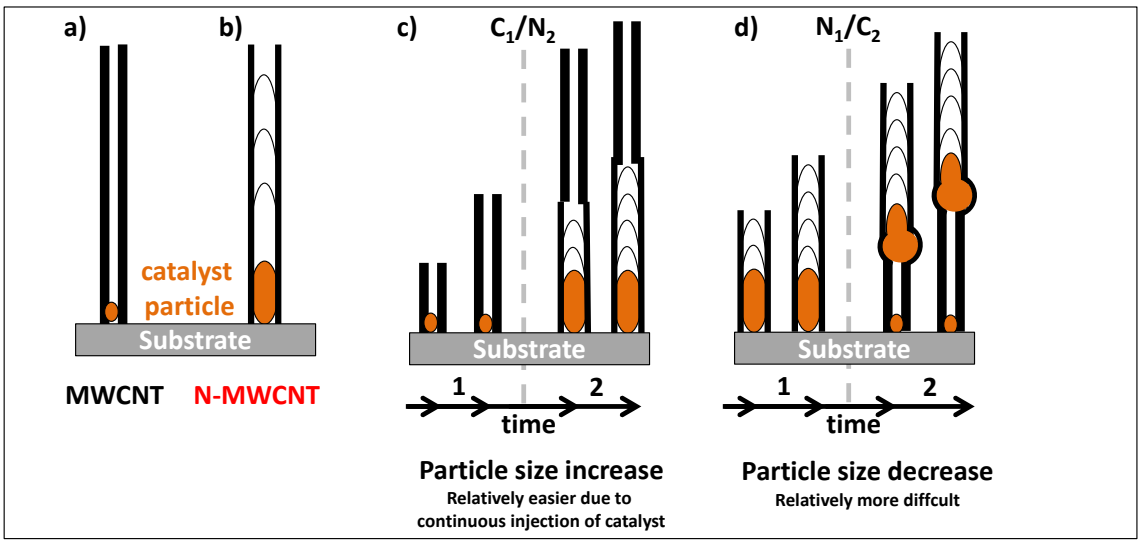

Figure 5.4. Schematic representation of (a) MWCNT, (b) N-MWCNT and a possible growth process for (c) C_1/N_2 and (d) N_1/C_2 structures.

Unfortunately, the liq/liq approach suffers several limitations. The junctions formed are not perfectly continuous since 'broken' MWCNTs are obtained at a C_1/N_2 interface: dotted circles in **Figure 5.3c** highlight these incontinuities (see also **Figure 2.6** for a higher magnification image). Also a strong morphological change is noticed at a N_1/C_2 interface in the form of sphere-like objects at the junction of the two sections, **Figure 5.3d**. An explanation for the presence of these objects breaking the continuity in the tube structure can be proposed based on two commonly observed phenomena. First, N-MWCNTs and un-doped MWCNTs have different inner diameters and MWCNT inner diameter depends on catalyst particle size [92, 184]. N-MWCNTs have a larger diameter than their un-doped counterpart as has been reported for previous C/N structures [184] and schematised in **Figure 5.4a,b**. To grow a N-MWCNT or a N section, the particle size required is expected to be larger than to grow an un-doped MWCNT or a C section. Creation of a N_1/C_2 or C_1/N_2 structure then requires particle size modifications: a C_1/N_2 junction would require particles size increase, a N_1/C_2 junction a particles size decrease. The catalyst required for MWCNT synthesis is continuously injected in the AACVD technique. A particle size increase should

be easier than a particle size decrease due to continuous supply of ferrocene which is the source of iron for the metal catalyst particles, **Figure 5.4c**. This can explain a slightly more continuous C_1/N_2 junction compared to a N_1/C_2 junction, **Figure 5.3c,d**. Second, nitrogen is likely to 'poison' the catalyst particles responsible for CNT growth: the N atoms are expected to agglomerate and remain on the catalyst particles since it is possible but energetically unfavourable to incorporate them into carbon nanotubes [243]. It can be hypothesised that removal of those nitrogen atoms from the catalyst particles will not occur spontaneously. Therefore, presence of nitrogen can be seen as a 'poison' [244, 245] easier to add on the catalyst than to remove. This would favour C_1/N_2 junctions, for which the poisoning agent is added, in contrast to N_1/C_2 junctions where the poisoning agent would need to be removed from the catalyst. Both arguments would favour more continuous C_1/N_2 junctions compared to N_1/C_2 junctions. These arguments are likely to account for the presence of particle-like objects attributed to residual catalyst particles at the non-continuous N_1/C_2 interface, **Figure 5.4c,d**. The rough growth model proposed will be confirmed by other synthesis approaches and further characterisation along this chapter. For instance, in **Figure 5.5** an SEM micrograph of a $N_{1\text{-liq}}/C_{2\text{-liq}}$ structure obtained for shorter time of synthesis is displayed. The $N_{1\text{-liq}}/C_{2\text{-liq}}$ structure is shorter and slightly more continuous than for structures in **Figure 5.3b**. In that case, the size-rearrangement of particles required to create N_1/C_2 junctions is less likely to occur because the particles have a smaller size for shorter injection time of catalyst [246]. Shorter synthesis time improves slightly the junction but limits the thickness of the forest. This observation is in conflict with the goal of this thesis, which is to create sharp and continuous junctions in forests thicker than 20 µm.

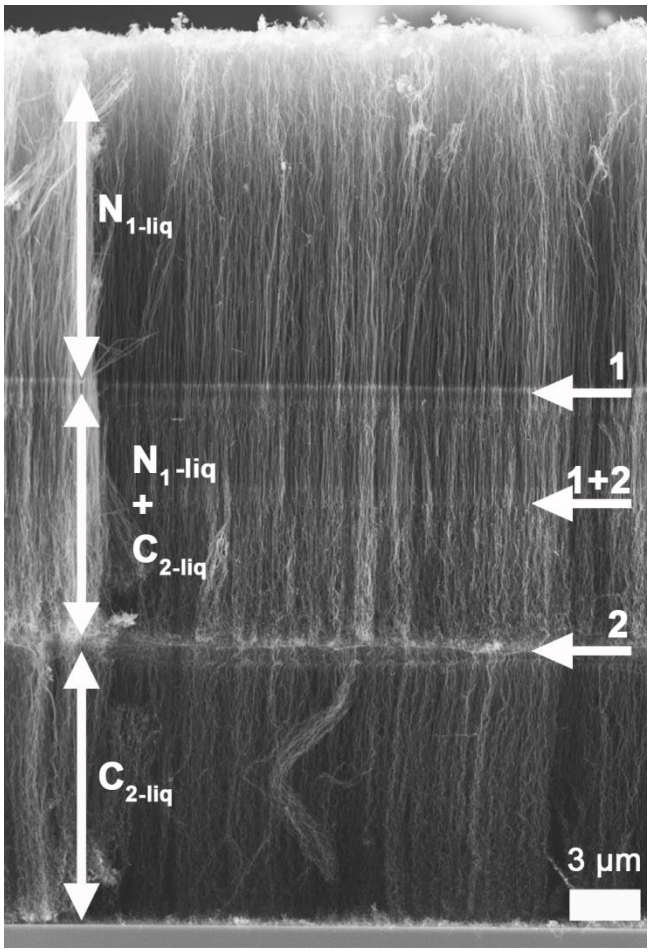

Figure 5.5. SEM micrograph of a $N_{1\text{-liq}}/C_{2\text{-liq}}$ structures where a flow perturbation is induced by mechanically opening and closing taps to switch precursors. This leads to MWCNT structure perturbation: lines marked by arrows 1 and 2. The progressive change in precursor composition between arrows 1 and 2, marked by the middle arrow 1+2, correlate with morphological change in the MWCNT structures.

Figure 5.5 illustrates a further limitation in attempts to grow N_1/C_2 or C_1/N_2 junctions by AACVD: flow fluctuations are introduced when switching from one liquid precursor to another. The mechanical opening and closure of taps on the two aerosol units used to allow a precursor into the furnace affects the MWCNT structures: 'white lines', marked by arrows 1 and 2 in **Figure 5.5,** are present in the forest. These lines are consistent with previous experimental evidence that flow fluctuation introduces disruption in the MWCNT structure [247, 248]. In the conditions of the present study, changing the nature of the precursor is not

instantaneous and an overlap period is required, where precursor 1 and precursor 2 are both present in the furnace to ensure a continuous supply of the hydrocarbon feedstock (**Figure 5.1**). The overlap time is difficult to manage and leads to uncontrolled transition in the MWCNT forest, illustrated by a progressive change in MWCNTs morphology from straight to wavy: arrow '1+2' between arrow 1 and 2 in **Figure 5.5**. A progressive change in structure is not suitable because an ideal MWCNT with junction should have a sharp and continuous interface between the two sections. The issue of flow fluctuation then needs to be addressed.

5.3.1.2. Synthesis of C_1/N_2 and N_1/C_2 junctions with a liq/[liq+gas] and [liq+gas]/liq approach

To minimise flow fluctuation in order to improve junctions, the mechanical opening and closing of taps during synthesis must be avoided. An alternative to the liq/liq approach is using a continuous flow of liquid precursor and inducing doping by addition of a gas. In this liq/[liq+gas] approach a mixture of toluene and catalyst (ferrocene at 5 wt %) precursor is continuously introduced through the whole experiment, **Figure 5.6**. A change in the composition of the hydrocarbon flow used to grow the MWCNTs is introduced by a minimal modulation of the carrier gas composition by adding ammonia. Introducing ammonia at 30 sccm was found to be a low enough value to induce a change in the structure of MWCNTs and at the same time to ensure a safe procedure since ammonia is a toxic chemical. During the whole experiment still performed at 800 °C, a total flow rate of gas at 2500 sccm was maintained. The flow of carrier gas was split as illustrated in **Figure 5.6** to prevent a direct contact of ammonia with the ultrasonic unit and avoid damage of the ultrasonic cell and the piezo. The flow fluctuation in this approach comes from changing the carrier gas composition but should be minimal since the flow of ammonia introduced accounts for only 1.2 % of the total flow. In the absence of ammonia the C section of the

MWCNT is grown (**1** in **Figure 5.6**) and in the presence of ammonia the N section is grown (**2** in **Figure 5.6**). The C section was grown for 5 to 10 minutes and the N section was grown by addition of ammonia for 15 to 20 minutes to promote nitrogen doping. The other advantage of this approach is to require only one aerosol generator and one unit. This is more cost-efficient than the liq/liq approach in the long term for scaling up the production of MWCNTs with intratubular junctions.

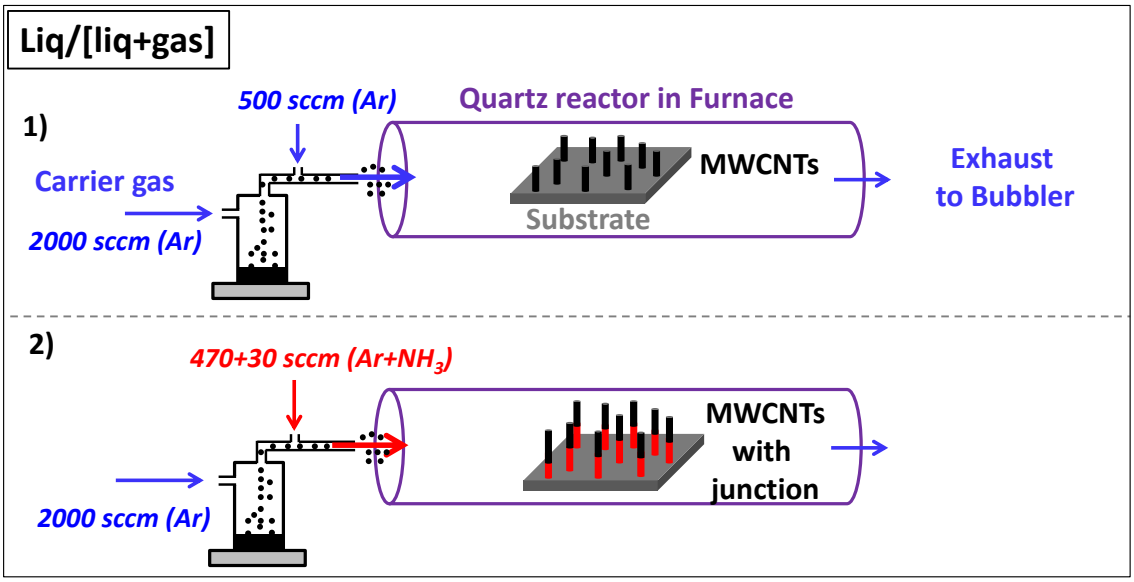

Figure 5.6. Schematic representation of the various steps required in the liq/[liq+gas] approach. MWCNT growth on the silicon wafer (substrate) is illustrated and follows a root-growth mechanism. The same scheme would apply for the [liq+gas]/liq approach by inverting steps 1) and 2).

Structures obtained with this liq/[liq+gas] approach are similar to those obtained with the liq/liq approach when characterised by SEM and Raman spectroscopy, **Figure 5.7**. A section with a wavy morphology and another with a straight morphology are again observed. They correspond to sections made of MWCNTs and N-MWCNTs respectively, in agreement with the expected root-growth mechanism, the sequence of precursors used but also the Raman data. For instance, the I_D/I_G value from Raman analysis for the section obtained by using ammonia is more than 0.7, so higher than the value inferior to 0.6 observed for the toluene-only counterpart. Also the 2D peak for the section grown in the presence of

ammonia is relatively smaller than for the toluene-only counterpart which confirms that using ammonia induces defects in the carbon structures, **Figure 5.7e-f**. A small improvement is obtained with the liq/[liq+gas] approach compared to the liq/liq approach because no 'broken' MWCNTs could be observed at a C_1/N_2 junction. However, creating a N_1/C_2 junction is still more challenging due to the formation of non-continuous and non-sharp interfaces. In **Figure 5.7d** for instance, particle-like objects highlighted by a dotted circle are present at the interface of the morphologically straight (N) and wavy (C) sections of the MWCNTs. Such particle-like objects could not be observed at the C_1/N_2 interface. By analogy with the liq/liq approach (**Figure 5.3**), a continuous N_1/C_2 interface is likely to be more difficult to create due to a necessary particle-size rearrangement when growing N-MWCNTs compared to MWCNTs (**Figure 5.4**).

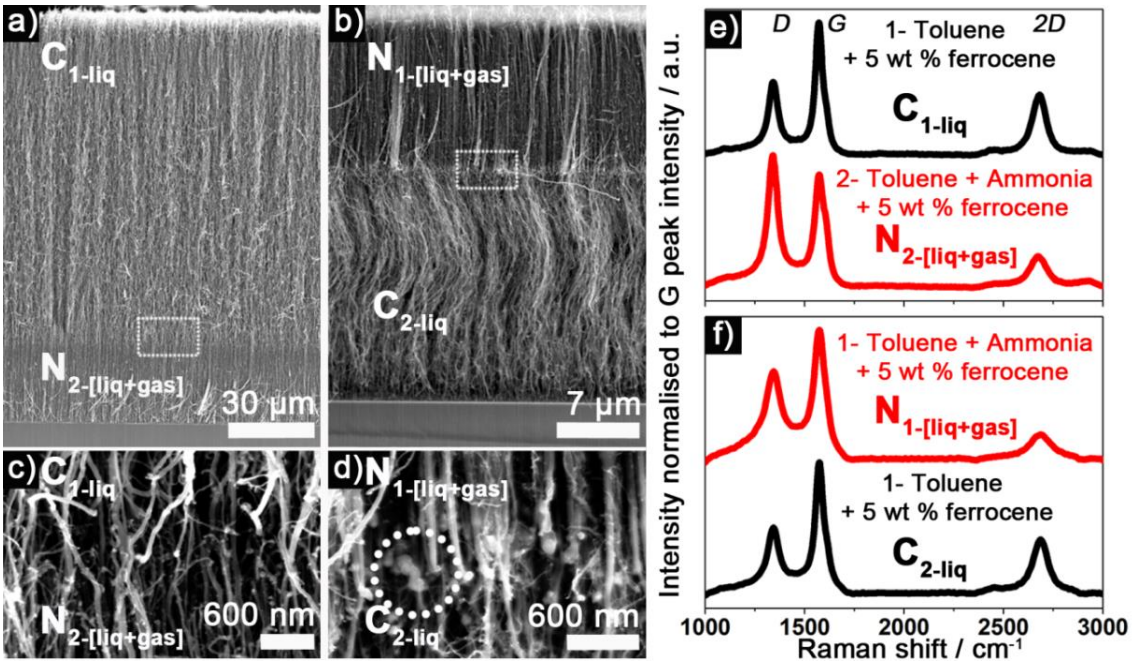

Figure 5.7. SEM micrographs of (a) $C_{1\text{-liq}}/N_{2\text{-[liq+gas]}}$ and (b) $N_{1\text{-[liq+gas]}}/C_{2\text{-liq}}$ vertically-aligned MWCNT forests. Higher resolution images for the interface between N and C sections identified by the square boxes in (a) and (b) are displayed in (c) and (d) respectively. Particle-like structures can be found at the N_1/C_2 interface and are highlighted in a dotted circle in (d). Raman spectra of each section for each structure are reported in (e) for a $C_{1\text{-liq}}/N_{2\text{-[liq+gas]}}$ and (f) for a $N_{1\text{-[liq+gas]}}/C_{2\text{-liq}}$ forest.

5.3.1.3. Synthesis of C_1/N_2 and N_1/C_2 junctions with a liq/gas approach

Since N_1/C_2 structures are still challenging to obtain (**Section 5.3.1.2**) an improved synthesis route is needed. Based on additional experimental observation, this section suggests a possible improvement to the liq/liq and [liq+gas]/liq approaches. In AACVD experiments, the precursor required to form the catalyst particle responsible for CNT growth is continuously injected during synthesis. It has been reported however that stopping the injection of the chemicals responsible for the formation of the catalyst particles, while maintaining an hydrocarbon supply, leads to continuous growth of un-doped CNT in CVD [249]. The same phenomenon was reproduced with the presented liq/liq approach and extended in this thesis to the case where growth with and without catalyst precursor supply is induced by different hydrocarbon precursors (**Figure 5.3**). Continuous growth is possible because the catalyst particles formed during the first part of the process (liquid precursor 1) and used for the growth of the first section of the MWCNTs remains active long enough to support the growth of the second section. This is confirmed for instance with $C_{1\text{-liq}}/N_{2\text{-liq}}$ structures. The SEM micrographs displayed in **Figure 5.8** show catalyst particles at the root of a $C_{1\text{-liq}}/N_{2\text{-liq}}$ structure. These particles have a shape and size compatible with the inner diameter of the typical bamboo structures of N-MWCNT [92], schematised in **Figure 5.4**. However those particles were originally introduced, deposited and formed during the first step where ferrocene (catalyst and hydrocarbon precursor) was co-injected with toluene (hydrocarbon precursor for the C section). Observing the same effect for $N_{1\text{-liq}}/C_{2\text{-liq}}$ structures was not as straightforward. The catalyst particles associated with the growth of C section of MWCNTs are probably smaller and so more difficult to identify, in agreement with the smaller inner diameter of un-doped MWCNTs [92]. Nevertheless, this observation confirms that the second section of the MWCNTs can be developed without continuous injection of ferrocene during the entire synthesis.

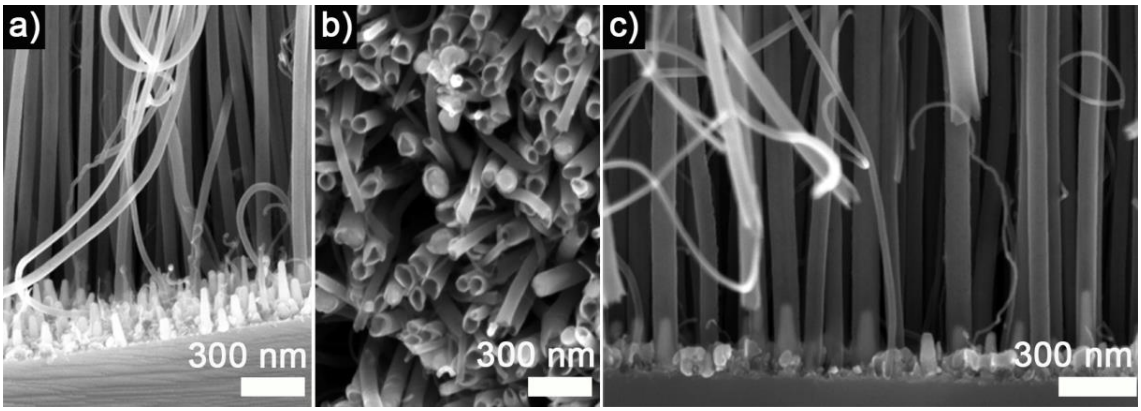

Figure 5.8. SEM micrographs of the N root of a $C_{1\text{-liq}}/N_{2\text{-liq}}$ MWCNT forest. Catalyst particles were originally deposited during the synthesis of the C section of the forest (toluene+ferrocene precursor) since no catalyst precursor was introduced during the time the N section was grown from benzylamine without ferrocene. (a) Catalyst particles from which MWCNTs have been disconnected. (b) Root of the N-MWCNT in the N section originally connected to the catalyst particles. (c) N-MWCNTs in the N section still connected to the catalyst particles.

Coupling AACVD and CVD is then a promising concept to improve the interface between the two sections, especially in the case of a N_1/C_2 structure. A possible 'liq/gas' method is schematised in **Figure 5.9**. The first step of the synthesis is the introduction of a mixture of liquid precursor and catalyst precursor in the furnace, as for the first step of the liq/liq approach. The second step differs from the liq/liq approach because it consists of introducing a gaseous precursor only, without catalyst precursor. Just like the liq/[liq+gas] approach detailed in **Section 5.3.1.2**, the liq/gas approach only requires one aerosol generator and one unit which is cost-efficient for possible scale up of the production of MWCNTs with intratubular junctions in the long term. The liq/gas approach also combines the advantages of the AACVD technique (co-injection of precursor and catalyst and possibility to scale up MWCNTs production) while it minimises the amount of catalyst required for MWCNT growth. Flow fluctuations are also minimised since it is faster and easier to inject a gas than a second aerosol. The junctions should therefore be improved

compared to a liq/liq or a [liq+gas]/liq approach, especially in the case of a N_1/C_2 structure for which none of the previous approaches gives continuous junctions.

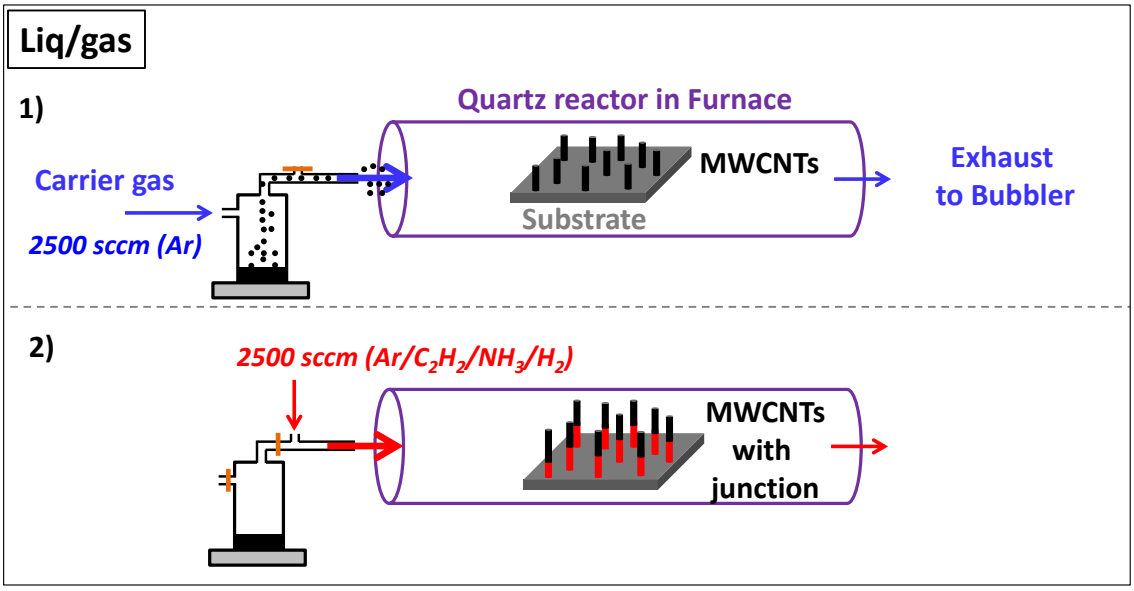

Figure 5.9. Schematic representation of the various steps required in the liq/gas approach. MWCNT growth on the silicon wafer substrate is illustrated and follows a root growth mechanism.

The liq/gas approach proposed was then performed experimentally with the same liquid precursors as for the liq/liq approach (**Section 5.3.1.1**). The gaseous precursors used were acetylene (for C section of MWCNTs) or acetylene and ammonia (for N section of MWCNTs) in combination with dihydrogen and argon, typically introduced for 20 minutes. These precursors and mixtures of precursors were selected because they lead to different MWCNT structures [250]. Experiments were performed at 800 °C with a total gas flow rate of 2500 sccm. Compositions of precursors of argon/hydrogen/acetylene with flow rates in sccm: 2000/400/100 respectively and argon/hydrogen/acetylene/ammonia with flow rates in sccm: 2000/400/50/50 respectively were suitable to perform the coupling of AACVD and CVD. In the liq/gas approach the change of precursors is much faster than for the liq/liq approach and so no overlap time interval for precursors to mingle was necessary.

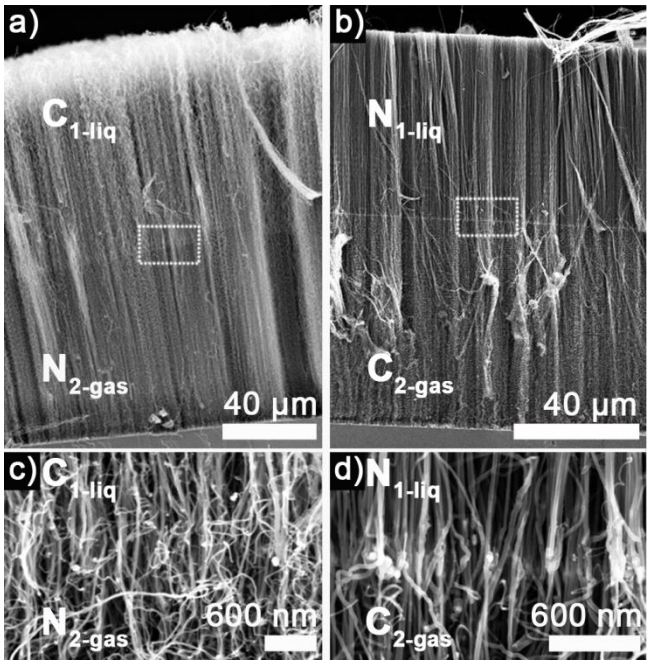

Figure 5.10. SEM micrographs of (a) $C_{1\text{-liq}}/N_{2\text{-gas}}$ and (b) $N_{1\text{-liq}}/C_{2\text{-gas}}$ vertically-aligned MWCNT forests. Higher resolution images obtained for the interface between N and C sections identified by the square box in (a) and (b) are displayed in (c) and (d) respectively and suggest continuous interfaces in a liq/gas approach.

SEM micrographs of the nanotubes obtained with the liq/gas approach are shown in **Figure 5.10** and **Figure 5.11**. MWCNT forests with a length of about 100 µm are formed. A morphological change is marked by a different contrast on the SEM images between the two sections in **Figure 5.10a**, or a pronounced change in morphology from straight to wavy in **Figure 5.11a**. Unlike the previous approaches, both N_1/C_2 and C_1/N_2 junctions appear continuous and the SEM micrographs taken at the interface of both sections do not show obvious 'broken' MWCNTs or presence of particle-like structures breaking the continuity of the MWCNTs, **Figure 5.10c-d**. This is an important improvement compared to the previous approaches (**Figure 5.3**, **Figure 5.5** and **Figure 5.7**). Also the $N_{1\text{-liq}}/C_{2\text{-gas}}$ interface is marked by the presence of a characteristic brighter line in the SEM micrographs, **Figure 5.10d** and **Figure 5.11a**. This line results from presence of conductive particles inside the tubes: brighter features in **Figure 5.11b** (see also **Figure A20**), and EDS mapping confirms that

these particles are mainly made of iron (**Figure A21**). The particles are then likely to be residual iron-based catalyst particles as observed by others [175, 183]. The presence of these particles at the exact N_1/C_2 interface is a convenient interface-marker for further characterisation. For instance, TEM micrographs of $N_{1\text{-liq}}/C_{2\text{-gas}}$ structures are shown in **Figure 5.11c** (**Figure A20**). The typical morphology observed with TEM for independent batches of N-MWCNTs and MWCNTs presented in **Chapter 3** (**Figure 3.2a-b**) are found here in a single MWCNT. On one side of the interface, marked by the presence of darker particles in **Figure 5.11c**, the typical structure of N-MWCNTs can be observed: corrugated structures with a larger inner diameter. On the other side the typical structure of un-doped MWCNTs can be observed with smaller inner diameter and thicker walls. The change in structure assessed by SEM and TEM along a MWCNT confirms that MWCNTs with continuous junctions were successfully obtained. It will be important to note for further discussion that residual catalyst particles can be found sometimes in all N-MWCNTs and all un-doped MWCNTs samples (**Figure 2.8**). However, these particles are not all located at the same position in the MWCNT forest and not associated with a structural change within the MWCNTs as it is the case in **Figure 5.11a-c**.

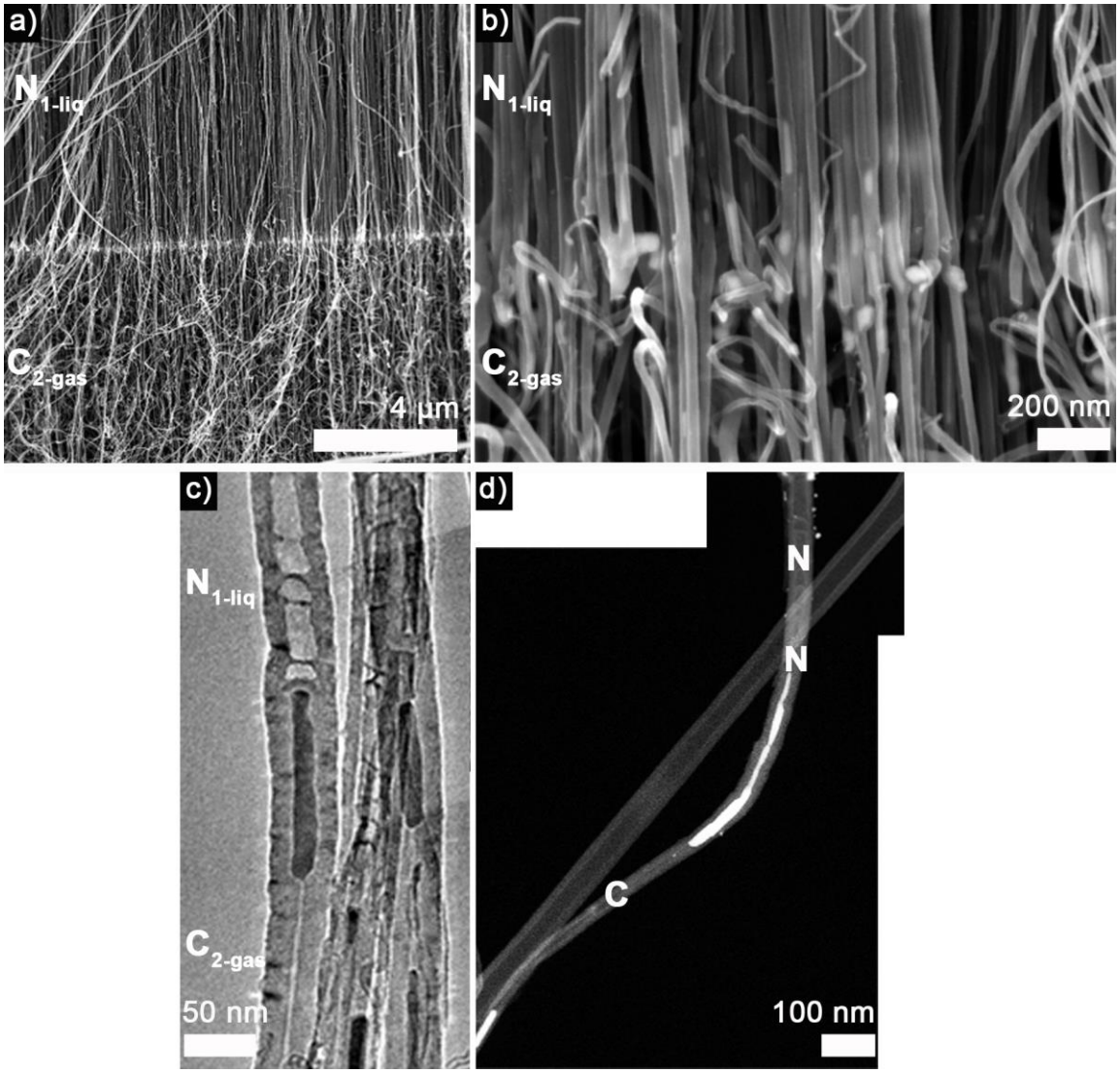

Figure 5.11. (a) and (b) SEM micrographs of $N_{1\text{-liq}}/C_{2\text{-gas}}$ MWCNT structures at different magnification. The presence of catalyst particles marks the interface. (c) TEM micrograph of the previous interface, reconstructed from 3 TEM micrographs taken at the same magnification. (d) STEM-ADF micrographs of $N_{1\text{-liq}}/C_{2\text{-gas}}$ MWCNT structures. Presence of catalyst particles appear with a brighter contrast in the image. A letter N on the micrograph (d) indicates an area of the tubes where a peak at 400 eV was observed in the EELS spectra recorded in this area. This peak at 400 eV is indicative of presence of gaseous nitrogen. A letter C on the micrograph (d) indicates an area in the tubes where no peak at 400 eV could be observed in the EELS spectra recorded in this area.

EELS measurements were further performed to confirm a change in composition in the MWCNTs (**Section 2.3.6**). EELS spectra were acquired on both side of the junctions identified by a change in the structure of the MWCNTs and/or conveniently marked by presence of iron-based particles: bright features in the tubes in the STEM-ADF images in **Figure 5.11d**. The change in composition was assessed by the presence of gaseous nitrogen characterised by an energy loss peak around 400 eV in the EELS spectrum. A letter in **Figure 5.11d** identifies areas of the nanotube where EELS spectra were recorded. If a peak at 400 eV was observed in the EELS spectrum, the area is marked by the letter 'N'. Areas of the nanotube where this peak was not observed are marked with a letter C. On one side of the junction, no peak from bound nitrogen or gaseous nitrogen could be observed. On the other side, whether straight after the interface or few nanometres further, the presence of mainly gaseous nitrogen (marked by a peak at 400 eV in the EELS spectra) was observed, usually associated with the bamboo structures characteristic of N-MWCNTs. This confirms that within 100 nm before and after the interface, within a single MWCNT, a complete change in structure and composition can be induced by a change in precursor during synthesis. Also, as expected from the minimal but still present flow fluctuation during synthesis, branched MWCNT junctions [185] could be obtained (in **Figure 2.10** a single un-doped MWCNT section is connected to several N-MWCNT branches). In all samples analysed by TEM, a mixture of MWCNT with morphologies typically related to un-doped MWCNTs or N-MWCNTs can be observed.

These characterisations confirm that using a gaseous precursor in the second step of the growth improves the formation of continuous and sharp N_1/C_2 and C_1/N_2 interfaces compared to other synthesis routes. The liq/gas approach was then investigated further.

5.3.2. Sharp and continuous junctions of various nature by the liq/gas approach

In this section, the robustness of AACVD to develop MWCNTs with junctions is further illustrated by identifying what makes the liq/gas approach specific. A variety of junctions of different nature are also obtained based on this approach.

5.3.2.1. A possible mechanism to obtain sharp and continuous C_1/N_2 and N_1/C_2 junctions by the liq/gas approach

To further exploit the liq/gas approach, a possible mechanism for the growth of MWCNTs with junctions is proposed based on previous experimental observations. In particular, the presence of iron based particles at a N_1/C_2 junction is peculiar and deserves more investigation before it can be explained and possibly controlled. Indeed, the presence of iron-based particles in MWCNTs with junctions have been reported previously [175, 183] but more as a fortunate experimental observation than as evidence to support a growth mechanism. For instance it was not established in those publications [175, 183] whether the particles are located at the exact position of the interface for all MWCNTs within the forest. In contrast, this is the case for the N_1/C_2 junction obtained in this work for the liq/gas (**Figure 5.11a-b**, **Figure A20**), the liq/liq (**Figure 5.3**) or the [liq+gas]/liq (**Figure 5.7**) approaches. This iron is likely to come from residual catalyst particles and their presence at this position illustrates the more difficult formation of N_1/C_2 structures (**Figure 5.4**). Also such particles could not be observed at the C_1/N_2 junction, supporting the hypothesis that a size rearrangement of the catalyst particles is necessary to develop N_1/C_2 junction. A growth mechanism for MWCNT forests with intratubular junctions obtained with the liq/gas approach is proposed in **Figure 5.12**. The expected decrease in particle size to form a N_1/C_2 junction (detailed in **Section 5.3.1.1**) could explain the presence of residual iron-based metal catalysts at the junctions. The catalyst particles catalysing the growth of the N_1 section may

be too big to be compatible with the growth of the C_2 section which requires smaller size particles. One possible mechanism to promote a catalyst particle size decrease could be to release part of the catalyst within the growing nanotube and this release could be triggered by a change in the experimental conditions, like introduction of a new precursor. This simple model explains the observations made and accounts for the non-continuous N_1/C_2 junctions in the liq/liq and liq/[liq+gas] approach (**Figure 5.4**) and presence of the catalyst particles at the continuous N_1/C_2 junction in the liq/gas approach (**Figure 5.12**).

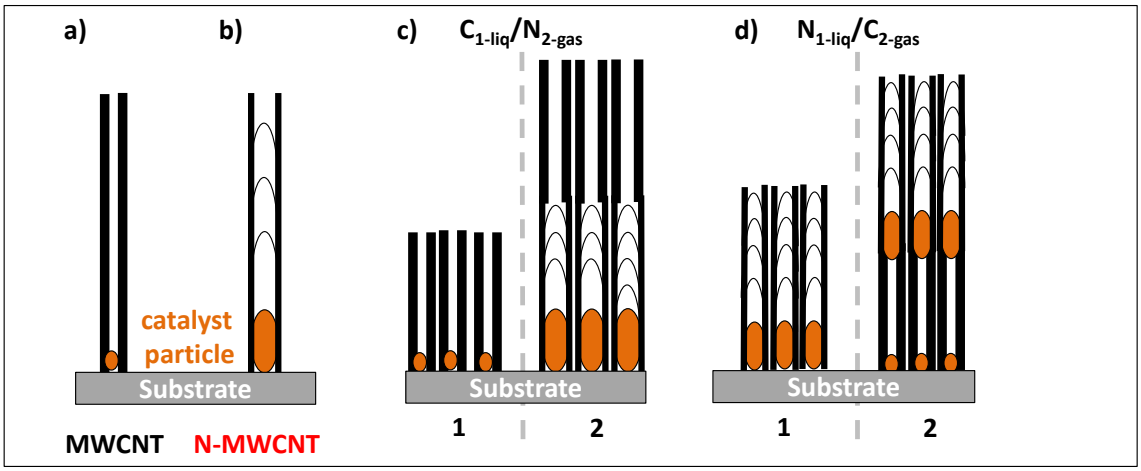

Figure 5.12. Schematic representation of (a) MWCNT, (b) N-MWCNT and a possible root-growth process for (c) C_1/N_2 and (d) N_1/C_2 forests obtained by the liq/gas approach.

5.3.2.2. Synthesis of C_1/C_2 and N_1/N_2 junctions by the liq/gas approach and challenges

Since the liq/gas approach is suitable to develop sharp and continuous junctions, further control over the properties of the MWCNT forests was investigated. For instance, an important achievement in the liq/gas approach is that structures obtained are longer than 20 µm and actually closer to 100 µm long, **Figure 5.13**. The length of each N or C section can be controlled by modifying the duration of synthesis for each section. A longer injection time is associated with a longer section for the various approaches presented and this will be

exploited in **Section 5.3.3**. However, precise control over the length of each section was not the main goal of this work.

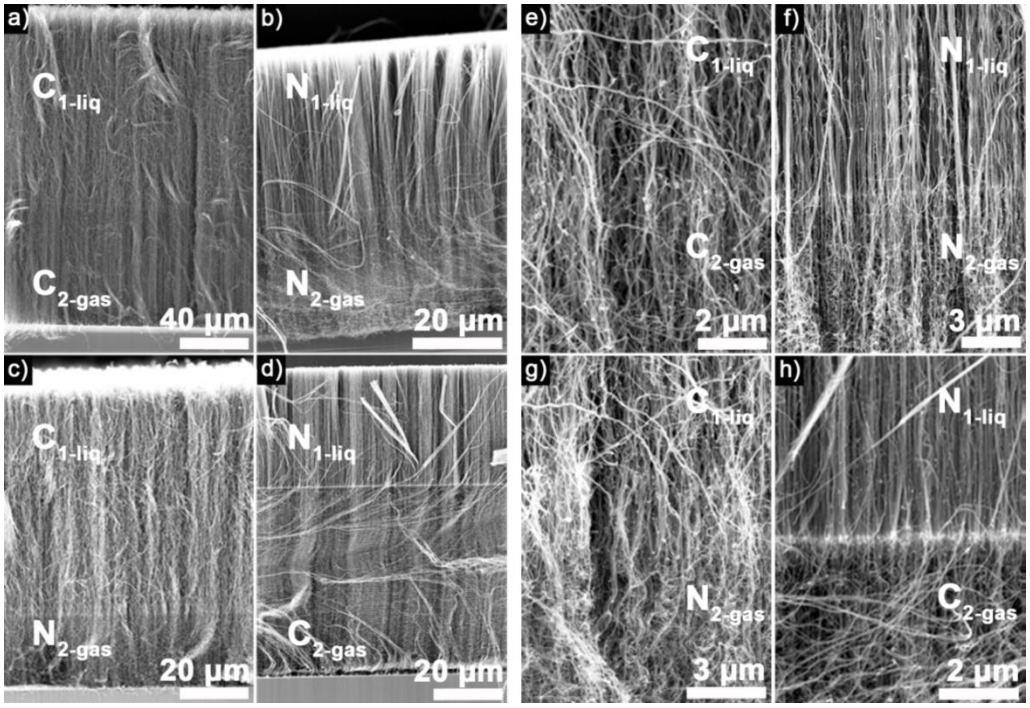

Figure 5.13. SEM micrographs of all possible combinations for the liq/gas synthesis approach: $C_{1\text{-liq}}/C_{2\text{-gas}}$, $N_{1\text{-liq}}/N_{2\text{-gas}}$, $C_{1\text{-liq}}/N_{2\text{-gas}}$ and $N_{1\text{-liq}}/C_{2\text{-gas}}$ structures at low magnification: (a), (b), (c) and (d) respectively. Higher magnification micrographs of the expected junctions are displayed in (e), (f), (g) and (h) respectively.

The focus in this thesis is on achieving different types of junctions to further control the properties *along* the MWCNT. In this sense, the suitability of the liq/gas approach to grow sharp intratubular junctions is not limited to junctions associated with a change in composition. $C_{1\text{-liq}}/C_{2\text{-gas}}$ and $N_{1\text{-liq}}/N_{2\text{-gas}}$ junctions can also be obtained as displayed in **Figure 5.13**. Their characterisation is however challenging. For example, in **Figure 5.13a,e** a SEM micrograph of a $C_{1\text{-liq}}/C_{2\text{-gas}}$ junction does not show a strong morphological change and only a small change in contrast on the image suggests two distinct sections in the same forest. The difference between the two sections in $C_{1\text{-liq}}/C_{2\text{-gas}}$ and $N_{1\text{-liq}}/N_{2\text{-gas}}$ junctions comes from a difference in the nature of the precursor used, without necessarily inducing a strong change in composition or morphology. The electron microscopy techniques (SEM,

TEM, EELS) presented in this thesis so far to characterise C_1/N_2 and N_1/C_2 junctions confirm the presence of junctions based on strong morphological changes or different atomic composition along the tube. These techniques are then not as simple and reliable to characterise $C_{1\text{-liq}}/C_{2\text{-gas}}$ and $N_{1\text{-liq}}/N_{2\text{-gas}}$ junctions. Alternative techniques reported for the characterisation N/C structures like EDS and XPS (**Table 1.3**) will not be suitable either. EDS would require a strong change in composition to be useful to characterise the junction. XPS is usually a bulk measurement that is less suitable to characterise tubes with junctions. The possibility to focus on each section with a spatial resolution of at least 50-100 µm would give deeper insight into the structures obtained. There is then a lack of a simple method to characterise MWCNTs with junctions and in particular C_1/C_2 or N_1/N_2 structures.

For C_1/C_2 and N_1/N_2 junctions both sections will probably give similar results by SEM, EDS, XPS, TEM or EELS characterisation, which are all relatively advanced and complex techniques requiring access to specific equipment. In contrast, this thesis shows that C_1/C_2 and N_1/N_2 junctions are simple to characterise by Raman spectroscopy (**Section 2.3.4**). It has been established by Raman spectroscopy studies that using different precursors lead to MWCNTs with different graphitic structures, even when a change in composition is not induced [179]. Different graphitisation should then be observed along tubes with sections grown from different hydrocarbon precursors, for example when toluene and acetylene are used in the liq/gas approach, **Figure 5.13a,e**. The use of Raman spectroscopy to characterise CNT with junctions has however been limited and probably overlooked to date (**Section 1.2.5.4**). In particular it has not been exploited for the characterisation of C_1/C_2 or N_1/N_2 junctions. This is mainly due to practical limitation on the length of forests achieved. These limitations are successfully overcome in this thesis, **Figure 5.13**. A novel focus on Raman spectroscopy to complete the characterisation of MWCNT with junctions is then

proposed in the next section. It is shown that Raman spectroscopy is a fast, simple and reliable technique useful to get more knowledge on the nature of MWCNTs with junctions.

5.3.2.3. Controlled graphitisation along MWCNT forests with junctions obtained by the liq/gas approach

In this thesis, the MWCNT forest can easily be characterised by Raman spectroscopy because the forest thickness is usually longer than 20 µm. As-grown structures on substrates can then be un-ambiguously characterised by Raman microscopy as already demonstrated along this chapter for C/N structures obtained by the liq/liq (**Figure 5.3**) or liq/[liq+gas] (**Figure 5.7**) approach. Raman spectroscopy is also useful to characterise structures obtained by the liq/gas approach, **Figure 5.14**.

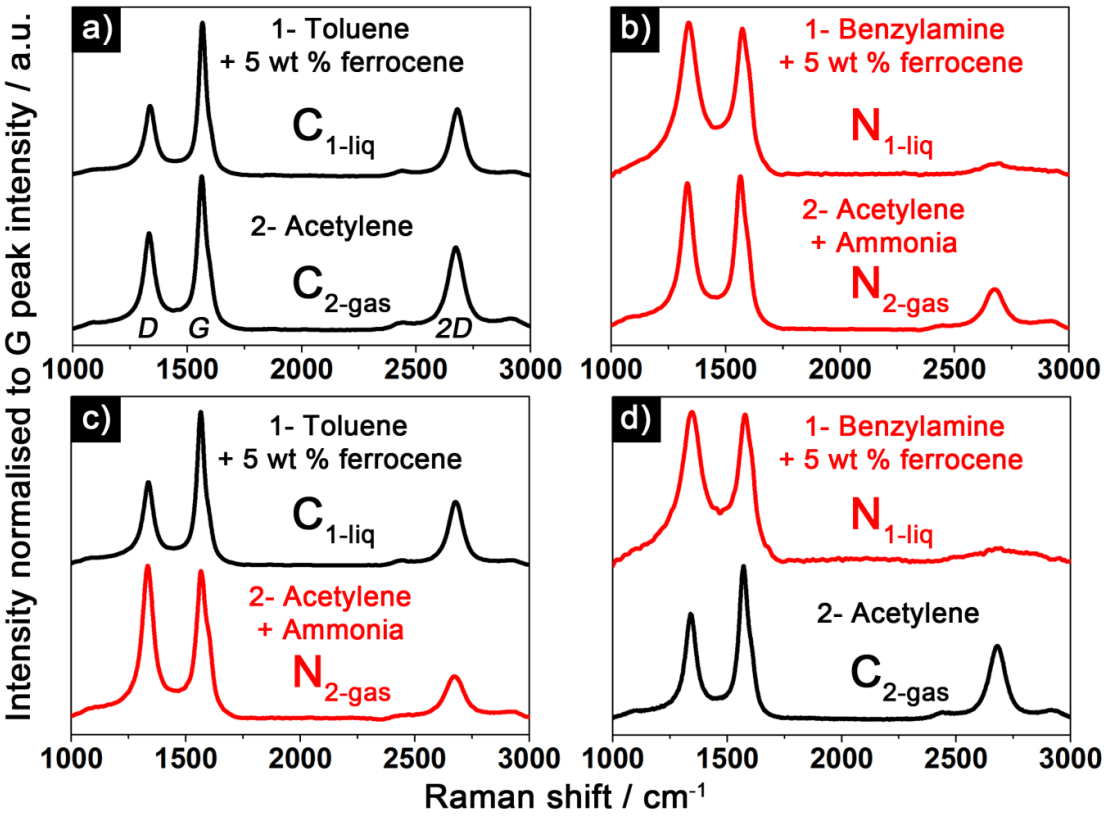

Figure 5.14. Raman spectra for each section of MWCNT forests with intratubular junctions obtained with the liq/gas approach: C_1/C_2, N_1/N_2, C_1/N_2 and N_1/C_2 junctions: (a), (b), (c) and (d) respectively. The associated SEM micrographs can be found in Figure 5.13. The laser excitation wavelength used was 532 nm.

In good agreement with previous results on un-doped MWCNTs and N-MWCNTs separately [93, 250], C sections grown with toluene precursor, **Figure 5.14a,c**, or acetylene, **Figure 5.14a,d**, show an I_D/I_G value smaller than 1 and presence of a 2D peak. Sections obtained from benzylamine (N) have a I_D/I_G value about 1 and a nearly non-existent 2D peak, **Figure 5.14b,d**. The latter is consistent with a more defective structure due to presence of nitrogen atoms in the carbon lattice [93]. In a similar way, a N section grown from acetylene+ammonia shows a I_D/I_G ratio about 1 and small 2D peak, **Figure 5.14b,c**. This 2D peak is more pronounced that in the case of N sections grown from benzylamine, **Figure 5.14b,d**. However, it is still smaller than in the case of growth from acetylene only, **Figure 5.14a,d**. A higher D peak and smaller 2D peak are also observed compared to tubes grown from acetylene without ammonia. This is consistent with the expected influence of ammonia in developing the N section: ammonia introduces nitrogen atoms in the carbon lattice and favours a more disordered carbon structure [250]. Hence, a strong change in the Raman spectrum is always noticed when spectra are acquired from a section on one side of the junction compared to the section on the other side. Also Raman spectra are consistent within a single section. This makes Raman spectroscopy a simple technique to characterise C_1/N_2 or N_1/C_2 structures by simply considering the I_D/I_G value and intensity of the 2D peak.

Figure 5.14 also illustrates that $C_{1\text{-liq}}/C_{2\text{-gas}}$ and $N_{1\text{-liq}}/N_{2\text{-gas}}$ junctions can be characterised. For instance the I_D/I_G value is smaller for toluene grown (0.46 ±0.02) than acetylene grown (0.63 ±0.02) sections within a same MWCNT forest, **Figure 5.14a**. Also for $N_{1\text{-liq}}/N_{2\text{-gas}}$ junctions, the 2D peak has a higher intensity for acetylene+ammonia grown MWCNTs compared to benzylamine grown MWCNTs, **Figure 5.14b**. This difference in Raman signal for $C_{1\text{-liq}}/C_{2\text{-gas}}$ and $N_{1\text{-liq}}/N_{2\text{-gas}}$ can even be stressed further. It has been observed experimentally that changing the excitation wavelength of the laser used for Raman spectroscopy modifies particular features in the spectra associated with CNTs. For instance,

the intensity of the D and D′ peak is expected to increase at higher excitation wavelength [251]. The D' peak is more pronounced with the abundance of sp^2 domains with a micrometre size and is identified as a shoulder at higher wavenumber on the G peak. The D' peak is not easily identified with a green laser excitation at 532 nm, **Figure 5.14**, but can be observed with a laser excitation at 633 nm, **Figure 5.15**. The $I_{D'}/I_G$ values are about 1 for MWCNTs grown from acetylene or acetylene+ammonia, but is smaller than 1 for toluene grown MWCNTs, **Figure 5.15e,g**. The ratio is even close to 0 for benzylamine grown MWCNTs since the D' peak is not clearly identified, **Figure 5.15f,h**. MWCNTs obtained from a gaseous precursor then have a relatively more pronounced D' peak than the one obtained from liquid precursors in this study. Using a red laser (633 nm excitation wavelength), the nature of precursor (liquid or gaseous) for each MWCNT section can be inferred from the Raman spectra by considering the D' peak intensity.

In conclusion, the type of junction and the precursors used to develop the junctions in the MWCNTs can be inferred from Raman characterisation. A change in I_D/I_G value and intensity of the 2D peak along a MWCNT forest can be attributed to doping with hetero-atom (N/C and C/N junctions) or to different precursors without a strong compositional change (C/C and N/N junctions), since different graphitisation levels are developed in each case. The phase of the precursor used for each section can even be inferred from the relative intensity of the D' peak between the two sections for the examples presented. By characterising MWCNT forests on substrates as proposed in this thesis, the forest orientation remains the same relative to the substrate and so no information is lost on the top and bottom sections of the forest. The sequence of precursors used during synthesis can then be simply inferred from the Raman data. This information would not be as easily extracted from SEM or TEM images. Raman microscopy is therefore a powerful tool not only to characterise, but also to extract synthesis information on MWCNTs with various intratubular junctions. This

is an important demonstration because Raman characterisation coupled to optical microscopy is fast and reliable while being accessible in most research laboratories, as opposed to more specific microscopic technique like SEM or TEM. Raman microscopy could then be a useful tool to facilitate further research and applications of MWCNTs with junction in fields like chemistry or biology, where electron microscopes are not always routine equipment.

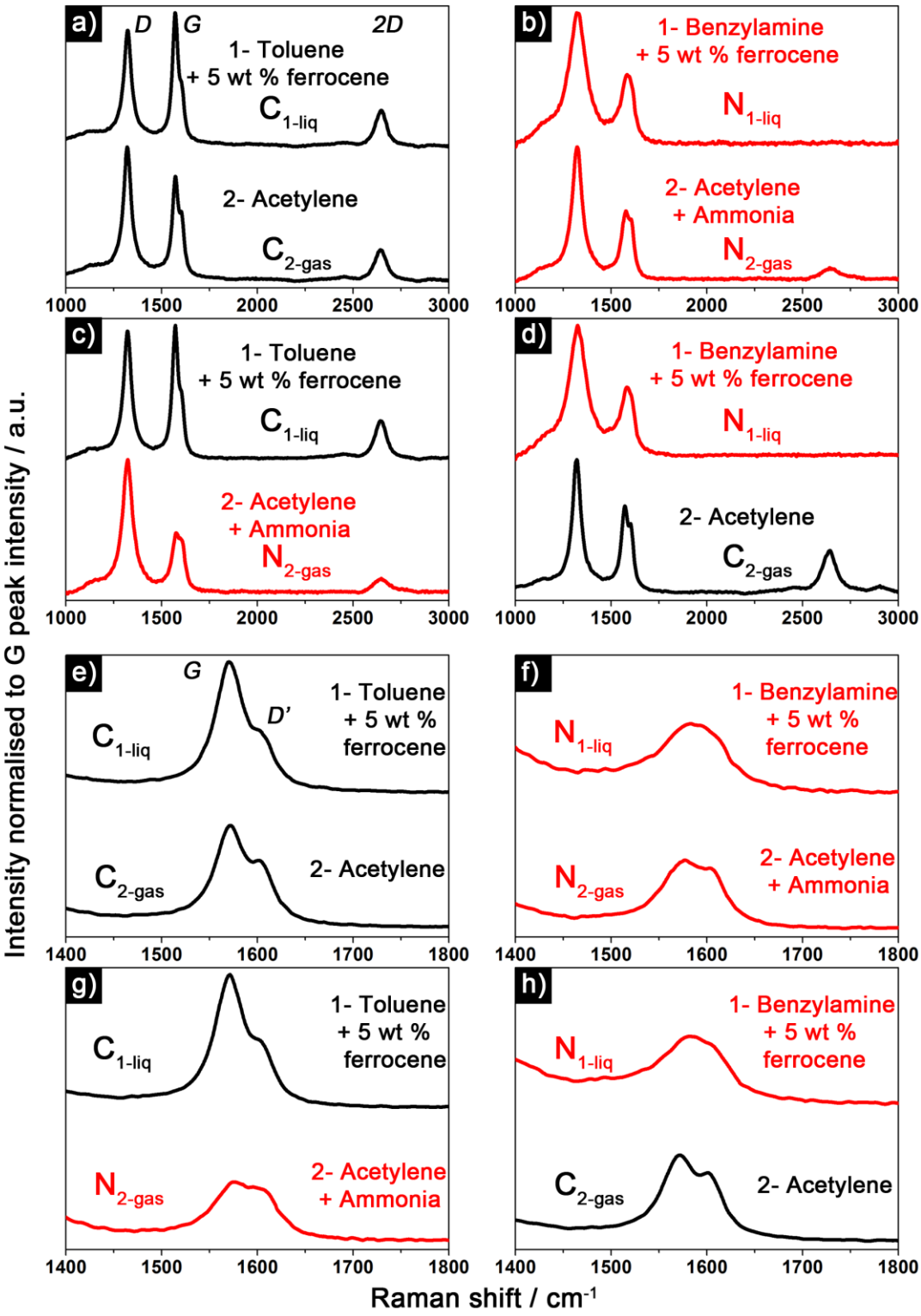

Figure 5.15. Raman spectra (red laser excitation: 633 nm) of various structures obtained with the liq-gas approach: C_1/C_1, N_1/N_2, C_1/N_2 and N_1/C_2, (a), (b), (c) and (d) respectively; the G and D' peaks region is displayed in (e), (f), (g) and (h) respectively.

5.3.2.4. Further benefits of the liq/gas approach: large quantities, multiple junctions and unusual nanoball structures

The liq/gas approach not only leads to long MWCNT forests with junctions, which facilitates their characterization by simple techniques like Raman microscopy, but also gives large quantities of materials. For the first time in this thesis, a method to produce MWCNTs with junctions is quantified in terms of yield of material obtained (**Section 1.2.5**). From the synthesis conditions and approaches discussed previously, various simple junctions were created and are summarised in **Table 5.1**. The quantity of material obtained per experiment is typically between 100 and 325 mg for the longest synthesis time of up to 40 minutes. The largest quantities usually obtained with the liq/gas approach. This amount is relatively large for lab-scale production of CNTs by AACVD which is reported to give between 50 to 100 mg of MWCNTs in 30 minutes [93].

Table 5.1. Summary of all types of syntheses explored leading to MWCNTs with a single intratubular junction, associated precursors and abbreviations.

Precursor 1	Carrier gas	Precursor phase	Precursor 2	Carrier gas	Precursor phase	Structure
Toluene + 5 wt % Fc	Ar	liquid	**Benzylamine + 5 wt % Fc**	Ar	liquid	$\mathbf{C_{1\text{-}liq}/N_{2\text{-}liq}}$
Benzylamine + 5 wt % Fc	Ar	liquid	**Toluene + 5 wt % Fc**	Ar	liquid	$\mathbf{N_{1\text{-}liq}/C_{2\text{-}liq}}$
Toluene + 5 wt % Fc	Ar	liquid	**Toluene (no catalyst)**	Ar	liquid	$\mathbf{C_{1\text{-}liq}/C_{2\text{-}liq}}$
Benzylamine + 5 wt % Fc	Ar	liquid	**Benzylamine (no catalyst)**	Ar	liquid	$\mathbf{N_{1\text{-}liq}/N_{2\text{-}liq}}$
Toluene + 5 wt % Fc	Ar	liquid	**Benzylamine (no catalyst)**	Ar	liquid	$\mathbf{C_{1\text{-}liq}/N_{2\text{-}liq}}$
Benzylamine + 5 wt % Fc	Ar	liquid	**Toluene (no catalyst)**	Ar	liquid	$\mathbf{N_{1\text{-}liq}/C_{2\text{-}liq}}$
Toluene + 5 wt % Fc	Ar	liquid	**Toluene + 5 wt % Fc + NH_3**	Ar	liquid + gas	$\mathbf{C_{1\text{-}liq}/N_{2\text{-}[liq+gas]}}$
Toluene + 5 wt % Fc + NH_3	Ar	liquid + gas	**Toluene + 5 wt % Fc**	Ar	liquid	$\mathbf{N_{1\text{-}[liq+gas]}/C_{2\text{-}liq}}$
Toluene + 5 wt % Fc	Ar	liquid	**Acetylene**	Ar + H_2	gas	$\mathbf{C_{1\text{-}liq}/C_{2\text{-}gas}}$
Benzylamine + 5 wt % Fc	Ar	liquid	**Acetylene + NH_3**	Ar + H_2	gas	$\mathbf{N_{1\text{-}liq}/N_{2\text{-}gas}}$
Toluene + 5 wt % Fc	Ar	liquid	**Acetylene + NH_3**	Ar + H_2	gas	$\mathbf{C_{1\text{-}liq}/N_{2\text{-}gas}}$
Benzylamine + 5 wt % Fc	Ar	liquid	**Acetylene**	Ar + H_2	gas	$\mathbf{N_{1\text{-}liq}/C_{2\text{-}gas}}$

Fc=Ferrocene

The robustness of the synthesis approach proposed in this thesis can be extended even further. By repeated switches between various precursors, multiple junctions are obtained by different routes such as: $C_{1\text{-liq}}/N_{2\text{-liq}}/C_{3\text{-liq}}/C_{4\text{-liq}}$ junctions in **Figure 5.16** and $N_{1\text{-liq}}/C_{2\text{-gas}}/N_{3\text{-liq}}/C_{4\text{-gas}}$ junctions in **Figure 5.17**. Combining the various approaches is also possible, for instance in a liq/[liq+gas]/gas approach to lead to $C_{1\text{-liq}}/N_{2\text{-[liq+gas]}}/C_{3\text{-gas}}$ structures, **Figure 5.18**. In all cases the SEM and Raman characterisation discussed above transfers well for characterisation: a change in morphology between straight and wavy is assessed in SEM images together with a change in the Raman spectra between each section (I_D/I_G value and relative intensity of 2D peak). This supports the argument that AACVD in an extremely robust technique to develop various types of MWCNTs with junctions and larger quantities of materials than previously reported.

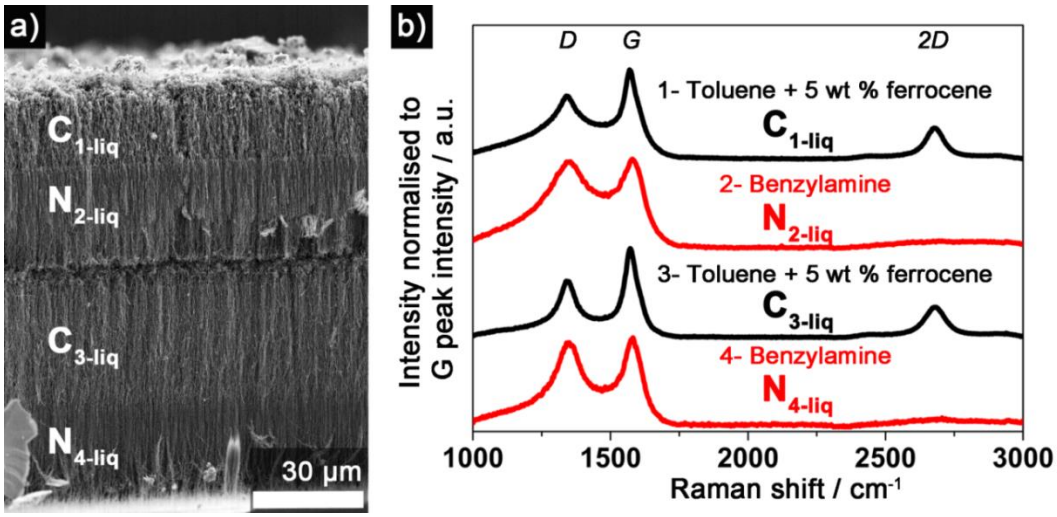

Figure 5.16. (a) SEM micrograph of a $C_{1\text{-liq}}/N_{2\text{-liq}}/C_{3\text{-liq}}/N_{4\text{-liq}}$ structure and (b) associated Raman spectra (532 nm wavelength excitation) for the various sections obtained. No catalyst was co-injected with the benzylamine precursor to grow the N sections.

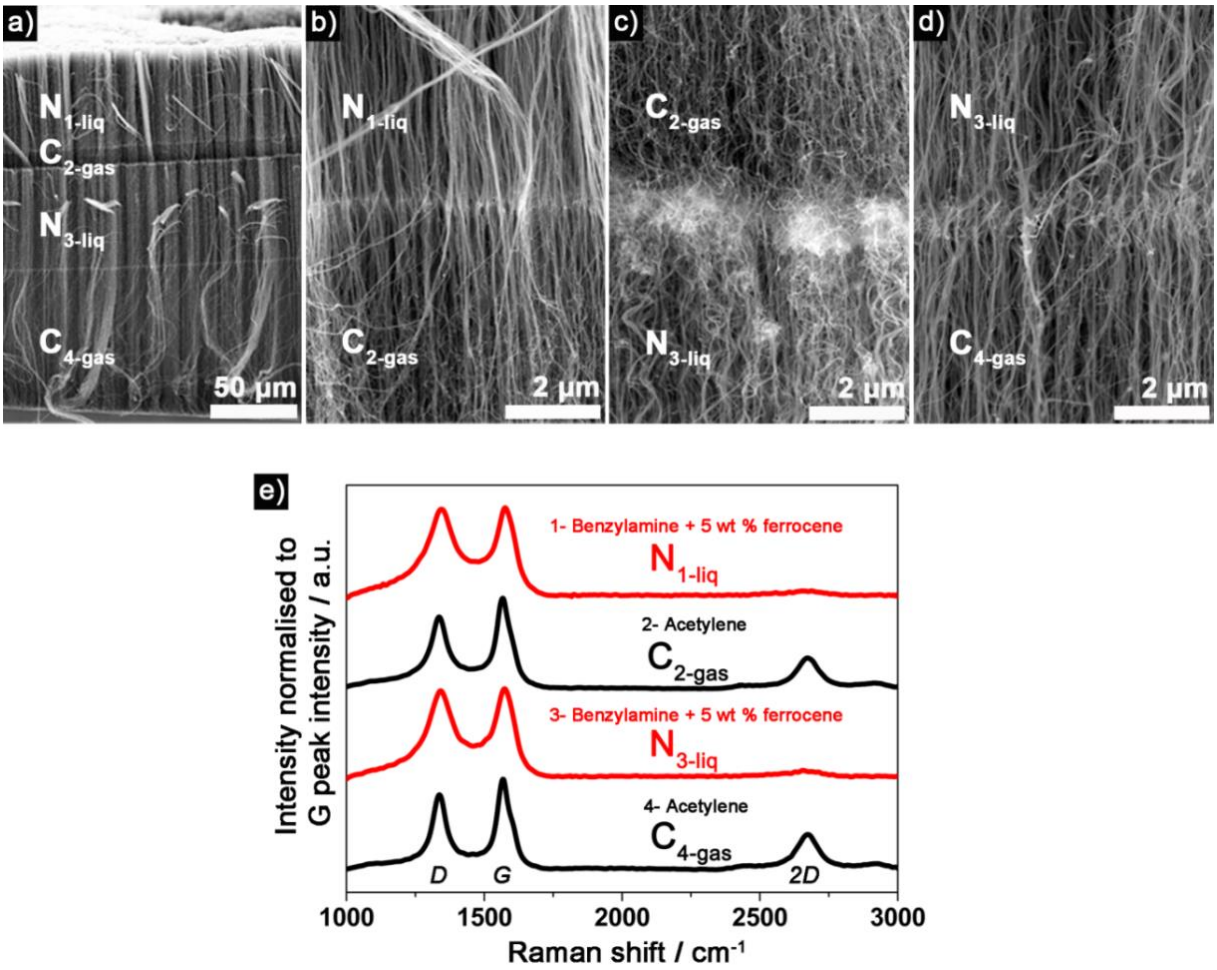

Figure 5.17. (a) SEM micrographs of $N_{1\text{-liq}}/C_{2\text{-gas}}/N_{3\text{-liq}}/C_{4\text{-gas}}$ structures obtained from the liq/gas approach. The various interfaces between the different sections at higher magnification are reported in (b), (c) and (d). (e) Raman spectra (532 nm wavelength excitation) of each section of a $N_{1\text{-liq}}/C_{2\text{-gas}}/N_{3\text{-liq}}/C_{4\text{-gas}}$ structure.

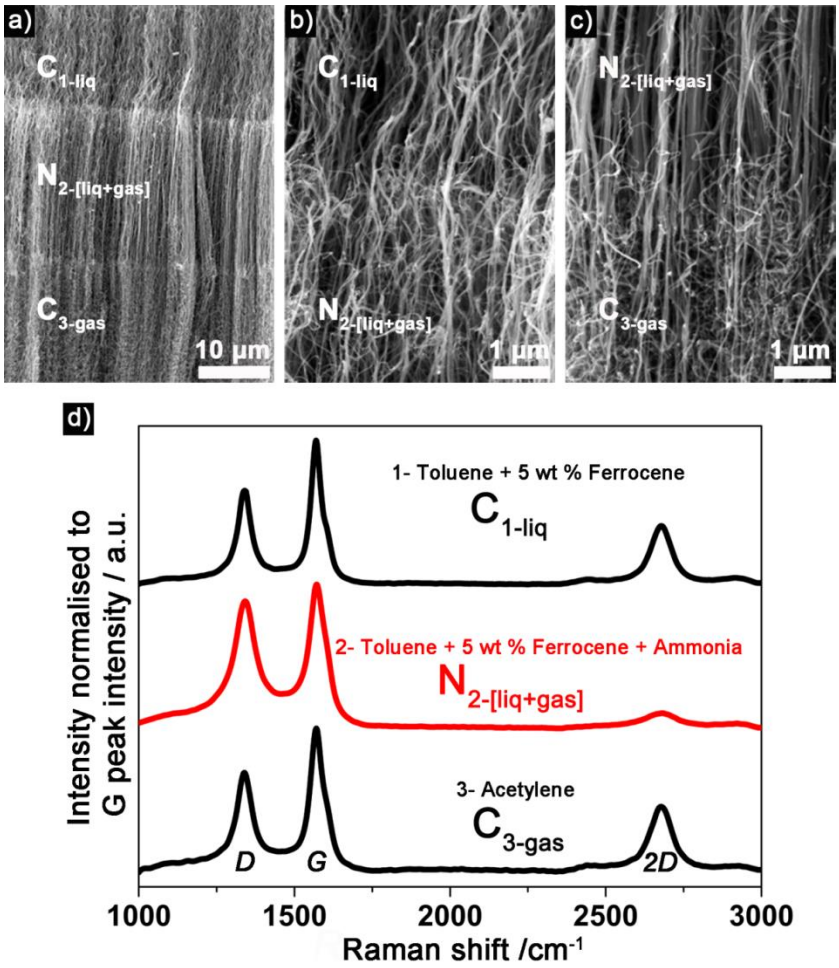

Figure 5.18. (a) SEM micrographs of possible $C_1/N_2/C_3$ structures obtained from a combination of the liq/[liq+gas] and liq/gas approach. The various interfaces between the different sections at higher magnification are displayed in (b) and (c). (d) Raman spectra (532 nm wavelength excitation) of each section of a $C_{1\text{-liq}}/N_{2\text{-[liq+gas]}}/C_{3\text{-gas}}$ structure.

Alongside the main goal of developing MWCNT forests with intratubular junctions, unusual MWCNT structures were also obtained. These structures are worth reporting because they illustrate further the versatility of the synthesis approach presented in this thesis and support the growth mechanism suggested in **Figure 5.4** and **Figure 5.12** for N_1/C_2 junctions. In some cases it is observed with the naked eye that individual layers of the MWCNT forests peel off spontaneously after synthesis. Further investigation by SEM of samples where this peeling off was observed are reported in **Figure 5.19a**. The SEM image

reveals that the peeled off layers are detached from another supporting MWCNT layer. Such 'peeling off' is not observed when no compositional change from one layer to another is induced but seems to happen preferentially at an N/C interface which is less continuous and probably weaker than a C/N interface (**Section 5.3.1**). Another experimental observation is that under the conditions of the liq/[liq+gas]/gas approach more 'peeling off' occurs. By simply bending the quartz tube used as a reactor for synthesis it is possible to collect several milligrams of a CNT powder after the experiment. SEM images of the collected powder are shown in **Figure 5.20**. The materials have not been mechanically scrapped from the surface of the reactor where MWCNTs growth normally happens. The powder obtained, made of ball-like structure (**Figure 5.20b**) is then not detached from a substrate but completely peeled off of the forest.

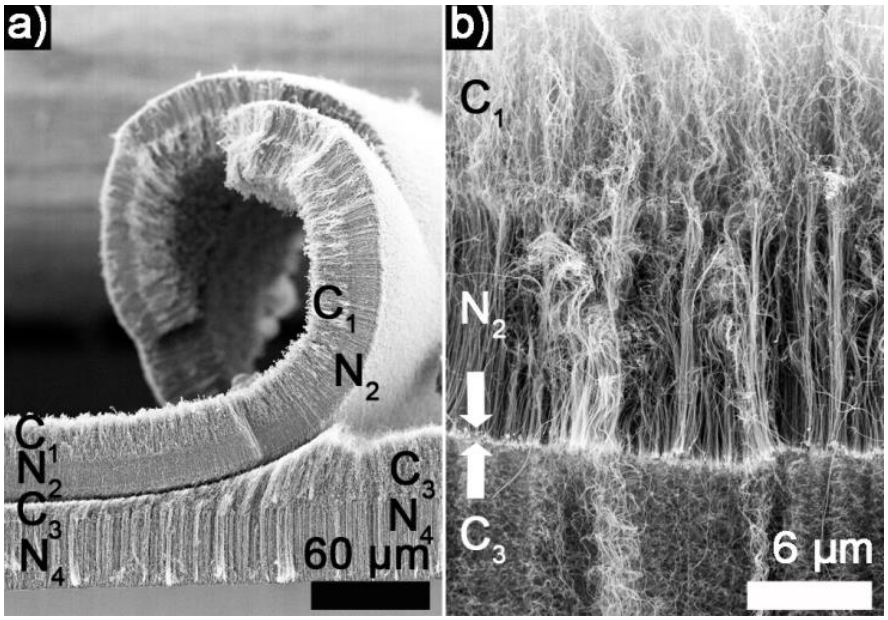

Figure 5.19. SEM micrographs of (a) $C_{1\text{-liq}}/N_{2\text{-liq}}/C_{3\text{-liq}}/N_{4\text{-liq}}$ structure where a break between the middle N_2 and C_3 part leads to MWCNT layers peeling-off. (b) $C_{1\text{-liq}}/N_{2\text{-[liq+gas]}}/C_{3\text{-gas}}$ structures where the N_2/C_3 interface displays iron based particles: brighter line between the two arrows in the image associated with a strong morphological change from straight to wavy MWCNTs.

After peeling off, a 'rolling step' seems to occur explaining the curvature of the structures obtained, **Figure 5.20**. The outer part of the ball-like structure is made of residual catalyst-like particles shown in **Figure 5.20d**. Those same particle-like objects can usually be observed at N/C interfaces (**Section 5.3.1**, **Figure 5.19b**). The N section of a broken N/C interface then becomes the outer surface of the balls. The presence of catalyst-like particles at this N/C interface accounts for the presence of catalyst-like particles at the outer surface of the rolled structures. The peeling off can be promoted by developing weak interfaces between different sections of a MWCNT like developing an N/C junction. The reasons for the rolling phenomena are not established yet and could come from the different length between the C and N sections. The different sections possibly develop different interactions with each other, leading to the resulting unusual spherical geometry, **Figure 5.20**. These explanations are in line with recent observations from other groups working on compositional change along MWCNTs [186]. These results are interesting for continuous production of MWCNTs with intratubular junctions by spontaneous and continuous peeling off of grown MWCNT layers when further control is achieved in the future. Together with the previous observations, this proves that AACVD based synthesis approaches are suitable and robust to produce a range MWCNT structures with various tailored junctions.

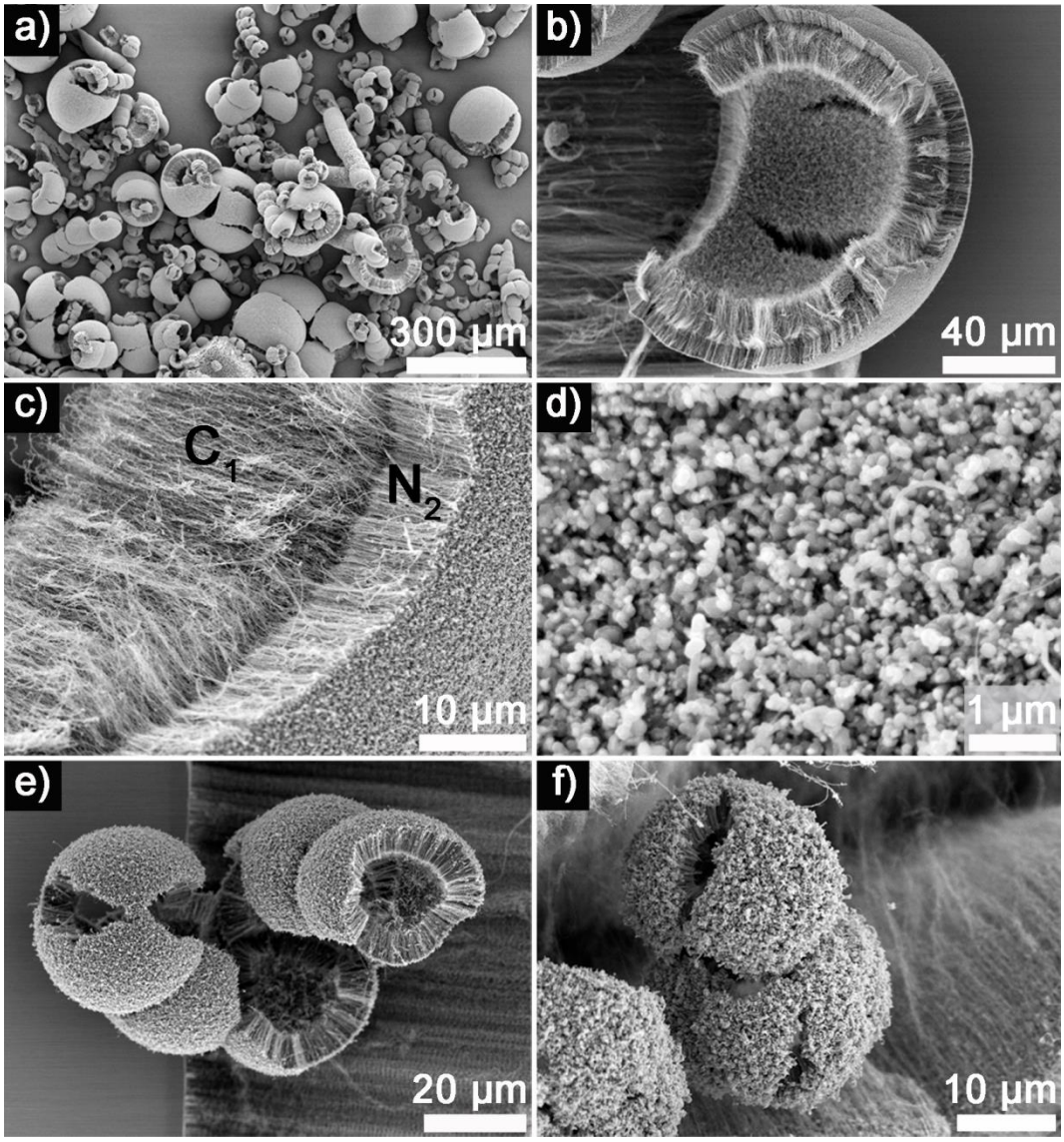

Figure 5.20. (a-f) SEM images of unusual structures present in the powder collected after synthesis. (b) typical open-ball structures (c) higher magnification of spherical structures showing a C_1/N_2 interface. The N part forms the outside part of the ball. (d) the outer surface of the balls are made of catalyst-like particles. (e-f) other ball-like structures obtained.

5.3.3. Towards selective reactivity of MWCNT forests with intratubular junction

This section details the first TGA analysis of MWCNTs with N/C junctions. For the first time, experimental evidence is given to illustrate a localised reactivity along a MWCNT forest with junctions.

5.3.3.1. Unusual oxidation behaviour of MWCNTs with N/C junctions

The characterisations performed so far in this chapter focus on MWCNT structures. The strong structure-properties relationships in nanomaterials suggest that different chemistry could be achieved on various segments of the MWCNTs with intratubular junctions. For the first time, TGA analysis was performed on MWCNTs with junctions because this simple technique (**Section 2.3.7**) gives information of the reactivity of CNTs with oxygen. **Figure 5.21** displays the thermogravimetric analysis (TGA) of various MWCNTs. It is well established that N-MWCNTs have lower oxidation resistance than un-doped MWCNTs due to a more defective graphitic structure [93]. The mass loss associated with MWCNT oxidation happens at higher temperature for un-doped MWCNTs compared to N-MWCNTs, curves I and II in **Figure 5.21** respectively. Mass loss during oxidation of a typical un-doped MWCNT starts at *ca.* 600 °C (I) whereas for a N-MWCNT sample (II) it starts at *ca.* 450 °C. TGA was also performed on numerous N_1/C_2 and C_1/N_2 samples obtained from various synthesis approaches (**Table 5.1**). The most reproducible results were obtained on $N_{1\text{-liq}}/C_{2\text{-gas}}$ samples. Unlike usual TGA curves for MWCNTs without junctions, such samples show two distinct parts in the oxidation curve, separated by an inflection at *ca.* 550-555 °C: curves III and IV in **Figure 5.21a**.

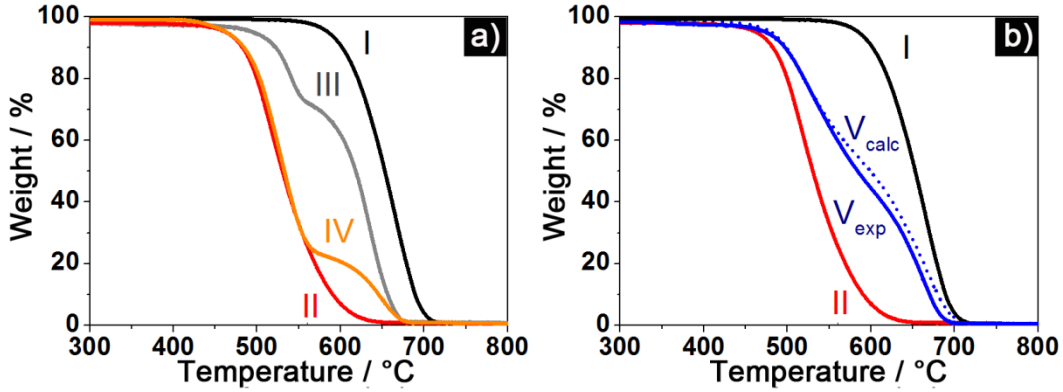

Figure 5.21. Thermogravimetric analysis (TGA) of various MWCNT structures. (a) TGA curves of an un-doped MWCNT sample (I), a N-MWCNT sample (II) and two $N_{1\text{-liq}}/C_{2\text{-gas}}$ MWCNT samples (III and IV). The difference between III and IV is detailed in the text. (b) TGA of un-doped (I) and N-MWCNT (II) samples. A sample made of the powder material I and II with a mass ratio of 50:50 was made to create an artificial N/C powder structure. The experimental (V_{exp}) TGA curve and the expected curve by adding TGA curves I and II weighted by ½ each (V_{calc}) for this mix-sample are also represented.

5.3.3.2. Towards localised oxidation behaviour by control over MWCNT junctions

No previous TGA characterisation has been reported on MWCNTs with intratubular junctions (**Table 1.4**) to the best of my knowledge. Since the MWCNTs have both un-doped and nitrogen-doped sections, it is likely that the mass loss for temperature lower than the temperature of inflection (550 °C) is related to the N section and the mass loss at higher temperature is related to the C section. To confirm this hypothesis, TGA was performed on samples differing in the ratio of N to C sections (assessed by the length of each section with SEM). The first sample has a N:C length ratio about 1:4 (III, **Figure 5.21a**) whereas the second sample has a N:C length ratio about 1:2 (IV, **Figure 5.21a**). The first sample has a more pronounced C section (III) and shows a TGA curve close in shape to the one expected for an un-doped MWCNTs samples (I): temperature at which mass loss starts is around

510 °C (III, **Figure 5.21a**). The percentage of mass loss after the inflection is also more prominant than the mass loss before. In contrast, the second sample with a more pronounced N component (IV, **Figure 5.21a**) shows a TGA curve closer to the characteristic curve of a N-MWCNT sample (II, **Figure 5.21a**) and the mass loss before the inflection is more prominent than the mass loss after. In addition, the extrapolated onset temperatures are: 482 °C for the curve II (N-MWCNTs) as well as for the part of the curve IV before the inflection, 520 °C for the part of the curve III before the inflection. The onset temperature is 612 °C for I (MWCNTs), 616 °C for the part of the curve IV after the inflection and 610 °C for the part of the curve III after the inflection. The onset temperature for the part of the curves after the inflection was estimated considering the initial mass was the mass at the point of inflection. Several observations can then be attributed to the intratubular junction and a difference in composition within the MWCNTs as detailed in the next section. First is the presence of the inflection. Second is the correlation of mass loss before and after the inflection to the ratio of N to C sections. Third the fact that the onset temperatures fall into two categories: a N-MWCNT-like onset temperature of 480-520 °C and a MWCNTs- like onset temperature of 610-616 °C.

5.3.3.3. Peculiar oxidation behaviour of MWCNT with N_1/C_2 junctions obtained by the liq/gas approach

To understand further the previous new results, a 'mimic' N/C sample was experimentally produced by adding a known amount of un-doped MWCNT powder and N-MWCNT powder. For each sample, TGA curves were first acquired separately before mixing: I and II respectively in **Figure 5.21b**. The 'mimic' sample was obtained by mixing the previous with a N:C mass ratio of 1:1. The mixed powder sample (V) was experimentally analysed by TGA (V_{exp}). Also the two original TGA curves were mathematically added, weighted to the mass ratio of N-MWCNTs and un-doped MWCNTs (V_{calc}). A small inflection is noted

experimentally and predicted by calculation, but it is not as pronounced as the previously detailed case of $N_{1\text{-liq}}/C_{2\text{-gas}}$ structures. Experimental TGA curves for other N_1/C_2 or C_1/N_2 structures obtained by different synthesis routes usually also show a less pronounced inflection than $N_{1\text{-liq}}/C_{2\text{-gas}}$ structures. The reason for this may be a more pronounced difference in oxidation resistance between the $N_{1\text{-liq}}$ section and the $C_{2\text{-gas}}$ section. Also the MWCNT length achieved with the $N_{1\text{-liq}}/C_{2\text{-gas}}$ approach is longer than in the other routes in this study. The change in composition at the interface between the two sections is also sharper than in the other synthesis routes (**Figure 5.11**). Finally, the possible role of the catalyst particles present at the N_1/C_2 interface that also makes $N_{1\text{-liq}}/C_{2\text{-gas}}$ junctions specific is difficult to establish at this stage. Despite these singularities, the samples of MWCNTs with $N_{1\text{-liq}}/C_{2\text{-gas}}$ junctions are ideal to prove for the first time that the oxidation behaviour expected from N-MWCNTs and un-doped MWCNTs are successfully combined in MWCNTs with a change in composition.

5.3.4. Localised oxidation behaviour of MWCNTs with N/C junctions

Results obtained with an analytical technique (TGA) on $N_{1\text{-liq}}/C_{2\text{-gas}}$ suggest different oxidation behaviours between the N and the C sections. However, TGA does not give any information on the localised behaviour along a MWCNT forest. To fully prove for the first time a spatially localised difference in reactivity along the nanomaterial this would need to be pictured along the MWCNT forest. MWCNT forests obtained from various syntheses approaches (**Table 5**.1) showing N/C or C/N junctions were simply oxidized in air at 520 ºC for time between 30 minutes and 2 hours. The temperature 520 °C was chosen because it is a temperature lower than the temperature of the inflection around 555 °C, **Figure 5.22a**, and should correspond to a temperature where only the N section is completely oxidised. It was found that the time of oxidation did not have a strong influence on the results presented.

Raman microscopy was used to acquire spectra selectively on both sections of the sample. Results for a $N_{1\text{-liq}}/C_{2\text{-gas}}$ sample are displayed in **Figure 5.22b**. Raman analysis before and after oxidation shows that in the N section the D and G peaks are absent from the Raman spectrum after oxidation. This suggests that the N section (red in **Figure 5.22b**) does not contain carbon anymore. In contrast, the C section (black in **Figure 5.22b**) still contains a carbon material, as indicated by the presence of the D, G and 2D peak after oxidation, **Figure 5.22b**. A higher D peak compared to G peak intensity is observed after oxidation compared to the case before oxidation which is consistent with nanotube damage during the oxidation process. It is also observed with an optical microscope that the N section has a brighter contrast than the C section, **Figure 5.22c**. All these observations confirm that a modification has occurred during oxidation but mainly on the N section, as schematised in **Figure 5.22d**. The N section (red) is converted to a section of different nature (orange) during oxidation.

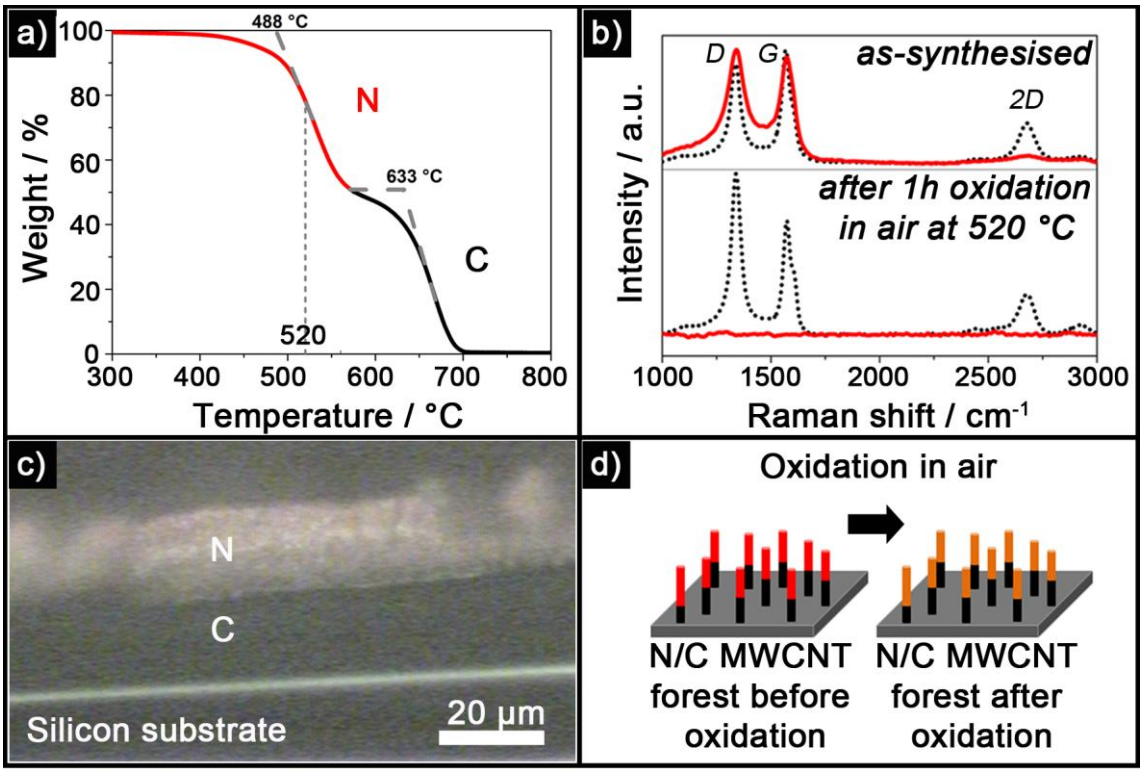

Figure 5.22. (a) TGA curve for N/C MWCNTs. (b) Raman spectra of both N (continuous) and C (dotted) sections before (top) and after (bottom) oxidation in air for 1 hour at 520 °C. (c) Optical microscope image (x50) of a N/C MWCNT structure showing the possibility to focus on the N (white) or C (dark) sections of the forest after oxidation in air to locally acquire the associated Raman spectra. (d) Schematic representation of a change in N (red) /C (black) MWCNTs with junction after oxidation.

This first demonstration for a localised reactivity along MWCNTs with junction is further investigated with photos and SEM images in **Figure 5.23**. N-MWCNTs (N), un-doped MWCNTs (C) and MWCNT forests with a N/C junction have been oxidised 2 hours at 520 °C. After oxidation, the N-MWCNT and the sample with junction turn orange, **Figure 5.23-I**. Also, all of the N sample as well as the N section of the N/C sample is turned into a network of particle-like objects consisting of 'nanospherules'. These nanospherules appear brighter than CNTs in the SEM for similar acquisition parameters, **Figure 5.23-II**, and are attributed to the formation of iron-oxide based species [191] from

residual catalyst particles coalescing after oxidation at high temperature. This explanation for the nature of the 'nanospherules' is consistent with the orange colour observed and the absence of a D, G and 2D peak in the Raman spectrum of the expected N section after oxidation (**Figure 5.22b**). In contrast, the C only sample remains mainly black after oxidation, **Figure 5.23-I**. The C section of this C sample and the C section of the N/C sample still show typical MWCNT structures in SEM, **Figure 5.23-II**. This is in agreement with the associated Raman spectrum showing a D, G and 2D peak (**Figure 5.22b**). These results confirm that after oxidation the N section of the N/C MWCNT can be selectively converted into a non-carbon material and so the N section of each MWCNT undergoes more modification than the C section as schematised in **Figure 5.23-III**.

The results presented are reproduced with other MWCNTs with junctions synthesised (**Table 5.1**). TGA analysis of some MWCNTs with junctions developed in this thesis does not always show an inflection in the TGA curve (**Section 5.3.3.3**). Nevertheless, preferential oxidation of the N section of these nanotubes can always be confirmed by SEM (change in the contrast of the N section) and Raman spectroscopy (absence of D, G and 2D peak) as described in the previous paragraphs. This is illustrated with different structures: $N_{1\text{-liq}}/C_{2\text{-gas}}$ in **Figure 5.24a-b**, $C_{1\text{-liq}}/N_{2\text{-[liq+gas]}}$ in **Figure 5.24c** and $C_{1\text{-liq}}/N_{2\text{-[liq+gas]}}/C_{gas}$ in **Figure 5.25**, $N_{1\text{-liq}}/C_{2\text{-gas}}/N_{3\text{-liq}}/C_{4\text{-gas}}$ in **Figure 5.26**. In all cases the N section, more affected that the C section by heat treatment in air, is converted into a section made of spherule-like structures brighter in the SEM images. In contrast, the C section remains dark and mainly made of MWCNTs. These results confirm for the first time to the best of my knowledge that localised reactivity along a MWCNT forest with intratubular junctions can be achieved, regardless of the production route selected.

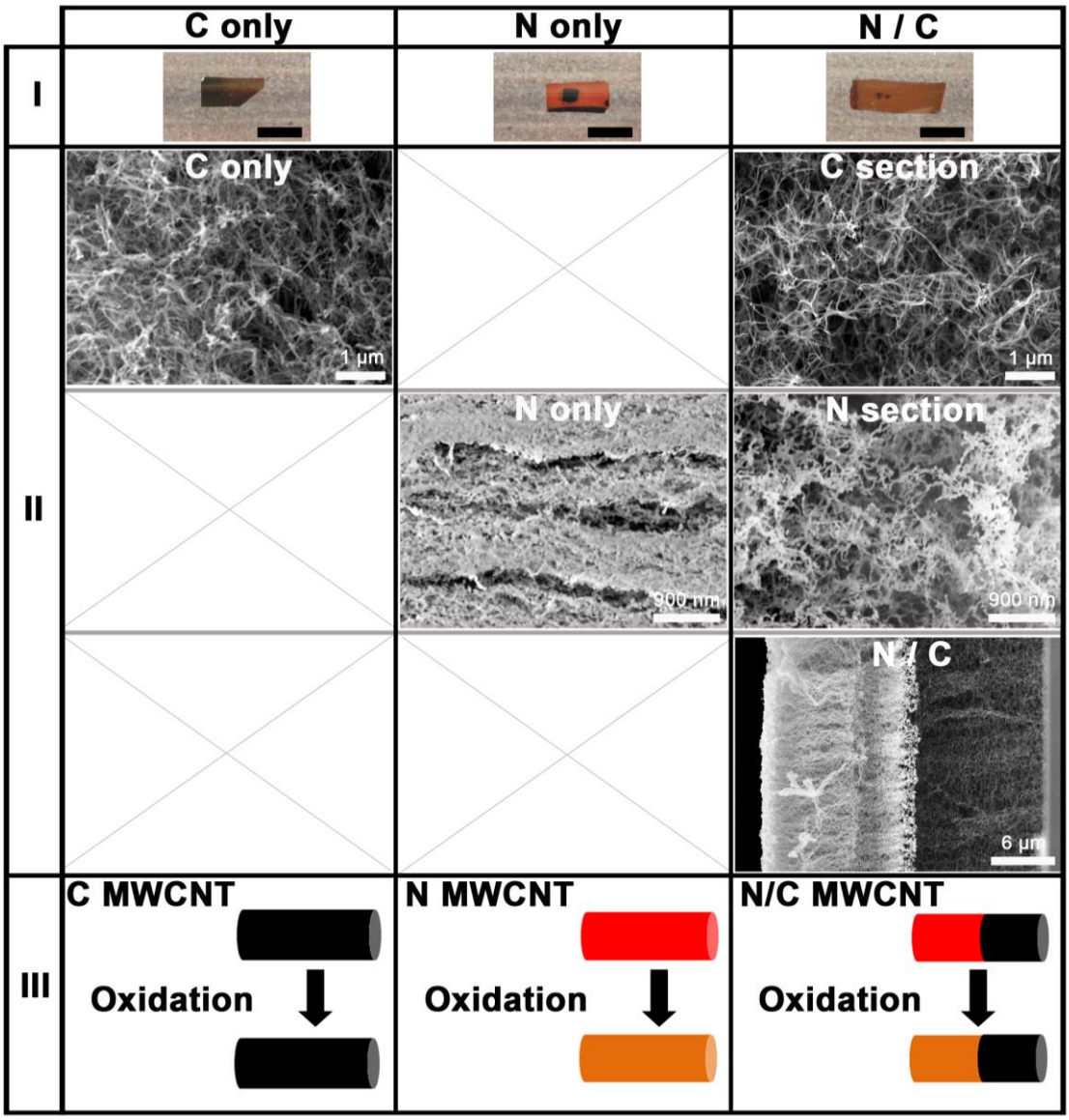

Figure 5.23. (I) Top view photos of MWCNT forests grown on silicon wafers after 2 hours oxidation in air at 520 °C for C only, N only and N/C samples. The scale bar in black is 5.3 mm. Photos were taken with a grey background. (II) SEM micrographs of the previous samples: C only, N only and N/C structures, as well as higher magnification micrographs of the C and N sections of the N/C structure. (III) Schematic illustration of the effect of oxidation on the MWCNT structure. The C and N only samples were obtained from liquid precursors and the N/C samples were obtained from the liq/gas approach.

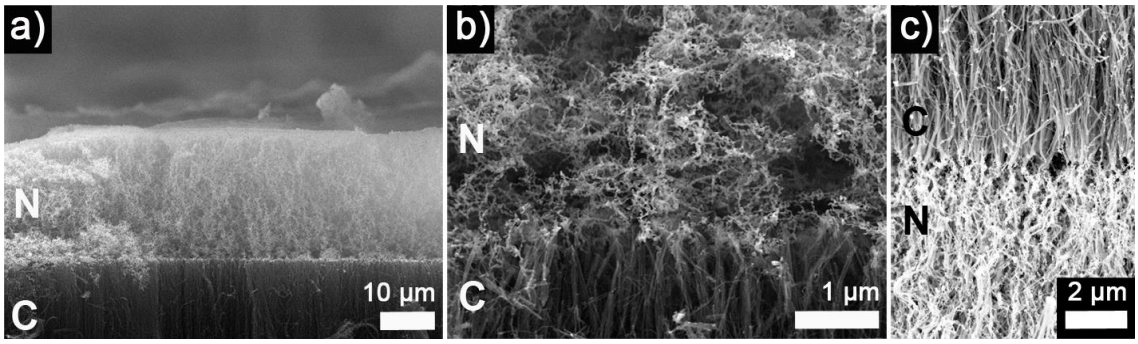

Figure 5.24. SEM micrographs after 30 minutes oxidation in air at 520 °C of (a and b) $N_{1\text{-}liq}/C_{2\text{-}gas}$ and (c) $C_{1\text{-}liq}/N_{2\text{-}[liq+gas]}$ forests.

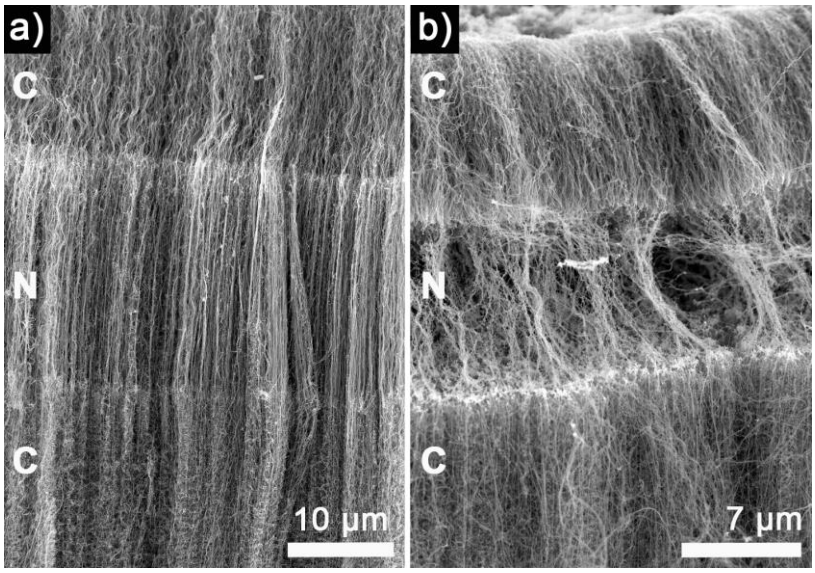

Figure 5.25. SEM micrographs of $C_{1\text{-}liq}/N_{2\text{-}[liq+gas]}/C_{3\text{-}gas}$ MWCNTs. (a) before and (b) after oxidation at 520 °C for 30 minutes.

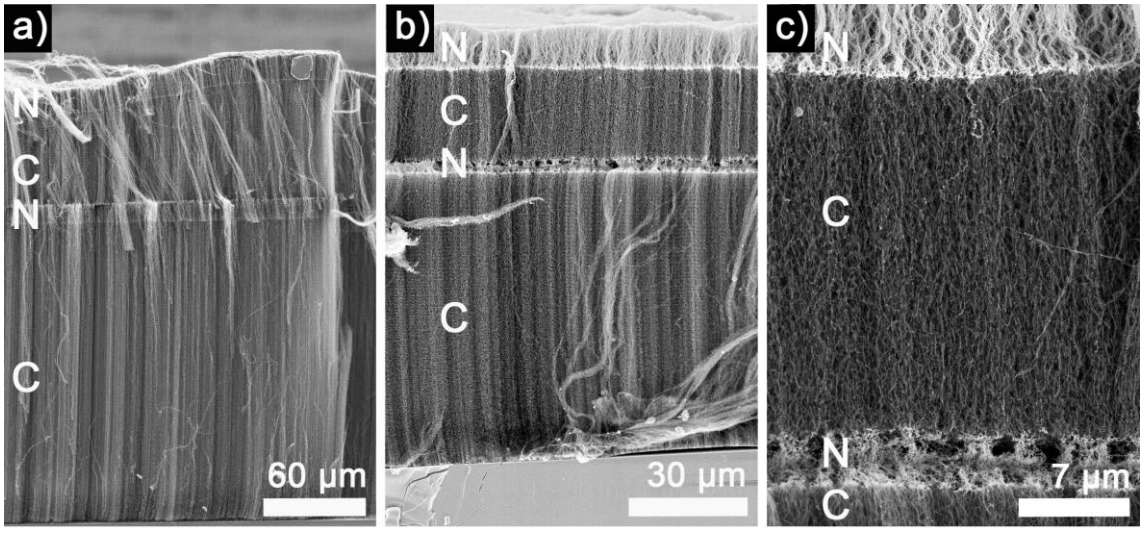

Figure 5.26. (a-c) SEM micrographs of $N_{1\text{-}liq}/C_{2\text{-}liq}/N_{3\text{-}liq}/C_{4\text{-}liq}$ structure before (c) and after (d-e) oxidation in air for 30 minutes at 520 °C.

5.3.5. Localised immobilisation of particles on MWCNTs with N/C junctions

The previous results in **Section 5.3.4** confirm for the first time that different reactivity with oxygen can be induced along MWCNT forests with junctions *via* their tailored design. The present section takes a step further and focuses on the asymmetric decoration of these MWCNTs. The idea is to exploit the established difference in structure and reactivity along the MWCNT forest to achieve a spontaneous asymmetric functionalisation.

5.3.5.1. Case study of platinum deposition

Since the approach to obtain asymmetrically functionalised nanomaterials proposed in this thesis is completely new to the best of my knowledge, a solid proof of concept is required. Hydrogenases are catalysts with low surface coverage and to establish their localised immobilisation specific equipment like scanning electro-chemical microscope [208] would be required. A simpler nano-object like platinum particles is then preferred. First, platinum deposition can easily be identified by SEM and EDS measurements (**Chapter 2**). In particular SEM was preferred to TEM because it is more convenient to study the platinum particle depositions along a MWCNT forest. Second, among the different reports in the literature, immobilisation of platinum particles on N-MWCNTs and un-doped MWCNTs gives different results [164]. On N-MWCNTs platinum coverage is reported to be more uniform than for un-doped MWCNTs. This different coverage is due to platinum nucleation being promoted on a more defective N-MWCNT surface, as well as possible interaction with the nitrogen atoms [71, 252, 253]. In reports investigating the effect of nitrogen doping, the comparison is performed between different batches: one made of N-MWCNTs, one made of un-doped MWCNTs. The comparison is never performed within a single CNT forest with a compositional change. There is no experimental evidence to date that within a single MWCNT or a MWCNT forest, control over reactivity or particle deposition can be achieved

by simply developing C/N junctions. This thesis addresses for the first time the possibility to achieve a spontaneous and localised control over nano-objects with the case study of platinum particle loading on MWCNTs with junctions.

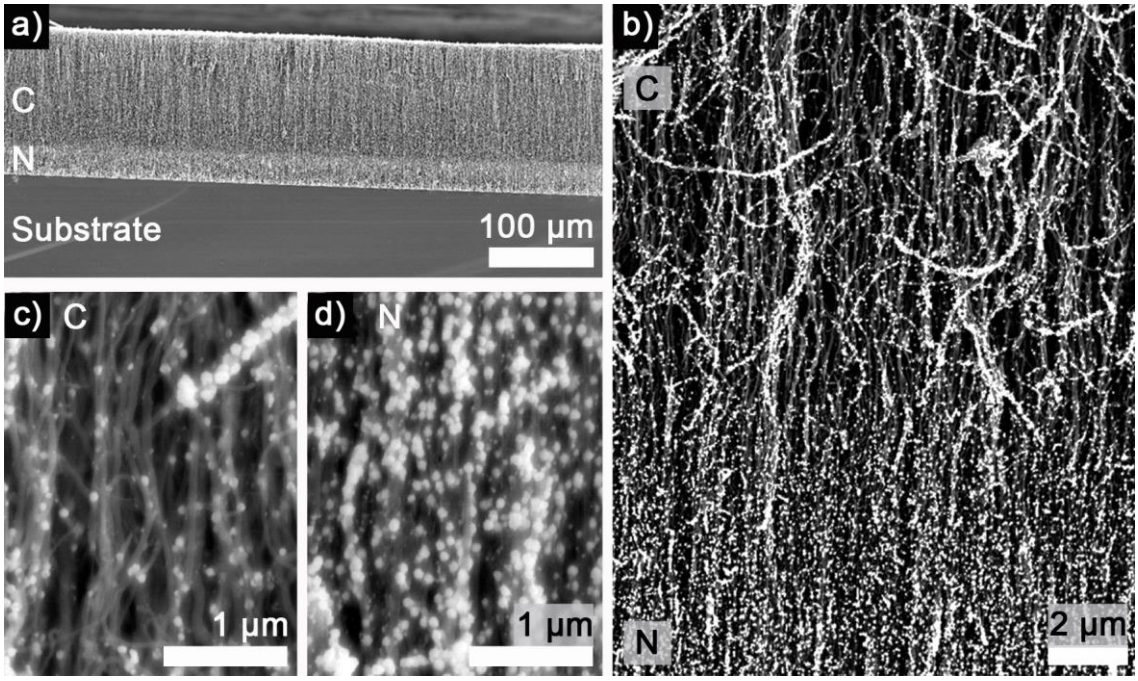

Figure 5.27. (a) and (b) SEM micrographs of platinum particles electrodeposited on a $C_{1\text{-liq}}/N_{2\text{-liq}}$ MWCNT structure. (c) and (d) are respectively higher magnification SEM micrographs of the $C_{1\text{-liq}}$ and $N_{2\text{-liq}}$ sections displayed in (a) and (b).

For forests of MWCNTs with N/C or C/N junctions obtained from different synthesis routes, immobilisation of platinum particles by bulk electrodeposition of platinum salts [72] and by bulk chemical reduction [215-217] was performed (**Section 2.7**). In all cases, both N and C sections along a single MWCNT were dipped into the same salt solution. **Figure 5.27** and **Figure 5.28** show secondary electron SEM images of the MWCNTs after platinum deposition. Platinum particles are observed as white spots covering the MWCNTs. The particle coverage differs from the C, **Figure 5.27c**, and the N, **Figure 5.27d**, section of the forest. Both C and N sections are connected within the same forest but the N section is more uniformly covered. This observation is consistent for different electrolytes (KPB, 100mM, pH 7 or KCl, 50 mM) and number of scans during cyclic voltammetry for the bulk

electrodeposition, **Figure 5.28**; for different times of reduction for the bulk chemical reduction. Regardless of the bulk approach used to nucleate the platinum particles, a difference in platinum particle loading is established between the N and C sections. The localised asymmetric loading is then dependent on the design of the MWCNT forests only.

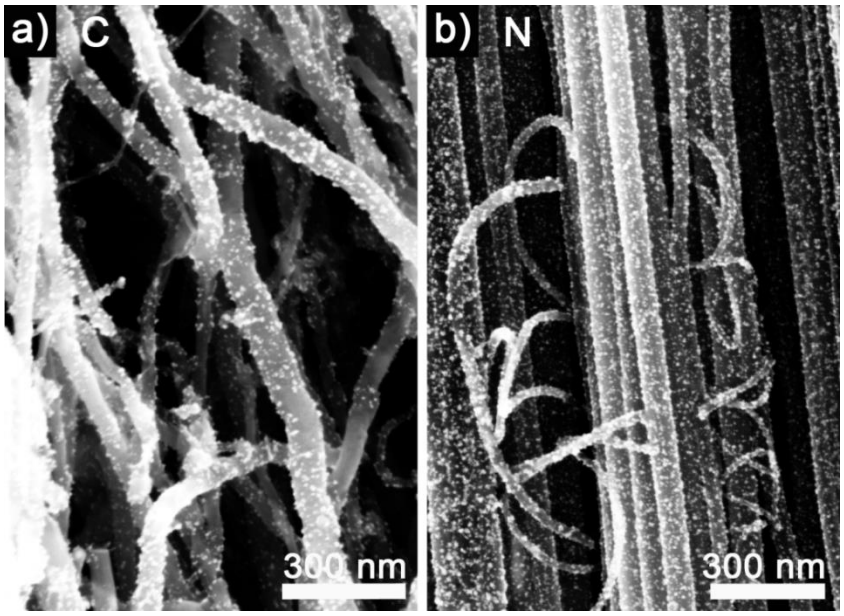

Figure 5.28. SEM micrographs of platinum particles electrodeposited on a $C_{1\text{-liq}}/N_{2\text{-liq}}$ MWCNT forest. The particle coverage differs from the (a) $C_{1\text{-liq}}$ and the (b) $N_{2\text{-liq}}$ section of the forest. The difference with Figure 5.27 is a lower number of voltammetric scans during platinum electrodeposition leading to smaller particle size.

SEM images based on backscattered electrons in **Figure 5.29** also confirm that species with a higher atomic number are deposited predominantly on the N rather than the C section because the N section appears brighter than the C section, **Figure 5.29a-d** (**Figure 2.7b**). The difference in contrast between the N and C sections is not observed for control samples without deposited platinum, **Figure 5.29e-f**, **Figure 2.7c**. The fact that the N section appears brighter after platinum deposition is then attributed to presence of platinum particles with a more uniform coverage. Finally EDS makes it possible to acquire compositional maps across the junctions. EDS maps in **Figure 5.30** show a more uniform coverage of platinum (green

dots) on the N section rather than the C section. For various N/C samples obtained from various synthesis routes (**Table 5.1**) similar results were obtained.

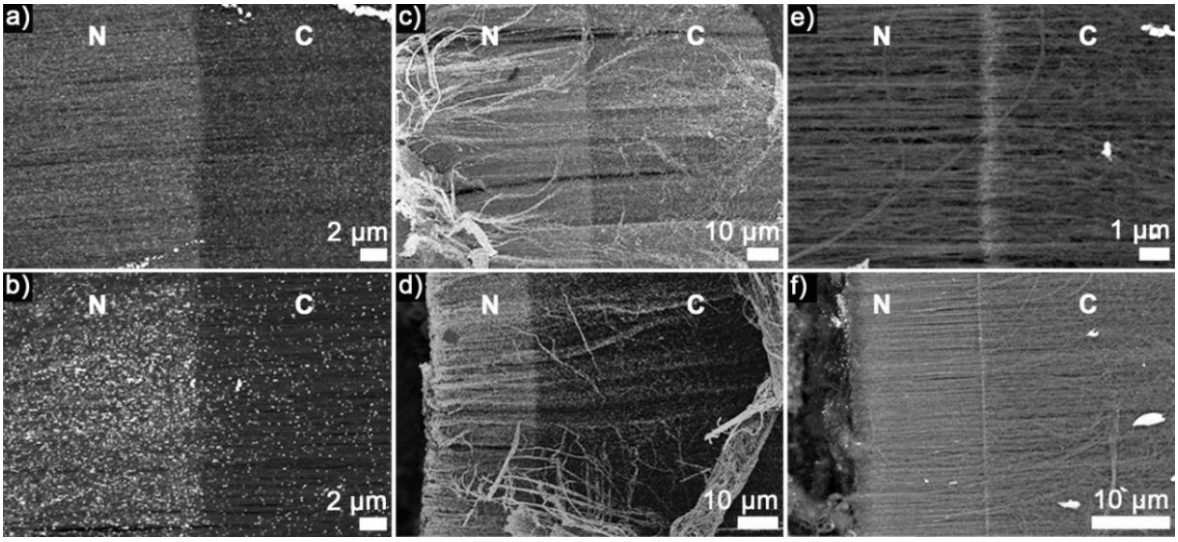

Figure 5.29. SEM micrographs (backscattered electron detector) at the junction for two different MWCNT forests with $N_{1\text{-liq}}/C_{2\text{-gas}}$ junction. (a), (c) and (e) refer to a N(60 µm long)/C(70 µm long) structure and (b), (d) and (f) to N(20 µm long)/C(70 µm long) structures. (a), (b), (c) and (d) show samples after platinum bulk electrodeposition. (e) and (f) represent images from part of the samples where no platinum was immobilised. The lighter line in (e) and (f) comes from iron based particles marking the junction.

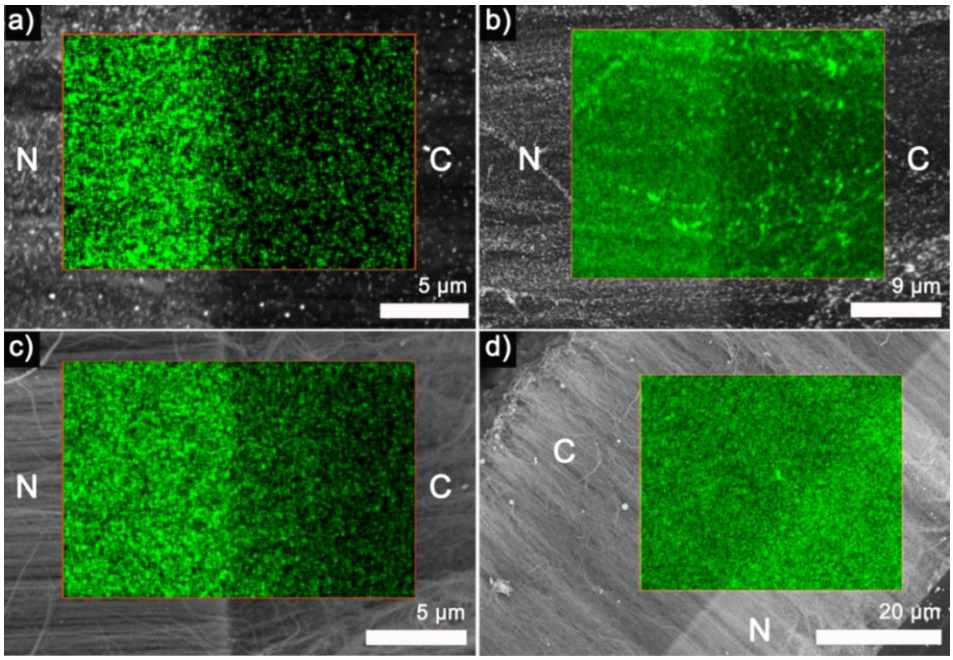

Figure 5.30. Backscattered electron micrographs and platinum (green, intensity of peak at 2.100 keV) EDS maps of (a-c) $N_{1\text{-liq}}/C_{2\text{-gas}}$ and (d) $C_{1\text{-liq}}/N_{2\text{-gas}}$ structures on which platinum was deposited whether by (a) and (b) electrodeposition or (c) and (d) chemical reduction. The difference between samples displayed in (a) and (b) is a different N/C length ratio of N(20 µm)/C (70 µm) and N (60 µm)/C(70 µm) respectively.

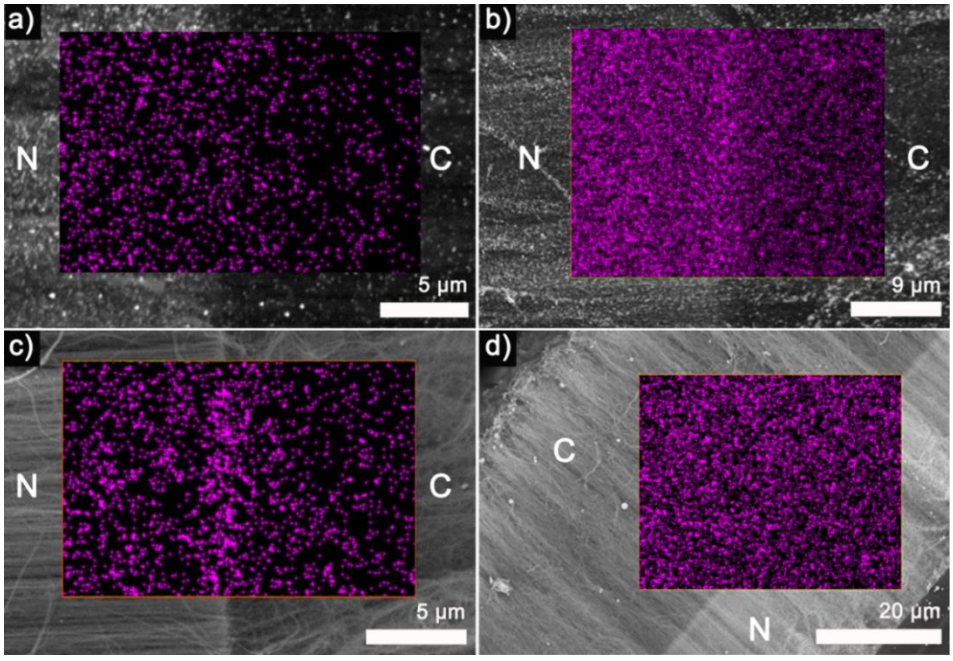

Figure 5.31. Iron EDS maps (purple, intensity of peak at 6.399 keV) counterpart of Figure 5.30.

5.3.5.2. New application of MWCNTs with junction: direct evidence of the effect of doping MWCNTs with nitrogen for platinum deposition

The results presented show for the first time the possibility to spontaneously control an asymmetric repartition of nano-objects on a MWCNT forest by developing a change in composition along the forest. A step further is achieved by giving evidence to explain this asymmetric partitioning. First, it can be hypothesised that elements different than platinum have an asymmetric repartition along the forest and promote the nucleation of platinum in an asymmetric way. Second, asymmetric functionalisation can originate from different precursors leading to different graphitic structures and this induces different nucleation process on the different sections. Third, it is more specifically the use of nitrogen containing precursors to promote a stronger difference in graphitisation and addition of nitrogen atoms in the carbon lattice [92, 250] that favours an asymmetric nucleation of platinum.

Only iron is the element that could be detected on EDS maps of MWCNT forests with junction to show an asymmetric repartition along the tubes. This is due to the synthesis route where ferrocene is introduced only for the growth of the first section in the liq/gas approach. The EDS maps for iron associated with the results presented in **Figure 5.30** are presented in **Figure 5.31**. The maps for the residual iron in the forest do not correlate with maps for platinum. Therefore the asymmetric repartition of platinum is not due to the asymmetric repartition of iron. The first possible explanation for the localised immobilisation of platinum can be ruled out. To investigate the effect of the nature of precursors on the deposition of platinum, C/C and N/N structures are conveniently obtained by the liq/gas synthesis. Each section in these structures is grown from a different precursor (liquid or gaseous). Platinum deposition is performed on these structures and assessed by EDS as previously detailed, **Figure 5.32**. C/C and N/N structures do not lead to a pronounced difference in platinum loading on each section because the coverage of green dots related to presence of platinum is rather uniform across the junction. This is especially clear on the

N/N structure where coverage is uniform across the interface, **Figure 5.32b**. The strongest differences in platinum loading are then achieved on C/N or N/C structures.

In conclusion, a difference in platinum loading is mainly favoured by a compositional change (nitrogen doping) and not a simple change in graphitic structures induced by using different precursors. These results give an example of a new application of MWCNTs with N/C junctions. The influence of nitrogen in MWCNTs can be assessed by direct comparison of defined and controlled regions with or without nitrogen. In this thesis, tailored properties of the materials are used to successfully develop asymmetrically functionalised MWCNTs.

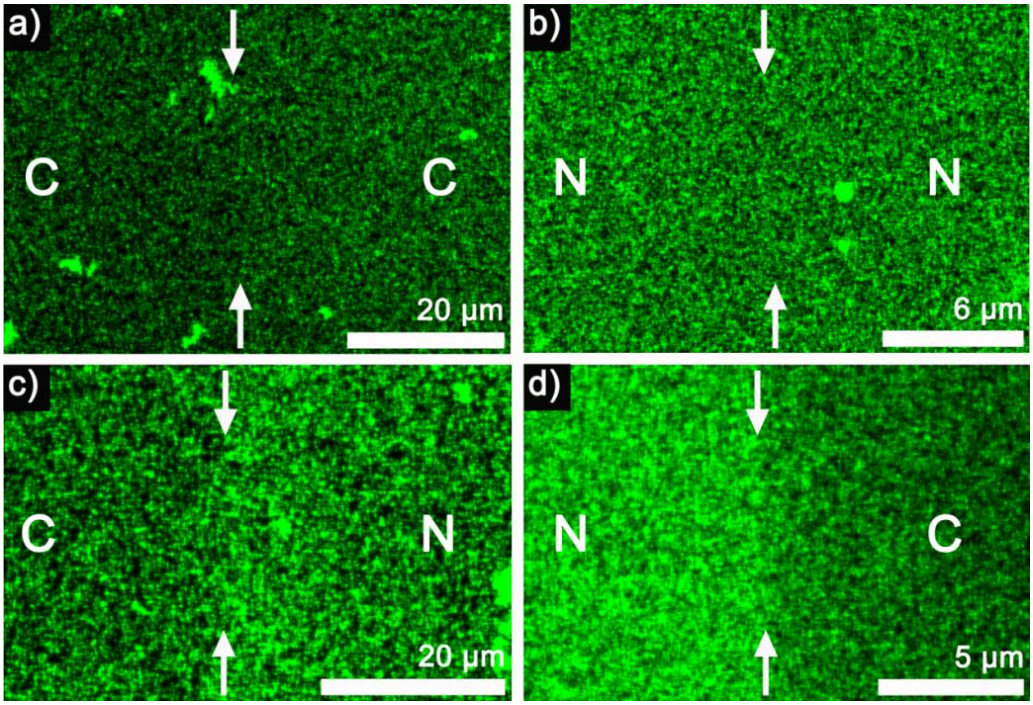

Figure 5.32. Platinum (green, intensity of peak at 2.100 keV) EDS maps of (a) $C_{1\text{-liq}}/C_{2\text{-gas}}$, (b) $N_{1\text{-liq}}/N_{2\text{-gas}}$, (c) $C_{1\text{-liq}}/N_{2\text{-gas}}$ and (d) $N_{1\text{-liq}}/C_{2\text{-gas}}$ structures after chemical reduction of a platinum salt. The white arrows mark the expected interface between the N and C sections established by analysis of the backscattered electron micrographs used to record the EDS data.

5.4. Conclusions

Several interdependent challenges related to MWCNTs with junctions are successfully addressed. A combination of AACVD and CVD is first presented to obtain large quantities of MWCNTs with continuous junctions. By using a succession of liquid and gaseous hydrocarbon precursors during a single experiment, MWCNT/(N-MWCNT), (N-MWCNT)/MWCNT, MWCNT/MWCNT and [N-MWCNT]/[N-MWCNT] junctions were successfully obtained by a root-growth mechanism. Multiple junctions and original ball-like MWCNT structures were also created with this synthesis approach, illustrating the versatility of the technique. Due to the improved synthesis proposed, larger quantities of MWCNT forests with junctions than in previous works were obtained.

Due to this first achievement, a second achievement is that different localised oxidation resistance along MWCNTs with intratubular junction is proved for the first time by TGA, SEM and optical microscopy coupled to Raman spectroscopy. The strong structure-property relationship in CNTs suggests that different surface properties could also differ along the tubes.

A third achievement is then to prove for the first time by SEM and EDS analysis a preferential and spontaneous immobilisation of platinum particles on a nitrogen-doped section of a MWCNT forest rather than the un-doped section. The particles deposition was performed with bulk deposition methods like electrodeposition and chemical reduction. The spontaneous asymmetric decoration achieved pave the way to the facile creation of objects on which asymmetric functionalisation could be induced by the structural design of the CNTs rather than the technique used for functionalisation. The concept of MWCNT forests with intratubular junctions for simple asymmetric structures proved in this thesis is better pictured and summarised in **Figure 5.33**. The MWCNT with junctions presented are a

versatile yet simple scaffold for applications where a spatial control at the nanoscale over structures, properties and reactivity along a single nanomaterial is required.

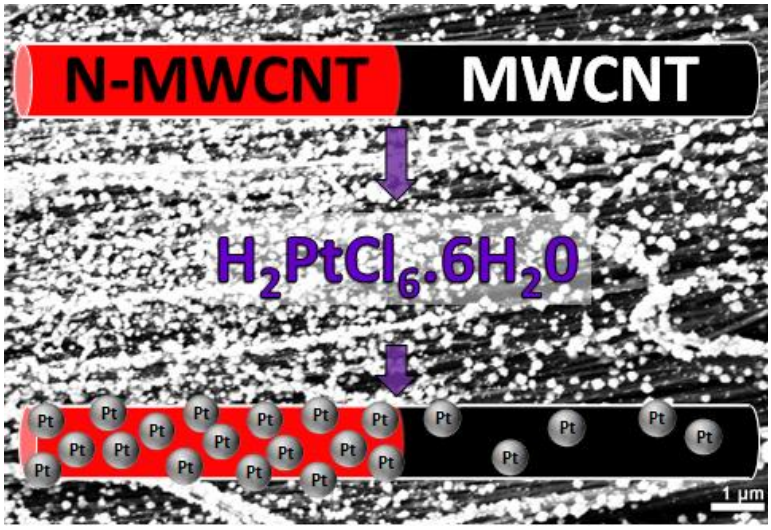

Figure 5.33. Illustration of the concept behind MWCNTs with intratubular junction for spontaneous localised immobilisation of nano-objects along a single MWCNT.

With the proposed synthesis, design, characterisation and use of MWCNTs with junctions, broader applications can be envisioned outside the field of electronics that is their niche application to date. The results presented bridge together the previous research performed on doped and un-doped CNTs, studied so far separately, to exploit the benefits of chemical doping to tune CNT properties. For instance MWCNTs with junctions could be used to assess the effect of different graphitisation or composition on the localised immobilisation of particles, molecules or proteins by direct comparison of the effect of a structural change along a single nanomaterial. For this purpose, Raman microscopy is shown in this thesis to be a simple, fast and reliable technique for characterisation of MWCNTs with various junctions. This is an important demonstration because it opens opportunities for scientists and collaborators with limited access to electron microscopy facilities, to simply explore the potential of CNTs with junctions. A step further could be achieved by coupling optical microscopy with IR and/or fluorescence spectroscopy to investigate and control further the spontaneous asymmetric immobilisation demonstrated.

Chapter 6: Summary and future research

"Learn from yesterday, live for today, hope for tomorrow.
The important thing is to not stop questioning."
Albert Einstein

6.1. Summary of research

Different degrees of design were successfully explored in this thesis to tailor carbon materials for specific goals, opening new opportunities in studies and applications of immobilised bio-redox-catalysts in the field of energy production and chemical synthesis.

The first comparison of the same hydrogenase immobilised onto various powdered carbon materials under equivalent experimental conditions is performed (**Chapter 3**). Eleven carbon materials with different features like size, morphology, surface area, porosity, graphitic structures, commercially available or synthesised are all shown to be promising electrode materials for hydrogenase adsorption. The materials with the highest specific surface area lead to the highest electrocatalytic current from the immobilised hydrogenase in this study. The most graphitic materials lead to the highest loading of electro-active enzyme per total surface area of electrode. The nanoscale of the nanomaterials investigated is also proved to be suitable for IR spectroscopic studies under electrochemical control of FMN and hydrogenase (Hyd-1) directly adsorbed on electrodes assembled from the carbon materials. This achievement opens the way to further investigation of bio-electrocatalysts in new ways, possibly revealing new key catalytic features.

Despite MWCNTs being hydrophobic and relatively difficult to disperse in aqueous solution for hydrogenase immobilisation, they offer opportunities to develop carbon scaffolds that could not easily be obtained with powdered materials. The AACVD technique used to synthesise the MWCNTs in this thesis is for instance a suitable technique to obtain vertically-aligned forests of MWCNTs. Instead of using flat substrate as often preferred in the literature, the opportunity to grow MWCNT forests directly into quartz tubular substrates

is studied. The final structure obtained is a MWCNT column (CNC, **Chapter 4**) which has inner walls made of a porous, interconnected and conductive carbon network. These CNCs were studied in detail for the first time and synthesis parameters examined to achieve controlled filling with MWCNT. The flow rate of carrier gas is shown to be a key parameter to control the CNCs properties. Without any further treatment the CNCs are demonstrated as simple, readily available and successful scaffolds to support catalytic reactions performed by enzyme cascades in a flow catalysis configuration. The CNCs are then a versatile scaffold which may be relevant for industrial production of fine chemicals.

In order to explore even more the opportunity to tailor carbon nanomaterials the question of localised immobilisation of objects along a MWCNT has been successfully addressed (**Chapter 5**). Without using a localised immobilisation technique, the opportunity to induce spatial control over reactivity and immobilisation of nano-objects like particles along CNT forests is proved for the first time. This is achieved by careful design of MWCNTs with intratubular junction. An original AACVD-based synthesis of MWCNTs with a structural change is established in order to induce different properties along the MWCNT. In particular, N-MWCNT/MWCNT junctions were created in relatively large quantities. This enables the first TGA analysis of those structures to confirm that different oxidation resistance occurs with a spatial control along the tubes. Furthermore, these structures are considered and successfully demonstrated for the first time as scaffolds to promote ‘spontaneous’ control over the localised immobilisation of platinum nanoparticles along MWCNT forests.

6.2. Future work

The work presented in this thesis and/or performed during the DPhil project led to a range of publications or ongoing projects opening a range of new opportunities (summarised in **Table A5**).

Regarding the development of carbon nanomaterials as electrodes for hydrogenase studies or applications, a material combining a high surface area and abundance of edge planes would be ideal to optimise a hydrogenase electrode and this material is still to be identified. In parallel, mass transport across nano-materials electrodes is a severe limitation to fully exploit hydrogenase activity. Further electrochemical cell and materials design would be beneficial to address more specifically these issues to improve power density in enzyme fuel cells. For instance, a promising option recently investigated is to mix carbon materials with different morphology to control the pore size distribution in the electrode [254]. Regarding the successful coupling of ATR-IR spectroscopy and electrochemistry at a carbon electrode, the results presented in this thesis are promising for further investigation of various (bio)electrocatalysts. Due to the range of carbon materials identified to be compatible with the technique, detailed studies on the influence of a carbon support on the catalytic activity of a particular catalyst are now possible. Together with the opportunity to study the effect of pH or temperature on catalytic properties, further spectro-electrochemical studies of redox species directly adsorbed on carbon materials could reveal important bio-electro-catalytic features not explored yet. This has just recently been achieved by Prof Vincent's group by studying one of the catalytic state of Hyd-1 during H_2 oxidation using BP as electrode material [255].

Since the control over CNCs has been demonstrated, further investigation of the influence of the flow of carrier gas on the nature of MWCNTs grown could be a relevant study to perform. This could potentially involve flow modelling around tubular substrates. The benefit would be to understand better how to develop and control higher quality MWCNTs in terms of length and graphitic structure with AACVD systems. This research could also be relevant to understand better what drives MWCNT growth in general, since preliminary experiments suggest that growing N-MWCNTs in the CNC is challenging.

Furthermore the important field of flow catalysis provides a broad range of applications for these materials. Other solvents and other catalytic reactions could be performed under different conditions to make to the most of the CNCs as flow reactors. In particular, future research should be directed towards the optimisation of catalyst immobilisation in the CNCs for long term stability. In parallel, applications like water purification, an important technological and geo-political challenge for the coming years, can also be safely envisioned by filtration or using cascade of enzyme and particles [256] according to the results presented.

Finally, the possibility to obtain large amounts of MWCNTs with intratubular junctions, the established proof that the material design can induce spontaneous localised immobilisation of objects along MWCNT, plus the opportunity to use simple optical microscopy methods to investigate the structures, all considerably broaden the scope of applications of MWCNTs with junctions. For instance, localised immobilisation of other catalysts than platinum, like other particles, molecules, or enzymes could be of great fundamental interest. To study these systems, characterisation techniques allowing a spatial resolution of few micrometres could be exploited to compare on a single sample different properties induced by the junctions. For instance, scanning electrochemical microscopy [208] could be used to locally probe the redox-properties along the junction of raw materials or materials after (asymmetric) functionalisation with redox-active enzymes. On a synthesis note, the liq/gas approach presented could be transferred to the production of other materials with junctions like carbon/chalcogenides or carbon/boron nitride structures possibly leading to new nanomaterials with new properties. In particular, it must be stressed that the possibility conferred by the liq/gas approach to control the encapsulation of iron particles at the junction of $N_{1\text{-liq}}/C_{2\text{-gas}}$ MWCNTs is extremely promising. This encapsulation is usually not a simple task but is interesting because it could confer specific electronics or magnetic

properties to the CNTs [257]. These properties can be exploited to develop magnetic storage, magnetoresistive sensors, drug delivery or simplify catalyst recovery by magnetic filtration [257]. The $N_{1\text{-liq}}/C_{2\text{-gas}}$ MWCNTs presented in this thesis are then an extremely promising platform to bridge asymmetrically functionalised materials and these diverse scientific areas to possibly open new fields of research in the future.

In a much longer term, the opportunity to develop MWCNTs with intratubular junction in CNCs could be addressed to make the most of the different degrees of carbon materials design successfully investigated in this thesis.

When the miracle happens again it is not a miracle anymore: it is data.

That is why we keep looking for miracles

Bibliography

[1] International Energy Agency. Key world energy statistics. 2014. https://www.iea.org/publications/freepublications/publication/KeyWorld2014.pdf, Last consulted 22/07/2015.

[2] McKay DJC. Sustainable Energy - without the hot air. England: UIT Cambridge Ltd, 2008.

[3] Khasnis AA, Nettleman MD. Global warming and infectious disease. *Archives of Medical Research*. 2005;36(6):689-96.

[4] Arian R. Brief history of oil prices and Middle East tensions: fear of a black gold shortage. *PennEnergy*, published online October 9, 2013. http://www.pennenergy.com/articles/pennenergy/2013/10/a-brief-history-of-oil-prices-and-middle-east-tensions-fear-of-a-black-gold-shortage.html, Last consulted 22/07/2015.

[5] Omoto A. The accident at TEPCO's Fukushima-Daiichi nuclear power station: what went wrong and what lessons are universal? *Nuclear Instruments & Methods in Physics Research Section a-Accelerators Spectrometers Detectors and Associated Equipment*. 2013;731:3-7.

[6] Wang H, Ren ZJ. A comprehensive review of microbial electrochemical systems as a platform technology. *Biotechnology Advances*. 2013;31(8):1796-807.

[7] Kim J, Grate JW, Wang P. Nanobiocatalysis and its potential applications. *Trends in Biotechnology*. 2008;26(11):639-46.

[8] Lojou E. Hydrogenases as catalysts for fuel cells: strategies for efficient immobilization at electrode interfaces. *Electrochimica Acta*. 2011;56(28):10385-97.

[9] Schmid A, Dordick JS, Hauer B, Kiener A, Wubbolts M, Witholt B. Industrial biocatalysis today and tomorrow. *Nature*. 2001;409(6817):258-68.

[10] Jimenez-Gonzalez C, Poechlauer P, Broxterman QB, Yang B-S, Ende DA, Baird J, et al. Key green engineering research areas for sustainable manufacturing: a perspective from pharmaceutical and fine chemicals manufacturers. *Organic Process Research & Development*. 2011;15(4):900-11.

[11] Anastas PT, Kirchhoff MM. Origins, current status, and future challenges of green chemistry. *Accounts of Chemical Research*. 2002;35(9):686-94.

[12] Yang X-Y, Tian G, Jiang N, Su B-L. Immobilization technology: a sustainable solution for biofuel cell design. *Energy & Environmental Science*. 2012;5(2):5540-63.

[13] Tran DN, Balkus KJ, Jr. Perspective of recent progress in immobilization of enzymes. *Acs Catalysis*. 2011;1(8):956-68.

[14] Jesionowski T, Zdarta J, Krajewska B. Enzyme immobilization by adsorption: a review. *Adsorption-Journal of the International Adsorption Society*. 2014;20(5-6):801-21.

[15] de Poulpiquet A, Ciaccafava A, Lojou E. New trends in enzyme immobilization at nanostructured interfaces for efficient electrocatalysis in biofuel cells. *Electrochimica Acta*. 2014;126:104-14.

[16] Feng W, Ji P. Enzymes immobilized on carbon nanotubes. *Biotechnology Advances*. 2011;29(6):889-95.

[17] Yang W, Ratinac KR, Ringer SP, Thordarson P, Gooding JJ, Braet F. Carbon Nanomaterials in biosensors: should you use nanotubes or graphene? *Angewandte Chemie-International Edition*. 2010;49(12):2114-38.

[18] Calvaresi M, Zerbetto F. The devil and holy water: protein and carbon nanotube hybrids. *Accounts of Chemical Research*. 2013;46(11):2454-63.

[19] Matsumoto T, Eguchi S, Nakai H, Hibino T, Yoon K-S, Ogo S. NiFe Hydrogenase from *Citrobacter sp. S-77* surpasses platinum as an electrode for H_2 oxidation reaction. *Angewandte Chemie-International Edition*. 2014;53(34):8895-8

[20] Reeve HA, Lauterbach L, Ash PA, Lenz O, Vincent KA. A modular system for regeneration of NAD cofactors using graphite particles modified with hydrogenase and diaphorase moieties. *Chemical Communications*. 2012;48(10):1589-91.

[21] Sheldon RA. Enzyme immobilization: The quest for optimum performance. *Advanced Synthesis & Catalysis*. 2007;349(8-9):1289-307.

[22] Goldstein DC, Thordarson P, Peterson JR. The bioconjugation of redox proteins to novel electrode materials. *Australian Journal of Chemistry*. 2009;62(10):1320-7.

[23] Hanefeld U, Gardossi L, Magner E. Understanding enzyme immobilisation. *Chemical Society Reviews*. 2009;38(2):453-68.

[24] Alonso-Lomillo MA, Rudiger O, Maroto-Valiente A, Velez M, Rodriguez-Ramos I, Munoz FJ, et al. Hydrogenase-coated carbon nanotubes for efficient H_2 oxidation. *Nano Letters*. 2007;7(6):1603-8.

[25] Lojou E, Luo X, Brugna M, Candoni N, Dementin S, Giudici-Orticoni MT. Biocatalysts for fuel cells: efficient hydrogenase orientation for H_2 oxidation at electrodes modified with carbon nanotubes. *Journal of Biological Inorganic Chemistry*. 2008;13(7):1157-67.

[26] Luo X, Brugna M, Tron-Infossi P, Giudici-Orticoni MT, Lojou E. Immobilization of the hyperthermophilic hydrogenase from *Aquifex aeolicus* bacterium onto gold and carbon nanotube electrodes for efficient H_2 oxidation. *Journal of Biological Inorganic Chemistry*. 2009;14(8):1275-88.

[27] McPherson IJ, Vincent KA. Electrocatalysis by Hydrogenases: Lessons for building bio-Inspired devices. *Journal of the Brazilian Chemical Society*. 2014;25(3):427-41.

[28] Mostofizadeh A, Li Y, Song B, Huang Y. Synthesis, properties, and applications of low-dimensional carbon-related nanomaterials. *Journal of Nanomaterials*. 2011; http://dx.doi.org/10.1155/2011/685081

[29] Kim J, Jia HF, Wang P. Challenges in biocatalysis for enzyme-based biofuel cells. *Biotechnology Advances*. 2006;24(3):296-308.

[30] Vamvakaki V, Tsagaraki K, Chaniotakis N. Carbon nanofiber-based glucose biosensor. *Analytical Chemistry*. 2006;78(15):5538-42.

[31] Ambrosi A, Sasaki T, Pumera M. Platelet graphite nanofibers for electrochemical sensing and biosensing: the influence of graphene sheet orientation. *Chemistry - An Asian Journal*. 2010;5(2):266-71.

[32] Cracknell JA, Vincent KA, Armstrong FA. Enzymes as working or inspirational electrocatalysts for fuel cells and electrolysis. *Chemical Reviews*. 2008;108(7):2439-61.

[33] Krishnan S, Armstrong FA. Order-of-magnitude enhancement of an enzymatic hydrogen-air fuel cell based on pyrenyl carbon nanostructures. *Chemical Science*. 2012;3(4):1015-23.

[34] Armstrong FA, Heering HA, Hirst J. Reactions of complex metalloproteins studied by protein-film voltammetry. *Chemical Society Reviews*. 1997;26(3):169-79.

[35] Léger C, Bertrand P. Direct electrochemistry of redox enzymes as a tool for mechanistic studies. *Chemical Reviews*. 2008;108(7):2379-438.

[36] Li HH, Liu SQ, Dai ZH, Bao JC, Yang XD. Applications of nanomaterials in electrochemical enzyme biosensors. *Sensors*. 2009;9(11):8547-61.

[37] Kihara T, Liu X-Y, Nakamura C, Park K-M, Han S-W, Qian D-J, et al. Direct electron transfer to hydrogenase for catalytic hydrogen production using a single-walled carbon nanotube forest. *International Journal of Hydrogen Energy*. 2011;36(13):7523-9.

[38] Karyakin AA, Morozov SV, Voronin OG, Zorin NA, Karyakina EE, Fateyev VN, et al. The limiting performance characteristics in bioelectrocatalysis of hydrogenase enzymes. *Angewandte Chemie-International Edition*. 2007;46(38):7244-6.

[39] Dunn S. Hydrogen futures: toward a sustainable energy system. *International Journal of Hydrogen Energy*. 2002;27(3):235-64.

[40] Hamdan AA, Liebgott P-P, Fourmond V, Gutiérrez-Sanz O, Lacey ALD, Infossi P, et al. Relation between anaerobic inactivation and oxygen tolerance in a large series of NiFe hydrogenase mutants. *Proceedings of the National Academy of Sciences of the United Sates of America*. 2012;109(49):19916–21.

[41] Helm ML, Stewart MP, Bullock RM, DuBois MR, DuBois DL. A synthetic nickel electrocatalyst with a turnover frequency above 100,000 s^{-1} for H_2 production. *Science*. 2011;333(6044):863-6.

[42] Le Goff A, Artero V, Jousselme B, Tran PD, Guillet N, Metaye R, et al. From hydrogenases to noble metal-free catalytic nanomaterials for H_2 production and uptake. *Science*. 2009;326(5958):1384-7.

[43] Wang M, Chen L, Li X, Sun L. Approaches to efficient molecular catalyst systems for photochemical H_2 production using FeFe-hydrogenase active site mimics. *Dalton Transactions*. 2011;40(48):12793-800.

[44] Smith SE, Yang JY, DuBois DL, Bullock RM. Reversible electrocatalytic production and oxidation of hydrogen at low overpotentials by a functional hydrogenase mimic. *Angewandte Chemie-International Edition*. 2012;51(13):3152-5.

[45] Tran PD, Morozan A, Archambault S, Heidkamp J, Chenevier P, Dau H, et al. A noble metal-free proton-exchange membrane fuel cell based on bio-inspired molecular catalysts. *Chemical Science*. 2015;6(3):2050-3.

[46] Léger C, Jones AK, Roseboom W, Albracht SPJ, Armstrong FA. Enzyme electrokinetics: hydrogen evolution and oxidation by *Allochromatium vinosum* NiFe-hydrogenase. *Biochemistry*. 2002;41(52):15736-46.

[47] Léger C, Jones AK, Albracht SPJ, Armstrong FA. Effect of a dispersion of interfacial electron transfer rates on steady state catalytic electron transport in [NiFe]-hydrogenase and other enzymes. *Journal of Physical Chemistry B*. 2002;106:13058-63.

[48] Chen D, Wang G, Li J. Interfacial bioelectrochemistry: fabrication, properties and applications of functional nanostructured biointerfaces. *Journal of Physical Chemistry C*. 2007;111(6):2351-67.

[49] Yaropolov AI, Karyakin AA, Varfolomeev SD, Berezin IV. Mechanism of H_2-electrooxidation with immobilized hydrogenase. *Bioelectrochemistry and Bioenergetics*. 1984;12(3-4):267-77.

[50] Robertson J. Amorphous-carbon. *Advances in Physics*. 1986;35(4):317-74.

[51] Karyakin AA, Morozov SV, Karyakina EE, Varfolomeyev SD, Zorin NA, Cosnier S. Hydrogen fuel electrode based on bioelectrocatalysis by the enzyme hydrogenase. *Electrochemistry Communications*. 2002;4(5):417-20.

[52] Morozov SV, Karyakina EE, Zorin NA, Varfolomeyev SD, Cosnier S, Karyakin AA. Direct and electrically wired bioelectrocatalysis by hydrogenase from *Thiocapsa roseopersicina*. *Bioelectrochemistry*. 2002;55(1-2):169-71.

[53] Morozov SV, Karyakina EE, Zadvornyi OA, Zorin NA, Varfolomeev SD, Karyakin AA. Bioelectrocatalysis by hydrogenase *Th. roseopersicina* immobilized on carbon materials. *Russian Journal of Electrochemistry*. 2002;38(1):97-102.

[54] Jones AK, Sillery E, Albracht SPJ, Armstrong FA. Direct comparison of the electrocatalytic oxidation of hydrogen by an enzyme and a platinum catalyst. *Chemical Communications*. 2002(8).

[55] Szot K, de Poulpiquet A, Ciaccafava A, Marques H, Joensson-Niedziolka M, Niedziolka-Joensson J, et al. Carbon nanoparticulate films as effective scaffolds for mediatorless bioelectrocatalytic hydrogen oxidation. *Electrochimica Acta*. 2013;111:434-40.

[56] Xu L, Armstrong FA. Optimizing the power of enzyme-based membrane-less hydrogen fuel cells for hydrogen-rich H_2-air mixtures. *Energy & Environmental Science*. 2013;6(7):2166-71.

[57] Wang M-x, Liu Q, Sun H-f, Ogbeifun N, Xu F, Stach EA, et al. Investigation of carbon corrosion in polymer electrolyte fuel cells using steam etching. *Materials Chemistry and Physics*. 2010;123(2-3):761-6.

[58] Rudiger O, Abad JM, Hatchikian EC, Fernandez VM, De Lacey AL. Oriented immobilization of *Desulfovibrio gigas* hydrogenase onto carbon electrodes by covalent bonds for nonmediated oxidation of H_2. *Journal of the American Chemical Society*. 2005;127(46):16008-9.

[59] Pimenta MA, Dresselhaus G, Dresselhaus MS, Cancado LG, Jorio A, Saito R. Studying disorder in graphite-based systems by Raman spectroscopy. *Physical Chemistry Chemical Physics*. 2007;9(11):1276-91.

[60] Blanford CF, Armstrong FA. The pyrolytic graphite surface as an enzyme substrate: microscopic and spectroscopic studies. *Journal of Solid State Electrochemistry*. 2006;10(10):826-32.

[61] Léger C, Elliott SJ, Hoke KR, Jeuken LJC, Jones AK, Armstrong FA. Enzyme electrokinetics: using protein film voltammetry to investigate redox enzymes and their mechanisms. *Biochemistry*. 2003;42(29):8653-62.

[62] Vincent KA, Li X, Blanford CF, Belsey NA, Weiner JH, Armstrong FA. Enzymatic catalysis on conducting graphite particles. *Nature chemical biology*. 2007;3(12):761-2.

[63] Healy AJ, Reeve HA, Parkin A, Vincent KA. Electrically conducting particle networks in polymer electrolyte as three-dimensional electrodes for hydrogenase electrocatalysis. *Electrochimica Acta*. 2011;56(28).

[64] Hexter SV, Grey F, Happe T, Climent V, Armstrong FA. Electrocatalytic mechanism of reversible hydrogen cycling by enzymes and distinctions between the major classes of hydrogenases. *Proceedings of the National Academy of Sciences of the United States of America*. 2012;109:11516–21.

[65] Armstrong FA, Hirst J. Reversibility and efficiency in electrocatalytic energy conversion and lessons from enzymes. *Proceedings of the National Academy of Sciences of the United States of America*. 2011;108(34):14049-54.

[66] Schnorr JM, Swager TM. Emerging applications of carbon nanotubes. *Chemistry of Materials*. 2011;23(3):646-57.

[67] Monthioux M, Kuznetsov VL. Who should be given the credit for the discovery of carbon nanotubes? *Carbon*. 2006;44:1621-3.

[68] Iijima S. Helical microtubules of graphitic carbon. *Nature*. 1991;354(6348):56-8.

[69] Ishigami N, Ago H, Motoyama Y, Takasaki M, Shinagawa M, Takahashi K, et al. Microreactor utilizing a vertically-aligned carbon nanotube array grown inside the channels. *Chemical Communications*. 2007(16):1626-8.

[70] Su DS, Perathoner S, Centi G. Nanocarbons for the development of advanced catalysts. *Chemical Reviews*. 2013;113(8):5782-816.

[71] Chen Y, Wang J, Liu H, Li R, Sun X, Ye S, et al. Enhanced stability of Pt electrocatalysts by nitrogen doping in CNTs for PEM fuel cells. *Electrochemistry Communications*. 2009;11(10):2071-6.

[72] Quinn BM, Dekker C, Lemay SG. Electrodeposition of noble metal nanoparticles on carbon nanotubes. *Journal of the American Chemical Society*. 2005;127(17):6146-7.

[73] Svedruzic D, Blackburn JL, Tenent RC, Rocha J-DR, Vinzant TB, Heben MJ, et al. High-performance hydrogen production and oxidation electrodes with hydrogenase supported on metallic single-wall carbon nanotube networks. *Journal of the American Chemical Society*. 2011;133(12):4299-306.

[74] Ciaccafava A, De Poulpiquet A, Techer V, Giudici-Orticoni MT, Tingry S, Innocent C, et al. An innovative powerful and mediatorless H_2/O_2 biofuel cell based on an outstanding bioanode. *Electrochemistry Communications*. 2012;23:25-8.

[75] Cano M, Benito A, Maser WK, Urriolabeitia EP. One-step microwave synthesis of palladium-carbon nanotube hybrids with improved catalytic performance. *Carbon*. 2011;49(2):652-8.

[76] Suzuki Y, Laurino P, McQuade DT, Seeberger PH. A capture-and-release catalytic flow system. *Helvetica Chimica Acta*. 2012;95(12):2578-88.

[77] De Volder MFL, Tawfick SH, Baughman RH, Hart AJ. Carbon nanotubes: present and future commercial applications. *Science*. 2013;339(6119):535-9.

[78] Liu A-R, Wakayama T, Nakamura C, Miyake J, Zorin NA, Qian D-J. Electrochemical properties of carbon nanotubes-hydrogenase conjugates Langmuir-Blodgett films. *Electrochimica Acta*. 2007;52(9):3222-8.

[79] Sun Q, Zorin NA, Chen D, Chen M, Liu T-X, Miyake J, et al. Langmuir-Blodgett films of pyridyldithio-modified multiwalled carbon nanotubes as a support to immobilize hydrogenase. *Langmuir*. 2010;26(12):10259-65.

[80] McDonald TJ, Svedruzic D, Kim Y-H, Blackburn JL, Zhang SB, King PW, et al. Wiring-up hydrogenase with single-walled carbon nanotubes. *Nano Letters*. 2007;7(11):3528-34.

[81] Blackburn JL, Svedruzic D, McDonald TJ, Kim Y-H, King PW, Heben MJ. Raman spectroscopy of charge transfer interactions between single wall carbon nanotubes and FeFe hydrogenase. *Dalton Transactions*. 2008(40):5454-61.

[82] Hoeben FJM, Heller I, Albracht SPJ, Dekker C, Lemay SG, Heering HA. Polymyxin-coated an and carbon nanotube electrodes for stable NiFe -hydrogenase film voltammetry. *Langmuir*. 2008;24(11):5925-31.

[83] Baur J, Le Goff A, Dementin S, Holzinger M, Rousset M, Cosnier S. Three-dimensional carbon nanotube-polypyrrole-[NiFe] hydrogenase electrodes for the efficient electrocatalytic oxidation of H_2. *International Journal of Hydrogen Energy*. 2011;36(19):12096-101.

[84] de Poulpiquet A, Ciaccafava A, Szot K, Pillain B, Infossi P, Guiral M, et al. Exploring properties of a hyperthermophilic membrane-bound hydrogenase at carbon nanotube modified electrodes for a powerful H_2/O_2 biofuel cell. *Electroanalysis*. 2013;25(3):685-95.

[85] de Poulpiquet A, Marques-Knopf H, Wernert V, Giudici-Orticoni MT, Gadiou R, Lojou E. Carbon nanofiber mesoporous films: efficient platforms for bio-hydrogen oxidation in biofuel cells. *Physical Chemistry Chemical Physics*. 2014;16(4):1366-78.

[86] de Poulpiquet A, Ciaccafava A, Gadiou R, Gounel S, Giudici-Orticoni MT, Mano N, et al. Design of a H_2/O_2 biofuel cell based on thermostable enzymes. *Electrochemistry Communications*. 2014;42:72-4.

[87] Burch HJ, Brown E, Contera SA, Toledo NC, Cox DC, Grobert N, et al. Effect of acid treatment on the structure and electrical properties of nitrogen-doped multiwalled carbon nanotubes. *Journal of Physical Chemistry C*. 2008;112(6).

[88] Kharissova OV, Kharisov BI, de Casas Ortiz EG. Dispersion of carbon nanotubes in water and non-aqueous solvents. *Rsc Advances*. 2013;3(47):24812-52.

[89] Premkumar T, Mezzenga R, Geckeler KE. Carbon nanotubes in the liquid phase: addressing the issue of dispersion. *Small*. 2012;8(9):1299-313.

[90] Chen H, Roy A, Baek J-B, Zhu L, Qu J, Dai L. Controlled growth and modification of vertically-aligned carbon nanotubes for multifunctional applications. *Materials Science & Engineering R-Reports*. 2010;70(3-6):63-91.

[91] Terranova ML, Sessa V, Rossi M. The world of carbon nanotubes: An overview of CVD growth methodologies. *Chemical Vapor Deposition*. 2006;12(6):315-25.

[92] Koós AA, Dowling M, Jurkschat K, Crossley A, Grobert N. Effect of the experimental parameters on the structure of nitrogen-doped carbon nanotubes produced by aerosol chemical vapour deposition. *Carbon*. 2009;47(1):30-7.

[93] Koós AA, Nicholls RJ, Dillon F, Kertesz K, Biro LP, Crossley A, et al. Tailoring gas sensing properties of multi-walled carbon nanotubes by in situ modification with Si, P, and N. *Carbon*. 2012;50(8).

[94] Banks CE, Davies TJ, Wildgoose GG, Compton RG. Electrocatalysis at graphite and carbon nanotube modified electrodes: edge-plane sites and tube ends are the reactive sites. *Chemical Communications*. 2005(7):829-41.

[95] Lai SCS, Patel AN, McKelvey K, Unwin PR. Definitive evidence for fast electron transfer at pristine basal plane graphite from high-resolution electrochemical imaging. *Angewandte Chemie-International Edition*. 2012;51(22).

[96] Miller TS, Ebejer N, Gueell AG, Macpherson JV, Unwin PR. Electrochemistry at carbon nanotube forests: sidewalls and closed ends allow fast electron transfer. *Chemical Communications*. 2012;48(60).

[97] Unwin PR. Concluding remarks: there's nowt so queer as carbon electrodes. *Faraday Discussions*. 2014;172:521-32.

[98] Lehman JH, Terrones M, Mansfield E, Hurst KE, Meunier V. Evaluating the characteristics of multiwall carbon nanotubes. *Carbon*. 2011;49(8):2581-602.

[99] Vignais PM, Billoud B. Occurrence, classification, and biological function of hydrogenases: an overview. *Chemical Reviews*. 2007;107(10):4206-72.

[100] Vincent KA, Parkin A, Armstrong FA. Investigating and exploiting the electrocatalytic properties of hydrogenases. *Chemical Reviews*. 2007;107(10):4366-413.

[101] Lubitz W, Ogata H, Ruediger O, Reijerse E. Hydrogenases. *Chemical Reviews*. 2014;114(8):4081-148.

[102] Vincent KA, Cracknell JA, Clark JR, Ludwig M, Lenz O, Friedrich B, et al. Electricity from low-level H_2 in still air – an ultimate test for an oxygen tolerant hydrogenase. *Chemical Communications*. 2006:5033–5.

[103] Healy AJ, Reeve HA, Vincent KA. Development of an infrared spectroscopic approach for studying metalloenzyme active site chemistry under direct electrochemical control. *Faraday Discussions*. 2011;148:345-57.

[104] Healy AJ, Ash PA, Lenz O, Vincent KA. Attenuated total reflectance infrared spectroelectrochemistry at a carbon particle electrode; unmediated redox control of a NiFe-hydrogenase solution. *Physical Chemistry Chemical Physics*. 2013;15(19):7055-9.

[105] Ash PA, Vincent KA. Spectroscopic analysis of immobilised redox enzymes under direct electrochemical control. *Chemical Communications*. 2012;48(10):1400-9.

[106] Miyake H, Ye S, Osawa M. Electroless deposition of gold thin films on silicon for surface-enhanced infrared spectroelectrochemistry. *Electrochemistry Communications*. 2002;4(12):973-7.

[107] Hartstein A, Kirtley JR, Tsang JC. Enhancement of the infrared-absorption from molecular monolayers with thin metal overlayers. *Physical Review Letters*. 1980;45(3):201-4.

[108] Mirabella FM. Internal-reflection spectroscopy. *Applied Spectroscopy Reviews*. 1985;21(1-2):45-178.

[109] Mitic A, Heintz S, Ringborg RH, Bodla V, Woodley JM, Gernaey KV. Applications, benefits and challenges of flow chemistry. *Chimica Oggi-Chemistry Today*. 2013;31(4):4-8.

[110] Newman SG, Jensen KF. The role of flow in green chemistry and engineering. *Green Chemistry*. 2013;15(6):1456-72.

[111] Anderson NG. Using continuous processes to increase production. *Organic Process Research & Development*. 2012;16(5):852-69.

[112] Jones E, McClean K, Housden S, Gasparini G, Archer I. Biocatalytic oxidase: batch to continuous. *Chemical Engineering Research and Design*. 2012;90(6):726-31.

[113] Wiles C, Watts P. Continuous flow reactors: a perspective. *Green Chemistry*. 2012;14(1):38-54.

[114] Puglisi A, Benaglia M, Chiroli V. Stereoselective organic reactions promoted by immobilized chiral catalysts in continuous flow systems. *Green Chemistry*. 2013;15(7):1790-813.

[115] Frost CG, Mutton L. Heterogeneous catalytic synthesis using microreactor technology. *Green Chemistry*. 2010;12(10):1687-703.

[116] Costantini F, Bula WP, Salvio R, Huskens J, Gardeniers HJGE, Reinhoudt DN, et al. Nanostructure based on polymer brushes for efficient heterogeneous catalysis in microreactors. *Journal of American Chemical Society*. 2009;131(5):1650-+.

[117] Costantini F, Benetti EM, Reinhoudt DN, Huskens J, Vancso GJ, Verboom W. Enzyme-functionalized polymer brush films on the inner wall of silicon-glass microreactors with tunable biocatalytic activity. *Lab on a Chip*. 2010;10(24):3407-12.

[118] Yuryev R, Strompen S, Liese A. Coupled chemo(enzymatic) reactions in continuous flow. *Beilstein Journal of Organic Chemistry*. 2011;7:1449-67.

[119] Itabaiana I, Jr., de Mariz e Miranda LS, Mendonca Alves de Souza RO. Towards a continuous flow environment for lipase-catalyzed reactions. *Journal of Molecular Catalysis B: Enzymatic*. 2013;85-86:1-9.

[120] Straathof AJJ, Panke S, Schmid A. The production of fine chemicals by biotransformations. *Current Opinion in Biotechnology*. 2002;13(6):548-56.

[121] Zhao HM, van der Donk WA. Regeneration of cofactors for use in biocatalysis. *Current Opinion in Biotechnology*. 2003;14(6):583-9.

[122] Reeve HA. New approaches for cofactor recycling; application to chemical synthesis and electrochemical devices. The University of Oxford, DPhil thesis. 2014.

[123] Lau WN, Yeung KL, Martin-Aranda R. Knoevenagel condensation reaction between benzaldehyde and ethyl acetoacetate in microreactor and membrane microreactor. *Microporous and Mesoporous Materials*. 2008;115(1-2):156-63.

[124] El Kadib A, Chimenton R, Sachse A, Fajula F, Galarneau A, Coq B. Functionalized inorganic monolithic microreactors for high productivity in fine chemicals catalytic synthesis. *Angewandte Chemie-International Edition*. 2009;48(27):4969-72.

[125] Smith CJ, Smith CD, Nikbin N, Ley SV, Baxendale IR. Flow synthesis of organic azides and the multistep synthesis of imines and amines using a new monolithic triphenylphosphine reagent. *Organic and Biomolecular Chemistry*. 2011;9(6):1927-37.

[126] Wildgoose GG, Banks CE, Compton RG. Metal nanoparticles and related materials supported on carbon nanotubes: Methods and applications. *Small*. 2006;2(2):182-93.

[127] Davis SC, Sheppard VC, Begum G, Cai Y, Fang Y, Berrigan JD, et al. Rapid flow-through biocatalysis with high surface area, enzyme-loaded carbon and gold-bearing diatom frustule replicas. *Advanced Functional Materials*. 2013;23(36):4611-20.

[128] Hashimoto K, Kumagai N, Shibasaki M. Self-assembled asymmetric catalyst engaged in a continuous-flow platform: an anti-selective catalytic asymmetric nitroaldol reaction. *Organic Letters*. 2014;16(13):3496-9.

[129] De Pra M, Kok WT, Schoenmakers PJ. Topographic structures and chromatographic supports in microfluidic separation devices. *Journal of Chromatography A*. 2008;1184(1-2):560-72.

[130] Chu Y, Li X, Xie H, Fu Z, Yang X, Qiao X, et al. Evaluating the interactions of organic compounds with multi-walled carbon nanotubes by self-packed HPLC column and linear solvation energy relationship. *Journal of Hazardous Materials*. 2013;263:550-5.

[131] Ehlert S, Kraiczek K, Mora J-A, Dittmann M, Rozing GP, Tallarek U. Separation efficiency of particle-packed HPLC microchips. *Analytical Chemistry*. 2008;80(15):5945-50.

[132] Tian Y, Gao B, Morales VL, Chen H, Wang Y, Li H. Removal of sulfamethoxazole and sulfapyridine by carbon nanotubes in fixed-bed columns. *Chemosphere*. 2013;90(10):2597-605.

[133] Walas SM. Chemical process equipment: selection and design. Boston: Elsevier; 1990.

[134] Tian Y, Gao B, Morales VL, Wu L, Wang Y, Munoz-Carpena R, et al. Methods of using carbon nanotubes as filter media to remove aqueous heavy metals. *Chemical Engineering Journal*. 2012;210:557-63.

[135] Popp A, Schneider JJ. A chip-sized nanoscale monolithic chemical reactor. *Angewandte Chemie-International Edition*. 2008;47(46):8958-60.

[136] Janowska I, Wine G, Ledoux M-J, Pham-Huu C. Structured silica reactor with aligned carbon nanotubes as catalyst support for liquid-phase reaction. *Journal of Molecular Catalysis A: Chemical*. 2007;267(1-2):92-7.

[137] Van Hooijdonk E, Bittencourt C, Snyders R, Colomer J-F. Functionalization of vertically aligned carbon nanotubes. *Beilstein Journal of Nanotechnoly*. 2013;4:129-52.

[138] Ye XR, Chen LH, Wang C, Aubuchon JF, Chen IC, Gapin AI, et al. Electrochemical modification of vertically aligned carbon nanotube arrays. *Journal of Physical Chemistry B*. 2006;110(26):12938-42.

[139] Liu Y, Janowska I, Romero T, Edouard D, Nguyen LD, Ersen O, et al. High surface-to volume hybrid platelet reactor filled with catalytically grown vertically aligned carbon nanotubes. *Catalysis Today*. 2010;150(1-2):133-9

[140] Srivastava A, Srivastava ON, Talapatra S, Vajtai R, Ajayan PM. Carbon nanotube filters. *Nature Materials*. 2004;3(9):610-4.

[141] Saridara C, Mitra S. Chromatography on self-assembled carbon nanotubes. *Analytical Chemistry*. 2005;77(21):7094-7.

[142] Speltini A, Merli D, Profumo A. Analytical application of carbon nanotubes, fullerenes and nanodiamonds in nanomaterials-based chromatographic stationary phases: A review. *Analytica Chimica Acta*. 2013;783:1-16.

[143] Ahn CH, Baek Y, Lee C, Kim SO, Kim S, Lee S, et al. Carbon nanotube-based membranes: fabrication and application to desalination. *Journal of Industrial Engineering Chemistry*. 2012;18(5):1551-9.

[144] Mogensen KB, Kutter JP. Carbon nanotube based stationary phases for microchip chromatography. *Lab on a Chip*. 2012;12(11):1951-8.

[145] Karwa M, Mitra S. Gas chromatography on self-assembled single-walled carbon nanotubes. *Analytical Chemistry*. 2006;78(6):2064-70.

[146] Hussain CM, Saridara C, Mitra S. Self-assembly of carbon nanotubes via ethanol chemical vapor deposition for the synthesis of gas chromatography. *Analytcial Chemistry*. 2010;82(12):5184-8.

[147] Jimenez V, Panagiotopoulou P, Sanchez P, Luis Valverde J, Romero A. Synthesis and characterization of ruthenium supported on carbon nanofibers with different graphitic plane arrangements. *Chemical Engineering Journal*. 2011;168(2):947-54.

[148] Burch HJ, Contera SA, de Planque MRR, Grobert N, Ryan JF. Doping of carbon nanotubes with nitrogen improves protein coverage whilst retaining correct conformation. *Nanotechnology*. 2008;19(38).

[149] Loget G, Kuhn A. Bulk synthesis of Janus objects and asymmetric patchy particles. Journal of *Materials Chemistry*. 2012;22(31):15457-74.

[150] Loget G, Roche J, Kuhn A. True bulk synthesis of Janus objects by bipolar electrochemistry. *Advanced Materials.* 2012;24(37):5111-6.

[151] Fattah Z, Loget G, Lapeyre V, Garrigue P, Warakulwit C, Limtrakul J, et al. Straightforward single-step generation of microswimmers by bipolar electrochemistry. *Electrochimica Acta*. 2011;56(28):10562-6.

[152] Banerjee S, Hemraj-Benny T, Wong SS. Covalent surface chemistry of single-walled carbon nanotubes. *Advanced Materials*. 2005;17(1):17-29.

[153] Lee KM, Li LC, Dai LM. Asymmetric end-functionalization of multi-walled carbon nanotubes. *Journal of the American Chemical Society*. 2005;127(12):4122-3.

[154] Wei Z, Kondratenko M, Dao LH, Perepichka DF. Rectifying diodes from asymmetrically functionalized single-wall carbon nanotubes. *Journal of the American Chemical Society*. 2006;128(10):3134-5.

[155] Yun Y, Dong Z, Shanov VN, Doepke A, Heineman WR, Halsall HB, et al. Fabrication and characterization of carbon nanotube array electrodes with gold nanoparticle tips. *Sensors and Actuators B-Chemical*. 2008;133(1):208-12.

[156] Tessonnier J-P, Ersen O, Weinberg G, Pham-Huu C, Su DS, Schloegl R. Selective deposition of metal nanoparticles inside or outside multiwalled carbon nanotubes. *Acs Nano*. 2009;3(8):2081-9.

[157] Qu LT, Dai LM, Osawa E. Shape/size-control led syntheses of metal nanoparticles for site-selective modification of carbon nanotubes. *Journal of the American Chemical Society*. 2006;128(16):5523-32.

[158] Peng Q, Qu L, Dai L, Park K, Vaia RA. Asymmetrically charged carbon nanotubes by controlled functionalization. *Acs Nano*. 2008;2(9):1833-40.

[159] Chopra N, Majumder M, Hinds BJ. Bifunctional carbon nanotubes by sidewall protection. *Advanced Functional Materials*. 2005;15(5):858-64.

[160] Qu L, Dai L. Polymer-masking for controlled functionalization of carbon nanotubes. *Chemical Communications*. 2007(37):3859-61.

[161] Chakrabarti S, Gong K, Dai L. Structural evaluation along the nanotube length for super-long vertically aligned double-walled carbon nanotube arrays. *Journal of Physical Chemistry C*. 2008;112(22):8136-9.

[162] Koós AA, Dillon F, Obraztsova EA, Crossley A, Grobert N. Comparison of structural changes in nitrogen and boron-doped multi-walled carbon nanotubes. *Carbon*. 2010;48(11):3033-41.

[163] Nevidomskyy AH, Csanyi G, Payne MC. Chemically active substitutional nitrogen impurity in carbon nanotubes. *Physical Review Letters*. 2003;91(10).

[164] Chen Y, Wang J, Liu H, Banis MN, Li R, Sun X, et al. Nitrogen doping effects on carbon nanotubes and the origin of the enhanced electrocatalytic activity of supported Pt for proton-exchange membrane fuel cells. *Journal of Physical Chemistry C*. 2011;115(9):3769-76.

[165] Jin Z, Li X, Zhou W, Han Z, Zhang Y, Li Y. Direct growth of carbon nanotube junctions by a two-step chemical vapor deposition. *Chemical Physics Letters*. 2006;432(1-3):177-83.

[166] Suh JS, Lee JS, Kim H. Linearly joined carbon nanotubes. *Synthetic Metals*. 2001;123(3):381-3.

[167] Cassell AM, Li J, Stevens RMD, Koehne JE, Delzeit L, Ng HT, et al. Vertically aligned carbon nanotube heterojunctions. *Applied Physics Letters*. 2004;85(12):2364-6.

[168] Lepro X, Vega-Cantu Y, Rodriguez-Macias FJ, Bando Y, Golberg D, Terrones M. Production and characterization of coaxial nanotube junctions and networks of CN_x/CNT. *Nano Letters*. 2007;7(8):2220-6.

[169] Liu L, Fan SS. Isotope labeling of carbon nanotubes and a formation of C^{12}-C^{13} nanotube junctions. *Journal of the American Chemical Society*. 2001;123(46):11502-3.

[170] Fan SS, Liu L, Liu M. Monitoring the growth of carbon nanotubes by carbon isotope labelling. *Nanotechnology*. 2003;14(10):1118-23.

[171] Ago H, Ishigami N, Yoshihara N, Imamoto K, Akita S, Ikeda K-i, et al. Visualization of horizontally-aligned single-walled carbon nanotube growth with C^{13}/C^{12} isotopes. *Journal of Physical Chemistry C*. 2008;112(6):1735-8.

[172] Guo JD, Zhi CY, Bai XD, Wang EG. Boron carbonitride nanojunctions. *Applied Physics Letters*. 2002;80(1):124-6.

[173] Liao L, Liu K, Wang W, Bai X, Wang E, Liu Y, et al. Multiwall boron carbonitride/carbon nanotube junction and its rectification behavior. *Journal of the American Chemical Society*. 2007;129(31):9562-+.

[174] Wang Z, Jia D, Liu S, Zhang M. Direct growth of carbon nanotube junctions by switching source gases in a continuous chemical vapor deposition. *Materials Letters*. 2008;62(17-18):3288-90.

[175] Cao Y, Liu B, Jiao Q, Zhao Y. Preparation of CN_x/carbon nanotube intramolecular junctions by switching gas sources in continuous chemical vapour deposition. *South African Journal of Chemistry-Suid-Afrikaanse Tydskrif Vir Chemie*. 2011;64:67-70.

[176] Pint CL, Sun Z, Moghazy S, Xu Y-Q, Tour JM, Hauge RH. Supergrowth of nitrogen-doped single-walled carbon nanotube arrays: active species, dopant characterization, and doped/undoped heterojunctions. *Acs Nano*. 2011;5(9):6925-34.

[177] Xu E, Wei J, Wang K, Li Z, Gui X, Jia Y, et al. Doped carbon nanotube array with a gradient of nitrogen concentration. *Carbon*. 2010;48(11):3097-102.

[178] Chai Y, Zhou XL, Li PJ, Zhang WJ, Zhang QF, Wu JL. Nanodiode based on a multiwall CN_x/carbon nanotube intramolecular junction. *Nanotechnology*. 2005;16(10):2134-7.

[179] Meysami SS, Koós AA, Dillon F, Grobert N. Aerosol-assisted chemical vapour deposition synthesis of multi-wall carbon nanotubes: II. An analytical study. *Carbon*. 2013;58:159-69.

[180] Ma XC, Wang EG. CN_x/carbon nanotube junctions synthesized by microwave chemical vapor deposition. *Applied Physics Letters*. 2001;78(7):978-80.

[181] Yao Z, Postma HWC, Balents L, Dekker C. Carbon nanotube intramolecular junctions. *Nature*. 1999;402(6759):273-6.

[182] Hu P, Xiao K, Liu YQ, Yu G, Wang XB, Fu L, et al. Multiwall nanotubes with intramolecular junctions (CN_x/C): preparation, rectification, logic gates, and application. *Applied Physics Letters*. 2004;84(24):4932-4.

[183] Chai Y, Zhang QF, Wu JL. A simple way to CN_x/carbon nanotube intramolecular junctions and branches. *Carbon*. 2006;44(4):687-91.

[184] Zhang WJ, Zhang QF, Chai Y, Shen X, Wu JL. Gate voltage dependent characteristics of p-n diodes and bipolar transistors based on multiwall CN_x/carbon nanotube intramolecular junctions. *Nanotechnology*. 2007;18(39).

[185] Wei DC, Liu YQ, Cao LC, Fu L, Li XL, Wang Y, et al. A new method to synthesize complicated multibranched carbon nanotubes with controlled architecture and composition. *Nano Letters*. 2006;6(2):186-92.

[186] Goswami GK, Nandan R, Nanda KK. Growth of branched carbon nanotubes with doped/un-doped intratubular junctions by one-step co-pyrolysis. *Carbon*. 2013;56:97-102.

[187] Xiao K, Fu Y, Liu Y, Yu G, Zhai J, Jiang L, et al. Photoelectrical characteristics of a C/CN_x multiwalled nanotube. *Advanced Functional Materials*. 2007;17(15):2842-6.

[188] Wei D, Liu Y. The intramolecular junctions of carbon nanotubes. *Advanced Materials*. 2008;20(15):2815-41.

[189] Dresselhaus MS, Jorio A, Hofmann M, Dresselhaus G, Saito R. Perspectives on carbon nanotubes and graphene Raman spectroscopy. *Nano Letters*. 2010;10(3):751-8.

[190] Kumar M, Ando Y. Chemical vapor deposition of carbon nanotubes: a review on growth mechanism and mass production. *Journal of Nanoscience and Nanotechnology*. 2010;10(6):3739-58.

[191] Meysami SS, Dillon F, Koós AA, Aslam Z, Grobert N. Aerosol-assisted chemical vapour deposition synthesis of multi-wall carbon nanotubes: I. Mapping the reactor. *Carbon*. 2013;58:151-8.

[192] Boulanger P, Belkadi L, Descarpentries J, Porterat D, Hibert E, Brouzes A, et al. Towards large scale aligned carbon nanotube composites: an industrial safe-by-design and sustainable approach. 3rd International Conference on Safe Production and Use of Nanomaterials (Nanosafe). Minatec, Grenoble, FRANCE; 2013.

[193] Quinson J, Hidalgo R, Ash PA, Dillon F, Grobert N, Vincent KA. Comparison of carbon materials as electrodes for enzyme electrocatalysis: hydrogenase as a case study. *Faraday Discussions*. 2014;172:473-96.

[194] Hernandez Y, Nicolosi V, Lotya M, Blighe FM, Sun Z, De S, et al. High-yield production of graphene by liquid-phase exfoliation of graphite. *Nature Nanotechology*. 2008;3(9):563-8.

[195] Li M, Li W, Liu S. Hydrothermal synthesis, characterization, and KOH activation of carbon spheres from glucose. *Carbohydrate Research*. 2011;346(8):999-1004.

[196] Sun XM, Li YD. Colloidal carbon spheres and their core/shell structures with noble-metal nanoparticles. *Angewandte Chemie-International Edition*. 2004;43(5):597-601.

[197] Mi Y, Hu W, Dan Y, Liu Y. Synthesis of carbon micro-spheres by a glucose hydrothermal method. *Materials Letters*. 2008;62(8-9):1194-6.

[198] Sun XM, Li YD. Hollow carbonaceous capsules from glucose solution. *Journal of Colloid and Interface Science*. 2005;291(1):7-12.

[199] Chen C, Sun X, Jiang X, Niu D, Yu A, Liu Z, et al. A Two-Step Hydrothermal Synthesis Approach to Monodispersed Colloidal Carbon Spheres. *Nanoscale Research Letters*. 2009;4(9):971-6.

[200] Wen Z, Wang Q, Zhang Q, Li J. Hollow carbon spheres with wide size distribution as anode catalyst support for direct methanol fuel cells. *Electrochemistry Communications*. 2007;9(8):1867-72.

[201] XiaoHong X, Lei S, HongBo L, Li Y, YueDe H. A facile production of microporous carbon spheres and their electrochemical performance in EDLC. *Journal of Physics and Chemistry of Solids*. 2012;73(3).

[202] Sevilla M, Fuertes AB. The production of carbon materials by hydrothermal carbonization of cellulose. *Carbon*. 2009;47(9):2281-9.

[203] Gao P, Fu J, Yang J, Lv R, Wang J, Nuli Y, et al. Microporous carbon coated silicon core/shell nanocomposite via in situ polymerization for advanced Li-ion battery anode material. *Physical Chemistry Chemicals Physics*. 2009;11(47):11101-5.

[204] Bulusheva LG, Okotrub AV, Kinloch IA, Asanov IP, Kurenya AG, Kudashov AG, et al. Effect of nitrogen doping on Raman spectra of multi-walled carbon nanotubes. *Physica Status Solidi B-Basic Solid State Physics*. 2008;245(10):1971-4.

[205] Rouquerol F, Rouquerol J, Sing KSW, Llewellyn P, Maurin G. Adsorption by powders and porous solids: principles, methodology and applications. Second Edition: Elsevier; 2014.

[206] Mullejans H, Bruley J. Electron energy-loss spectroscopy (EELS); comparison with X-ray analysis. *Journal de Physique IV*. 1993;03 (C7):C7-2083-C7-92.

[207] Smith BW, Luzzi DE. Electron irradiation effects in single wall carbon nanotubes. *Journal of Applied Physics*. 2001;90(7):3509-15.

[208] Lai SCS, Dudin PV, Macpherson JV, Unwin PR. Visualizing zeptomole (electro)catalysis at single nanoparticles within an ensemble. *Journal of the American Chemical Society*. 2011;133(28):10744-7.

[209] Bard AJ, Faulkner LR. Electrochemical methods: fundamentals and applications. Second Edition: John Wiley & Sons, Inc.; 2001

[210] Lukey MJ, Parkin A, Roessler MM, Murphy BJ, Harmer J, Palmer T, et al. How *Escherichia coli* is equipped to oxidize hydrogen under different redox conditions. *Journal of Biological Chemistry*. 2010;285(6):3928-38.

[211] Sawers G. The hydrogenases and formate dehydrogenases of *Escherichia Coli*. *Antonie Van Leeuwenhoek International Journal of General and Molecular Microbiology*. 1994;66(1-3):57-88.

[212] Leger C, Bertrand P. Direct electrochemistry of redox enzymes as a tool for mechanistic studies. *Chemical Reviews*. 2008;108(7):2379-438.

[213] Gopalan A, Ragupathy D, Kim HT, Manesh KM, Lee KP. Pd (core)-Au (shell) nanoparticles catalyzed conversion of NADH to NAD^+ by UV-vis spectroscopy-A kinetic analysis. *Spectrochimica Acta Part a-Molecular and Biomolecular Spectroscopy*. 2009;74(3):678-84.

[214] Rover L, Fernandes JCB, Neto GD, Kubota LT, Katekawa E, Serrano SHP. Study of NADH stability using ultraviolet-visible spectrophotometric analysis and factorial design. *Analytical Biochemistry*. 1998;260(1):50-5.

[215] Sun S, Jaouen F, Dodelet J-P. Controlled growth of Pt nanowires on carbon nanospheres and their enhanced performance as electrocatalysts in PEM fuel cells. *Advanced Materials*. 2008;20(20):3900-+.

[216] Sun S, Yang D, Zhang G, Sacher E, Dodelet J-P. Synthesis and characterization of platinum nanowire-carbon nanotube heterostructures. *Chemistry of Materials*. 2007;19(26):6376-8.

[217] Sun S, Zhang G, Zhong Y, Liu H, Li R, Zhou X, et al. Ultrathin single crystal Pt nanowires grown on N-doped carbon nanotubes. *Chemical Communications*. 2009(45):7048-50.

[218] Pantea D, Darmstadt H, Kaliaguine S, Roy C. Electrical conductivity of conductive carbon blacks: influence of surface chemistry and topology. *Applied Surface Science*. 2003;217(1-4):181-93.

[219] Zhu WZ, Miser DE, Chan WG, Hajaligol MR. HRTEM investigation of some commercially available furnace carbon blacks. *Carbon*. 2004;42(8-9):1841-5.

[220] Maja M, Orecchia C, Strano M, Tosco P, Vanni M. Effect of structure of the electrical performance of gas diffusion electrodes for metal air batteries. *Electrochimica Acta*. 2000;46(2-3):423-32.

[221] Banks CE, Compton RG. New electrodes for old: from carbon nanotubes to edge plane pyrolytic graphite. *Analyst*. 2006;131:15–21.

[222] Davidson MG, Deen WM. Hindered diffusion of water-soluble macromolecules in membranes. *Macromolecules*. 1988;21(12):3474-81.

[223] Fulvio PF, Mayes RT, Wang X, Mahurin SM, Bauer JC, Presser V, et al. "Brick-and-mortar" self-assembly approach to graphitic mesoporous carbon nanocomposites. *Advanced Functional Materials*. 2011;21(12):2208-15.

[224] Fried DI, Brieler FJ, Froeba M. Designing inorganic porous materials for enzyme adsorption and applications in biocatalysis. *Chemcatchem*. 2013;5(4):862-84.

[225] Sun XM, Li YD. Colloidal carbon spheres and their core/shell structures with noble-metal nanoparticles. *Angewandte Chemie-International Edition*. 2004;43(5):597-601.

[226] Liu M, Wang C, Wang X. Interface-facilitated hydrothermal synthesis of sub-micrometre graphitic carbon plates. *Journal of Materials Chemistry*. 2011;21(39):15197-200.

[227] Liu Z, Zhang C, Luo L, Chang Z, Sun X. One-pot synthesis and catalyst support application of mesoporous N-doped carbonaceous materials. *Journal of Materials Chemistry*. 2012;22(24):12149-54.

[228] Chen J, Chen Z, Wang C, Li X. Calcium-assisted hydrothermal carbonization of an alginate for the production of carbon microspheres with unique surface nanopores. *Materials Letters*. 2012;67(1):365-8.

[229] Liu M, Yan Y, Zhang L, Wang X, Wang C. Hydrothermal preparation of carbon nanosheets and their supercapacitive behavior. *Journal of Materials Chemistry*. 2012;22(23):11458-61.

[230] Ju S-Y, Papadimitrakopoulos F. Synthesis and redox behavior of flavin mononucleotide-functionalized single-walled carbon nanotubes. *Journal of the American Chemical Society*. 2008;130(2):655-64.

[231] Tan SLJ, Kan JM, Webster RD. Differences in proton-coupled electron-transfer reactions of flavin mononucleotide (FMN) and flavin adenine dinucleotide (FAD) between buffered and unbuffered aqueous solutions. *Journal of Physical Chemistry B*. 2013;117(44):13755-66.

[232] Spexard M, Immeln D, Thoeing C, Kottke T. Infrared spectrum and absorption coefficient of the cofactor flavin in water. *Vibrational Spectroscopy*. 2011;57(2):282-7.

[233] Wiles C, Watts P. Recent advances in micro reaction technology. *Chemical Communications*. 2011;47(23):6512-35.

[234] Meysami SS. Development of an aerosol-CVD technique for the production of CNTs with integrated online control. The University of Oxford, DPhil thesis. 2013.

[235] Gad-el-Hak M. The fluid mechanics of microdevices - The Freeman Scholar Lecture. *Journal of Fluids Engineering-Transactions of the Asme*. 1999;121(1):5-33.

[236] Nakayama-Ratchford N, Bangsaruntip S, Sun X, Welsher K, Dai H. Noncovalent functionalization of carbon nanotubes by fluorescein-polyethylene glycol: supramolecular conjugates with pH-dependent absorbance and fluorescence. *Journal of the American Chemical Society*. 2007;129(9):2448-+.

[237] Wang LL, Roitberg A, Meuse C, Gaigalas AK. Raman and FTIR spectroscopies of fluorescein in solutions. *Spectrochimica Acta Part a-Molecular and Biomolecular Spectroscopy*. 2001;57(9):1781-91.

[238] Hildebrandt P, Stockburger M. Surface enhanced resonance Raman-study on fluorescein dyes. *Journal of Raman Spectroscopy*. 1986;17(1):55-8.

[239] Yadav GD, Mewada RK. Selective hydrogenation of acetophenone to 1-phenyl ethanol over nanofibrous Ag-OMS-2 catalysts. *Catal Today*. 2012;198(1):330-7.

[240] Dorjgotov A, Ok J, Jeon Y, Yoon S-H, Shul YG. Activity and active sites of nitrogen-doped carbon nanotubes for oxygen reduction reaction. *Journal of Applied Electrochemistry*. 2013;43(4):387-97.

[241] Khodja H, Pinault M, Mayne-L'Hermite M, Reynaud C. Carbon nanotube growth mechanism investigated by ion beam analysis. *Nuclear Instruments & Methods in Physics Research Section B-Beam Interactions with Materials and Atoms*. 2006;249:523-6.

[242] Kunadian I, Andrews R, Qian D, Menguec MP. Growth kinetics of MWCNTs synthesized by a continuous-feed CVD method. *Carbon*. 2009;47(2):384-95.

[243] Sumpter BG, Meunier V, Romo-Herrera JM, Cruz-Silva E, Cullen DA, Terrones H, et al. Nitrogen-mediated carbon nanotube growth: diameter reduction, metallicity, bundle dispersability, and bamboo-like structure formation. *Acs Nano*. 2007;1(4):369-75.

[244] Tessonnier J-P, Su DS. Recent progress on the growth mechanism of carbon nanotubes: a review. *Chemsuschem*. 2011;4(7):824-47.

[245] Pattinson SW, Diaz RE, Stelmashenko NA, Windle AH, Ducati C, Stach EA, et al. In situ observation of the effect of nitrogen on carbon nanotube synthesis. *Chemistry of Materials*.25(15):2921-3.

[246] Andrews R, Jacques D, Qian DL, Rantell T. Multiwall carbon nanotubes: Synthesis and application. *Accounts of Chemical Research*. 2002;35(12):1008-17.

[247] Liu K, Jiang KL, Feng C, Chen Z, Fan SS. A growth mark method for studying growth mechanism of carbon nanotube arrays. *Carbon*. 2005;43(14):2850-6.

[248] Jackson JJ, Puretzky AA, More KL, Rouleau CM, Eres G, Geohegan DB. Pulsed growth of vertically aligned nanotube arrays with variable density. *Acs Nano*.4(12):7573-81.

[249] Pattinson SW, Prehn K, Kinloch IA, Eder D, Koziol KKK, Schulte K, et al. The life and death of carbon nanotubes. *Rsc Advances*. 2012;2(7):2909-13.

[250] Lee CJ, Lyu SC, Kim HW, Lee JH, Cho KI. Synthesis of bamboo-shaped carbon-nitrogen nanotubes using C_2H_2-NH_3-$Fe(CO)_{(5)}$ system. *Chemical Physics Letters*. 2002;359(1-2):115-20.

[251] Soin N, Roy SS, Ray SC, McLaughlin JA. Excitation energy dependence of Raman bands in multiwalled carbon nanotubes. *Journal of Raman Spectroscopy*. 2010;41(10):1227-33.

[252] Sun CL, Chen LC, Su MC, Hong LS, Chyan O, Hsu CY, et al. Ultrafine platinum nanoparticles uniformly dispersed on arrayed CN_x nanotubes with high electrochemical activity. *Chemistry of Materials*. 2005;17(14):3749-53.

[253] Lin YG, Hsu YK, Wu CT, Chen SY, Chen KH, Chen LC. Effects of nitrogen-doping on the microstructure, bonding and electrochemical activity of carbon nanotubes. *Diamond and Related Materials*. 2009;18(2-3):433-7.

[254] Xu L, Armstrong FA. Pushing the limits for enzyme-based membrane-less hydrogen fuel cells - achieving useful power and stability. *Rsc Advances*. 2015;5(5):3649-56.

[255] Hidalgo R, Ash PA, Healy AJ, Vincent KA. Infrared spectroscopy during electrocatalytic turnover reveals the Ni-L active site state during H_2 oxidation by a NiFe hydrogenase. *Angewandte Chemie-International Edition*. 2015;54(24):7110-3.

[256] Duca MW, Justin R., Fedor JGW, Joel H. Vincent, Kylie A. Combining noble metals and enzymes for relay cascade electrocatalysis of nitrate reduction to ammonia at neutral pH. *ChemElectroChem*. 2015. DOI: 10.1002/celc.201500166.

[257] Wei D, Cao L, Fu L, Li X, Wang Y, Yu G, et al. A new technique for controllably producing branched or encapsulating nanostructures in a vapor-liquid-solid process. *Advanced Materials*. 2007;19(3).

Appendices

Table A1. Experimental parameters investigated for the synthesis of the HNP material, mass obtained and particle characteristic. A 'X' means that not enough material was produced to be collected and characterised.

Glucose (M)	Time (h)	T (°C)	Mass (mg)	Mean size (nm)	Deviation (nm)	Deviation (%)
0.10	8	170	X	X	X	X
0.10	8	180	0.2	139	85	61
0.20	4	180	X	X	X	X
0.20	4	180	X	X	X	X
0.20	4	190	5.8	92	11	12
0.20	6	180	0.8	89	10	11
0.20	6	190	120.8	170	22	13
0.20	6	190	96.5	137	16	12
0.20	8	180	79.4	78	8	10
0.20	8	180	68.3	81	9	11
0.30	4	180	X	X	X	X
0.30	4	190	46.2	111	22	20
0.30	5	190	141.9	159	18	12
0.30	6	180	53.2	117	15	13
0.30	8	180	153.4	142	16	12
0.40	4	180	X	X	X	X
0.40	4	190	104.6	141	20	14
0.40	6	180	109.2	123	17	13
0.40	6	190	397.9	237	26	11
0.40	8	170	26.2	73	10	14
0.40	8	180	233.1	140	66	47
0.40	8	180	241.2	169	17	10
0.50	2	160	X	X	X	X
0.50	3	180	X	X	X	X
0.50	3	190	65.5	155	24	15
0.50	4	160	X	X	X	X
0.50	4	170	X	X	X	X
0.50	4	180	42.4	112	17	15
0.50	4	190	140.6	164	25	15
0.50	5	190	379.1	297	32	11
0.50	6	160	X	X	31	X
0.50	6	170	1.2	75	10	13
0.50	6	180	92.5	227	28	12
0.50	8	180	492.5	231	21	9

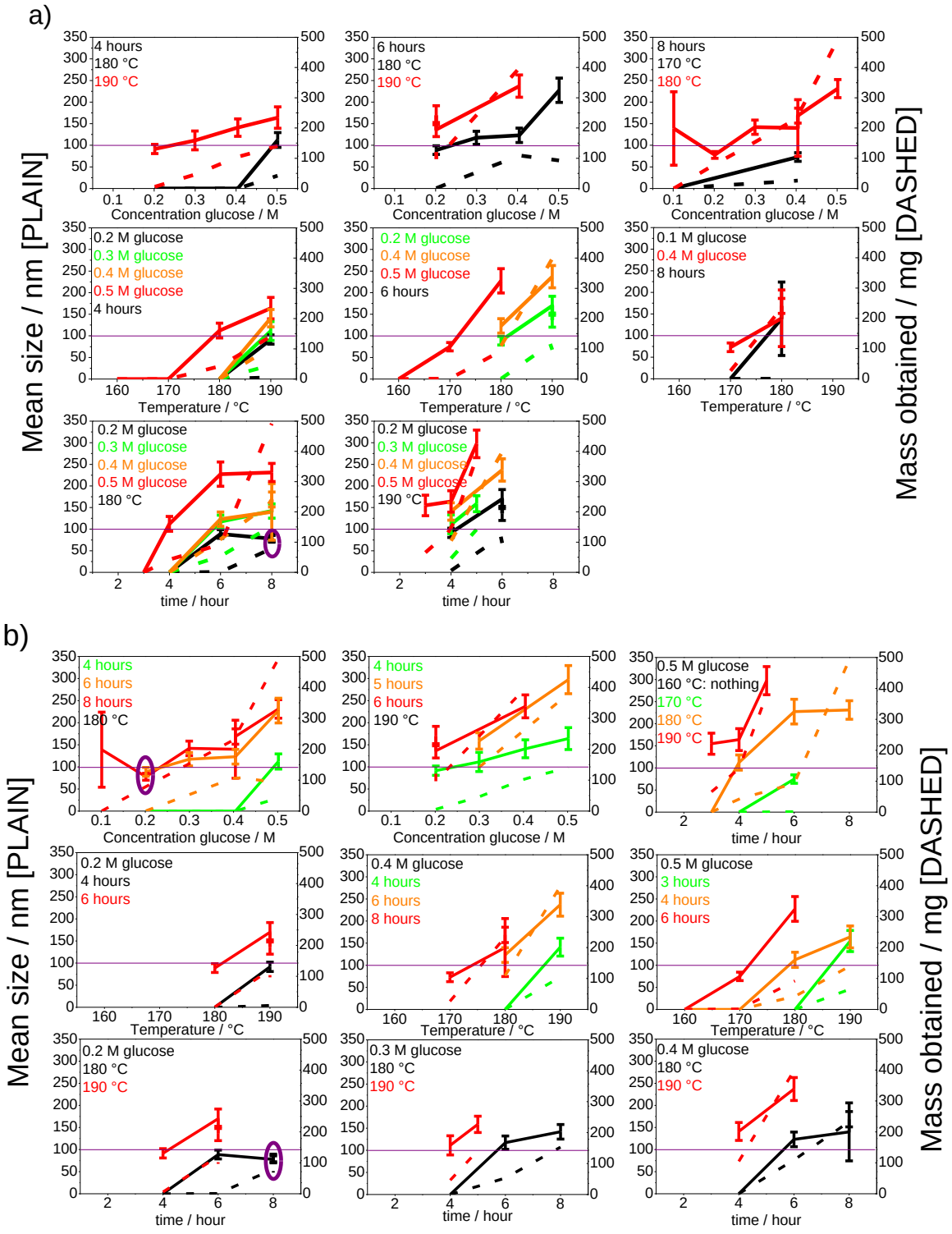

Figure A1. (a and b) Evolution of the mean size (left-hand axis) and the mass obtained (right-hand axis) for various experimental conditions in HNP synthesis. The vertical line marks 100 nm size. Data points circled highlight a compromise between a size inferior to 100 nm and a relatively high yield. The experimental parameters associated with this data point were considered optimal in this thesis.

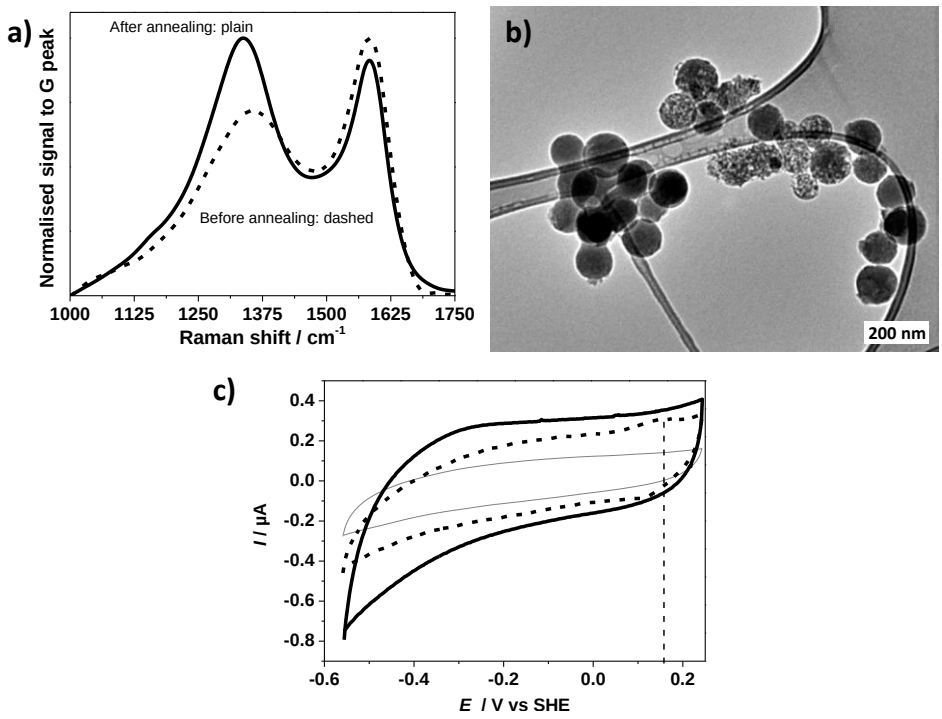

Figure A2. (a) Raman spectra of HNP before (dashed) and after (plain) annealing at 1000 °C for two hours under argon atmosphere. The intensity ratio of D and G peaks varies from 0.73 (±0.04) before annealing to 1.08 (±0.01) after annealing. (b) TEM image of HNP after annealing: no statistically meaningful change in size could be observed but some particles seem to express a different structure even though the majority of particles appear identical before and after annealing. (c) Cyclic voltammetry of HNP before (dashed) and after (plain) annealing. Spectra were recorded in a KPB (100 mM, pH 7) at a scan rate of 10 mV s^{-1}. The as-synthesised HNP (dashed) show a small oxidative behaviour around +0.15 V *vs* SHE (marked by a vertical dashed line) which disappears after annealing (plain) suggesting a more inert carbon surface after annealing. The signal from the bare PGE electrode is in grey (fine line).

Table A2. Experimental parameters investigated for the synthesis of hollow HNP material, mass obtained and particles characteristic (outer diameter size). A 'X' means that not enough material was produced to be collected.

Glucose (M)	SDS (mM)	Time (h)	T (°C)	Mass (mg)	Mean size (nm)	Deviation (nm)	Deviation (%)
-	32	8	180	X	X	X	X
0.10	6	6	170	0.6	X	X	X
0.10	6	8	160	X	X	X	X
0.10	13	6	160	X	X	X	X
0.10	13	8	180	18.5	470	112	24
0.10	32	8	160	0.5	840	72	9
0.10	32	8	180	14.8	2077	589	28
0.10	32	5	180	2.1	2044	2007	98
0.10	84	7	180	23.0	1182	726	61
0.20	13	6	160	1.4	122	24	19
0.20	13	8	170	18.3	324	48	15
0.50	6	4	160	0.2	X	X	X
0.50	6	4	170	1.4	54	7	14
0.50	6	4	180	60.5	239	27	11
0.50	6	6	160	1.2	74	25	33
0.50	6	6	160	4.1	65	11	17
0.50	6	6	180	210.6	291	33	11
0.50	6	8	160	17.1	108	18	17
0.50	6	8	180	409.7	311	33	11
0.50	13	6	160	2.6	154	31	20
1.00	6	6	160	8.8	135	14	10

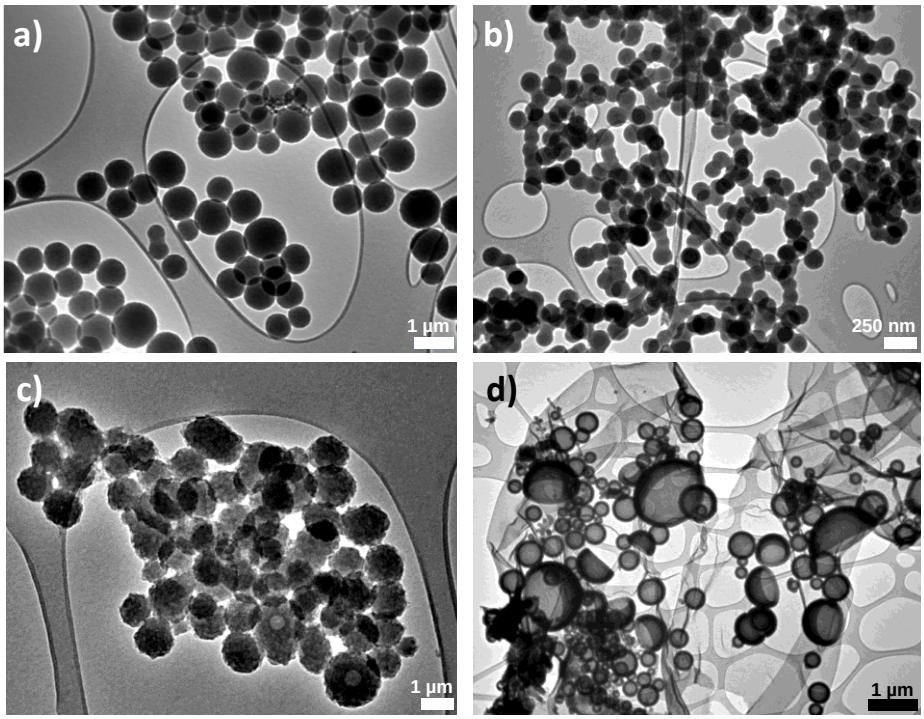

Figure A3. TEM micrographs of various structures obtained by the hydrothermal synthesis. (a) plain particles with a micron size, (b) nanoparticles, (c) plain and hollow particles, (d) too big hollow particles collapse on themselves and some amorphous carbon film can also be obtained.

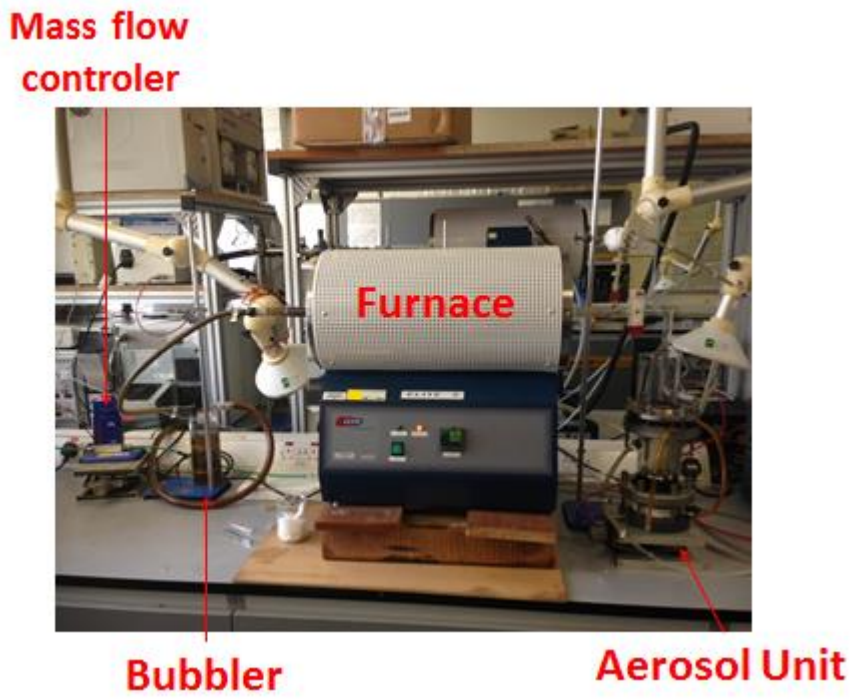

Figure A4. Picture of the AACVD set up used with its different parts.

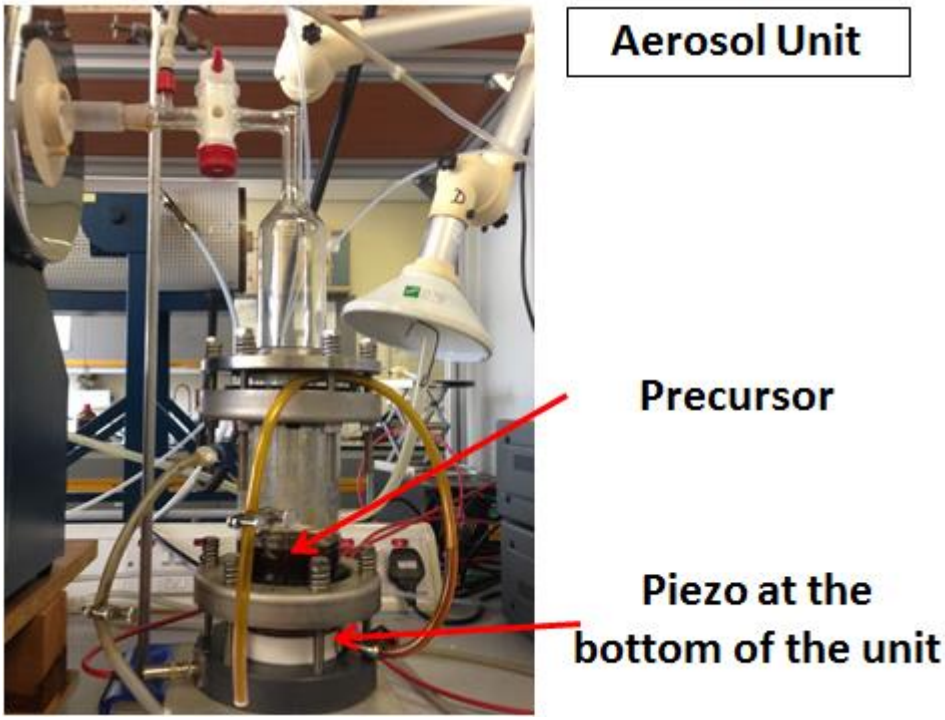

Figure A5. Picture of the aerosol unit used.

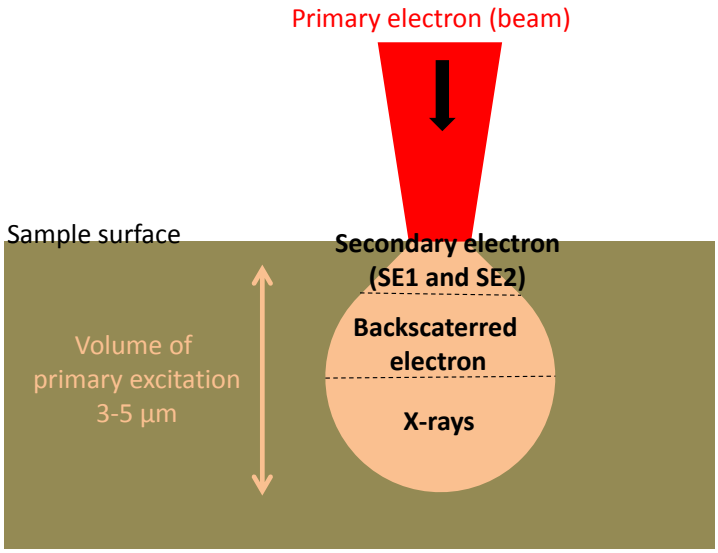

Figure A6. Schematic representation of various electrons obtained after a sample is submitted to an electron beam.

Table A3. Various types of electron and microscopy mode used in this report. The angle at which electron or radiations are emitted and the respective energy range enable to selectively look at one type or electron signal compared to another.

Technique	Electron type	Nature	Energy	Penetration depth in sample	Best for	Detector
SEM	primary electron	gun source	5-15 keV	3-5 µm		
SEM	secondary (SE1 and SE2)	inelastic scattering	< 50 eV	few nm	Surfaces topography	aside from sample
SEM	secondary (SE1)	inelastic scattering	< 50 eV	few nm	surfaces topography better contrast than with SE2	in the column (in-lens)
SEM	backscattered electron (BSE)	elastic scattering	> 50 eV	up to several 100s of nm	heavy element or composition dependent imaging	on top of the sample
EDS		X-ray		1-3 µm	Elemental analysis	EDX detector
TEM	primary	gun source	80-200 keV			
TEM	electron passing through a thin sample	interaction with the sample (wavefunction, adsorption)	transmitted electrons	through thin sample	inner morphology, individual nano-objects in projection	after the sample
EELS	electron passing through a thin sample	inelastic scattering	500 eV (loss)	through thin sample	inner composition analysis	low angle before sample

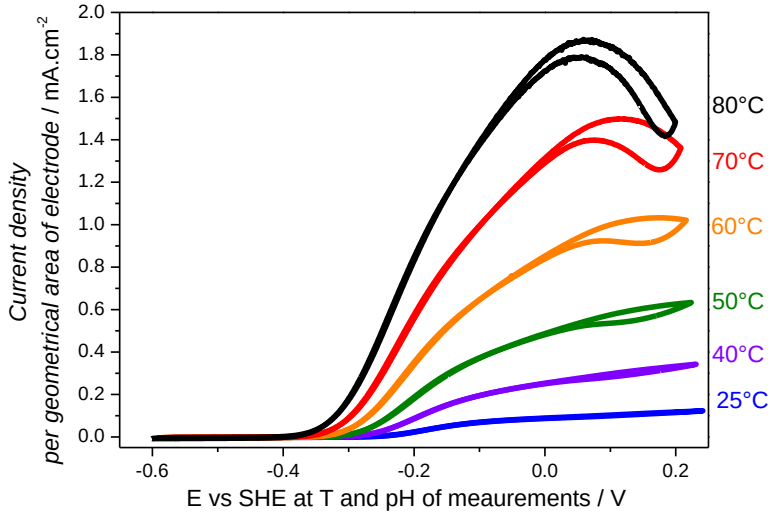

Figure A7. Cyclic voltammogram of the same film of Hyd-1 directly adsorbed on a PGE electrode. In a rather un-expected way Hyd-1 remains stable as the temperature increases. The maximum catalytic current at 25 °C is multiplied by 8.2 at 60 °C and by 15 to 80 °C. When going down in temperature after 3 hours at a temperature higher than 25 °C the enzyme activity was slightly higher than at the beginning of the experiments at 25 °C. This adds a new argument to the robustness of Hyd-1. The buffer used was KPB (100 mM, pH 6), the rotation rate was 2000 rpm and H_2 was passed into the cell at a flow rate of 1 L min^{-1}. Similar current enhancement with temperature was observed for Hyd-1 adsorbed on various carbon materials like MG, GNF, BP, or Si@C.

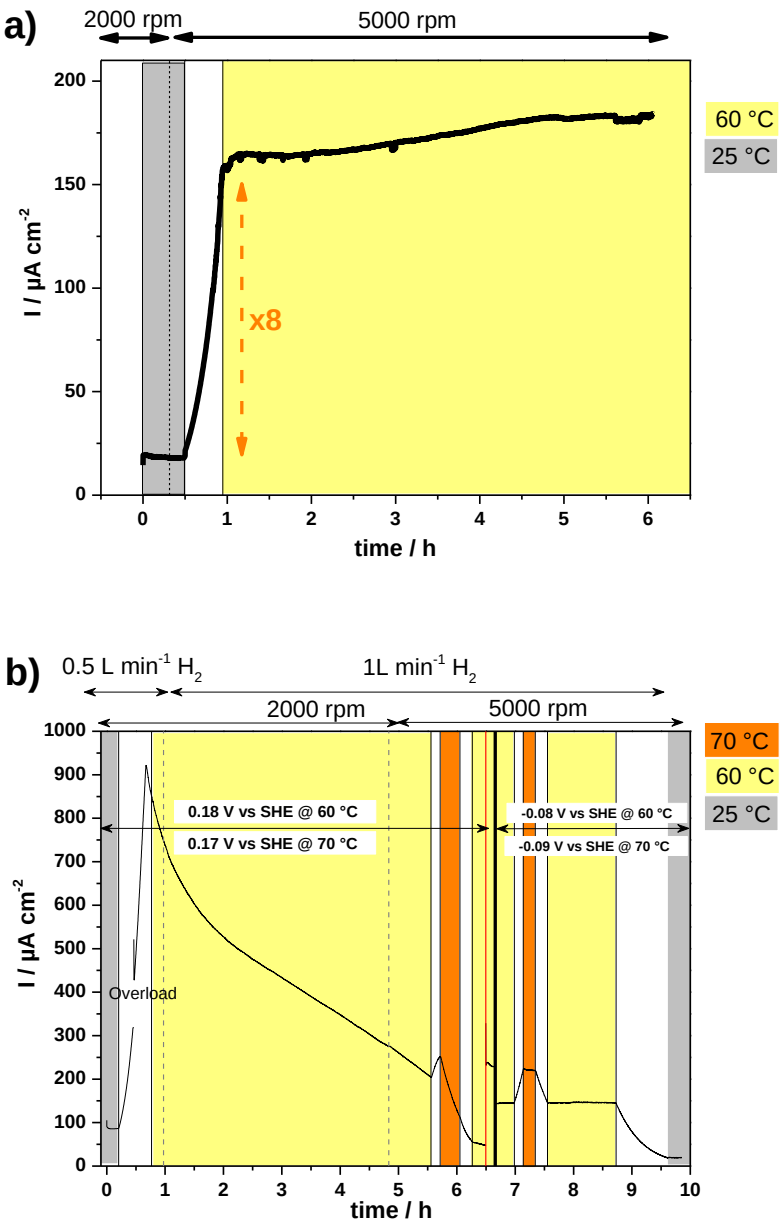

Figure A8. Chronoamperometry traces of the same film of Hyd-1 immobilised on a PGE-RDE in KPB 100 mM, pH 6 (a) under 1 L min^{-1} H_2 at -0.08 V *vs* SHE with a temperature variation during the experiment and (b) under various conditions. Results show stability of Hyd-1 over time and continuously operating at high temperature and/or under different flow rate of H_2 or rotation speed of the RDE.

Table A4. Successive potentials used in each Figure. Potentials are in V *vs* SHE.

Potentials from bottom to top as displayed in Figures in V *vs* SHE	Figure 3.17	Figure 3.18	Figure 3.19	Figure 3.21
	Top of the image			
	-0.49	**-0.49**	**0.21**	**0.21**
	-0.39	-0.39	0.11	0.11
	-0.34	-0.35	0.01	0.01
	-0.29	-0.32	-0.04	-0.04
	-0.19	-0.29	-0.09	-0.09
	-0.09	-0.24	-0.11	-0.11
	0.21	-0.19	-0.13	-0.13
	-0.09	-0.09	-0.15	-0.15
	-0.19	0.01	-0.17	-0.17
	-0.21	0.11	-0.19	-0.19
	-0.23	**0.21**	-0.21	-0.21
	-0.25	0.16	-0.23	-0.23
	-0.29	0.11	-0.25	-0.25
	-0.39	0.06	-0.27	-0.27
	-0.49	0.01	-0.29	-0.29
		-0.09	-0.31	-0.31
		-0.14	-0.33	-0.33
		-0.17	0.35	0.35
		-0.19	-0.37	-0.37
		-0.21	-0.39	-0.39
		-0.23	-0.44	-0.44
		-0.25	**-0.49**	**-0.49**
		-0.29	-0.44	-0.44
		-0.49	-0.39	-0.39
			-0.37	-0.37
			-0.35	-0.35
			-0.33	-0.33
			-0.31	-0.31
			-0.29	-0.29
			-0.27	-0.27
			-0.25	-0.25
			-0.23	-0.23
			-0.21	-0.21
			-0.19	-0.19
			-0.17	-0.17
			-0.15	-0.15
			-0.13	-0.13
			-0.11	-0.11
			-0.09	-0.09
			-0.04	-0.04
			0.01	0.01
			0.11	0.11
			0.21	**0.21**
	Bottom of the image			

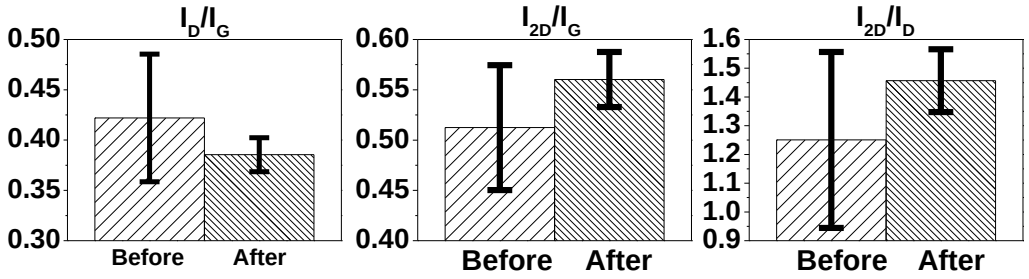

Figure A9. Comparison of various Raman intensity ratios before and after CNCs cleaning as schematised in Figure 4.2. Removing the outside MWCNTs makes it possible to assess more accurately the Raman intensity ratio of the entrance and exit of a CNC.

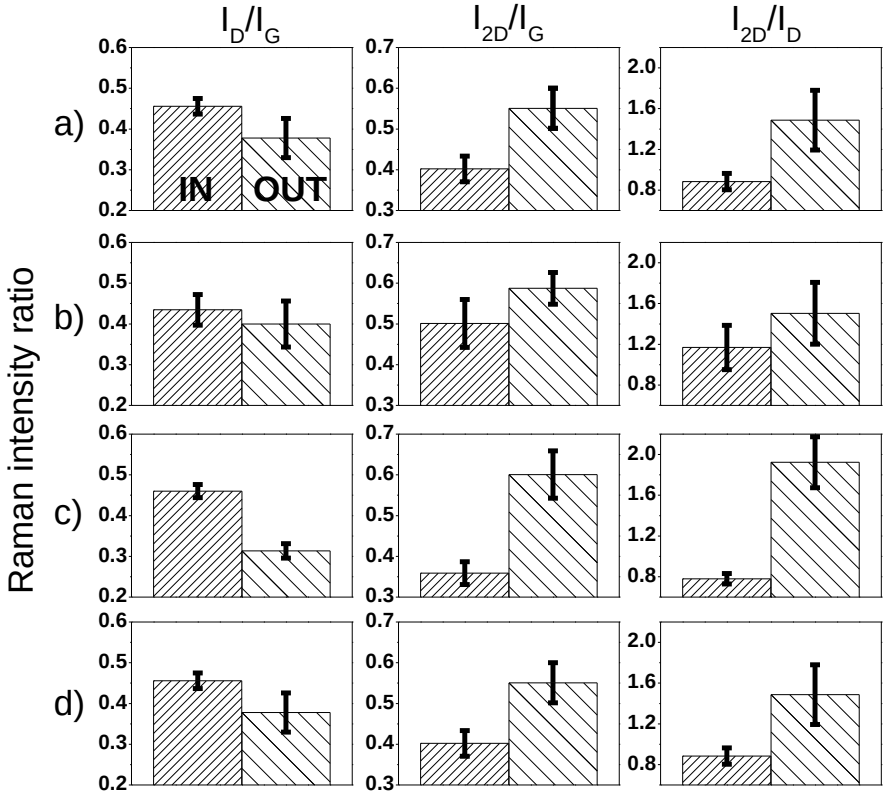

Figure A10. Raman intensity ratios comparing entrance (IN, dense stripes) and exit (OUT, sparse stripes) of a 2 cm long column with (a and b) 2 mm and (c and d) 1 mm ID. Carrier gas flow rate was 2500 sccm and experiment duration was 90 minutes. Substrates were at (a and c) 23 or (b and d) 29 cm into the furnace.

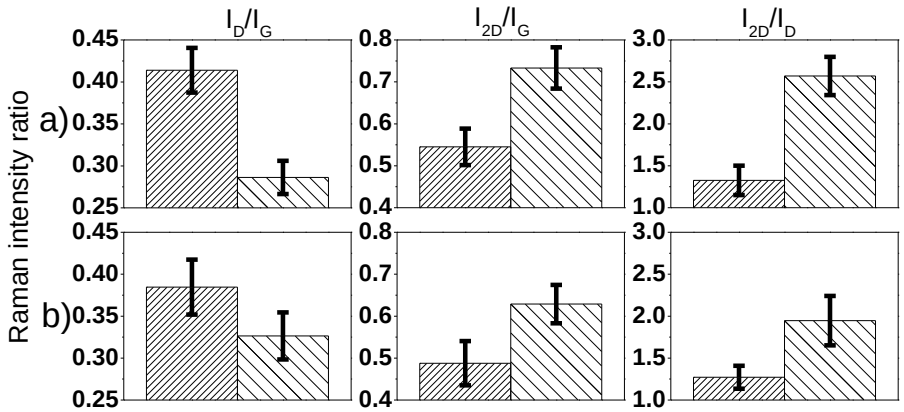

Figure A11. Raman intensity ratios of MWCNTs grown at the IN (dense stripes) and OUT (sparse stripes) positions of columns with: (a) 1 mm ID and 4 cm long; (b) 2 mm ID and 3 cm long. Carrier gas flow rate was 2500 sccm and the duration of the synthesis was 90 minutes. Substrates were placed 27 cm into the furnace.

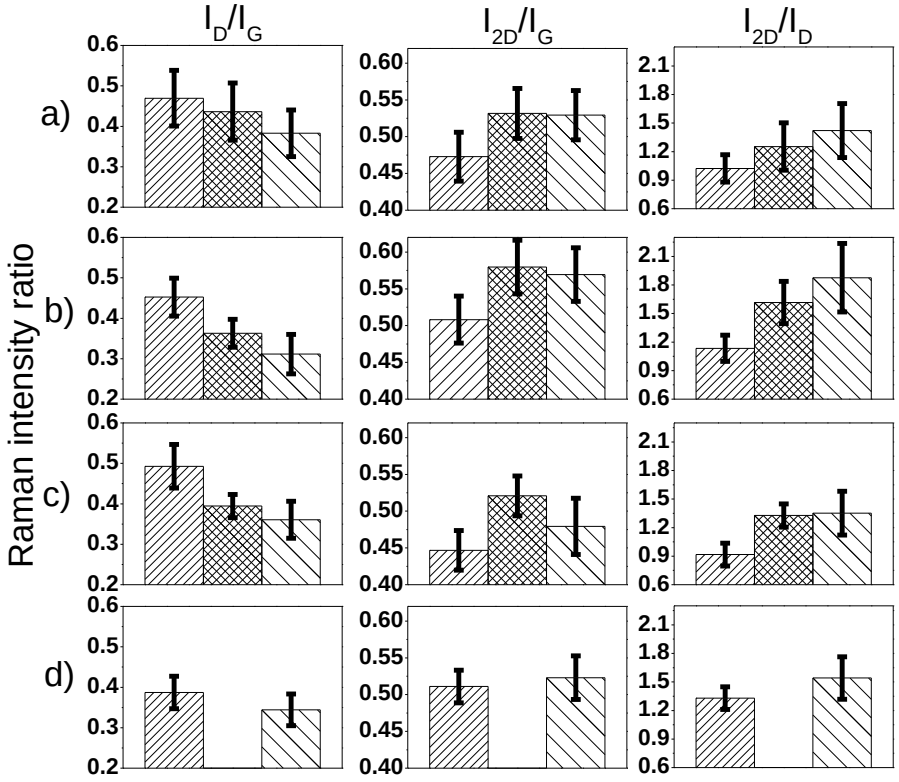

Figure A12. Raman intensity ratios of MWCNTs grown at the IN (dense stripes), middle (squared stripes) and OUT (sparse stripes) positions of columns with 2 mm ID. Columns are (a and b) 2 cm long and (c and d) 1 cm long. Carrier gas flow rate was 2500 sccm and the duration of the synthesis was 60 minutes. Substrates were at (a and c) 23 and (b and d) 29 cm into the furnace. Values of Raman intensity ratios in the middle of the column are usually not significantly different from entrance or exit.

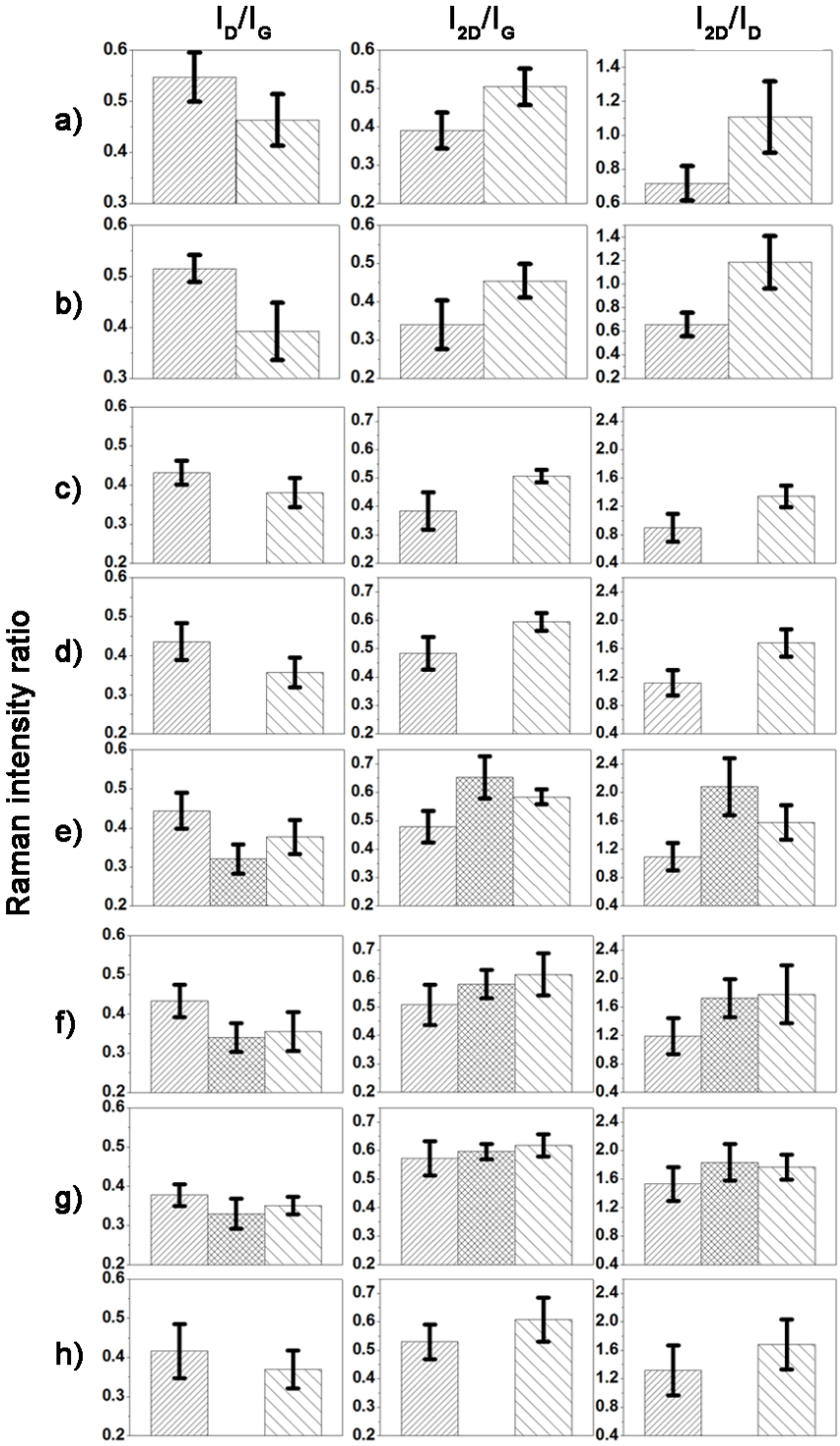

Figure A13. Raman intensity ratios of MWCNTs grown at the IN (dense stripes), middle (squared stripes) and OUT (sparse stripes) positions of columns placed at different position in the furnace: (a-b) 17, (c-e) 23 and (f-h) 29 cm. Columns were of (e and h) 1 mm and (a-d, f and g) 2 mm ID. Column length was (a, c and f) 1 cm long or (b, d and e, g and h) 2 cm long. Carrier gas flow rate was 2500 sccm and the duration of the synthesis was 150 minutes.

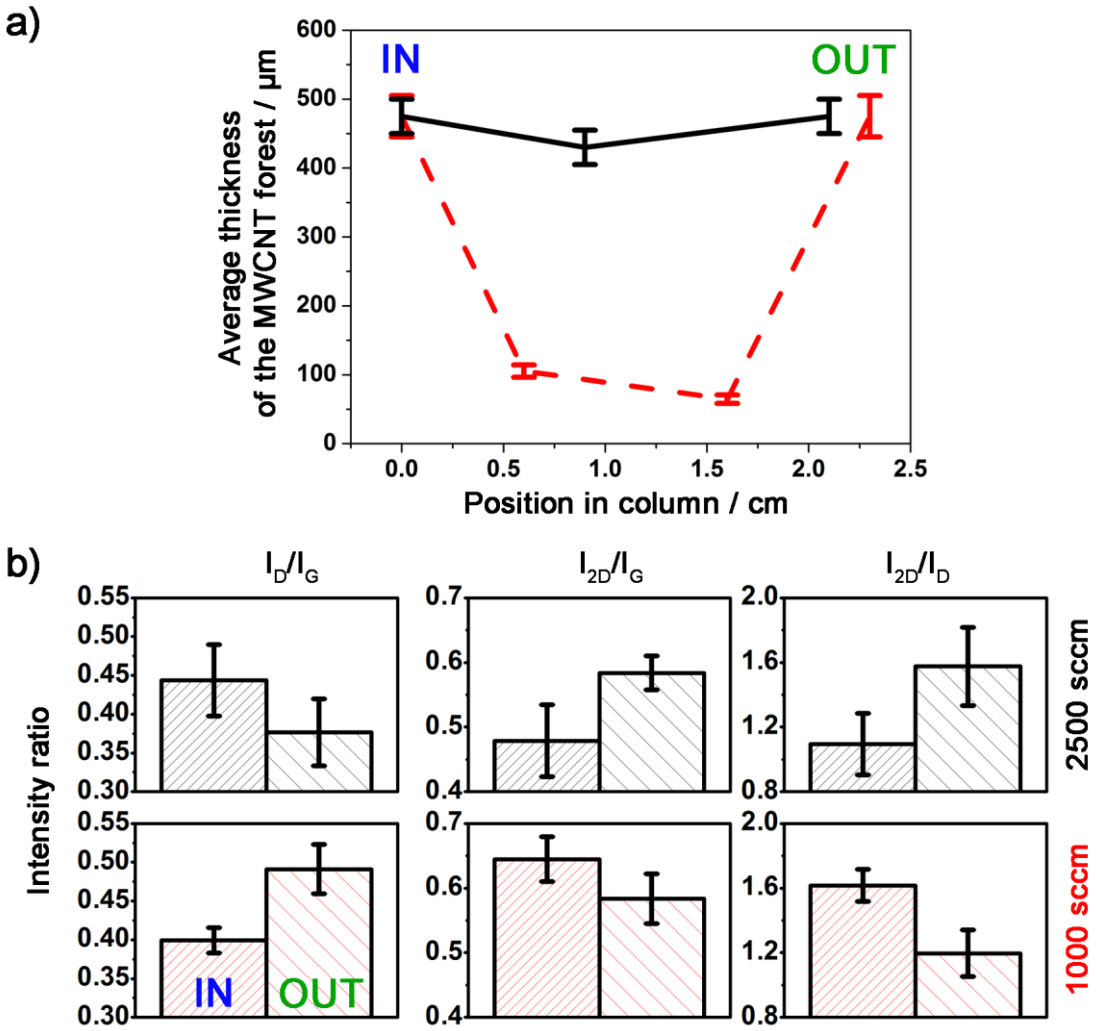

Figure A14. Effect of the carrier gas flow rate on (a) the MWCNT forest thickness profile in a column and (b) the Raman intensity ratio at the IN (dense stripes) and OUT (sparse stripes) position of a single CNC. The carrier gas flow rate was 2500 sccm (black) or 1000 sccm (red). All other experimental parameters were identical: the columns were 2 cm long with 1 mm ID, placed at 23 cm in the furnace during synthesis for a synthesis time of 150 minutes.

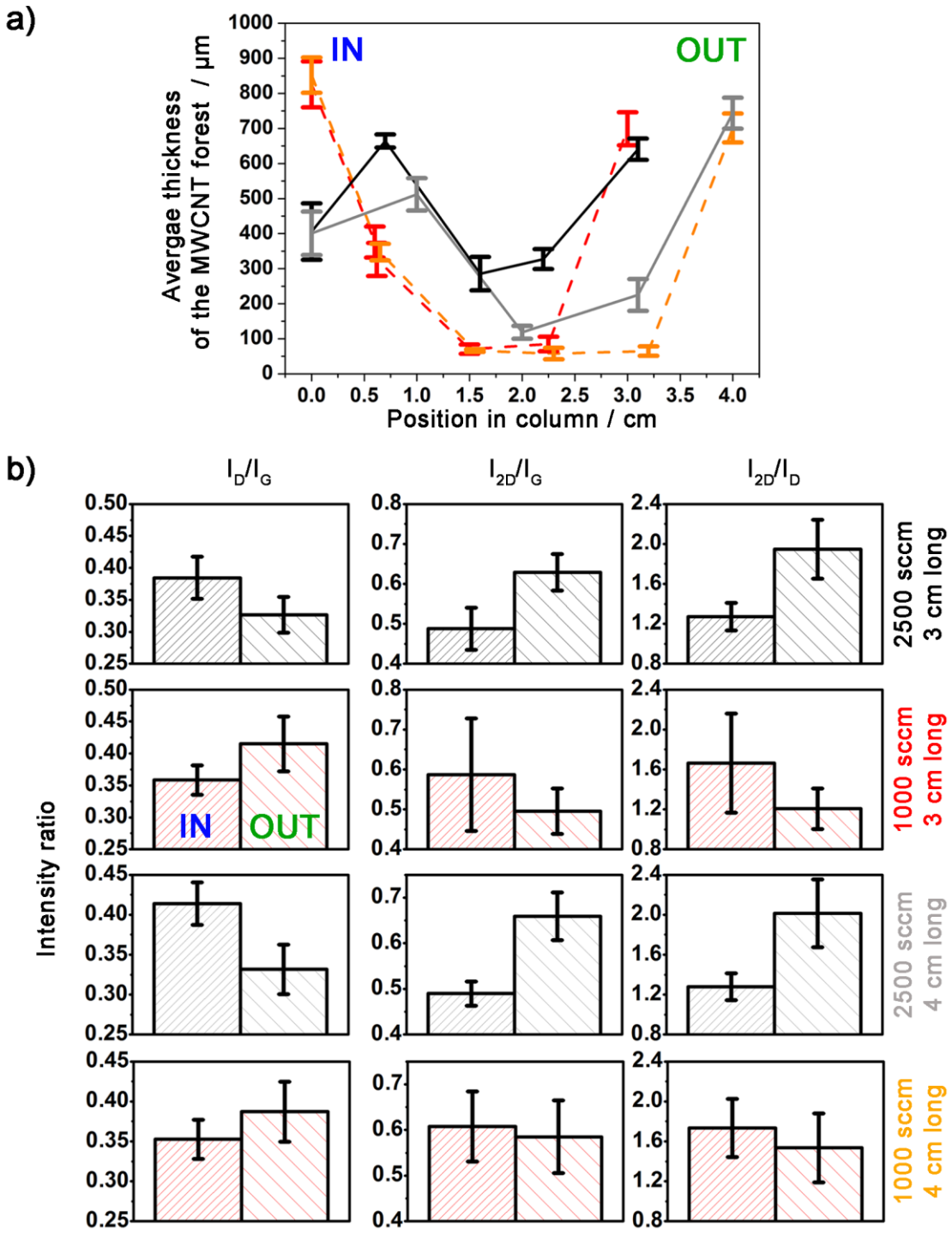

Figure A15. Effect of the carrier gas flow rate on (a) the MWCNT forests thickness profile in a column and (b) the Raman intensity ratio at the IN (dense stripes) and OUT (sparse stripes) position of a single CNC. The carrier gas flow rate was 2500 sccm (black and grey) or 1000 sccm (red and orange) and the column 3 cm (black and red) or 4 cm (grey and orange) long. All other experimental parameters were identical: the columns had 2 mm ID, were placed at 27 cm in the furnace during synthesis for a synthesis time of 90 minutes.

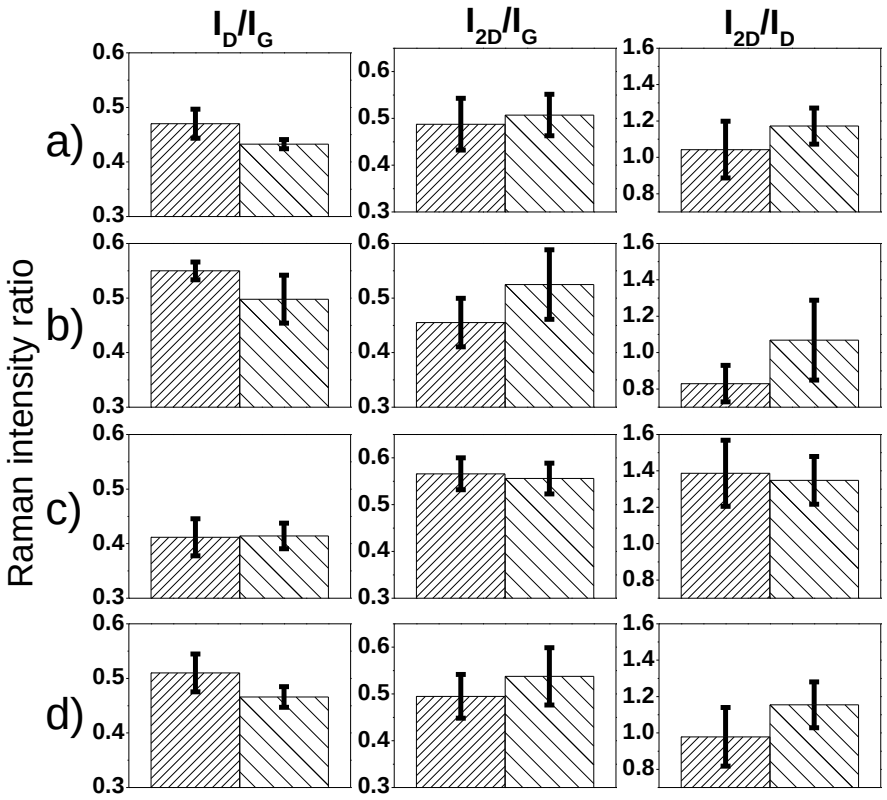

Figure A16. Raman intensity ratios of MWCNTs grown at the IN (dense stripes) and OUT (sparse stripes) positions of a 2 cm long column with (a and b) 2 mm and (c and d) 1 mm ID. Carrier gas flow rate was 5000 sccm and the duration of the synthesis was 150 minutes. Substrates were at (a and c) 39 and (b and d) 45 cm into the furnace.

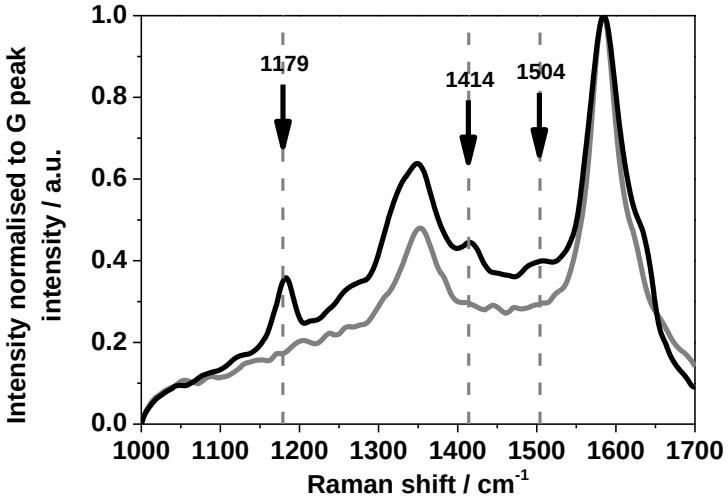

Figure A17. Raman spectra of MWCNTs grown into a CNC: before exposure to an aqueous solution of fluoresceinamine (grey line), after exposure to an aqueous solution of fluoresceinamine at a cross section in the middle of the column (black line). The column was 2 cm long.

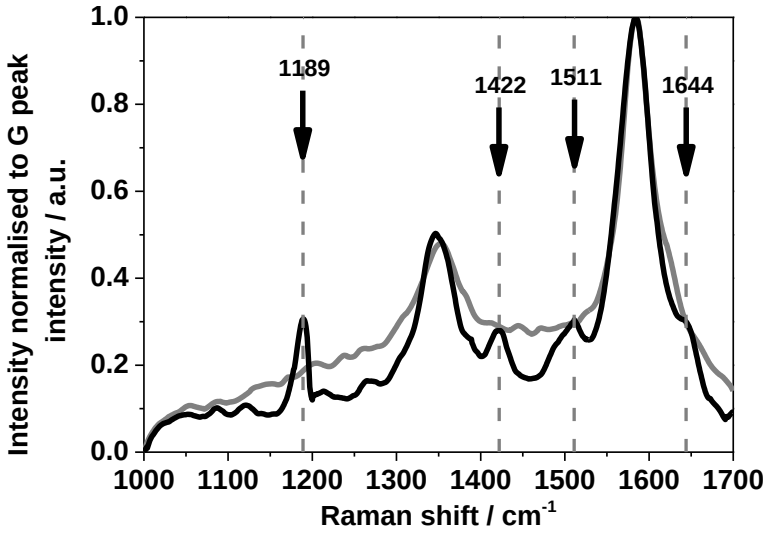

Figure A18. Raman spectra of MWCNTs grown into a CNC: before exposure to an aqueous solution of fluorescein (grey line), after exposure to an aqueous solution of fluorescein and after cross section in the middle of the column (black line). The column was 2 cm long.

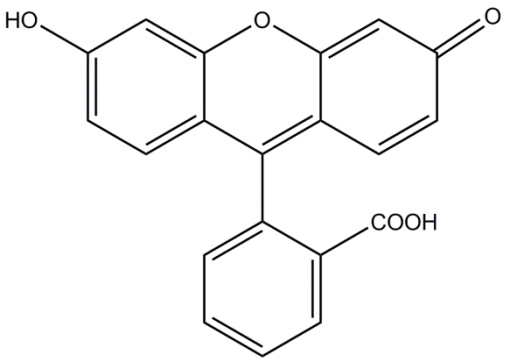

Figure A19. Molecular structure of fluorescein.

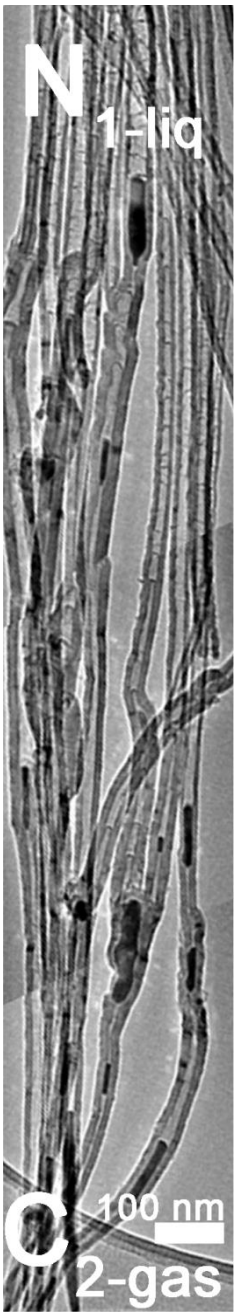

Figure A20. TEM images of several MWCNTs with junctions obtained by the liq/gas approach showing a change in structure from the $N_{1\text{-liq}}$ section (bamboo-like structure) to the $C_{2\text{-gas}}$ section (thicker walls). The image was obtained from different TEM images taken at the same magnification. The darker features are metal catalyst particles within the nanotubes.

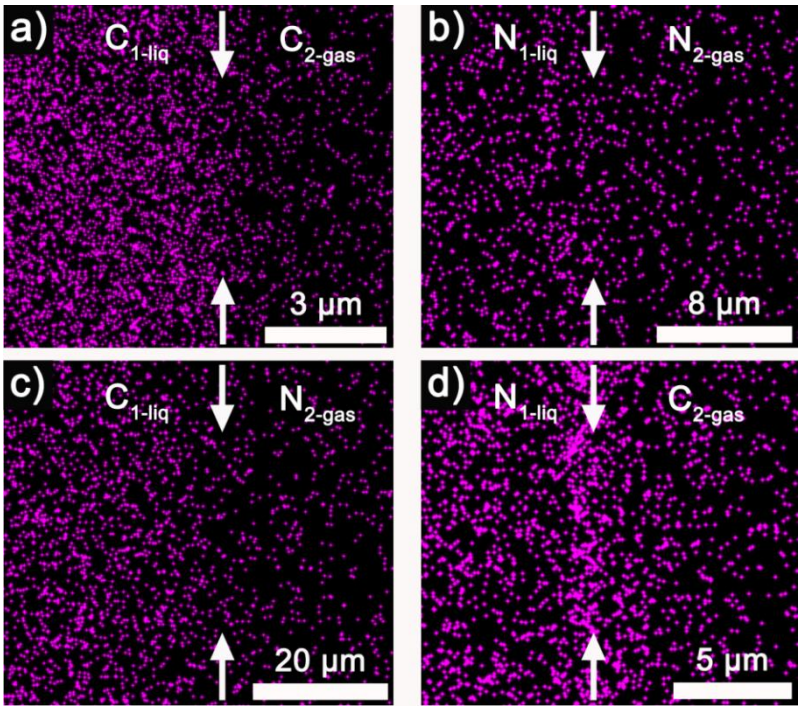

Figure A21. EDS maps of iron (from residual catalyst particles, purple, intensity of peak at 6.399 keV) on various as-synthesised structures obtained by the liq/gas approach for (a) C_1/C_2, (b) N_1/N_2, (c) C_1/N_2 and (d) N_1/C_2 structures. The iron-based catalyst particles line marking the interface is marked for the N_1/C_2 structure only (d). Arrows marked the expected interface according to related morphological change observed on back-scattered images used to define EDS mapping zones.

Table A5. Future or pending work based on research performed during the DPhil. All researchers apart from Prof Patrick Unwin (University of Warwick) are at the University of Oxford in the groups of Prof Vincent or Prof Grobert. The projects related to the results presented in Chapter 3 are in green, the projects related to Chapter 4 are in blue and the projects related to Chapter 5 are in orange. The projects without colours are results that are not detailed in the DPhil thesis even though a significant contribution has been made.

Project / Experiment	manuscript in preparation on	personal contribution	with
MWCNT forests with intratubular junction	synthesis and characterisation	concept, synthesis, characterisation	Dr Rebecca J. Nicholls Dr Frank Dillon Dr Antal A. Koós
MWCNT forests with intratubular junction	application for localised reactivity and immobilisation	concept, synthesis, characterisation, proof of concept	Dr Frank Dillon
MWCNT forests with intratubular junction	unusual nano-balls structures	observation, synthesis, characterisation	-
MWCNT columns	synthesis and characterisation	concept, synthesis, characterisation	Thomas F. Bottein (Master)
MWCNT columns	application in flow (bio-redox) catalysis	concept and proof of concept	Ceren Zor (Master) Thomas F. Bottein (Master) Dr Holly A. Reeve

Ongoing work based on research carried during the DPhil project / considered for publication	**personal contribution**	**with/for**
Spectro-electrochemistry of immobilised FMN including a set of experiments at the Diamond facility in Hartwell	help to complete the experiments and the experimental report	Ricardo Hidalgo (DPhil) Dr Philip A. Ash Prof Vincent's group
Hyd-1 operating at temperature higher than 30 °C	electrochemistry, proof of concept	Prof Vincent's group
Electrochemistry of chalcogenides	logistics, help with the electrochemistry	Arunvinay Prabakaran (DPhil) Dr Matteo Duca
Electrochemistry of nano-alloys	electrochemistry	Chris Lippard (Master) Dr Frank Dillon
Characterisation for Prof Grobert's group	13 samples characterisation (SEM)	Serena Bochereau (Master) Dr Frank Dillon
Characterisation for Prof Vincent's group	various carbon films (SEM, Raman)	Prof Vincent's group
Grand Experiment (Prof Grobert's group)	data acquisition, collection, analysis, write part of the protocols	Prof Grobert's group
Influence of substrate for the growth of MWCNTs by AACVD	characterisation (Raman)	Dr Lavina Snoek Dr Shayan Meysami
Buckypaper (specific project and group project)	supply MWCNTs, help in supervising, literature review	Benoit Grosjean (Master) Dr Shayan Meysami Prof Grobert's group
Magnetic buckypaper	concept of localised magnetic properties of buckypaper for magnetic actuators	Karwei So (DPhil)
Kier project (Prof Grobert's group)	transfer of knowledge and data on hydrothermal synthesis and Si@C nanoparticles	Dr Adrian T. Murdock
Combining MWCNT forests grown on flat substrate and chalcogenides for flow electrocatalysis (in a flow electro system different from the MWCNT column)	concept, project design, plan of action and possible gantt chart	Arunvinay Prabakaran (DPhil) Ceren Zor (Master) Dr Shayan Meysami Prof Vincent's group
Combining chalcogenides and MWCNT columns	transfer of knowledge, concept and knowhow, supply the first samples	Ceren Zor (Master)
Combining MWCNT with intratubular junction with MWCNT column (synthesis)	pre-experimental work: growing N-MWCNTs in the column is not straightforward but it is possible to combine the two concepts	-
Possible future work	**personal contribution**	**with**
Electronics (I-V curves) and/or magnetic properties of MWCNT with intratubular junction	synthesis and characterisation	Dr Juan G. Lozano Dr Frank Dillon
Localised electrochemical response and catalytic activity on MWCNT forests with intratubular junctions	concept, synthesis and characterisation	Possible collaboration: Prof Patrick Unwin's group
Combination of AACVD and CVD and/or MWCNT with intratubular junctions as template to develop other Janus-like nanomaterials	concept, synthesis, characterisation, proof of concept	Dr Shayan Meysami
Improved MWCNT columns filling by AACVD by promoting an isotropic flow distribution of the carrier gas during synthesis	general idea	Dr Shayan Meysami
Combining nitrate reductase and platinum particles for water purification	general concept of MWCNT columns for flow (redox) catalysis and filtration	Ceren Zor (Master) Justin Weeks (Master) Dr Matteo Duca
Combining MWCNT with intratubular junction and MWCNT column (applications)	general concept	-